EFFECT OF TITANIUM DIBORIDE PARTICLE SIZE ON AL-ALLOY PROPERTIES

by

James Michael Taylor DAVIES

UNIVERSITY OF BIRMINGHAM

A Thesis submitted to

University of Birmingham

for the degree of

DOCTOR OF PHILOSOPHY

School of Metallurgy and Materials

University of Birmingham

January 2017

ABSTRACT

Most experimental studies which investigate aluminium alloys and TiB_2 additions focus on varying the quantities of material added to the alloy. This thesis attempts to address the lack of information regarding to what effect the particle size distribution of the TiB_2 additions has on an A205 alloy. To do this the TiB_2 particles were removed from the A205 alloy by dissolution in hydrochloric acid. The resulting particles were then subjected to a particle size analysis procedure carried out on a Malvern Mastersizer particle size analysis machine.

Comparison of TiB_2 particle size distributions collected from; as-cast A205, solution heat-treated A205, solution heat-treated and precipitation hardened A205, and Al-5Ti-1B grain refiner rod, revealed a variation between results attributed to copper contamination. In effort to purify the experimentally collected material an electrochemical refinement procedure was trialled with partial success in reducing the measured TiB_2 particle size distribution collected from fully heat-treated A205. All resulting particle size distributions were combined with the measured grain size and grain to grain boundary volume fraction values, and incorporated into a predictive yield strength model.

Following the measurement of Al-5Ti-1B grain refiner's TiB_2 particle size distribution, a series of TP1 grain refinement tests were conducted to investigate the effects of different TiB_2 particle sizes found at both extremes of the measured grain refiner's TiB_2 particle size range. Through a series of Al-5Ti-1B settling experiments, samples containing different sizes of TiB_2 were created, compositionally analysed using ICP, and used for the TP1 tests. The results of which confirmed the resulting grain sizes to be statistically different from one another.

ACKNOWLEDGMENTS

I would like to express my most sincere thanks to my supervisor Dr W. D. Griffiths for providing me with the opportunity to study Metallurgy and carry out the research that resulted in this thesis. His encouragement and mentoring, throughout my PhD have been invaluable.

I would also like to thank Aeromet International PLC for funding this PhD project, and I wish them every success with their alloy.

I would also like to thank the many staff from various departments throughout the University of Birmingham who have helped with this research.

From the Metallurgy and Materials department; Mr. Adrian Caden who has helped with castings and emotional support, Dr Artemis Stamboulis for the use of her lab, Dr Daniel Reed for the use of his XRD equipment and support, Mr Jaswinder Singh for the use of his lab, Dr Felicity de Cogan for her help, and Mr Carl Meggs for his sense of humour.

From the electrochemistry department; Dr Neil Reiss for his kind support, advice and the use of his lab, Dr James Courtney for his help and advice, and Mr Haldane Robbs for his help and support.

From the chemistry department; Dr Jackie Deans for the use of her XRF and XRD equipment and kind support, and Dr Benjamin de Laune for his help and support.

And finally I would like to thank all my friends and family for their love and support throughout this PhD program, especially my mother and my father for always being supportive, my brother Tim for never giving up on me, my girlfriend Shiling for encouraging me, and those now above who look down and guide me.

It has been quite a ride.

Table of Contents

List of Figures

List of Tables

1 INTRODUCTION

1.1 Background

Traditionally cast materials have been viewed as low quality objects that often contain integrity flaws and hence were only used for non-critical components. Today aluminium alloys are becoming the go-to material in light-weight performance products and are fast becoming the new staple in the aeronautical and performance car industries. Such a change has been brought about by the sustained effort to further understand the metallurgy of cast components allowing for the creation of higher performance alloys for use in tomorrow's applications.

Aluminium copper alloy A205 has been developed by Aeromet International PLC as the new benchmark material for higher performance applications. Developed for use in the aeronautical industry, A205 markets itself as having excellent mechanical and fluidity properties brought about, in part, by its high TiB_2 weight percentage.

Although the effects of having such a large TiB_2 weight percentage are broadly known; a thamnitic microstructure and improved feeding, there is still a lack of fundamental understanding on how the TiB_2 particle size distribution effects the properties of the A205 alloy.

1.2 Aims and objectives

The broad aim of the research project was to explore and document the relationship between TiB_2 particle size and the mechanical properties of A205. To fulfil this ambition the most significant processes were:

- The development of a technique to remove in situ TiB_2 particles contained within the A205 alloy
- The subsequent measurement of the collected particle size distribution
- The measurement of various material characteristics including grain size, and grain to grain boundary volume fraction calculations
- The inclusion of the results into a predictive yield strength model and the subsequent comparison to experimentally measured yield strength results

To support this research an additional line of investigation in which the grain refining properties of qualitatively different sized TiB_2 particles was explored. To examine this effect a series of castings were held for various settling times and the resulting solidified material statistically compared using the TP-1 standard test procedure for aluminium alloy grain refiners.

2 LITERATURE REVIEW

2.1 A205

A205 is an aluminium copper alloy developed by Aeromet International PLC, and is considered to be the world's strongest commercially available cast Al-Cu alloy. A205's standing within the world's market place is due to its high 0.2% proof and UTS values which outperform more traditional aerospace alloys such as A356. Its composition includes: 4.5 wt% Cu, 0.6 wt% Ag, 0.3 wt% Mg and 0.25 wt% Ti and a 4.5 wt% TiB_2 micron-sized reinforcement phase.

Previous work directed towards the development of A205 investigates the effects of Ti and TiB_2 additions on the alloy. Simon Butler (2000)[1], the initial developer of the alloy, discovered that increasing the levels of TiB_2 within the alloy altered the solidification mechanisms such that the solidified grains were thamnitic in nature as opposed to dendritic. The resulting thamnitic, or globular nature of the alloy promoted better feeding during solidification and hence eliminated inter-dendritic shrinkage and porosity issues - known to reduce mechanical properties. During A205's development Butler also realised TiB_2's influence on the incipient melting of an Al-Cu-Mg-Ag phase found within the as-cast grain boundaries, and its subsequent prevention at TiB_2 levels of >2.9 wt%, therefore allowing for higher temperature heat treatment procedures.

The addition of TiB_2 to aluminium alloys is a common occurrence due to its well established grain refining properties. However, at such a high levels the effect of TiB_2 goes beyond exclusively grain refinement and also begins to act as a reinforcement phase within the grain boundary material. Hence A205's classification as a metal matrix

composite (MMC) material. As a reinforcing particulate, TiB_2 is an inert ceramic with a high heat conductivity and a high Vickers hardness value[2]. It is for this reason that this work will investigate the effects of TiB_2 particle size on aluminium alloy properties.

2.2 Solidification

A change from a liquid to a solid is a complex process when considered on a microscopic level. When a pure metal solidifies each individual crystal begins to grow from a centre of crystallisation. Pure aluminium solidifies at 660°C. The nucleus for aluminium is a unit of face-centred cubic (FCC) lattice, from which the crystal will grow. As the aluminium crystal grows additional atoms will have to conform to the FCC lattice parameters. During the crystals development, areas of the lattice will grow at a faster rate than other areas forming arms, known as dendrites, into the surrounding liquid, see Figure 2-1.

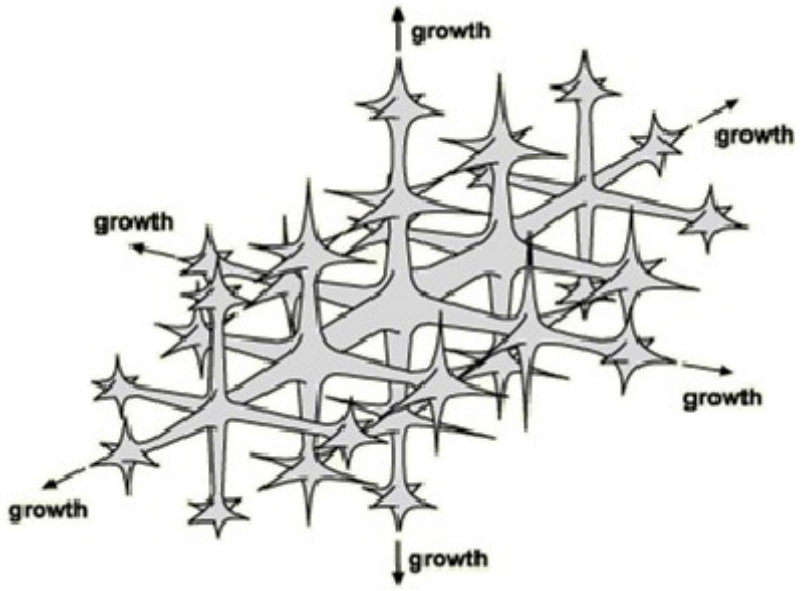

Figure 2-1 Pictorial representation of a dendritic crystal[3]

2.3 Columnar & Equiaxed Crystals

In general metals which have been cast have three distinct grain structure zones. A chill zone of small crystals resulting from rapid cooling at the very edge of the cast. A zone of long thin crystals which have grown in the direction of heat flow and an area of equiaxed, roughly symmetrical crystals at the casting's centre, see Figure 2-2.

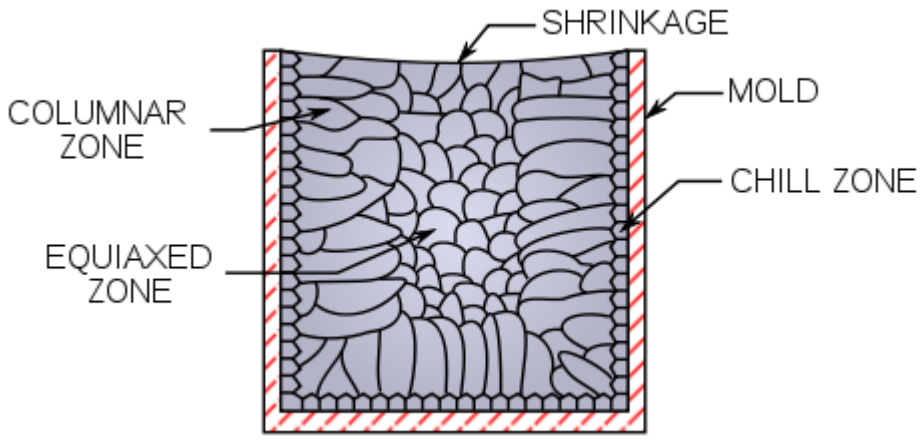

Figure 2-2 Crystal structure in a cast component (not to scale)[3]

The visible macrostructure of a casting is influenced by a range of factors. Variables which affect the macrostructure include the casting's size, the alloys' composition, super heat, fluid flow, mechanical processes, inoculations, and grain refiners. The size of the mould affects the macrostructure of the casting due to its relation with superheat. Increasing the superheat increases the extent of columnar growth[4–11]. It has been observed that increasing the cross section of a mould design, increases equiaxed grain productions[6,9,12]. Increasing the alloying content (C_0) reduces the columnar region[8–11,13–16]. Increased mechanical vibrations can increase the equiaxed zone due to grain refining effects[17,18]. The use of grain refiners can reduce the columnar region of

solidification[8,9,15,19–21]. Increasing the fluid flow can decrease the columnar region[4–6,8,22–25].

An important region of a cast component is the equiaxed zone. This zone is the largest by volume and contains small homogeneously shaped particles which play a significant role in the overall mechanical strength of the material. The formation of the equiaxed zone requires small seeding particles in the bulk during solidification. There are three mechanisms believed to be responsible for the production of these seed particles; constitutional supercooling driven heterogeneous nucleation, dendrite detachment mechanism and the big bag mechanism.

2.4 Constitutional supercooling driven mechanism

All liquids have a freezing point, the temperature at which the constituent elements no longer have enough energy to move around randomly but are more energetically suited to grouping with one another until the entire volume of liquid has fallen into a lower-energy solid state. However, lowering the temperature of a liquid to below its freezing point does not guarantee nucleation. As the temperature and hence energy of the system falls the movement of the liquid particles decreases[26]. This energy change is such that liquid particles can now join together in crystalline arrangements. For the small particles to survive as a solid, their free energy, ΔG, must be negative. Taking the theoretical scenario of a small cube of dimensions d of a newly formed solid just below its freezing point, its net energy will decrease in proportion to its volume d^3 and its associated free energy ΔG_v. Simultaneously the creation of a new surface area of $6d^2$ provides extra energy to this theoretical scenario due to the interfacial energy γ per unit area. Therefore, the final energy of this system is[27]:

$$\Delta G = 6d^2\gamma - d^3\Delta G_v \qquad \text{-Equation 1.}$$

Figure 2-3 shows a graphical representation of the relationship between surface energy (red line), volume energy (blue line) and the total energy (green line) of a small nucleating solid at its freezing temperature[27]. The figure shows that if the nucleating particle doesn't reach a critical size (d*) during its initial creation its free energy value will be positive resulting in the solid breaking apart. It is only when the temperature of the liquid is sufficiently low, allowing a greater number of coincident interactions to occur at the same time will the particle size pass the threshold size d*. When this condition is met subsequent particle additions to the nucleating solid will further reduce its free energy resulting in runaway growth[26]. The temperature at which this process occurs is known as the homogeneous nucleation temperature which for some metals, such as nickel, may be far lower than their equilibrium freezing point by several hundred degrees. In a casting scenario the areas which provide sufficient cooling for these freezing events to initiate is at the mould's walls[28].

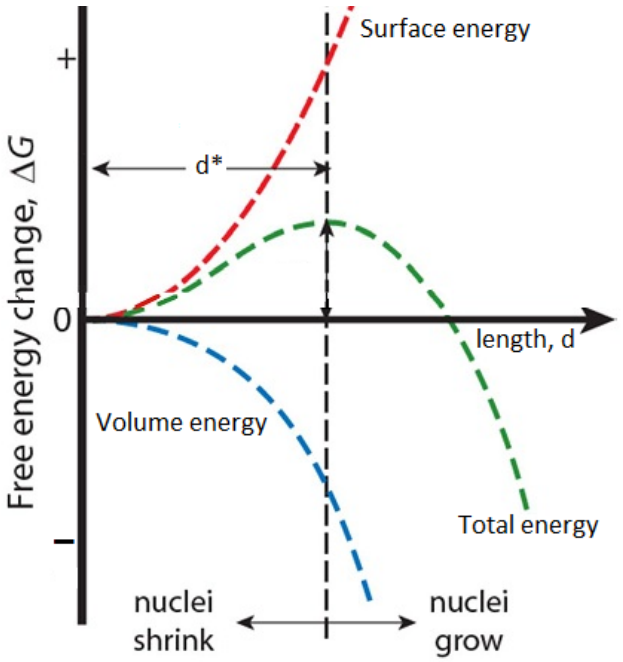

Figure 2-3 Surface and volume energies of nucleating particle[29]

For a liquid to continue to solidify the excess heat of the system must be extracted, this is only possible by conduction through the newly formed solid. This in turn reduces the thermal energy ensuring that the progression of the solidification continues. The speed of the advancing front R is linked to the temperature gradient between the solid and liquid fronts, and hence heat extraction[28]. For an alloyed melt, the solidifying of the primary phase increases the concentration of alloying agents at the solidifying front. As the composition of the liquid at the solidifying front changes, the increase in alloying elements acts so as to locally lower the melting point of the liquid to below that of the actual temperature. This phenomenon is referred to as constitutional supercooling[28].

Figure 2-4 highlights the relationship of the constitutional supercooling theory. When the composition C_0 first freezes the first solid of composition k_0C_0 is formed. The final liquid to solidify C_0/k_0 leaves behind a solid of composition C_0. The 'partition' coefficient

or the 'equilibrium distribution' coefficient is equal to the relative amount of the composition of the solid formed (C_s) to the composition of liquid frozen (C_L) to make that solid. It is common for the partition coefficient to have a fractional value. For values close to 1, the spacing between the solidus and liquidus lines is narrow therefore allowing a minimal chance of segregation in the melt. When k is small there is a large spacing between the solidus and liquidus lines indicating large partitioning[29].

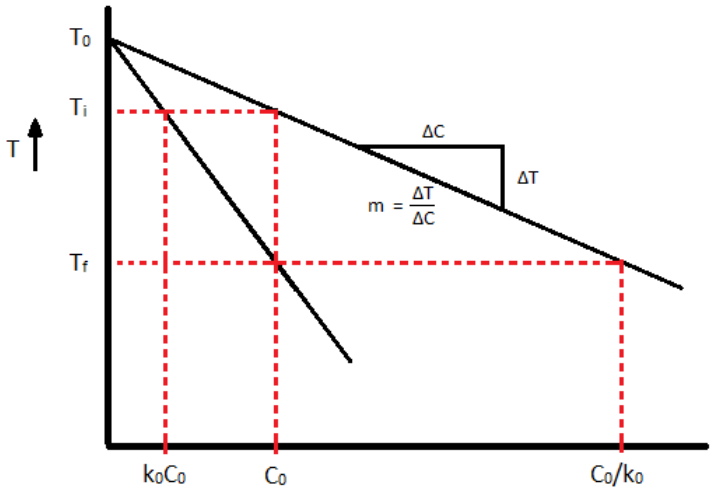

Figure 2-4 Phase diagram showing constitutional supercooling theory[29]

The equation which governs the constitutional undercooling, the ratio of the rate of the advancing solid interface R to the temperature gradient G is Equation 2. The right hand side is the constitutional supercooling parameter. High values of the constitutional supercooling produce equiaxed structures where as lower constitutional values promoted the formation of larger grained columnar structures[13].

$$\frac{G}{R} \leq \frac{m\,C_0}{D}\left(\frac{1-k_0}{k_0}\right)$$ -Equation 2.

Were m is the gradient of the liquidus line, C_0 is the original melts composition, D is the diffusion coefficient of the solute and k_0 is the partition coefficient. The ratio of the temperature gradient G and R, the rate of advance of the solid interface, has a large influence on the type of crystal structure formed in the solidifying melt. The driving force for solidification increases with time which alters the behaviour of the solidifying front. When a solidification event nucleates from a mould wall its growth is planar[28]. As the solidification rate increase the solidifying front develops regularly spaced intrusions which do not advance at the same rate as the solidifying front. These perturbations lead to the change from planar to columnar grain growth. Finally, with a further increase in the solidifying front's advancements, columnar grains become unstable resulting in the formation of dendritic grain growth[26].

2.5 Dendrite detachment mechanism

An alternate mechanism for explaining the formation of equiaxed crystals in the melt is the dendrite detachment mechanism. This explanation was developed due to the results collected from an experiment which noted that stirring or convective mixing of a similar material during solidification resulted in a larger number of nuclei forming in the cast[30]. From these results it was hypothesized that the increase of equiaxed crystals is due to fluctuations in the growth rate. This caused dendrite arms to melt and separate from their parent bodies which then become relocated into the centre of the melt. Other causes of dendrite arm detachment have been suggested to be caused from re-melting –as theoretically there may be sufficient solute present to locally alter the melting point around the dendrite, as well as mechanical agitation. Convection currents could cause

dendrite arms to become detached from their parents due to the yield point of the material being negligible when temperatures are so close to its melting point[31].

The dendrite detachment mechanism is consistent with the experimental results considering the coriolis force[22] and convection currents induced by a magnetic field[4,23,32]. However, the dendrite mechanism is unable to explain experimental results where, in the absence of pouring turbulence and also the absence of a convection promoting alternating magnetic field (removed after the melt had reached its freezing plateau), the solidifying melt did not show signs of equiaxed structure[28]. This result implies that the dendrite detachment mechanism was not present. This mechanism, however, is able to explain the equiaxed zone formation when the mould is heated so as to prohibit the chilling effect on the mould walls, and also when heterogeneous nuclei were absent from the melt – something that the constitutional undercooling and big bang mechanisms are unable to do.

2.6 Big bang mechanism

In the big bang mechanism equiaxed grains are formed in the initial pouring of the melt into the mould. As the liquid first comes into contact with the mould walls it solidifies and forms grains which are then carried into the body of the mould by fluid flow. Here the solidified crystal particles survive through melting until the superheat has been removed[33], at which point they will grow into equiaxed grains. The big bang mechanism has been tested using saturated NH_4Cl solution with promising results[34,35]. An advantage of the big bang nucleation mechanism theory is that it can explain the effects of convection and superheat in the initial stages of casting. Raising the pouring temperature reduces the dimensions of the equiaxed zone and raises the grain size. Reducing

convection in the melt can eliminate the equiaxed zone entirely. The big bang mechanism is able to provide an explanation for these effects. Reducing convection lowers the amount of nuclei produced at the edges of a casting which are able to reach the centre. Raising the superheat lowers the chilling of the melt as it is poured and raises the time required for the bulk superheat to dissipate. This leads to a lower number of nuclei being produced by pouring, and of these fewer will survive to grow into equiaxed grains as they are more likely to be re-dissolved by the melt as it cools.

2.7 Nucleation

Nucleation is the grouping together of clusters of atoms which characterize the development of a new phase. Nucleating particles grow until the liquid phase has been entirely converted into a lower energy solid form. Nucleation events can be either homogeneous or heterogeneous[27].

2.8 Homogeneous nucleation

Homogeneous nucleation is based upon the Gibbs free energy theory. The Gibbs free energy (G) is the energy between different phases and how this energy value is changed by the introduction of new surfaces i.e. the change from liquid to solid.

For the growth of a solid sphere of radius r and σ as the surface free energy per until area, the total change of the Gibbs free energy value ΔG is[27];

$$\Delta G = \frac{4}{3}\pi r^3 \, \Delta G_v + \, 4\pi r^2 \sigma \qquad \text{-Equation 3.}$$

When a liquid changes to a solid the surface free energy σ is negative. At temperatures below the melting temperature of the material the total Gibbs free energy is[26];

$$\frac{d\Delta G}{dr} = 4\pi r^2\,\Delta G_v + 8\pi r\sigma = 0 \qquad \text{-Equation 4.}$$

For small values of r, the value of ΔG initially increases until reaching a threshold value of r* before decreasing. This initial raise in the free energy at temperatures below the melting temperature of the material is due to the energy linked to the surface area of the growing phase. It is only after r* that the Gibbs free energy value, which is linked to volume, that the total free energy of the system starts to decrease. For this reason r* is referred to the critical radius for nucleation which is given by the equation[27];

$$r^* = -\frac{2\sigma}{\Delta G_v} \qquad \text{-Equation 5.}$$

Taking the critical radius of nucleation into consideration a value of the Gibbs free energy at this radius can be calculated to be[27];

$$\Delta G^* = -\frac{16\pi\sigma^3}{3\Delta G_v^2} \qquad \text{-Equation 6.}$$

The value for ΔG* is a threshold value for the formation of homogeneous nucleation. This value is linked to the solidification temperature of the material which for some materials may require several hundred degrees of undercooling before nucleation is permitted. It is for this reason that heterogeneous nucleation will be the preferential mechanism for the formation of solids as the homogeneous nucleation mechanism requires a far larger free temperature difference to occur[28].

2.9 Heterogeneous nucleation

It is rare for a melt to be pure, it is often the case that an alloy is being used for casting or that contamination particles have found their way into the liquid material. Regardless of

where these particles have come from they have the potential to act as nucleating sites for the solidification of the melt. Other nucleating sites include the mould walls.

Mechanisms which may be responsible for heterogeneous nucleation include the growth of additional phases which would act as nucleation sites for the growth of the phase in interest, or dissolution processes which would distribute nucleating particles within the melt[27,36].

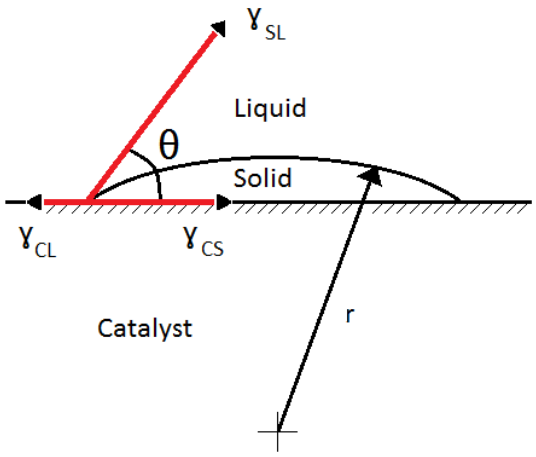

Figure 2-5 Heterogeneous nucleation[36]

Heterogeneous nucleation is dependent upon the ability of a crystal to adhere to the surface of a catalysing particle. This is given by the angle θ which is related to the materials wettability, see Figure 2-5. By measuring the contact angle θ it is possible to calculate the critical nucleation radius r*. Provided that the angle θ is between 0 and 90 degrees the solid-liquid area, the catalyst-solid area and the nucleus volume can be calculated[27,37];

$$solid - liquid\ area = 2\pi r^2(1 - cos\theta) \quad \text{-Equation 7.}$$

$$catalyst - solid\ area = \pi r^2(1 - cos^2\theta) \quad \text{-Equation 8.}$$

$$nucleus\ volume = \frac{2\pi r^3}{3}\left\{1 - \frac{3}{2}cos\theta + \frac{1}{2}cos^3\theta\right\} \quad \text{-Equation 9.}$$

Combining these values together, with the appropriate interfacial energies, allows a net work (W) value for heterogeneous nucleation to be determined[37];

$$W_f = 2\pi r^2(1 - cos\theta)\gamma_{SL} + \pi r^2(1 - cos^2\theta)\gamma_{CS} - \pi r^2(1 - cos^2\theta)\gamma_{CL} - \frac{2\pi r^2}{3}\left\{1 - \frac{3}{2}cos\theta + \frac{1}{2}cos^3\theta\right\}|\Delta H|\frac{(T_m - T)}{T_m} \quad \text{-Equation 10.}$$

Where [+] $\pi r^2(1 - cos^2\theta)\gamma_{CS}$ is the energy required to create a new interface between the solid and the catalyst and [-] $\pi r^2(1 - cos^2\theta)\gamma_{CL}$ is the energy released because of the reduction in area of the catalyst-liquid interface -as a result from the nucleation[37].

Taking into consideration the interfacial energies γ_{SL}, γ_{CS} and γ_{CL}, present at the edge of the forming solid, a mechanical equilibrium value can be determined hence allowing a simplification and reduction of the interfacial energy for heterogeneous nucleation to be[37];

$$W_f = \left\{1 - \frac{3}{2}cos\theta + \frac{1}{2}cos^3\theta\right\}\left\{2\pi r^2\gamma_{SL} - \frac{2\pi r^2}{3}|\Delta H|\frac{(T_m - T)}{T_m}\right\} \quad \text{-Equation 11.}$$

Which gives a critical radius of;

$$r* = \frac{2\gamma_{SL}T_m}{|\Delta H|\,(T_m - T)}$$ -Equation 12.

It should be noted that the value of the critical radius for both the homogeneous nucleation and the heterogeneous nucleation are the same[37]. It is the contribution provided by the volumetric component which allows heterogeneous nucleation to take place at temperatures closer to that of the melting temperature of the melt[38].

$$V^*_{homogeneous} = \frac{4}{3}\,\pi\,(r^*_{homogeneous})^3$$ -Equation 13.

$$V^*_{hetrogeneous} = \frac{2}{3}\,\pi\,(r^*_{hetrogeneous})^3\left\{1 - \frac{3}{2}cos\theta + \frac{1}{2}cos^3\theta\right\}$$ -Equation 14.

Which when equated gives;

$$r^*_{hetrogeneous} = \frac{r^*_{homogeneous}}{\left(\frac{1}{2}\left\{1 - \frac{3}{2}cos\theta + \frac{1}{2}cos^3\theta\right\}\right)^{1/3}}$$ -Equation 15.

This equation indicates that because a heterogeneous nucleation event is not spherical, due to its catalysation from an already present solid, its surface area is far larger than the spherical nucleation events present in homogeneous nucleation[38]. The result of this is that the effective critical radius is larger, allowing for nucleation events to occur at temperatures which are significantly closer to the melting temperature of the material, see Figure 2-6.

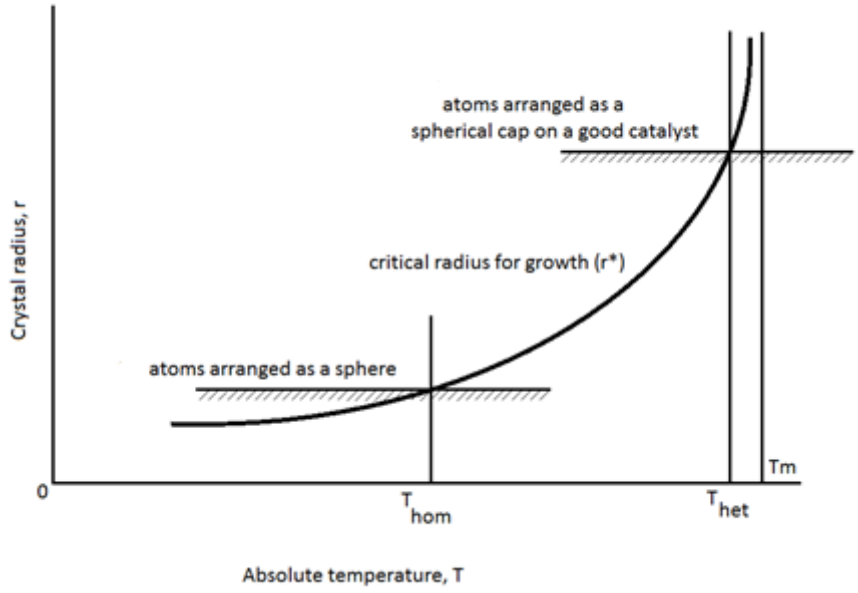

Figure 2-6 Graphical representation of the temperature comparison between homogeneous and heterogeneous nucleation[28,38]

2.10 Grain refinement

When casting metals it is often an advantage to have an equiaxed grain structure. Such compositions promote strength in a product and therefore are of great importance to many industries. It has been over half a century since it was discovered that additions of titanium to aluminium reduces grain size[39]. It was around the same time that scientists concluded that boron additions lead to further grain refinement[40]. It was found that elements which were peritectic in nature with aluminium were good grain refiniers[41] due to a nucleation energy barrier effect[42], although this did not explain why small additions of titanium added at less than the peritectic composition had such good grain refining properties, especially when introduced with boron[43–45]. More recently there has been research into whether TiB_2 particles are good nucleation sites for alpha aluminium or whether they are just providing substrates for Al_3Ti which in turn provide the nucleation[46–48]. It wasn't until the late 20th century that the importance of alloy

composition with regards to grain size was recognised[42,49–51]. As new ideas develop in the casting world there is often debate on how aluminium undergoes grain refinement. The two main schools of thought are; the nucleation and the solute theory's.

To quantitatively determine the effectiveness of a grain refining addition a factor was introduced called the growth restriction factor (GRF[51,52] or Q[53]);

$$Q = \sum_i m_i c_{0,i} (k_i - 1) \qquad \text{-Equation 16.}$$

For each element i, c_0 is the composition, k is the binary part coefficient and m is the liquidus gradient. The growth restriction factor is inversely proportional to steady-state dendritic growth (which is related to the rate of evolution of latent heat).

Classical nucleation theory suggests that a small grain size is the result of a large number of heterogeneous nucleation substrates present in the melt to act as effective nucleation sites[54]. For many years the focus of research was only on the addition of nucleation particels[55], which lead to researchers into experimenting with the grain refining properties of compounds on pure aluminium[56]. It is only recently that researchers have realised that the addition of solute is of significant importance for grain refiners[55,57].

The addition of solute promotes constitutional undercooling during solidification[58]. Due to the constitutional undercooling present at the leading edge of the growing grains further nucleation can occur more efficiently if the level of undercooling needed for nucleation around the available sites is reached[59]. If the level of undercooling is reached quickly then there will be less grain growth which will ensure a smaller final grain size[60]. The rate at which constitutional undercooling (Q) develops at the start of solidification[53,60] can be described as;

$$Q = \frac{d\Delta T_c}{df_s}|_{fs \to 0}$$ -Equation 17.

Where f_s is the fractional solid and ΔT_c is the development rate of constitutional undercooling.

Equally important in the refinement of grain particles is the particle on to which the material solidifies on, the nucleant particles. Where the density of the nucleating particles and their potency, defined as the inverse of the undercooling required for nucleation, are important.

If the solidified grain size is proportional to the growth which occurs to create the amount of undercooling needed for nucleation to occur. The rate of development of constitutional undercooling is equal to the rate of development of nucleation;

$$d \propto \frac{\Delta T_c}{Q}$$ -Equation 18.

To achieve a fine equiaxed grain both solute and nucleant elements are required to be successful. There have been studies which show that TiB_2 (and other borides) are very capable of nucleating α-aluminium at significantly low undercoolings (within 0.7°C of liquidus temperature). It has been noted that Al_3Ti is capable of forming within its nucleating particle, however this does not affect its potency. Despite TiB_2 being a capable nucleant, solute elements are required in the grain refining procedure. The reason for taking a solute element into consideration is because of their growth restricting features. Solute elements provide constitutional undercooling within the melt at the solidifying interface. It is within these constitutionally undercooled zones that further nucleation events can occur on the particles present within these regions. Ultimately the new grain refined structure of the melt is dependent upon a solute mechanism i.e. the degree of

constitutional undercooling determined by the composition and the properties of the liquid growing in front of the solidification, and a nucleant mechanism i.e. the potency and distribution of the particles on which the melt is nucleating[57].

2.10.1 Nucleation Poisoning

Different alloying agents have various affects on different melts. Not all solutes promote nucleation, some solutes even make it more difficult for solidification to occur. Two alloying agents which minimise the nucleating abilities of TiB_2 are silicone and zirconium. The addition of these alloying agents are required as they alter the properties of an aluminium melt by reducing the probability of hot tearing and also increasing the fluidity of the melt. Silicone reduces nucleation by increasing the dendritic growth rates which in turn decreases the formation of globular microstructures. The increased numbers of fast growing dendrites restrict the growth of new crystals and hence reduce the slower nucleation properties of TiB_2. A second reason for the poisoning effects of silicone is that it can promote the formation of small (100nm) layers of TiS_2 which can form on the surface of the TiB_2 particles -this reduces their nucleating efficiency. Zirconoium acts as a nucleation poison as it reacts with the TiB_2 in a substitution reaction to form ZrB_2. This change from titanium to zirconium boride alters the forming crystals lattice parameter to become dissimilar with that of the alpha aluminium, hence reducing the nucleation efficiency of the TiB_2 addition.

2.10.2 Particle Pushing

The solid-liquid interface and the behaviour on insoluble particles has been an area of research since the 1960's[61]. When an insoluble particle is met by an advancing solidification front it can either be pushed by the front or become engulfed by the front.

Engulfment is the growth of the solidifying front over the unmoving particle which then becomes trapped within the solidified melt. An alternative scenario to this mechanism is that the solidifying front evolves into cells, dendrites and equiaxed grains which then makes it possible for 2 solidification fronts to converge on the insoluble particle. The outcome of this scenario, provided that the particle is not engulfed by one of the solidifying fronts, is that the particle will be pushed by the solidifying front, which will eventually freeze trapping the particle[62]. Due to this mechanism the particles final location will be either within the grain boundary (or interdendritic regions) or, if engulfed by the front, within the primary grains. These interactions alter the solidifying fronts morphology as well as the distribution of the particles. This phenomenon is an important consideration for many solidification processes.

Factors, suggested by Stefanescu et al[63], which are important to consider when calculating the pushing or engulfing behaviours of particles met by an advancing solidification front include; the temperature gradient of the liquid material in front of the solidification front, the viscosity of the melt, the interface shape between the liquid and the solid (planar, columnar, dendritic ...), the insoluble particles size and shape, the volume fraction of the insoluble particles at the solidification front, the interfacial energies between the insoluble particle, the liquid melt and the solidification front, the densities of the melt and the particles, the convection levels within the melt and the tendency of the particles to agglomerate together[64].

2.10.3 Planar interface

Broadly there are two theoretical approaches to the consideration of particle pushing or engulfment, thermodynamic and kinetic.

2.10.3.1 Thermodynamic

Taking into consideration the scenario of a single particle becoming engulfed by an advancing solidification front, the net change in free energy can be calculated, neglecting buoyancy[37]. For the purpose of this calculation the reference frame which will be used will be that of the advancing solidifying melt[65].

$$\Delta F_{23} = \frac{1}{2}(\sigma_{PS} - \sigma_{PL}) - \frac{1}{4}\sigma_{SL} \qquad \text{-Equation 19.}$$

Considering Figure 2-7 it can be estimated that as the particle (seemingly) moves from the liquid to advance half way into the solidifying front its change in free energy per unit area is determined by the Thermodynamic engulfment change in free energy[65];

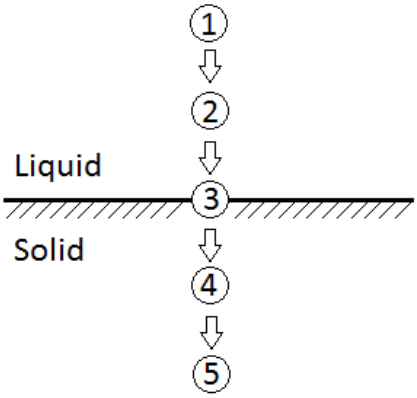

Figure 2-7 Thermodynamic particle pushing/engulfment[65]

Again considering Figure 2-7 it can be estimated that as the particle progresses from its position half way into the solidifying front to become completely engulfed by the solidifying front, the free energy per unit area is[65];

$$\Delta F_{34} = \frac{1}{2}(\sigma_{PS} - \sigma_{PL}) - \frac{1}{4}\sigma_{SL}$$ -Equation 20.

Where σ_{PS} is the interfacial energy between the particle and the solid, σ_{PL} is the interfacial energy between the particle and the liquid, and σ_{SL} is the interfacial energy between the solid and the liquid[37]. Which when combined gives the total net change in free energy for the engulfment of the solid particle to be[65];

$$\Delta F_{net} = \Delta F_{23} + \Delta F_{34} = \sigma_{PS} - \sigma_{PL}$$ -Equation 21.

From this equation it is possible to predict whether the particle in question can be engulfed or pushed. If the net force is less than zero then the particle will be engulfed. If the net force is greater than zero the particle will be pushed.

2.10.3.2 Kinetic

The kinetic theory for particle pushing is founded on the principal that if there is a liquid, of finite thickness, present between the solidifying front and the particle then the particle can be pushed along by the advancing solidifying front rather than becoming engulfed[37]. This mechanism is based upon the liquid between the particle and the solid being able to transport mass. If the liquid is capable of pushing the solid there must be a repulsive force present between it and the solid. This repulsive force may originate from the variation in surface free energy where[66];

$$\Delta\sigma = \sigma_{PS} - (\sigma_{PL} + \sigma_{SL})$$ -Equation 22.

Which varies with d, the particle solid distance, in such a manner[65];

$$\Delta\sigma = \Delta\sigma \left(\frac{d_0}{d}\right)^n$$ -Equation 23.

Where d is the particle solid distance, d_0 is the minimum separation between the solid and the particle and n = 4 or 5.

Presuming that diffusion is the prevalent mass transport mechanism in the particle solid region and that the only repulsive force is because of surface tension and that there is only viscous drag for large particles, then R_{cr} the critical growth rate can be derived to be[61,67–69];

$$R_{cr} = \frac{d_s h L a_0 d_1}{6\eta r r_b^2 n}\left[\left(1 + \frac{6\eta r n(n+1)V_0 D}{d_s h d_1 kT}\right)^{1/2} - 1\right]$$ -Equation 24.

For large particles and[65];

$$R_{cr} = \frac{1}{2}(n+1)\frac{La_0V_0D}{kTr_b^2}$$ -Equation 25.

For small particles, where η = liquid viscosity, T = temperature, h = contact distance, V_0 = atomic volume, k = Boltzmann's constant, d_1 = (100nm) minimum separation, d_s = contact distance, L = latent heat per unit volume, r_b = particle irregularity radius (for completely spherical particles r_b = r), D = liquid diffusivity, a_0 = molecular diameter.

Other methods of calculating the particle pushing mechanism, ie mass transport, take into consideration the integration of the particle with the fluid flow and its associated diffusion properties. For this interpretation calculations have been made which assume that the particle is not wetted by the melt and that the particle has an identical thermal conductivity to the melt[70].

For large smooth particles this is[67,70];

$$\eta R r^4 = \frac{2\alpha k T \sigma_{SL}}{\pi G \Delta \rho} \qquad \text{-Equation 26.}$$

and for smooth small particles whose radius is smaller than the radius of its bumps, this is[70];

$$\eta^2 R^2 r^3 = N \frac{4\psi(\alpha)}{9\pi} k T \sigma_{SL} a_0 \qquad \text{-Equation 27.}$$

Where α is a shape factor of the particle where α=1 for the interface being the same as that of a curved particle and α=0 for a flat interface. ψα is a function of α requiring calculation. N is the number of contact points between the interface and particle (N=1 flat surface, N=2 boundary region between grains, Δρ is the difference in density between the particle and the liquid.

The shape of the solidifying front has a great effect on whether an insoluble particle will be pushed along by a melt or engulfed. As Figure 2-8 indicates, if the solidifying interface is planar, engulfment of the particles results in distributed particles within the melt whereas if the particles are being pushed by the solidifying front then the melt will be clear from particles[62].

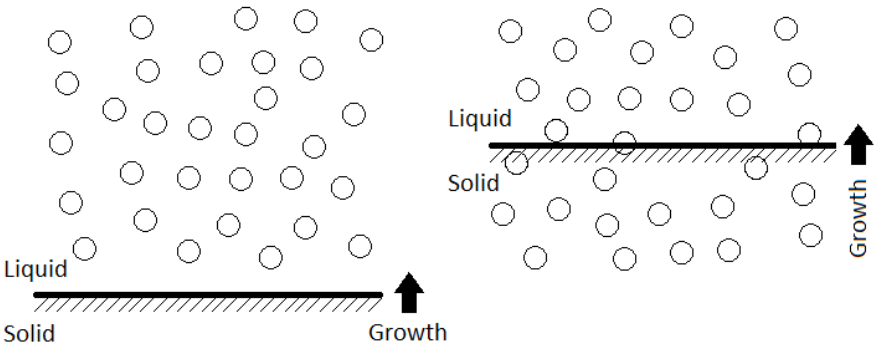

Figure 2-8 Planar faced solidification front showing particle engulfment[63]

If the solidifying front is forming a cellular structure then the particles will be pushed to the boundary regions between the cells, here they will eventually become trapped in the solidifying melt forming an aligned particle composite as visualised in Figure 2-9[61,62,71].

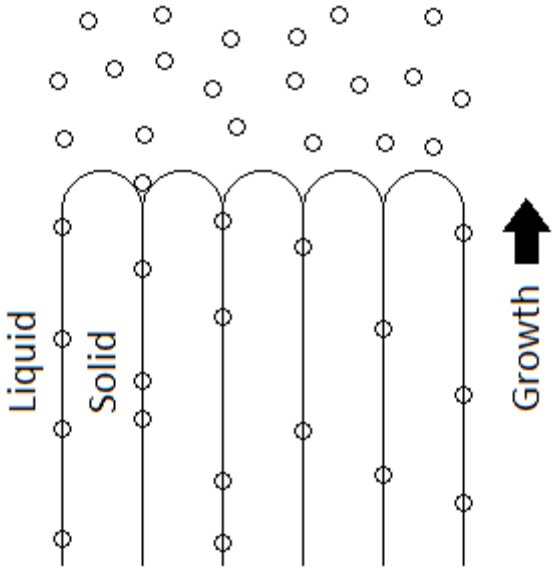

Figure 2-9 Image showing particles becoming entrapped in grain boundaries between columnar crystals[63]

When the solidifying front evolves into dendritic structures a more intricate scenario occurs. Small particles become engulfed by the advancing solidification front or trapped within the interdendritic spaces, large particles are pushed by the dendritic tips as shown in Figure 2-10[61,62,71].

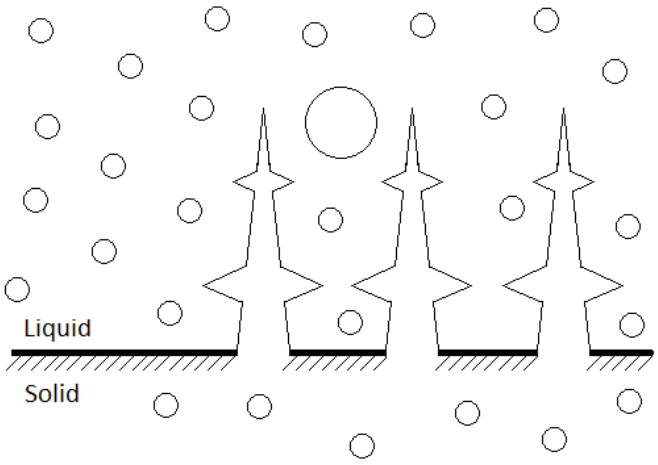

Figure 2-10 Image showing particle engulfment of small particles in the solidifying front and larger particles being pushed by dendritic structures from[63]

2.10.4 Particles

A particle must remain solid to undergo interactions with the solidifying front. Over the years particles which have been thoroughly investigated include Al_2O_3, TiB_2, ZrB_2, graphite, B_4C and glass, of which all apart from B_4C are pushed by aluminium dendrites in an Al-3Mg-0,004Be matrix alloy[72–79].

2.11 Properties and Behaviour of Composites

Composites are considered to be 2 or more separate materials which have distinguishable interfaces between them. Composites contain a continuous matrix element which binds the material together giving the material form and allowing for a stronger, stiffer

reinforcement. This allows the resulting composite material to have structural properties greater than either of its components. The improved structural properties are the effect of a load-sharing mechanism, although composites have been created for other functional properties such as greater electrical or thermal conductances[80]. It is typical of a composite to have a particle or fibre phase which is stronger and stiffer than the surrounding metal matrix. To distinguish between different composites their categorization is based on 2 levels. The first division provides a description regarding the metal matrix's composition, for example; Metal-Matrix Composites (MMC's) and Metal-Matrix Nano Composites (MMNC's)

The second division refers to the size and shape of the reinforcement. Types of reinforcement include; woven composites, continuous fibre laminated composites, whisker composites and particle reinforcements. Whisker particle reinforcements have an aspect ratio of between 20 and 100 and are regularly considered as particle reinforcements for metal-matrix composites. A reinforcement is described as a particle if its dimensions are approximately equal, examples of which include (but are not limited to); rods, spheres and platelets[80]. Together these methods of reinforcing a material are described as 'discontinuous' as the reinforcement materials length is similar to its cross-sectional area. Discontinuous or short fibre composites have properties which alter with the length of the reinforcement fibre. When a fibre-reinforced composite is described as 'continuous', its reinforcement material has a cross-section far smaller than its length -to such an extent that the length of the reinforcement fibre no longer has an effect on the materials mechanical properties. In some instances particles, usually polymers, may be added to a material for the purpose of cost reduction rather than to increase a materials properties, this is referred to as a filled system[80].

2.11.1 Metal-Matrix Composites (MMC's) / Aluminium metal composite (AMC's)

Through research and development the properties of Metal-Matrix Composites have progressed significantly over the last decade. Properties of a metal-matrix composite which have been improved upon and hence are superior to an unreinforced metal include; strength, modulus and fatigue, wear and thermal resistances. The benefits brought about by MMC's are based upon the principal of preserving the best characteristics from 2 materials, for example the strength of a ceramic reinforcement and the ductility of a metallic matrix[80]. These characteristics are then present after combining the materials together as a composite. There are 2 methods of adding the reinforcing particles to the metal-matrix; physically with the dimensional properties required, or chemically by the use of salts which form the reinforcement phase internally.

It is possible for Metal-Matrix Composites to be produced with either discontinuous or continuous reinforcements –or a mixture of the two. A manufacturing advantage of discontinuous reinforcements is that they can be fabricated cost-effectively as the processing stages required are similar to those required for the processing techniques used for the production of unreinforced metal-matrix materials. Discontinuous composite reinforcements also have preferentially isotropic properties which is a beneficial trait in most products. The final properties of the metal-matrix composite ultimately are linked to the reinforcement type, the metal-matrix and the interface between the two. Research has been made in the advancement MMC's exploring their development by using a variety of matrix materials, however most emphasis has been directed towards the development of lighter MMC's using titanium and aluminium -especially for use in the transport industry where power-to-weight ratio is of significant importance[80].

The significance of the metal matrix and its mechanical properties is of more importance to discontinuously reinforced composites than continuously reinforced composites. This is the result of a difference in strengthening mechanisms with respect to the composites types. For discontinuously reinforced composites, the metal matrix has a significant role in the overall strength of the composite. The strength not only originates from the load transfer between the matrix and the reinforcements but also the strengthening mechanisms present within the metal matrix itself[80]. This is dissimilar to the strengthening mechanisms of a continuously reinforced composite which is predominantly dictated by the ability of the material to transfer load between the composite fibre and the metal matrix. For this reason the mechanical properties of the reinforcing fibre and the fibre-matrix interface is of more importance than the matrix materials properties.

An important consideration in the design and manufacturing of a metal matrix is the compatibility between the reinforcement material and the metal-matrix material[80]. If a chemical reaction between the two materials occurred unwanted products, for example intermetallic compounds, may be formed at the materials interface which would have negative effects on the transference of load between the matrix and reinforcement particles. Such compounds may also act as sites for future crack nucleation.

2.12 Strengthening mechanisms

When considering the strength of a crystalline material there is a relation between the mechanical properties and the motion of dislocations within that material. The more restricted the dislocation movements are the greater the materials mechanical strength

will be. Any process which obstructs the movement of these dislocations therefore increases the strength of the material[81,82].

2.12.1 Hall-Petch strengthening mechanism

When a liquid metal starts to solidify, randomly orientated crystals form within the melt. The overall size of the crystal is determined by its growth rate and number density. It can be generalised that under a shallow temperature gradient crystal growth is large, whilst under a steep temperature gradient crystal size is small. Large grain sizes are linked to low hardness and strength values, whereas small grain sizes are linked to the opposite[26].

The strengthening mechanism which relates grain size to the strength of a polycrystalline material is the Hall-Petch mechanism. The strength contribution from this relationship is linked to the resistance provided by the grain boundaries opposing stress line propagation, hence increasing overall strength [81,83,84]. If there are few grain boundaries to impede its movement the strength of a material will be low, conversely, if there are many small grains with many grain boundaries strength will be high. One process responsible for limiting the motion of dislocations is due to the traverse of a dislocation across a grain boundary, which acts as a barrier. There are 2 reasons for this behaviour [29];

- If the grain of the first crystal has a different orientation to the second crystal, the dislocation will have to alter its direction which requires a greater energy and therefore increases the overall strength of the material. As the energy required is dependent upon the second crystals orientation, more energy is needed for larger angles of crystallographic disorientation (angle θ) see Figure 2-11.
- For the dislocation to reach the second grain it must first cross the grain boundary between the two grains. This is a region of atomic disorder which creates a

discontinuity in the traversing slip planes, again increasing the strength of the material.

This grain boundary strengthening affect is referred to as the Hall-Petch strengthening mechanism. This mechanism implies that the yield strength of a polycrystalline material will increase with a decreasing grain size, due to the increased number of grain boundaries available to impede dislocation motions within the material [85–88].

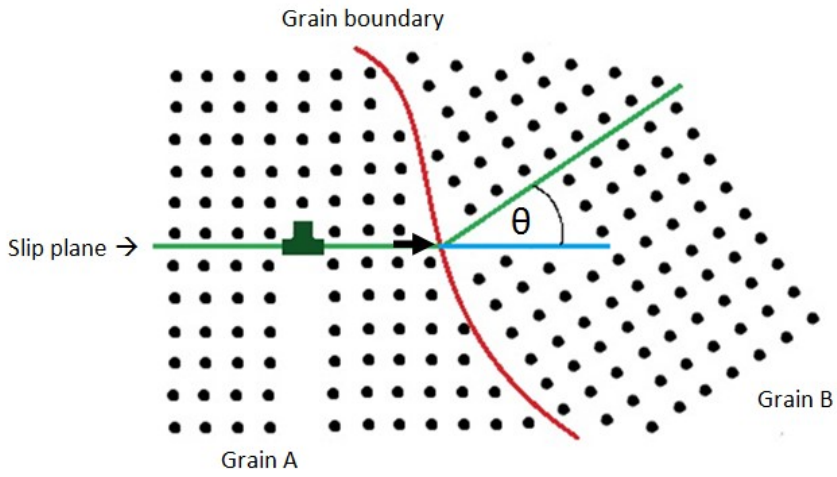

Figure 2-11 Hall-Petch strengthening mechanism[26]. The slip plane is travelling from grain A to grain B across a grain boundary. The second grain is at an angle of θ to the first.

The Hall-Petch Strengthening mechanism is an applicable strengthening mechanism for the crystal structure of the A20X material exclusively and is not applicable to the grain boundary material. This is through the definition of the mechanism as it is the grain boundary material which is required to halt the motion of the traversing slip plane.

The equation which describes the Hall-Petch strengthening mechanisms is[87,88];

$$\Delta\sigma_{Hall-Petch} = \sigma_{dislocation} + K\, d_m^{(1/2)} \qquad \text{-Equation 28.}$$

where the strength is related to the inverse square of the grain size, where;

- $\sigma_{dislocation}$ = The friction stress of an un-deformed crystal orientated for multiple slip (Pa).
- K = Hall-Petch coefficient (Pa $m^{1/2}$),
- d_m = Matrix grain diameter (m).

2.12.2 Orowan strengthening mechanism

The size of grain within a material is not the only feature contributing to the overall strength of the metal. The main alloying addition to A205 is Cu (at approximately 4.5wt.%), which is at a similar weight percentage to other 2xxx series aluminium alloys. Aluminium-copper alloys get a significant proportion of their strength through precipitation-hardening[28]. If an aluminium copper system, with sub 5wt.% copper, is increased in temperature to between 515-550°C the $CuAl_2$ within the alloy will go into solution. If the metal is then quenched, a super saturated solution will form. Reheating the metal to approximately 150°C, in a precipitation hardening process, will cause the copper to precipitate out of solution to form Ω and θ phase 10-150nm copper aluminide particles[83].

These particles allow an Orowan strengthening mechanism to come into effect. The Orowan strengthening mechanism occurs due to the interaction between the dislocation line and precipitates within the crystal[26]. Each precipitate within the crystal can be viewed as a row of obstacles impeding the progression of the dislocation line. For a dislocation slip to progress through the material it must either pass through the particles or

alternatively around the particles. The dislocation line will travel the path which takes the least amount of energy to complete. If the dislocation line does not have enough energy to complete either of these two options, its progression through the crystal will be halted by the particles. If the energy conditions are such that the dislocation line passes between the particles, the line becomes distorted and wraps itself around the particle in such a manner so as to form a closed loop, trapping a proportion of the dislocation line[82,88,89]. In this scenario the affect of the dislocation line is reduced and therefore the strength of the material is increased. If the obstructing particles are weak and closely spaced, then the energetically favourable mechanism for the dislocation line to progress through the crystal, is by shearing these particles (see Load bearing stress).

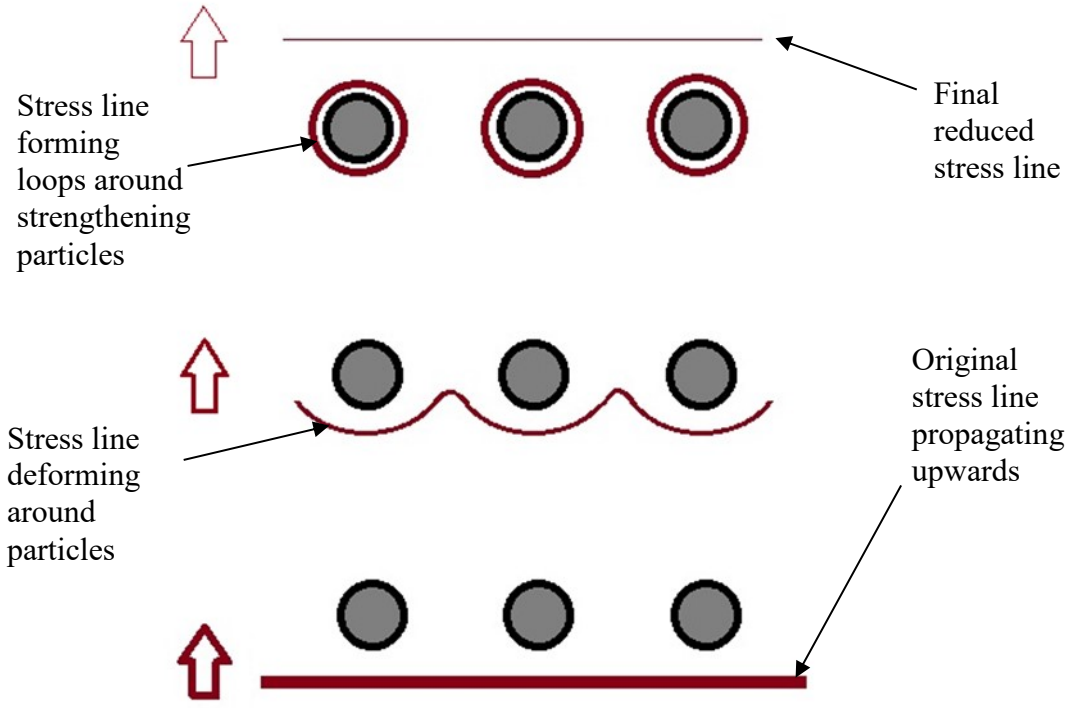

Figure 2-12 Orowan strengthening, progression from bottom to top[26]

As the effectiveness of this strengthening mechanism is dependent upon the size of the strengthening particles being in the low micron to nanometre range [82]. The Orowan

strengthening mechanism is applicable to the grain material of the A205 exclusively and is not applicable to the grain boundary material.

The Matrix Orowan looping strengthening mechanism;

Where the interaction between the non-shearable particles and the dislocations increase the strength of the material by trapping the dislocation lines around the particles [88]. There are several interpretations on how to calculate the Orowan strengthening mechanism. Despite Zhang's, Huskin's and Habibnejad's [82,87,88] work on strengthening mechanisms it was decided that the method of calculating the Orowan strengthening mechanisms to be used in this project was to be based upon Hou Yan-hui's work -Equation 29 [90]. This was chosen as the equations used in Hou's work[90] were based specifically around the omega phase precipitates, rather than the more general equations as used by Habibnejad[88] and Zhang[82]. Hou's formula also compared the predicted and measured values in the development of this equation, which is of particular interest as the precipitation hardening temperatures and times are comparable to those of A205.

The formula which describes this Orowan strengthening relationship is;

$$\Delta\tau_{\Omega/\theta} = 0.12\,MG\,\frac{b}{2\sqrt{rh}}\,.\left\{\phi^2 + 0.70\left(\frac{r}{h}\right)^2 + 0.12\left(\frac{r}{h}\right)^2\phi^{(3/2)}\right\}\ln\left[\frac{0.158\,r}{r_0}\right]$$ -Equation 29.

where;

- M = Magnitude of Taylor factor (Anisotropic contributions of θ and Ω $CuAl_2$ precipitates) (Pa).
- G = Magnitude of Shear modulus (Pa).
- b = Burgers vector (nm).

- r = Radius of precipitate (nm).
- h =Thickness of precipitate (where h << r) (nm).
- ϕ = Volume fraction.
- r_0 = Precipitate lower cut off radius (nm).

These strengthening equations can be applied to the two distinct areas of A205; the grain material (crystal) and the grain boundary material.

2.12.3 Load bearing strengthening mechanism

The load transfer between the matrix and a particle is caused by the load bearing effect. This is the result of transference of a shearing force from the matrix to the particles[91,92] . Since the particles do not shear at the same value as the matrix, the final value of the shear stress is calculated using the rule of mixtures [82,88].

The Load bearing strengthening mechanism is due to the interaction between particles within the material and progressing dislocation lines. As a dislocation line approaches a particle, its progression is dependent upon the lowest energy mechanism available. If the particles have a high strength then Orowan strengthening will be the most energetically favourable mechanism. If the energy required to shear the particles is low then the dislocation will shear through the opposing particle as it progresses through the material. The energy required to shear through the particle is proportional to the increase in the strength of the material[88,89].

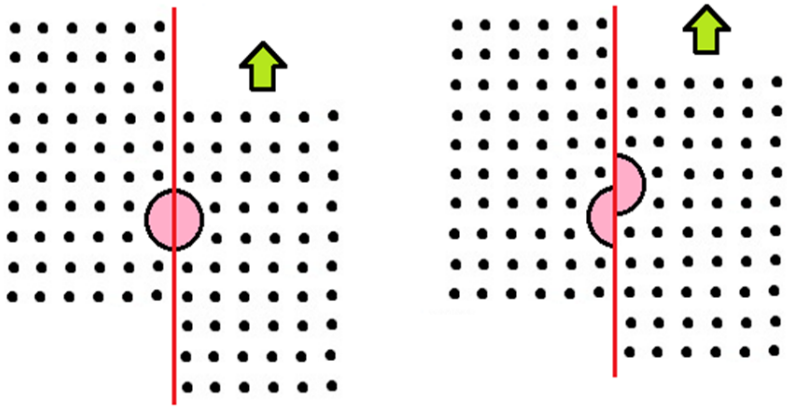

Figure 2-13 Load bearing strengthening mechanism[26]. The particle opposing the progression of the dislocation line is sheared.

The Load bearing strengthening mechanism is a viable strengthening mechanism for both the crystal structure and the grain boundary material as both areas have shearable particles present. The strength associated with this mechanism is linked to the volume fraction[82,88] in the Load bearing strengthening equation;

$$\Delta\sigma_{Load} = 0.5\, V_p\, \sigma_{ym} \qquad \text{-Equation 30.}$$

where;

- V_p = Volume fraction.
- σ_{ym} = Matrix yield stress (Pa).

2.12.4 Coefficient of thermal expansion strengthening mechanism

An additional method of increasing the strength of a material is to introduce particles into the metal which have a different Coefficient of Thermal Expansion (CTE) to the matrix [93]. The difference in CTE between the metal matrix and the strengthening particles leads to an increase in dislocation density which results in an increase in the overall strength of the material[93–95].

The CTE strengthening mechanism is due to the interaction between the strengthening particle and the crystal structure. As the melt is cast, features form during solidification. If there are two features which solidify at different temperatures, it is only at the temperature at which the second feature solidifies that there will be a near zero stress value between the components. If the 2 materials then expand or contract at the same rate with respect to an applied temperature then the forces between the materials remains zero. However if there is a difference between the coefficients of thermal expansion then a stress will be created which is dependent on the respective temperature differences between the solidification temperatures and testing temperatures of the materials. There are several variations on how this stress will arise. The two most prevalent net affects are either; the particle trapped inside of the surround material will contract away from the sides, or the particle will expand into the surrounding crystal -for both scenarios residual stresses are formed [88,96,97].

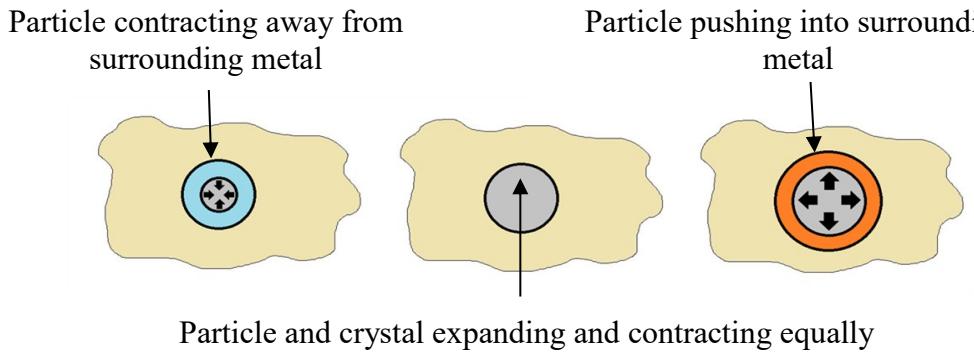

Figure 2-14 Pictorial representation of the coefficient of thermal expansion strengthening mechanism[26]. Left; particle contracting away from wall. Central; particle and crystal expand and contract equally. Right; particle expands and pushes into crystal.

The Coefficient of thermal expansion strengthening mechanism is a viable mechanism for both the crystal structure and the grain boundary material. This is because both areas

of the material have constituents with significantly different coefficients of thermal expansion, resulting in the formation of induced stresses and hence increased strength.

Where the CTE mismatch values, between the grain and reinforcing particles (TiB_2), generates thermally induced residual stresses. These thermal stresses, found at the matrix-particle interface, make plastic deformation more difficult[88]. The formula which describes this strengthening relationship is[88];

$$\Delta\sigma_{CTE} = \sqrt{3}\,\beta\,G_m\,b\sqrt{\frac{12\,V_p\,\Delta\alpha\,\Delta T}{(1-V_p)b\,d_p}} \qquad \text{-Equation 31.}$$

where;

- β = Strengthening coefficient (unit-less),
- G_m = Sheer modulus of the matrix (MPa),
- b = Burgers vector, a translation vector of a crystal lattice representing the displacement of the material to create a dislocation (nm),
- V_p = Volume fraction, of reinforcing particles to the matrix (unit-less),
- $\Delta\alpha$ = Difference between matrix (αm) and particle (αp) CTEs ($Kelvin^{-1}$),
- ΔT = Difference between processing ($T_{processing}$) and test (T_{test}) temperatures (Kelvin),
- d_p = Average diameter of the strengthening particle (usually in the nm range),

Equation 30 and Equation 31 can be linked together to give a total grain boundary material strengthening contribution by;

$$\Delta\sigma_{Grain\ Boundary} = \Delta\sigma_{Load} + \Delta\sigma_{CTE} \qquad \text{-Equation 32.}$$

Equations 28, 29, 30 and 31can all be linked together to give a strengthening contribution for the metal matrix material by [82,88,98,99] ;

$$\Delta\sigma_{matrix} = \Delta\sigma_{Load} + \Delta\sigma_{Hall-Petch} + \sqrt{(\Delta\sigma_{CTE})^2 + (\Delta\tau_{\Omega})^2} \quad \text{-Equation 33.}$$

where;

- σ_{Load} = The strengthening contribution from Load (Pa),
- $\sigma_{Hall\text{-}Petch}$ = The strengthening contribution from Hall-Petch (Pa),
- σ_{CTE} = The strengthening contribution from the Coefficient of Thermal Expansion mismatch (Pa),
- τ_{Ω} = The strengthening contribution from Orowan looping (Pa).

The strengthening mechanisms for the grain boundary material (Equation 32) and the grain material (Equation 33) are combined together based on their volume fractions.

It should be noted that Orowan strengthening has not been included in the grain boundary material's strengthening mechanism contributions as the TiB_2 particle sizes expected within the A205 are vastly disproportionate to previous research, as carried out by Zhang et al [92] in which an improvement factor for Orowan strengthening vs. particle size shows a sub 20% improvement for particle sizes above 50nm -as can be seen in Figure 2-15. It also should be noted that Zhang et al [82] also reported an increased improvement factor with increased volume fraction, however this is again slight for sub-micron particle sizes - Figure 2-16. Similarly the Hall-Petch strengthening mechanism has not been included for the grain boundary material as crystals do not form in this region.

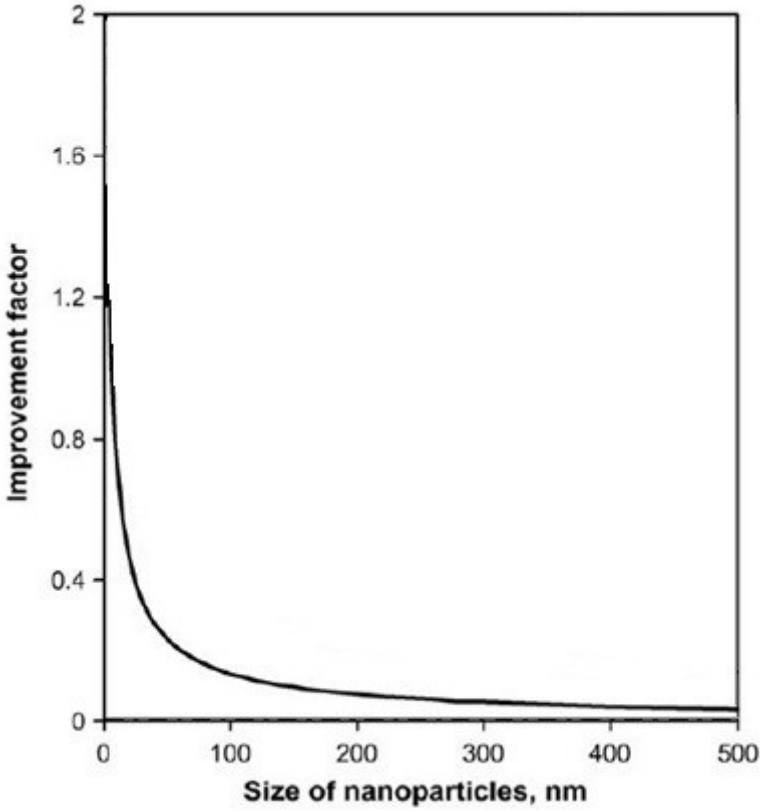

Figure 2-15 Extract from Zhang et al[82] showing improvement factor vs. particle size for Orowan strengthening -calculated for a volume fraction of 0.01

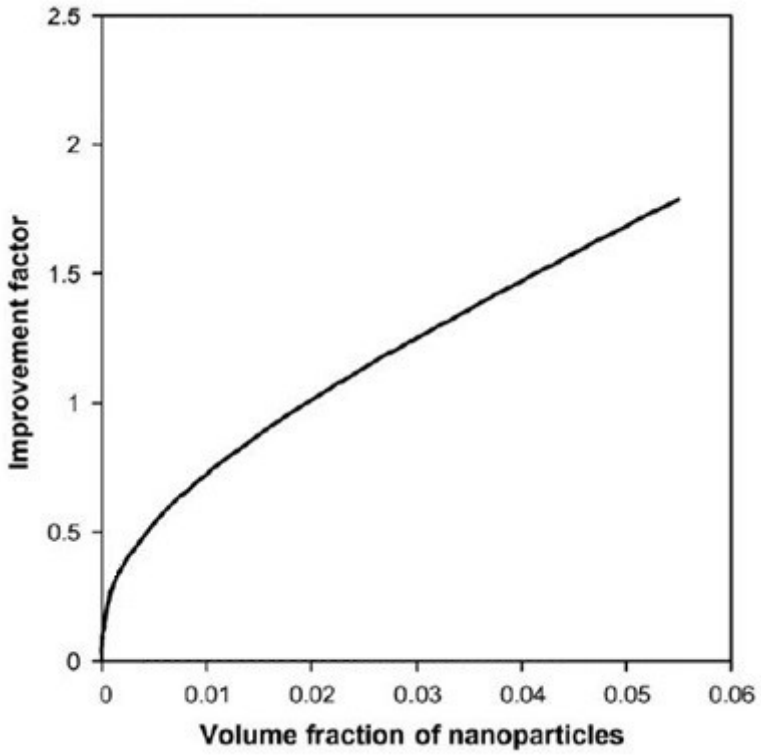

Figure 2-16 Extract from Zhang et al[82] showing improvement factor vs. particle volume fraction for Orowan strengthening -calculated for a particle size of 10nm

2.13 Particle size

Particle size is an important property of a material; it can be used to describe aspects such as viscosity, agglomeration, dissolution rate, gas absorption, combustion rate etc. The particle size of the Titanium Diboride (TiB_2) grain refining material within A205 is responsible, both directly and indirectly, for some of the strength characteristics of the alloy as described in strength section of this thesis.

Previous examples of particle size analysis are based upon SEM image analysis. Due to the sampling size of SEM images, this method of analysis gives a poor representation of the size distribution of the TiB_2 particles as a whole. By removing the TiB_2 particles from

the matrix (in a process described in the experimental procedure section of this thesis) it is possible to analyse the TiB_2 size distribution in its entirety.

2.13.1 Different sizes of the sample particle (equivalent spheres)

Particles are inherently three dimensional (3D) objects. The simplest 3D object to describe is a sphere as it requires only one dimension to fully explain its shape, the diameter. It is often the case that particles requiring size analysis are not spherical and need many length, width and depth measurements to accurately describe their shape[100]. For this reason many particle size analysis techniques report values based upon the diameter of an equivalent sphere. In most cases this is a sufficiently accurate method of describing a particles size providing that the individual particles do not have a significantly large aspect ratio.

There are several ways of reporting the equivalent spherical radius of a non-uniform particle. The diameter of an equivalent sphere could be based on the non-uniform particles; maximum length (d_{max}), its surface area (d_s), its minimum length (d_{min}), its volume (d_{vol}), its ability to pass through a sieve (d_{sieve}), its sedimentation rate (d_{sed}) or its weight (d_w) (see Figure 2-17)[100].

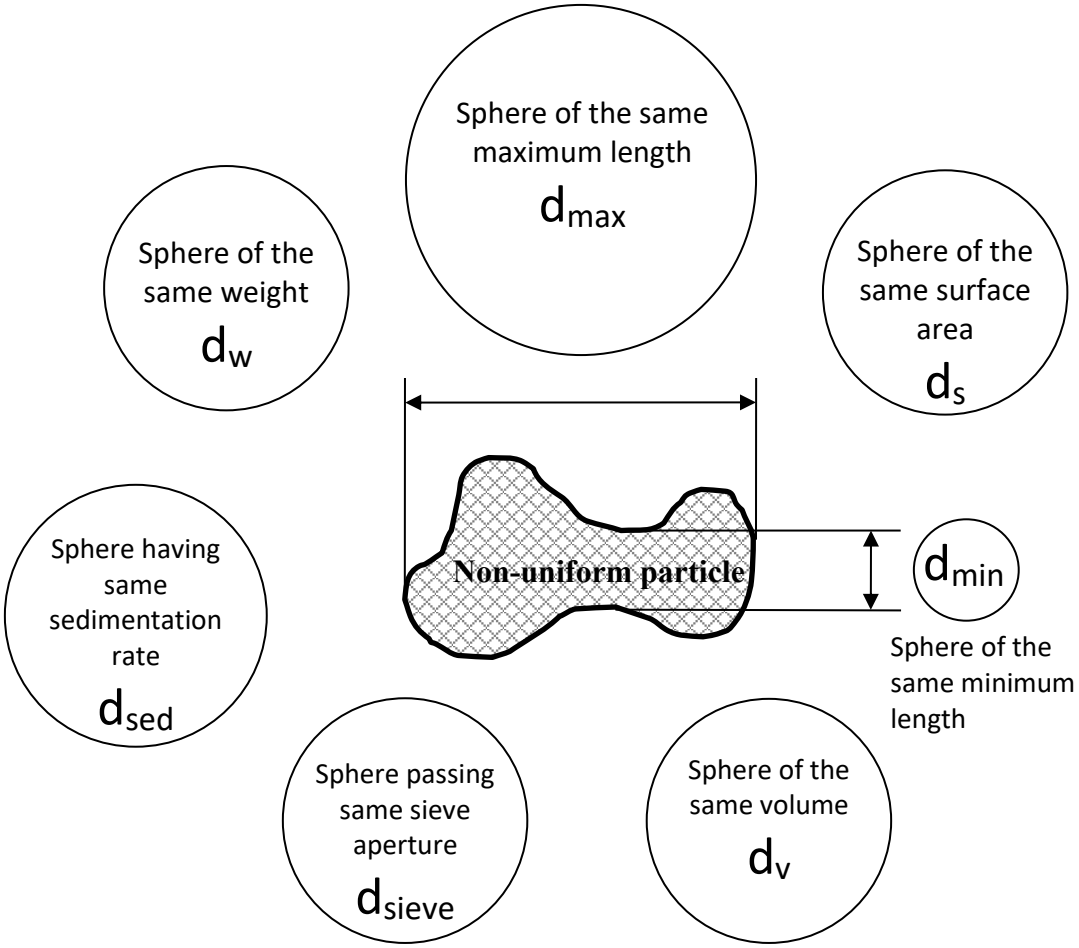

Figure 2-17 Various equivalent spheres[100]

2.13.2 Particle size measurement techniques

There are several methods of analysing the size characteristics of a distribution of particles. Methods have been developed either to explore the different techniques of analysing particle size or as a requirement for the analysis of different sample forms i.e. whether the particle is suspended in a liquid or is in the form of a dry powder etc. As each technique determines the size of the particle using a different property or the particle,

the reported particle size between the various techniques is slightly different. A brief overview of the main particle size measurement techniques is shown below:

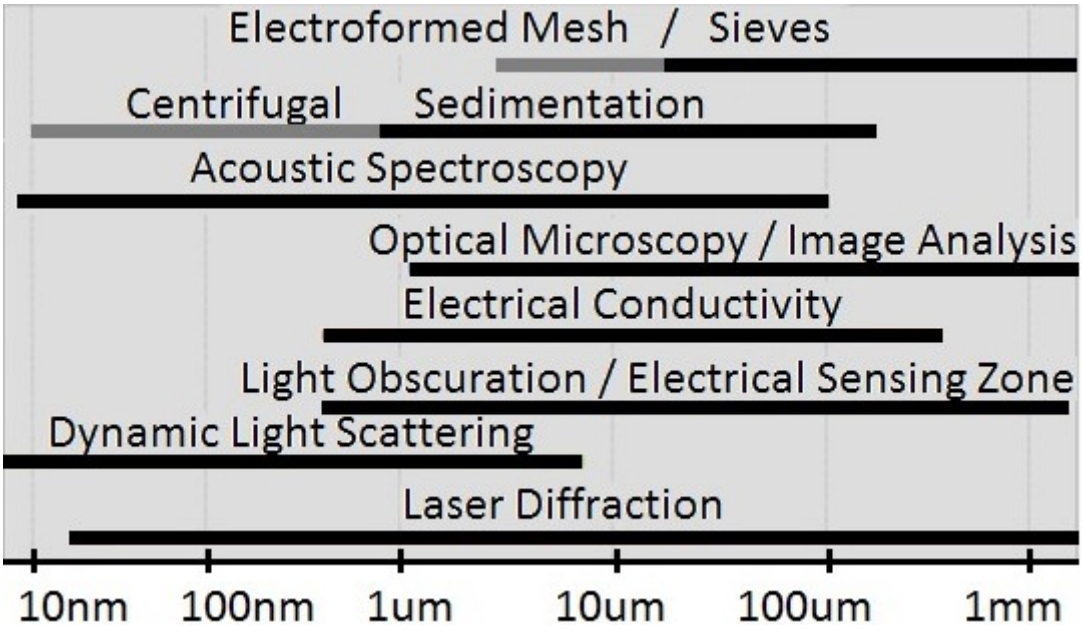

Figure 2-18 An approximation of which analysis techniques can be used for an expected particle size range from[100]

2.13.2.1 Sieving

Sieving is a physical method of determining the particle size of a sample. By offering a distribution of particles to a mesh of known aperture size, larger particles will be retained and smaller particles will be allowed to pass through. It requires zero computing power but is affected by particle shape –especially when considering rod like particles. Currently the smallest sieve grades are in the order of 20microns, although finer sieves are being developed[101].

2.13.2.2 Sedimentation (settling rate)

Sedimentation is based upon the settling rates of different sized particles. The settling rate of different sized particles can be described using Stokes's law. Provided information is known about the particles density, the density and dynamic viscosity of the liquid the particle is settling through, an estimate of particle size can be made[100]. Stokes' law assumes that the particles are spherical, homogeneous, have smooth particles and do not interact with each other. Laminar flow is also assumed for Stokes law calculations

2.13.2.3 Acoustic spectroscopy (equivalent spherical diameter)

Acoustic spectroscopy relies on the change in a bulk liquid's material properties from the addition of a known weight percentage of particles. By propagating ultrasonic waves at a selection of know frequencies through a particulate suspension and measuring the attenuated signal at a known displacement, particle size information about the suspension can be ascertained[100].

2.13.2.4 Direct observation

Direct observation is perhaps the most obvious method of determining a particles size. A representative sample of the material is digitally imaged and subsequently analysed using an image analysis software package (such as ImageJ). Particle properties which can be quantified include; area, maximum and minimum width, circularity etc. The most significant advantage of this particle sizing technique is that particles can be analysed on an individual basis. The major disadvantage of this technique is linked to the time required to take and analyse the necessary amount of images for a representative sample. Due to the (relatively) low numbers of particles which can be realistically processed using this technique it is most suited to small sample batches.

2.13.2.5 Coulter counter (electrozone sensing)

The Coulter principal is based on the change in conductivity of a small aperture due to the crossing of a particle. As the X-axis and Y-axis conductivity across the aperture can be measured separately, by taking into consideration time dependence, a high resolution image of individual particles can be determined[100].

2.13.2.6 Light based

2.13.2.6.1 Light obscuration

Light obscuration particle size analysis is the process by which a single particle is allowed to fall through a light beam. The particles shadow is detected and analysed on a charged coupled device (CCD) detector.

2.13.2.6.2 Dynamic Light Scattering

Dynamic Light Scattering (DLS) is also known as photon correlation spectroscopy and quasi-elastic light scattering (hydrodynamic radius). Analysing particle size using DLS exploits Brownian motion. DLS a method founded on the Stokes-Einstein equation. The velocity of the motion is based on a property known as translation diffusion, whereby smaller particles are disturbed to a greater affect than larger particles. As the particles are required to be measured within a liquid medium the size calculated is referred to as the hydrodynamic diameter. This measurement is indicative of a sphere which has an equivalent transitional diffusion coefficient to that of the particle being measured. This measurement is not only determined by the particle but also by the surface structure. The surface structure may increase the apparent particle size due to the formation of an extended double-layer of ions around the particles surface –which would decrease the apparent movement velocity of the particle and hence indicate a larger particle[100].

2.13.2.6.3 laser diffraction (aka photon correlation spectroscopy or equivalent spherical diameter)

The diffraction of light can also be used to indicate the size of a particle. Laser light is used as it has a precise known frequency. As the light is diffracted around the particle a characteristic, ring-shaped pattern or intensity distribution is created. By measuring the spacing of the intensity rings produced the size of the particle can be determined. Small particles produce an intensity pattern with widely spaced rings, as opposed to larger particles which produce tightly spaced diffraction rings. There are two main theory's which described this behaviour; the Fraunhoffer theory and the Mie theory. These theories can be used to translate an intensity distribution to a volume equivalent sphere model/distribution[102].

Fraunhoffer theory describes the amount of light deflection which is a direct result of diffraction. The Fraunhoffer theory requires the light incident upon the particles to be parallel and the diffracted light to be in the forwards direction (i.e. the scattering angle is less than 90°). The Fraunhoffer theory requires the particle size to be relatively large at a minimum of ten times the laser wavelength. A significant advantage of the Fraunhoffer theory is that the optical properties of the sample material are not required for the calculation steps[103].

Mie theory is a more precise method of using the diffraction of light to measure particle size. Mie theory is the complete solution to the Maxwell equations for electromagnetic radiation (i.e. light) scattering around spherical particles. Unlike the Fraunhoffer theory, it can be applied to the characteristic diffraction patters created by very small particles – which can be similar in size to the wavelength of light used. Mie theory also takes into

consideration light scattering at angles greater than 90° (backward scattering). A disadvantage of this theory is that it requires information on the refractive and absorptive indexes of the sample material[104].

Mie theory assumes that; the only source of scattering is from the particles present, there is no error in the collected intensity distribution, the optical properties of the particles in question are completely described by their real and complex refractive indexes, the particles are spherical and homogeneous, all scattering is elastic (therefore the frequency of the scattered light is equal to that of the incident light), scattering event occur on an individual basis, for collections of particles the numbers are large and particle separations are random (hence the scattered light can have no systematic phase relationship) and that the medium in which the particles are suspended is homogenous and isotropic[105].

The method chosen for analysing the TiB_2 particles was laser diffraction. Laser diffraction was chosen as liquid samples can be accommodated for, the entire sample is measured, the method is non-destructive and non-intrusive, a volume distribution is generated and a high resolution can be achieved. The equipment used to carry out this analysis procedure was a Malvern 2000MU particle size analysis machine -set up for liquid based samples. The machine circulates a liquid sample (which minimises error in the readings) by using a stirring mechanism, through a series of pipes into the diffraction chamber. After introducing the sample to the system it is possible to subject the material to ultrasonic agitation, in a pre-size-analysis stage, to break apart any agglomerated or aggregated particles which may have developed during transportation[106].

To assess whether ultrasonic agitation would damage the TiB_2 sample and hence affect any subsequent measurements or calculations, a sample of pure TiB_2 -with a known size

distribution <10μm, provided by the supplier (Sigma Aldrich), was analysed by the machine following various exposures to ultrasonic agitation.

2.13.3 Interpreting size distribution calculations

As previously described there are many different ways of measuring the size characteristics of a distribution of particles, hence as each characterisation technique determines the distribution using a different aspect of the particles size, the mean size calculated will be technique dependent. These mean particle size calculations are described as follows:

2.13.3.1 Particle number dependent calculations

The following 3 formulas are different techniques used to find the mean particle size of a distribution of particles. For these equations the number of particles must be known - because of this it is possible for a large number of small particles to significantly skew the results even though they may only constitute a small fraction of the entire sample.

2.13.3.1.1 D[1,0] the number mean

$$D[1,0] = \frac{\sum d}{n} \qquad \text{-Equation 34.}$$

If a visual examination of a number of particles is made then their mean length is calculated using the D[1,0] equation[102].

2.13.3.1.2 D[2,0] the number-surface mean

$$D[2,0] = \frac{\sum d^2}{n} \qquad \text{-Equation 35.}$$

If a comparison is to be made between particles with different surface areas the D[2,0] formula is chosen.

2.13.3.1.3 D[3,0] the number-volume mean

$$D[3,0] = \frac{\sum d^3}{n}$$ -Equation 36.

If the consideration of a particles weight is required then the D[3,0] calculation allows for the comparison of (spherical) particles based on their weight[102].

2.13.3.2 Particle number independent calculations

It is often impossible to accurately calculate the number of particles within a sample, because of this D[1,0], D[2,0] and D[3,0] become unsuitable to calculate the mean particle size of the distribution. A solution to this problem is to calculate the mean of a distribution without knowing the number of particles present. This can be achieved by dividing a property of a sphere with radius^(n) by that of a different property of a sphere with radius^(n-1), for example the volume of a particle by its area (i.e. the Sauter mean diameter).

2.13.3.2.1 D[3,2] – the surface area moment mean or Sauter Mean Diameter (SMD)

$$D[3,2] = \frac{\sum d^3}{\sum d^2}$$ -Equation 37.

The Sauter mean diameter is the volume (numerator) divided by the surface area (denominator). SMD is used in applications where the surface area (denominator) is an important consideration –such as in catalytic studies. D[3,2] is sensitive to fine particles[102].

2.13.3.2.2 D[4,3] – volume or mass moment mean

$$D[4,3] = \frac{\sum d^4}{\sum d^3} \qquad \text{-Equation 38.}$$

The volume based median mean is equivalent to the mass moment mean and is also known as the De Brouckere Mean Diameter (DBMD). It is the most common method of calculating the mean particle size from laser diffraction measurements. The [4,3] value emphasizes the detection of the larger particles within the sample[102].

2.13.4 Number vs. volume distributions

As there are many different ways of calculating the mean particle size of a distribution it is possible to choose the method used to provide information on the different size properties of the sample. The mean particle size result calculated by the Malvern apparatus (using laser diffraction) is the volume or mass moment mean. The volume based mean weights the relative percentage within each size class towards larger particles due to the r^3 term when calculating volume[100]. For example using this method a one 10micron particle will give the same relative percentage value in its class as one thousand 1micron particles. This is acceptable in some cases, where the volume or mass of the particles is important. The direction of this research requires the number distribution of the measured particles.

Most particle size distributions have a larger number of smaller particles than larger particles, for this reason a widely used function for plotting the analysis data is a log-normal distribution[100]. A significant benefit of using a log-normal distribution is that the geometric standard deviation remains constant for the various distributions including; surface, number and mass. As these distributions are parallel on a log-probability plot

the distributions can be converted from one type to another. It is therefore possible to convert a D[4,3] distribution to a number distribution using a Hatch-Choate transformation[102] with the correct conversion parameter i.e. k=0.5.

$$\ln \bar{x}_{g,k} = 1 \ln \bar{x}_{g,0} + k\left(\ln \sigma_g\right)^2 \qquad \text{-Equation 39.}$$

This calculation is made internally within the Malvern apparatus and allows for transformations from volume to surface area, length and number –which will be demonstrated in the following section.

3 EXPERIMENTAL PROCEDURE

3.1 Supply of ingot

The material used for this research was aluminium copper alloy A205 created by Aeromet International PLC. All experiments detailed within this project originate from a supply of A205 ingot provided by the aforementioned company, the specification of which is detailed in Table 3.1.1.

Table 3.1.1 Standard A205 specification as given by Aeromet International PLC

	Ti	**Cu**	**Mg**	**Ag**	**TiB_2**	**Excess Ti**
Specification wt%	2.75-3.9	4.2-4.7	0.2-0.35	0.5-0.85	4-5	0.25 Aim

3.2 Alloy development

Within this research A205 alloy variations were created. The method used to produce these alloys was to calculate the weight composition of each of the alloying additions given in a specified weight of melt. Then, with the use of Microsoft Excels solver function, calculate the required amounts of alloying additions for each melt composition -including additions to keep the alloy within the defined specification.

For the TiB_2 dilution experiments the following alloys were created and compositionally analysed using XRF (see Table 3.2.1):

Table 3.2.1 TiB_2 Dilution 1 and TiB_2 Dilution 2 values measured using XRF

	TiB_2 (wt%)	**Excess Ti (wt%)**
Standard	4.26±0.04	0.26
TiB_2 Dilution 1	2.49±0.02	0.26
TiB_2 Dilution 2	1.16±0.01	0.26

For the Free Titanium experiments the following alloys were created and compositionally analysed using XRF (see Table 3.2.2):

Table 3.2.2 Sample 1 and Sample 2 free Titanium values measured using XRF

	% Ti added	**Excess Ti value (%)**
Standard	0.00	0.26±0.01
Sample 1	0.17	0.43±0.02
Sample 2	0.22	0.48±0.02

3.2.1 Preparation of sand mould

All experiments described in this work, unless stated otherwise, used a standard test bar mould design shown Figure 3-1, which consists of a central down sprue, 10 standard test bars and 2 larger feeder bars. The mould was designed to incorporate two 20 (pores per inch) ppi filters before the melt reached the test bars.

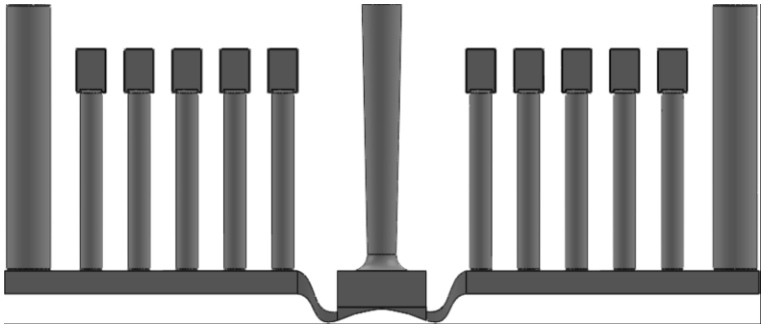

Figure 3-1 Schematic diagram showing the test bar mould design

The sand moulds were created in two 15kg sections. A two-part epoxy resin was then used to bind them together. After the 2 sections of the mould had been glued together a standard 3kg pouring basin was glued on top of the assembled mould. The mould was ready for casting after the glue had been allowed to set for a period of 2 hours.

3.2.2 Casting

The casting procedure used for all experiments begins with the melting of a pre-weighed approximately 10kg quantity of A205 ingot in a salamander A25 crucible. After the ingot had melted the temperature was stabilised at 800°C and the alloying additions were introduced, if required, allowing half an hour for full dissolution. After the additions had been made to the alloy, a 30minute lance degassing procedure was initiated where argon was gently bubbled through the melt. Half way through the degassing procedure the melt temperature was lowered to 780°C. Within a 5minute period after degassing the melt was cast and allowed to cool in air.

3.2.3 Heat treatment

Post casting several the samples required either a partial or full heat treatment. Samples which required a partial heat treatment underwent a solution heat treatment procedure.

Samples which required a full heat treatment underwent a solution heat treatment, and a precipitation hardening heat treatment. Samples which did not require a heat treatment were left in the 'as-cast' state.

3.2.3.1 Solution heat treatment

Standard test bar samples -a product of the casting procedure detailed in the Casting section, which required heat treatment, were processed in a Carbolite muffle furnace. In each case the samples were placed on top of a refractory brick so as to raise the samples to half the internal height of the furnace. A standard 'k' type thermocouple, supplied by TC Direct, was placed centrally on top of the refractor brick to ensure the correct required temperature offset between the machine and controller was used. The solutionising heat treatment procedure used is shown in Table 3.2.3.

Table 3.2.3 Standard solution heat treatment procedure for A205 (water quench)

Segment	Temp (°C)	Rate (°C/min)	Dwell (hrs)
1	495	50	/
2	/	/	4
3	505	50	/
4	/	/	6
5	525	50	/
6	/	/	10
7	538	50	/
8	/	/	24

Following solutionising the test bars were quenched in room temperature water.

3.2.3.2 Precipitation hardening heat treatment procedure

The ageing/precipitation hardening treatment consisted of 16hrs at 170°C, followed by an air quench.

3.3 Microscopy

3.3.1 Sample preparation

Samples were sectioned from the centre of test bars and mounted in conductive Bakelite. The samples were then polished using the following procedure:

Plane grinding: with silicon carbide paper from 120 grit through 240, 400, 800 to 1200 grit with water as a lubrication, using an approximate force of 20N at a speed of 300rpm for a time of 5minutes.

Fine grinding: with MD-Mol 3µm diamond polishing compounds (provided by Struers) at an approximate force of 20N and a speed of 150rpm for a time of 6mins. Followed by an OP-Chem cloth using 0.05µm colloidal silica (OP-S) at an approximate force of 20N and a speed of 150rpm for a time of 6mins (again provided by Struers).

3.3.2 Optical microscopy

A Carl Zeiss microscope was used for the optical microstructural examination of the samples. The digital images of each sample were first processed using PhotoShop so as to accurately trace around each grain within the sample. This image was then saved as a tiff file and reopened in image analysis software ImageJ where the threshold values were modified and the image converted into binary, black and white image. From this point it was then possible to use ImageJ's particle analysis function to calculate the area and perimeter of each traced grain within the image. So as to ensure only complete grains were analysed, any grain which touched the edge of the image was discounted from grain size analysis measurements -however these grains were included for the volume fraction measurements of the grain to grain boundary calculations.

3.3.3 Electron microscopy

For scanning electron microscopy (SEM) of the grain and grain boundary materials the following analysis machines were used: Philips Xl-30, Joel 6060 and Joel 7000. Each SEM machine used an energy dispersive X-ray spectroscopy (EDX) detector and a back

scatter electron (BSE) both of which were used for the quantitative elemental measurements of samples.

3.4 Tensile machine

Each of the cast test bars were machined post heat treatment. The machining requirements of this project were outsourced to Axis Precision (Mosley, Birmingham UK), who machined the bars to a standard design shown in Figure 3-2[107]. With a gauge length of 30mm, a length of reduced section of 37mm, a gauge diameter of 6.75mm, and a radius of fillet of 26mm. The end tabs had a radius of 10mm and a length of 20mm.

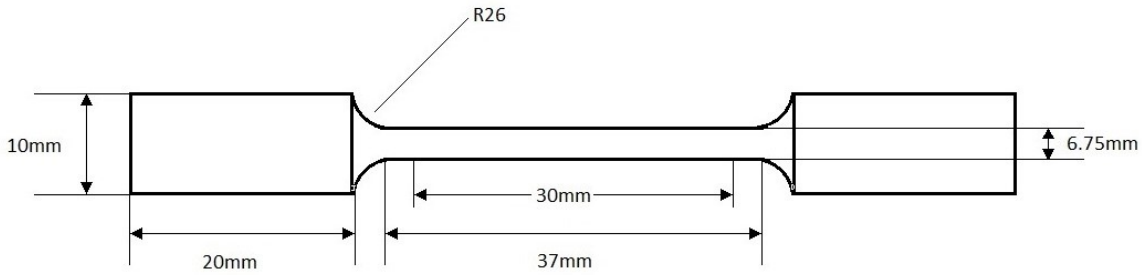

Figure 3-2 Cylindrical tensile test bar with dimensions

Following machining the test bars were pulled on a Zwick Mechanical Test Machine. The load used for the test was 100kN with an extension rate of 0.5mm/min. From the resulting force extension graph the Young's modulus, UTS and elongation were calculated using Microsoft Excel. The Young's modulus was calculated using the 0.2% offset method.

3.5 Composition analysis

3.5.1 XRF

For quantitative elemental analysis of samples greater than sodium in atomic weight a Bruker S8 Tiger X-Ray Fluorescence (XRF) Spectrometer was used. For solid sample analysis the samples were prepared so that the face requiring analysis was flat and ground with silicon carbide paper from 120 grit through 240, 400 to 800 grit. The size of the face requiring analysis had to be a minimum of $1cm^2$. The total sample size had to fit within a 5cm diameter, 3cm deep cylindrical volume. The samples were analysed under a Helium atmosphere for a period of 18 minutes.

For powder samples requiring XRF analysis, the sample had to be finely ground using a polished marble pestle and mortar. The minimum sample weight capable of being analysed was 0.5g. The samples were placed in a XRF safe sample cup (Series 2100 provided by Chemplex Industries INC), using a 2.5µm SpectroMembrane Mylar thin film (also supplied by Chemplex). The samples, similarly to the solid specimens, were analysed under a Helium atmosphere for a period of 18 minutes.

For liquid sample analysis a small volume (approximately 10ml) of pH7 liquid was transferred to the XRF sample cup. After the liquid had been transferred the sample was allowed to sit for a period of 30 minutes on top of blotting paper to allow for the material to settle to the analysis window of the cup, and also to ensure the sample was not leaking. The sample was analysed under a He atmosphere for a period of 6 minutes as specified.

3.5.2 XRD

For qualitative elemental analysis a Philips X'pert X-ray diffractometer (XRD) was used. For powder based samples approximately 0.1g of material was required. The powders were collected from the dissolution experiments (section 3.6.1) via filtration. A small aliquot of settled material was removed from the larger volume of dissolved, settled material using a 10ml glass pipette. The material was passed through a 47mm 0.2µm membrane filter provided by Advantec and the solid material was allowed to dry. The dried material was then removed from the filter paper and inserted into 5cm lengths of 1mm internal diameter, thin walled, quartz capillary. The first 5mm of the tubes were sealed with superglue before filling, the last 5mm of the tube was sealed after the tube had been filled. The tubes were held in the XRD machine using a purpose built holder which secured the samples into location using a grub screw. The holder rotated at 200rpm. As the sample width was smaller than the impinging X-ray beam a 5x10x0.3cm (h.w.d) lead sheet was positioned 2mm above the rotating sample so as to remove any stray X-rays passing straight though the specimen zone to the detector on the opposite side.

The X-ray diffractometer used was a Philips X'pert X-ray diffractometer with a Cu-Kα radiation wavelength of λ=1.540598 Å created using a current of 25mA and an accelerating voltage of 35 kV. The monochromatic X-ray beam incident on the surface created a diffraction spectrum which was collected using a solid-state detector over the angles of 0° to 110°. The resultant spectrum collected from the analysis of each sample was analysed using the X'pert High Score Plus V.2 analytical software using the PDF2004 peak database.

3.6 TiB_2 particle size analysis

3.6.1 Sample preparation

3.6.1.1 A205 alloy dissolution

To characterise the TiB_2 content accurately it was necessary to remove the TiB_2 from the A205 metal. This was achieved by dissolving the sample of A205 using 2M hydrochloric acid (HCl) detailed in the reaction;

$$2\,Al + 6\,HCl \rightarrow\ 2\,Al\,Cl_3 +\ 3\,H_2$$

The cast bars were skimmed to remove any surface oxides and cleaned using ethanol before weighing and subsequent dissolution. To ensure that the entire sample was dissolved by the acid, a theoretical excess of 20% was added to the weight of the sample before the volume of acid was calculated. This was then left for 140 hours to completely dissolve at room temperature.

3.6.1.2 Serial dilution to pH7

For particle size analysis and XRF analysis the sample material was required to be pH7. To raise the pH of the dissolved samples a series of serial dilution processes were undertaken. Following the initial dissolution, 90% of the supernatant for each experiment was removed via a pipette. This was then replaced with an identical quantity of deionised water. The sample was then left for a period of 48hrs for the precipitate to re-settle on the bottom of the beaker. This process was repeated 5 times for each sample.

3.6.2 Particle size analysis

A Malvern particle size analysis machine was used to analyse the collected undissolved materials following the alloys dissolution in HCl. The apparatus back calculates particle size information by using Mie theory which describes the scattering of (laser) light around particles -which are of a similar size to the wavelength of light used. The theory requires both the dispersants and the particles refractive indexes to be know, as well as the particles absorption coefficient. The refractive index of the dispersant i.e. water, was taken to be 1.33. The refractive index and the absorption coefficient of TiB_2 were taken to be 2.5 and 1.0 respectively[108].

For the experimental series described the machine had all piping, seals, glass wear and lenses replaced prior to a full calibration. The machine was flushed with 3 litres of deionised water between experiments. Following the cleaning procedure, a 1 litre beaker, filled with 500ml of deionised water was placed in the sample zone of the machine. The pump system was lowered into the beaker and the pump system activated to 100rpm for 30seonds to flush the larger trapped air bubbles out of the internal piping and measurement cell of the machine. The pump system was then disengaged for a period of 30seconds then reengaged to 150rpm during which time all lengths of piping where checked for any remaining small trapped air pockets. The standard operation procedure began with setting the machines stirring system to 2000rpm. Material to be analysed was then added to the dispersant via pipette until the laser obscuration value increased to between 5 and 10%. The ultrasonic agitator was then engaged for an experimentally considered value of 10 for a time of 10minutes. The measurement procedure was then initiated which consisted of:

10 measurements taken per sample with each measurement comprising of a 30 seconds background time and a 30 second measurement time -each consisting of 30,000 snaps. The final result was an average of the 10 measurements.

3.7 Electrochemistry

The material sent for particle size analysis contained copper, efforts were made into removing copper from the sample. The technique deemed most suitable for this task was electrochemistry. Electrochemistry was chosen as elements could be removed from the sample material and deposited into the electrolytic solution.

The process of electrochemistry is based on electron mechanics. Electrons on a metallic material can be (partially) described by their Fermi-level. If this level has more energy than the electron orbital levels of an atom incident upon the electrode, electrons will transfer from the electrode to fill the available electron energy level. As the required energy is compound specific, different elements can be target for oxidation or reduction as required.

3.7.1 Sample preparation

To ensure that TiB_2 was electrochemically stable within the used voltage ranges a sample was prepared for electrochemical analysis. For this experimental verification 0.500g of TiB_2 was mixed with 1000ml of 2M HCl for a period of 100 hours. This was then ultrasonically agitated for 5minutes before 10µL was removed via pipette and 'dropped' onto the prepared surface of a Glassy Carbon (GC) electrode. The protocol followed for the preparation of the GC electrodes (and the EPPG and BPPG electrodes) commenced with 100 figure-of-eight traces on a Struers 'Mol' polishing pad with a coarse 45µm Struers diamond suspension paste. The electrode was then washed in deionised water

before having this process repeated using 9µm, 3µm, 1µm, 0.5µm and 0.05µm polishing compounds on separate 'Mol' polishing pads. The 'dropped' sample was cured onto the respective electrode 20cm under a 100W lamp for a period of 40minutes.

The carrier electrolyte solution was 50ml of 0.1M KCl. The solution was degassed with nitrogen for 60 minutes prior to the electrodes being introduced to the system. The reference electrode used was a saturated leak-less Ag/AgCl reference electrode. The counter electrode was platinum. The working electrode was glassy carbon (GC). During analysis the surface of the carrier electrolyte was maintained under a nitrogen atmosphere. The potentiostat used was an Ivium CompactStat.h. The analysis sweep performed for this test was at a scan rate of 50mV/s in 2mV steps.

The samples required for the electrochemical experimental series follow on from the casting section previously defined within this chapter. The cast test bar material chosen for this experimental series was fully heat treated and precipitation hardened A205. These test bars were then skimmed on a lathe to remove any surface oxides and cleaned with ethanol. Following dissolution in 2M HCl for a period of 140 hours, 95% of the supernatant material was removed via pipette with care taken so as not to disturb the resultant settled material. This material was then transferred to a 100ml sealable reagent bottle for transport and storage.

3.7.2 Indium Tin Oxide electrode

For the Indium Tin Oxide (ITO) electrode experiments the experimental method was as follows:

The transferred material was vigorously shaken for 30seconds. From this the required volumes i.e. 5, 10, 15 and 20µL of sample were removed from the reagent bottle using a variable 0-20µL pipette and 'dropped' onto a 2cm x 1cm section of an ITO coated glass slide (provided by Sigma Aldrich). This was then placed 20cm below a 100W bulb for a period of 40minutes. The carrier electrolyte (0.1M KCl) was degassed as previously mentioned by bubbling nitrogen through the solution for a period of 60 minutes. For this experimental series the scans were carried out between -0.4V and +0.4V -with respect to the Ag/AgCl reference electrode and were cycled at a scan rate of 25mV/s in 2mV steps.

3.7.3 Glassy Carbon electrode

For the ph7 Glassy Carbon (GC) electrode experiments the experimental method was as follows:

The samples required for this experimental series follow on from the casting, dissolution and dilution sections of this chapter. The diluted ph7 material was chosen for electrochemical processing as the electrochemically processed material would require post-process analysis on machines incapable of handling acidic solutions. The ph7 material was vigorously shaken for 30 seconds. From this the required volumes of sample i.e. 5, 10 and 20µL were removed from the reagent bottle using a variable 0-20µL pipette and 'dropped' onto the surface of the prepared GC electrode surface. This was then placed 20cm below a 100W bulb for a period of 40minutes so the sample could dry to the surface of the electrode. The prepared electrode was then submerged in the degassed carrier electrolyte along with the Ag/AgCl reference electrode and the platinum counter electrode. The scans were carried out between -0.3V and +0.7V at a scan rate of 100mV/s

in 2mV step increments. The experiment was carried out underneath a nitrogen atmosphere.

For the re-acidified Glassy Carbon (GC) electrode experiments the method was as flows:

The ph7 material to be analysed was again vigorously shaken for 30 seconds before samples were removed via pipette and 'dropped' onto the prepared surface of a Glassy Carbon electrode and dried under a 100W lamp for 40minutes. The carrier electrolyte solution was altered from 50ml 0.1M KCl to 0.1H H_2SO_4 in effort to reduce to formation of unwanted peaks during the electrochemical processing. The carrier electrolyte solution was similarly degassed for a 40-minute period pre-analysis and maintained under a nitrogen atmosphere for the duration of the experiment. For this experimental series the scan was carried out between -0.3V and +0.3V at 100mV/s in 2mV steps.

3.7.4 CV scan analysis

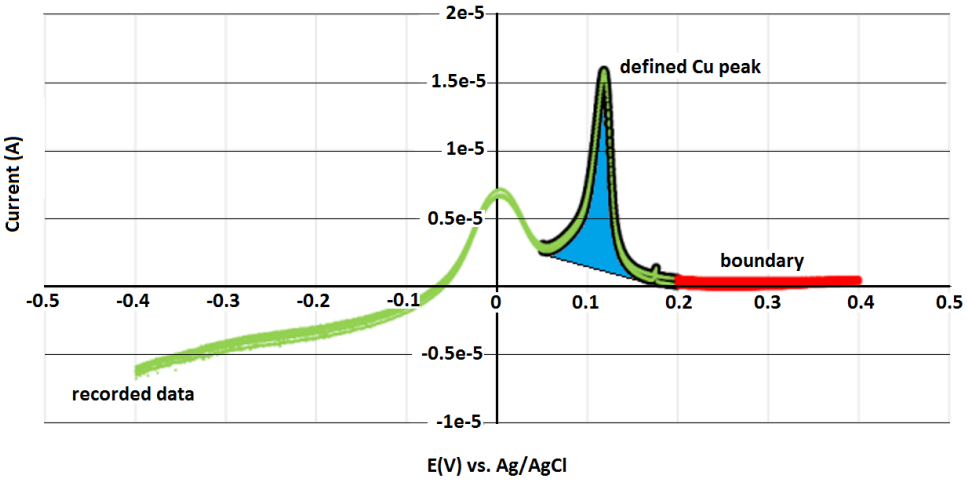

Figure 3-3 Graphic example of the 'reviewed' peak analysis profile used in excel

Figure 3-3 shows an example of how each electrochemical peak was analysed. For Cyclic-Voltammetry (CV) peaks the scan sequence swept from -0.4V to +0.4V to -0.4V

(for example). The second half of the CV peak, i.e. from +0.4V back to -0.4V was removed from the analysis calculations. In the remaining first half of the cycle (an example of which is shown in the figure) the copper peak was outlined between two voltage values. Data points outside of these values were excluded from further calculations. The area of the contained peak, shown in the image as blue, was then calculated.

3.7.5 Chronoamperometry

For the chronoamperometry experiment the method was as flows:

The carrier electrolyte material was changed to 50ml of ph7 material as detailed previously in the dilution section of this chapter, to this 0.1M of H_2SO_4 was added. This material was then subjected to 5minutes of ultrasonic agitation in an ultrasonic bath. The reference electrode was Ag/AgCl, the counter electrode was platinum. The working electrode was a 2mm thick poco graphite sheet with 2 sides each having an area of 6.25cm^2 and 3 edges having an area of 1.5cm^2 (total area 7.75cm^2). A small 10mm magnetic flea was also introduced to the cell which was rotating throughout the experiment at a rate of 60Hz. The solution was degassed with nitrogen for 1hr pre-analysis and was maintained under a nitrogen atmosphere throughout the experiment. The working electrode was held at +0.8V for three sequential 1hr periods.

3.7.6 Electro-bombardment

For the electro-bombardment experiment the method was as flows:

The carrier electrolyte material was 50ml of 0.1M KCl. The reference electrode was Ag/AgCl, the counter electrode was platinum. The working electrode was a poco graphite

sheet with total area 12.5cm^2. A small 10mm magnetic flea was also introduced to the cell which was rotating throughout the experiment at a rate of 60Hz. The solution was degassed with nitrogen for 1hr pre analysis and was maintained under a nitrogen atmosphere throughout the experiment. The working electrode was held at -0.1V, 0.0V, +0.1V, +0.2V and +0.4V for each experiment respectively.

3.8 TP1 grain refinement settling experiments

The material used for the TP1 grain refining settling experiments was Al–5Ti–1B grain refining rods provided by London Scandinavian Metals (LSM). The rods were melted at a temperature of 800°C in a conduction furnace and transferred to Salamander A3 crucibles (0.49L) -preheated to 780°C in a resistance oven. The filled crucibles were left in the electric element oven at 780°C for the settling times required. Upon reaching the individual settling times the crucibles were removed from the oven and allowed to cool in air.

3.8.1 Initial XRF investigation

An arbitrary settling time of 10mins was initially selected for XRF analysis to determine the most suitable material locations for use in the TP1 tests. The resulting solidified melt was sectioned equally down its vertical axis. Four samples, with a surface finish of 800 grit, were sectioned for XRF analysis as shown in Figure 3-4.

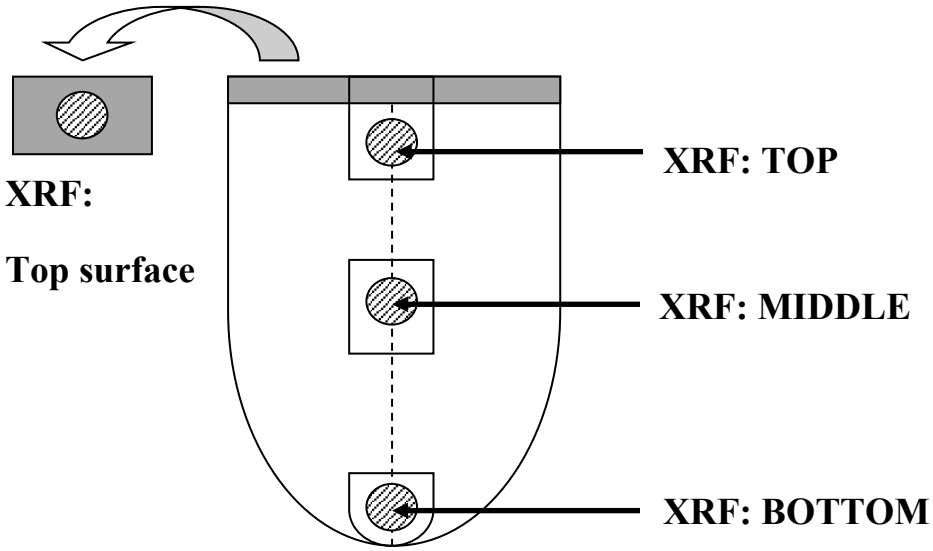

Figure 3-4 Locations of settled material selected for XRF analysis

3.8.2 TP1 sample preparation

The samples which had undergone specific settling times were removed from their crucibles and halved vertically. 2 horizontal slice samples were taken from each casting, one form the top just below the settling line, and one from approximately 1cm above the bottom of the casting (see Figure 3-5). Following Inductively Coupled Plasma (ICP) analysis carried out by Rotech LTD, calculations could be made to determine the correct weight of sample required to add to a 10kg commercially pure aluminium melt for TP1 analysis.

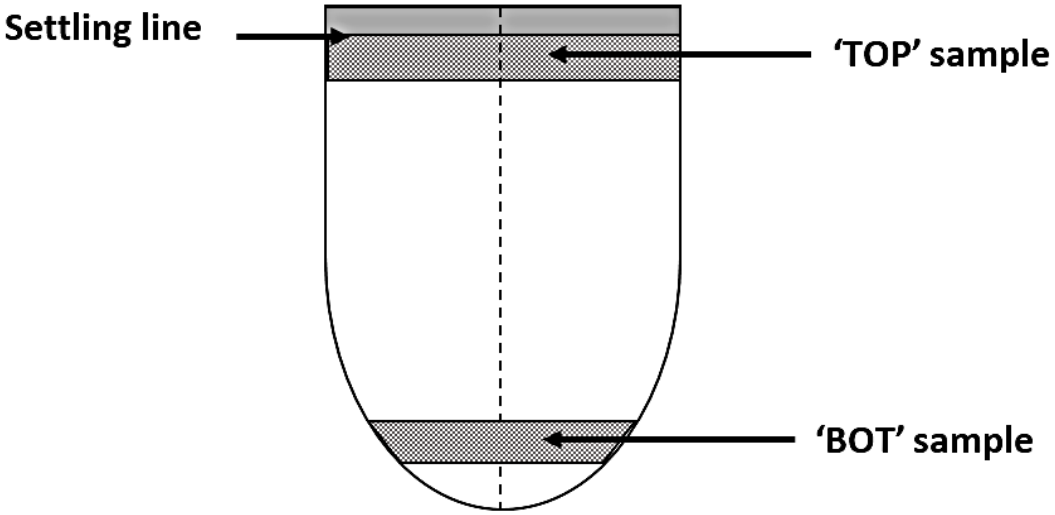

Figure 3-5 TP1 settling sample locations

The standard test procedure for aluminium alloy grain refiners is the TP1 test as described by the Aluminium Association. For this test approximately 10kg of commercially pure aluminium was melted and stabilised at 718±5°C. As the additions were added the melt was stirred for 15 seconds with a Silon rod. The TP1 samples were taken from the melt using a pre-heated standard TP1 ladle. A thermocouple ensured that each TP1 sample removed from the crucible was at 718±5°C. The TP1 samples were immediately quenched in the prescribed running water TP1 quench tank. The resulting TP1 samples were then cut and dressed to a length of 38mm, followed by polishing and etching using Poulton's solution[1].

[1] Poulton's solution: 60% concentrated HCl, 30% concentrated HNO_3, 5% HF and 5% H_2O

3.8.3 Grain size analysis

After sample preparation, grain size observation was carried out using a digital microscope. The grains were traced in Adobe Photoshop and analysed using the image analysis software ImageJ. The outputted data was then exported to excel and subjected to statistical analysis.

4 RESULTS

4.1 Microstructure of A205 alloy

The microstructure of fully heat treated A205 is shown in Figure 4-1. Unlike other aluminium-copper alloys, A205 solidifies with a globular (thamnitic) structure as opposed to dendritic. The contrast between the grain interior and grain boundary regions, shown in Figure 4-1, have been increased by etching the material using Keller's solution and imaging the sample using Back Scattered Electron (BSE) microscopy.

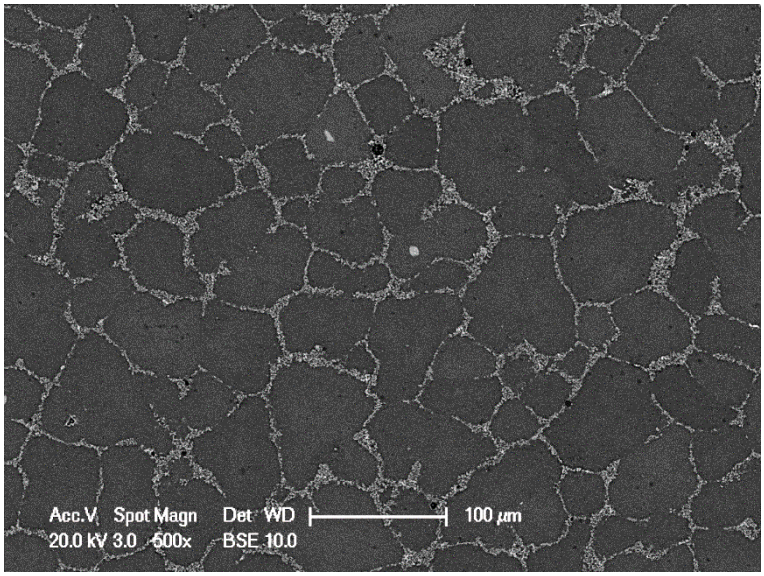

Figure 4-1 BSE SEM image of fully heat treated A205 etched using Keller's solution showing a globular microstructure

Figure 4-2 (a) is an optical micrograph image of fully heat treated A205 and shows the globular grain structure as well as the surrounding grain boundary material. Figure 4-2 (b) is a converted image taken from Figure 4-2 (a) and shows a black and white (binary) image of A205 used for calculating the volume fraction analysis of grain to grain

boundary material within the alloy. The image was created by tracing the recorded optical micrographs in Adobe Photoshop then modifying the image so that the grain boundaries appeared black and the grain material appeared white. The traced images were then analysed using ImageJ. The reported volume fraction of the grain boundary material was 27.3 ± 1.2% and was calculated from the average of 9 micrographs taken from 3 separate sectioned test bar samples originating from 3 individual castings of A205. The calculated error was the standard deviation of the measured results.

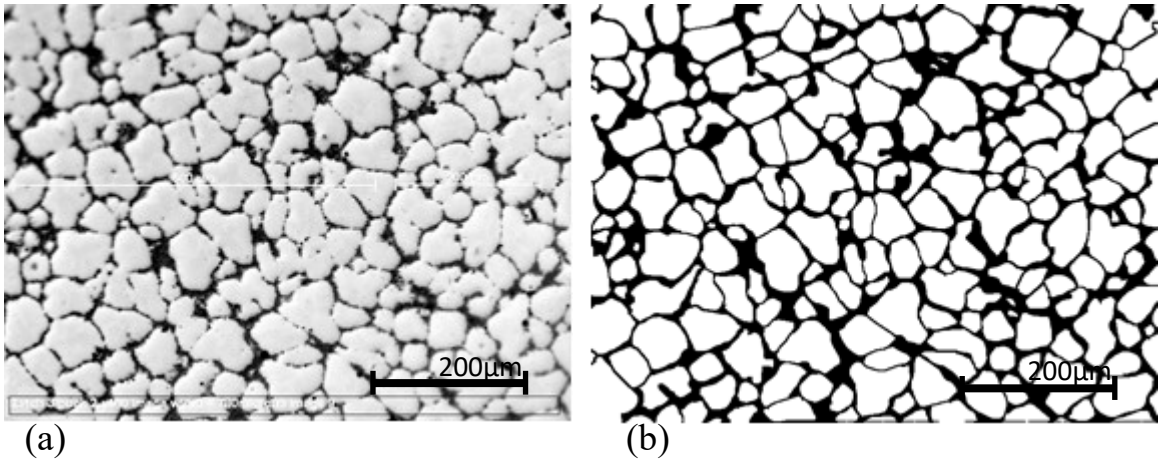

Figure 4-2 (a) optical a micrograph of fully heat treated A205 showing the globular microstructure and the grain boundary material, (b) a converted binary image created using Figure 4-3 (a) used for calculating the grain to grain boundary material volume fractions using ImageJ

Figure 4-4 (a) shows an SEM image of the heat treated alloy, the image shows the grain material to be compositionally different from the darker surrounding grain boundary material. Energy Dispersive X-ray (EDX) spectroscopy mapping for aluminium and titanium shows; the grain material to be aluminium and the grain boundary material to be comprised of titanium (i.e. TiB_2), Figure 4-4 (b and c) respectively.

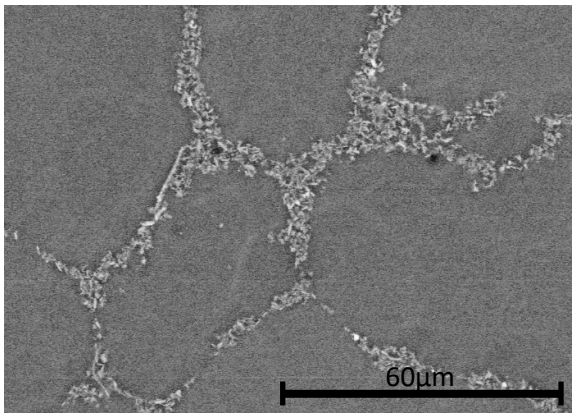

(a)

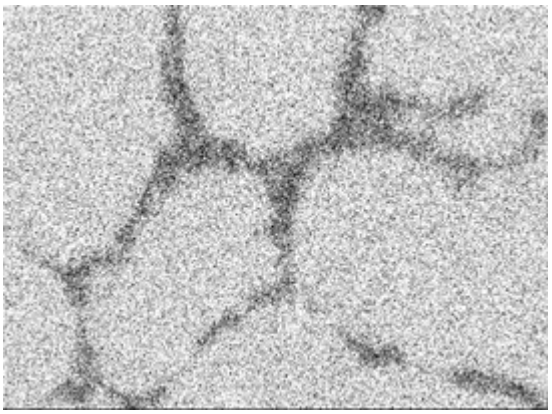

(b)

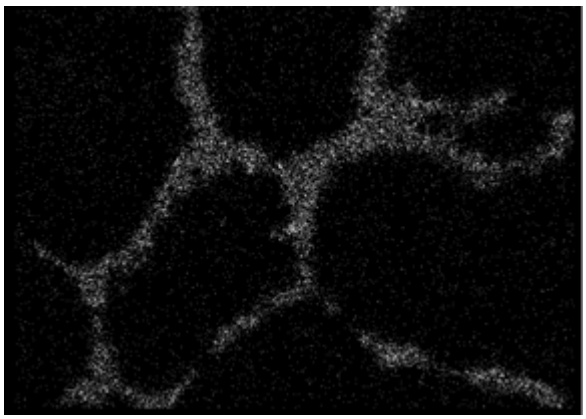

(c)

Figure 4-4 (a) SEM image of fully heat treated A205, (b) EDX map showing location of Al within the sample, (c) EDX map showing location of Ti within the sample

Figure 4-5 shows a close up of the grain boundary region. The lighter coloured features are Titanium Diboride (TiB_2) particles as confirmed by EDX. The outer fringes of the image show the surrounding grain material as labelled in the figure. The particles within the grain boundary are randomly orientated and hence give the impression of being more rod-like than plate-like within the SEM image -as highlighted in the circular region of interest. When individually analysed the TiB_2 particles appear to be around a micron in size.

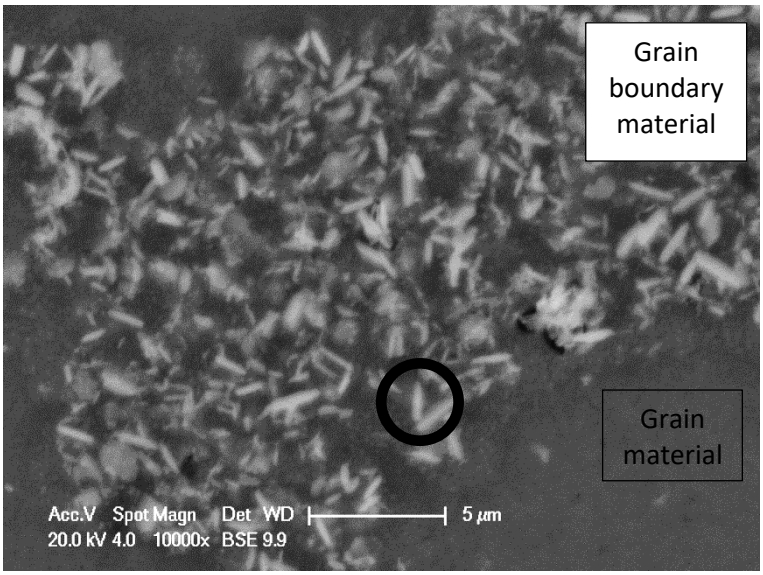

Figure 4-5 SEM image of heat treated A205 showing the TiB_2 containing grain boundary region. The figure highlights an individual TiB_2 particle, measured to be approximately 1µm in length.

To determine the strength contributions of the different mechanisms contained within the alloy as a whole, the volume fraction of the TiB_2 particles in the grain boundary material was determined. Figure 4-6 is an altered version of the SEM image shown in Figure 4-5, the grain material has been removed from the image using Adobe Photoshop and a white rectangular area of interest is highlighted to indicate the area selected for TiB_2 volume fraction analysis. The image was taken from a centrally located section of grain boundary material from within a standard test bar sample. In total 9 such measurements were made, with images taken from 3 non-adjoining samples from each of the as-cast, solution heat-treated, and solution heat-treated and precipitation hardened materials.

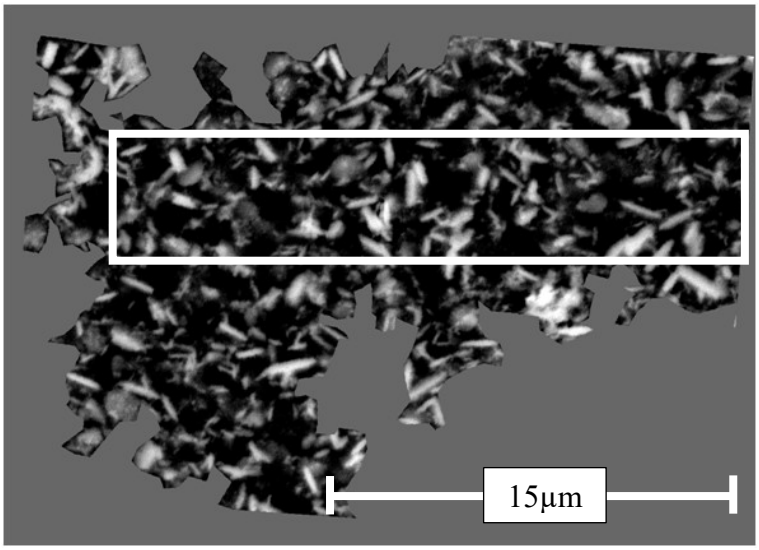

Figure 4-6 An area of centrally located grain boundary material (from fully heat treated material) selected for TiB_2 volume fraction analysis

Figure 4-7 shows an expanded view of the region of interest highlighted in Figure 4-6. The figure shows the random orientation and distribution of the TiB_2 particles within the grain boundary material.

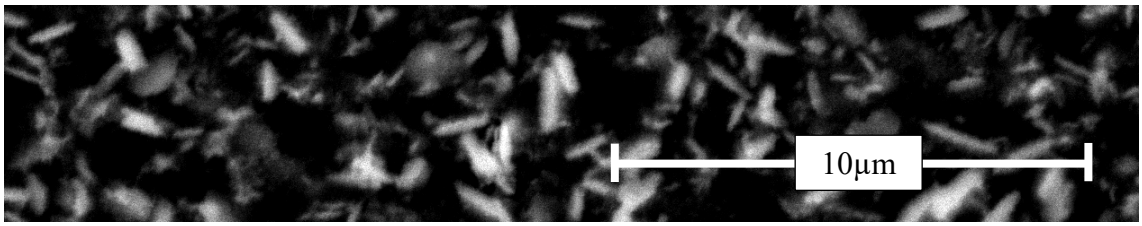

Figure 4-7 Section of grain boundary material chosen for volume fraction analysis

Converting Figure 4-7 into a black and white binary image, using ImageJ, Figure 4-8 was created. Using Figure 4-8 it was then possible to determine the volume fraction of TiB_2 particles within the grain boundary region. The reported volume fraction TiB_2 particles within the grain boundary region was 40 ± 2.4% and was calculated from the average of 9 micrographs taken from 3 separate sectioned test bar samples originating from 3

individual castings of A205. The calculated error was the standard deviation of the measured results.

Figure 4-8 Converted black and white region of interest shown in Figure 4-7 used for volume fraction analysis of TiB_2 particles within the grain boundary material

4.1.1 Heat treatment

The heat treatment of A205 consisted of a solution heat treatment procedure and a precipitation hardening procedure. The solution heat treatment procedure was for 44hrs and consisted of 4 stages: 4hrs at 495°C, 6hrs at 505°C, 10hrs at 525°C, and 24hrs at 538°C followed by a water quench. The precipitation hardening procedure consisted of 16hrs at 170°C, followed by an air quench.

4.1.2 Strengthening Mechanisms

Yield strength is caused by many different mechanisms; however, it is possible to disassemble this value into its constituent parts. The strength of A205 can be broadly considered as coming from the matrix (or grain) and the grain boundary material. In the matrix material, 4 types of strengthening mechanisms would be active; Orowan, Hall-Petch, Coefficient of Thermal Expansion (CTE) and the Load strengthening mechanisms. Within the grain boundary material, the Load and the CTE strengthening mechanisms would occur. The formulas describing these mechanisms were given in the strengthening mechanisms section of the literature review.

Regarding the matrix; the Orowan strengthening mechanisms and the load strengthening mechanisms are active around the Ω and θ precipitates, which were precipitated out during heat treatment. The Hall-Petch strengthening mechanism is linked to the grain size of the alloy. Regarding the grain boundary material; the CTE and load strengthening mechanisms occur, and are linked to the TiB_2 particle size distribution.

The contributions to the yield strength were estimated by considering the grain and grain-boundary areas of the material individually with contributions to the strength weighted according to their respective volume fractions and measured TiB_2 particle size distributions.

4.2 Effect of composition on globularity

A significant property of the A205 alloy is its thamnitic crystal structure, as globular crystal structures have improved feeding properties when compared to their dendritic counterparts. For this reason, a study was undertaken to explore the globularity of the alloy when alterations were made to its composition. The composition of the base A205 alloy provided by Aeromet can be found in Table 4.2.1.

The alloying elements chosen for the study were; TiB_2 and the free Ti component of the alloy's composition.

Table 4.2.1 A205's specification limits and specific composition of the base alloy sample provided and measured by Aeromet International using Optical Emission Spectroscopy. The TiB_2 wt% was calculated using the stoichiometric ratio of Ti to B_2 with the remainder as free Ti.

Element	Ti	B	Fe	Si	Cu	Mg	Ag	V	TiB_2	Excess Ti
Specification wt%	2.75-3.9	1.25-1.55	0.05 max	0.07 max	4.2-4.7	0.2-0.35	0.5-0.85	0.05	4-5	0.25 Aim
Ingot wt%	3.37	1.45	0.02	0.06	4.43	0.30	0.69	0.04	4.66	0.26

4.2.1 TiB_2 wt% dilution

To determine the effect of the TiB_2 concentration on globularity a series of castings were made with various amounts of TiB_2. This was achieved by adding commercial purity aluminium, copper, silver, magnesium and titanium to a melt of A205 alloy to halve the TiB_2 concentration, see Table 4.2.2.

Following alloy modification, a series of test bars were cast, 3 of each modification series were analysed using XRF -as a more accurate form of compositional analysis compared to OES (Table 4.2.2). The mean composition of each series of 3 test bars were as follows:

Table 4.2.2 TiB_2 dilution experiment specifications as measured by XRF

Element	Ti	Cu	Mg	Ag	TiB_2	Excess Ti
Specification wt%	2.75-3.9	4.2-4.7	0.2-0.35	0.5-0.85	4-5	0.25 Aim
Standard A205	3.19	3.95	0.19	0.65	4.26±0.04	0.26
TiB_2 Dilution 1	1.98	4.33	0.19	0.75	2.49±0.02	0.26
TiB_2 Dilution 2	1.06	4.27	0.26	0.75	1.16±0.01	0.26

The TiB_2 content for the original alloy was calculated to be 4.26 wt% TiB_2. Following dilution (Dilution 1) the TiB_2's content decreased to 2.49 wt%. Following a second dilution (Dilution 2) the TiB_2 weight percentage was reduced to 1.16%.

Figure 4-9 (a) shows an optical microscopy image of the initial A205 alloy, taken from the centre of a test bar. The micrograph shows light globular crystals and darker grain boundary material. Tracing these grains (see Figure 4-9 (b)) gave the size and shape of each grain using image analysis. To remove edge effects from grain size measurements, any grain which was touching the edge of the image was removed from the calculations.

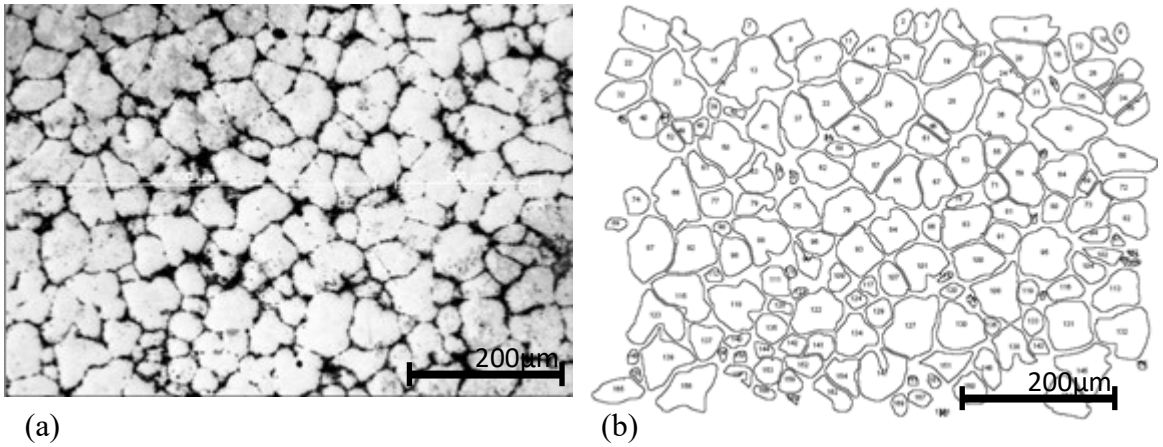

(a) (b)

Figure 4-9 (a) optical micrograph of standard A205, (b) traced grains for use in size calculations

Figure 4-10 (a) shows an optical microscopy image of diluted A205 which was measured to contain 2.49wt% TiB_2, taken from the centre of a sectioned test bar. Tracing the grains, (see Figure 4-10 (b)) produced an accurate determinate of the size and shape of each grain using image analysis. To remove edge effects from grain size measurements, any grain which was touching the edge of the image were removed from calculations.

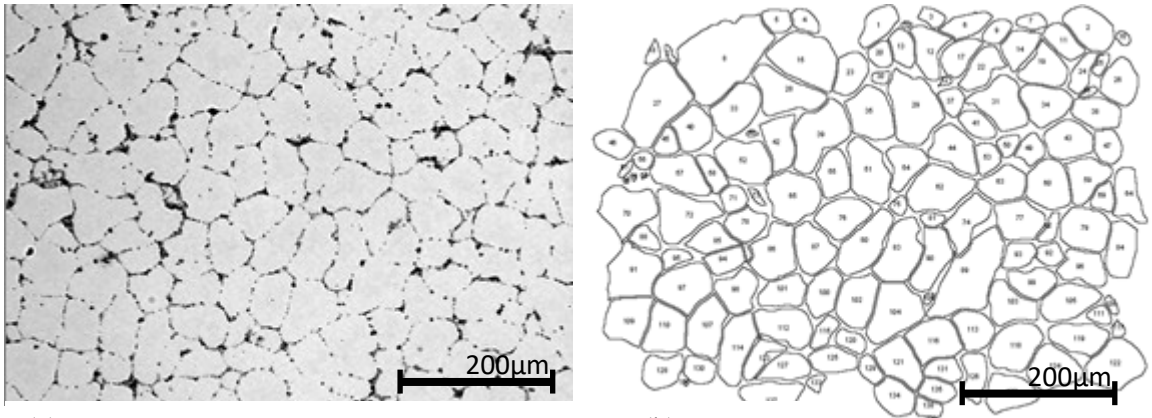

(a) (b)

Figure 4-10 (a) optical micrograph of TiB_2 Dilution 1, (b) traced grains for use in size calculations

Figure 4-11 (a) shows an optical microscopy image of diluted A205 alloy which was measured, using XRF, to contain 1.16wt% TiB_2.

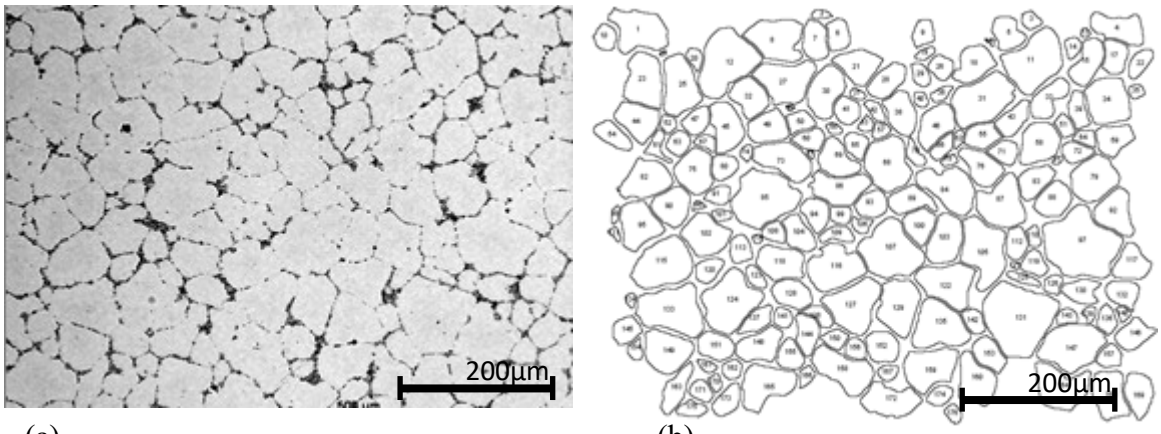

(a) (b)

Figure 4-11 (a) optical micrograph of TiB_2 Dilution 2, (b) traced grains for use in size calculations

Image analysis of the micrographs produced a determination of each grains circularity value with respect to its composition. For each composition, 3 non-adjoining sections were traced and analysed, with each micrograph typically containing between 100-200 grains. (The circularity value is a value between 0 and 1 with 1 representing a perfect circle, and was calculated by comparing the area of a shape against its perimeter using the equation; circularity = 4π Area / Perimeter^2).

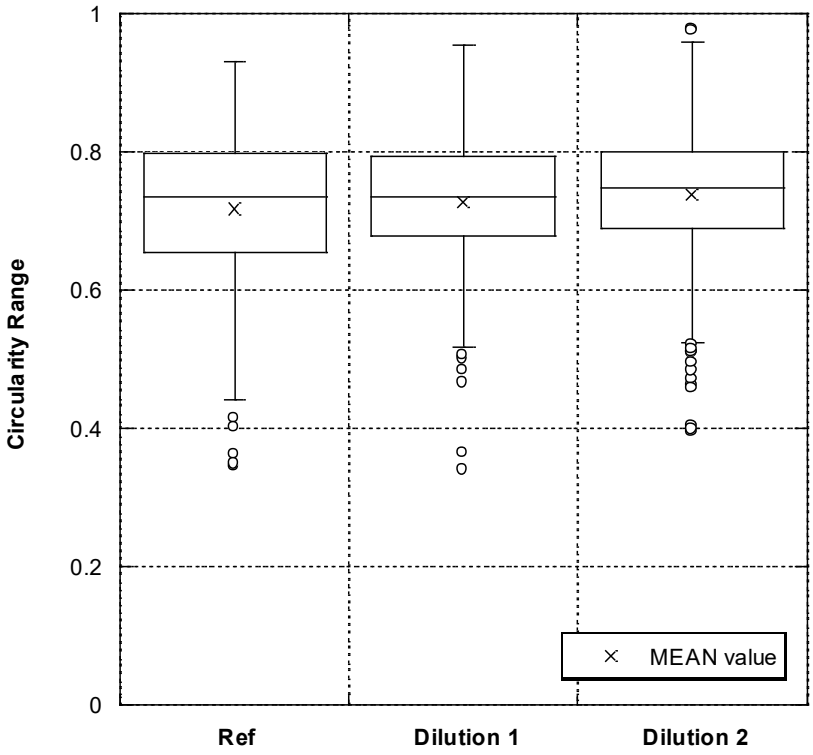

Figure 4-12 Circularity range for a standard 'reference' sample of A205 (4.26wt%) and the circularity values for the Dilution1 (2.49wt%) and Dilution2 (1.16wt%) experiments

Figure 4-12 shows a circularity box plot for the initial as cast A205 alloy, labelled 'Ref', and the experimental alloys 'Dilution 1' and experimental series 'Dilution 2'. With regards to the initial A205 alloy, of which 335 grains were analysed, the mean circularity value was calculated to be 0.72. For the Dilution 1 alloy, of which 379 grains were analysed, the mean circularity value was calculated to be 0.73. The Dilution 2 sample, of which 465 grains were analysed, gave a mean circularity value of 0.74. The analysis of Figure 4-12 is tabulated in Table 4.2.3.

Table 4.2.3 Statistical analysis of the dilution experiments circularity results

	Reference (4.26wt%)	**Dilution 1 (2.49wt%)**	**Dilution 2 (1.16wt%)**
Number of grains	335	379	465
Mean	0.718	0.729	0.740
Max value	0.930	0.955	0.979
Q3+1.5(IQR)	Fixed at 1	0.966	0.971
Quartile 3	0.799	0.794	0.802
Quartile 2	0.735	0.736	0.748
Quartile 1	0.654	0.679	0.689
Q1-1.5(IQR)	0.438	0.506	0.520
Min value	0.345	0.340	0.395

Table 4.2.3 shows the statistical analysis of Figure 4-12. In relation to the initial alloy 75% of the data had a circularity measurement of greater than 0.65. For the Dilution 1 alloy 75% of the measured grains had a circularity value of greater than 0.68. For the Dilution 2 alloy 75% of the grains had circularity values greater than 0.69. Due to the high circularity values calculated for these samples it was deemed acceptable to assume each grain to be circular for the purpose of grain size analysis.

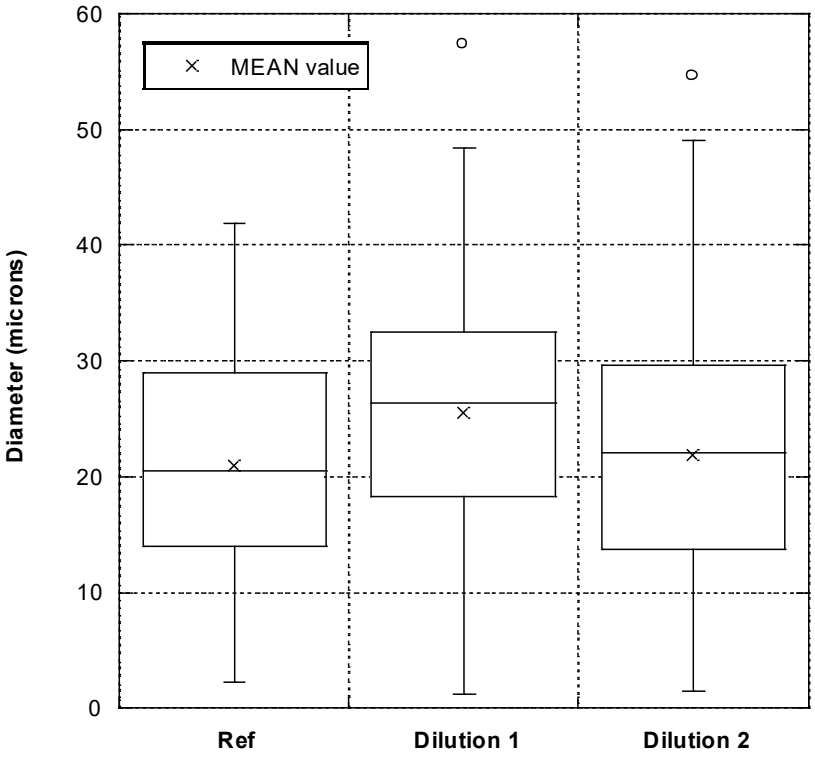

Figure 4-13 Diameter range for a standard 'reference' sample of A205 (4.26wt%) and the diameter values for the Dilution1 (2.49wt%) and Dilution2 (1.16wt%) experiments

Figure 4-13 shows the statistical analysis of the grain size measurements for the initial alloy and the Dilution 1 and Dilution 2 alloys. With regards to the standard alloy; the width of the distribution, i.e. between Q3+1.5(IQR) and Q1-1.5(IQR), where IQR is the inter quartile range calculated by Q3-Q1, was narrower than both the Dilution 1 and 2's results. The Dilution 1 experiment had a higher mean (25.6µm) than both the standard sample (20.9µm) and the Dilution 2 sample (21.9µm).

Table 4.2.4 Statistical analysis of the dilution experiments' diameter results

	Reference (4.26wt%)	**Dilution 1 (2.49wt%)**	**Dilution 2 (1.16wt%)**
Number of grains	335	379	465
Mean (μm)	20.90	25.57	21.86
Max value (μm)	41.84	57.34	54.60
Q3+1.5(IQR) (μm)	51.46	54.25	53.61
Quartile 3 (μm)	29.06	32.61	29.66
Quartile 2 (μm)	20.53	26.38	22.14
Quartile 1 (μm)	13.95	18.19	13.69
Q1-1.5(IQR) (μm)	Fixed at 0	Fixed at 0	Fixed at 0
Min value (μm)	2.29	1.18	1.45

Table 4.2.4 shows the grain size of the TiB_2 dilution experiments. Comparison of the mean grain size values reveals the initial alloy to have the smallest grain size at 20.9μm, next in increasing size was the mean grain size of 21.9μm for Dilution 2, followed by Dilution 1's grain size of 25.6μm.

Table 4.2.5 Volume fraction of grain to grain boundary material for the TiB_2 dilution experiments

	Grain (%)	**Grain boundary (%)**
Standard A205 (4.26wt%)	72.70 ± 1.22	27.30 ± 1.22
Dilution 1 (2.49wt%)	83.28 ± 1.33	16.72 ± 1.33
Dilution 2 (1.16wt%)	77.74 ± 0.71	22.26 ± 0.71

Table 4.2.5 shows the volume fraction of grain to grain boundary material for the standard sample of A205, and TiB_2 dilution experiments 1 and 2. The standard A205 sample had the largest volume fraction of grain boundary material at 27% followed by Dilution 2 sample with 22%. Dilution 1 sample had the lowest volume fraction of grain boundary material at 17%.

4.2.2 Free Titanium

To investigate the effect of excess titanium levels, i.e., the titanium not bound to boron as TiB_2, 2 casting trials were carried out with increased 'free' titanium in the melt obtained by the addition of AlTi10 rod.

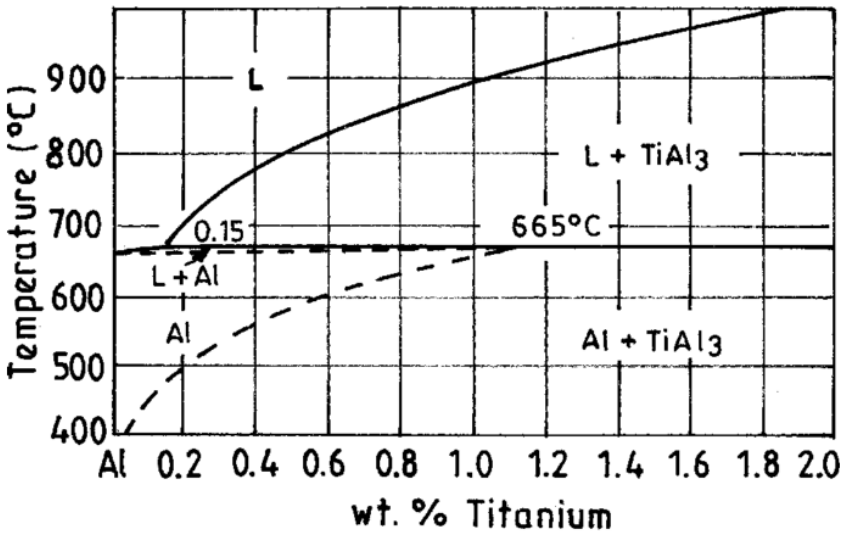

Figure 4-14 Al rich end of the binary Al - Ti phase diagram[109]

To ensure the titanium present in the grain refining rod went into solution, the melt was raised and kept at a temperature of 800°C for 1 hour, as illustrated by the binary Al-Ti phase diagram (Figure 4-14). The alloy was kept within specification limits of the A205 alloy by adding pre-determined amounts of copper to each experimental trial.

Table 4.2.6 Percentage of Ti added to each melt and therefore the excess Ti level of Sample 1 and Sample 2 determined by XRF

	% Ti added	Excess Ti value (%)
Standard A205	0.00	0.26±0.01
Sample 1	0.17	0.43±0.02
Sample 2	0.22	0.48±0.02

Table 4.2.6 shows the amount of excess titanium present. XRF analysis showed the standard A205 sample to contain 0.26 wt% of excess ('free') titanium. Following addition of AlTi10 and copper, the excess Ti value was raised for 'Sample 1' to 0.43 wt%. For the second series of free titanium experiments the Ti content was raised further to a value of 0.48 wt%.

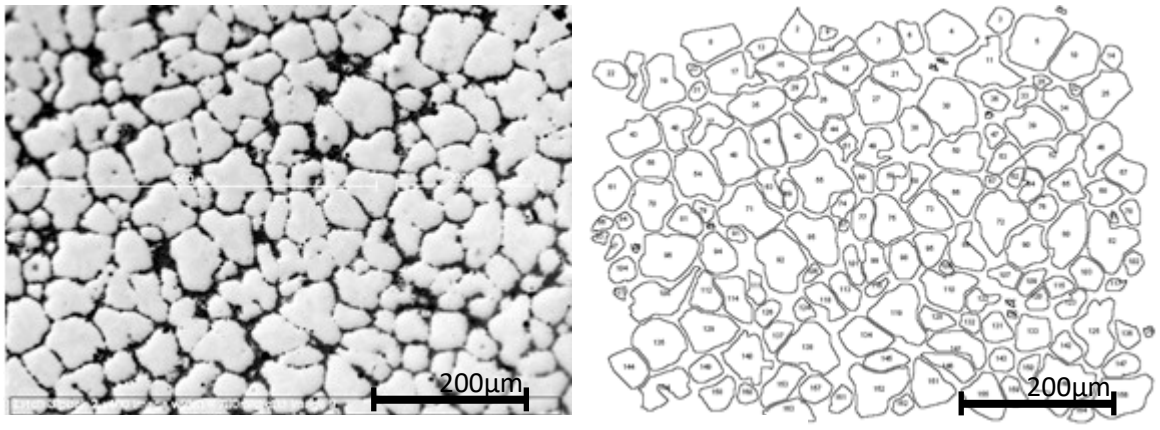

(a) (b)

Figure 4-15 (a) optical micrograph of standard A205 (free Ti = 0.26%), (b) traced grains for use in size calculations

Figure 4-15 (a) shows a micrograph of A205 alloy. Figure 4-15 (b) shows the tracing of the grains from Figure 4-15 (a).

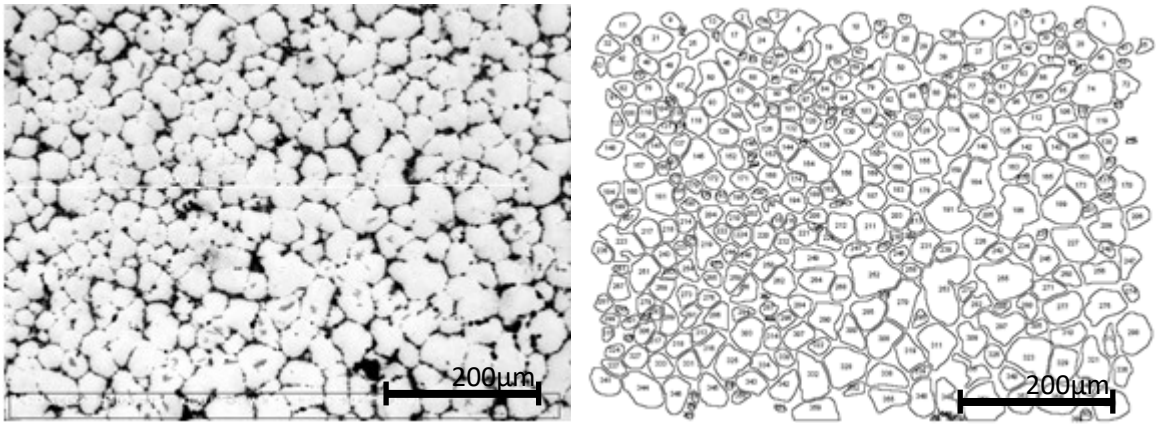

(a) (b)

Figure 4-16 (a) optical micrograph of Sample 1 (free Ti = 0.43%), (b) traced grains for use in size calculations

Figure 4-16 (a) shows a micrograph of Sample 1. Figure 4-16 (b) shows the tracing of the grains from Figure 4-16 (a).

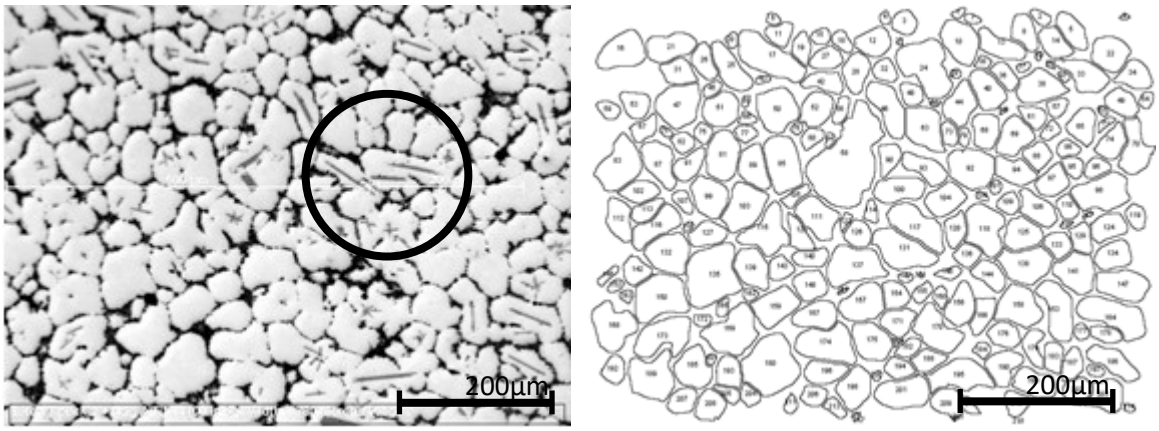

(a) (b)

Figure 4-17 (a) optical micrograph of Sample 2 (free Ti = 0.48%), the circled region of interest highlights large aluminide features, (b) traced grains for use in size calculations

Figure 4-17 (a) shows a micrograph of Sample 2. In the highlighted region of interest found in image (a) it is possible to see large needle-like titanium aluminide features which are of a similar size to the grain structure. Figure 4-17 (b) shows the tracing of the grains from Figure 4-17 (a).

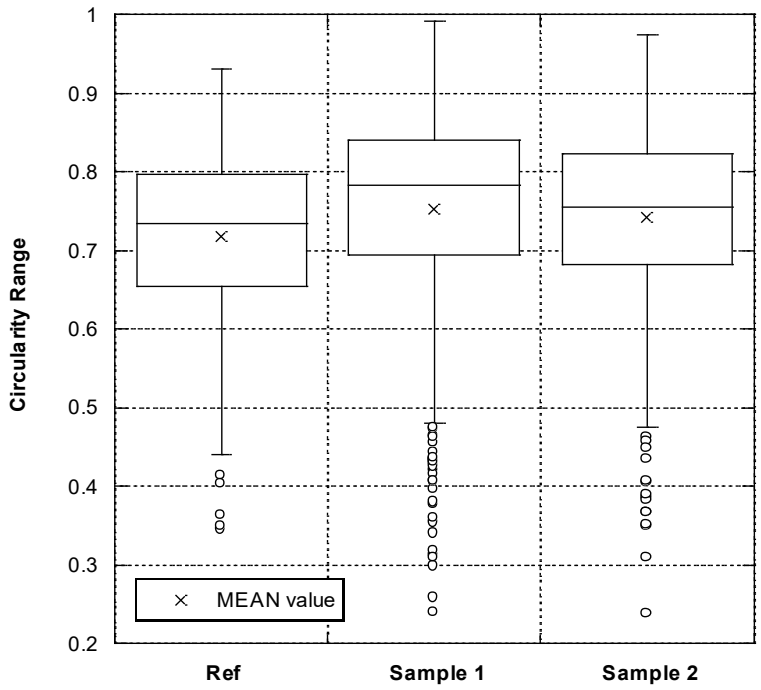

Figure 4-18 Circularity range for a standard sample of A205 (0.26wt%) and the circularity values for the free Titanium experiments; Samples 1 (0.43wt%) and 2 (0.48wt%) respectively

Figure 4-18 shows the circularity range for alloy A205 and Samples 1 and 2 from the excess Ti experiments, showing the reference sample to have a similar mean circularity value to Samples 1 and 2.

Table 4.2.7 Statistical analysis of the circularity values for the free titanium experiments

	Reference (0.26wt%)	**Sample 1 (0.43wt%)**	**Sample 2 (0.48wt%)**
Number of grains	335	786	675
Mean	0.718	0.753	0.742
Max value	0.930	0.993	0.974
Q3+1.5(IQR)	Fixed at 1	Fixed at 1	Fixed at 1
Quartile 3	0.799	0.841	0.825
Quartile 2	0.735	0.783	0.755
Quartile 1	0.654	0.694	0.681
Q1-1.5(IQR)	0.438	0.474	0.467
Min value	0.345	0.240	0.237

Table 4.2.7 shows the statistical analysis from Figure 4-18. The mean value calculated from the data sets showed Sample 2 to have the highest mean circularity value (0.74) followed by Sample 1 (0.75) then the A205 alloy (0.72). A similar pattern was observed when comparing the quartile 1 result, as the reference sample had a value of 0.65 than when compared to Samples 1 and 2 (0.69 and 0.68 respectively).

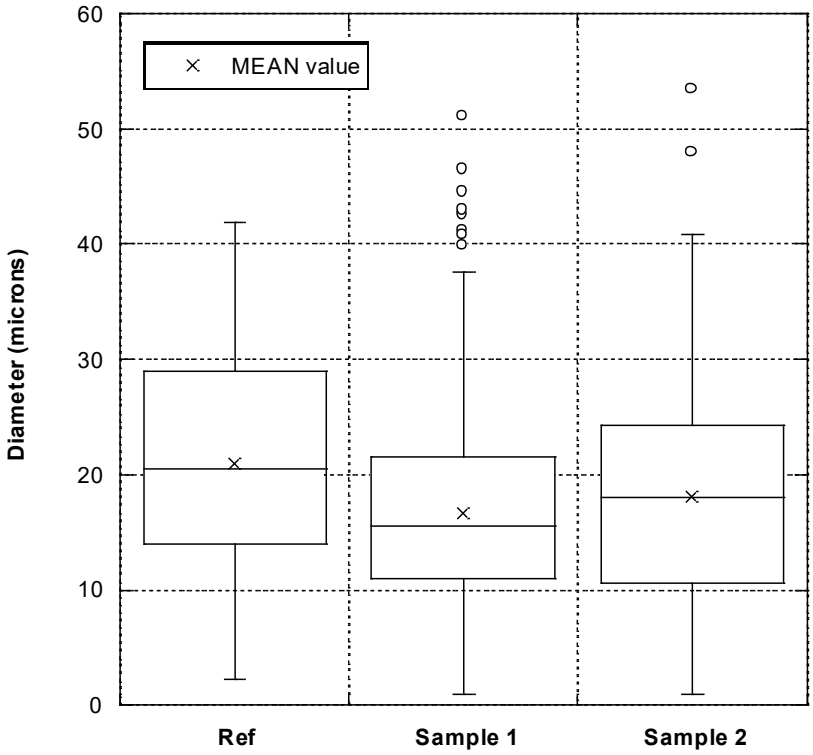

Figure 4-19 Diameter range for a standard 'reference' sample of A205 (0.26wt%) and the circularity values for the free Titanium experiments; Samples 1 (0.43wt%) and 2 (0.48wt%) respectively

Figure 4-19 shows the range of diameters range of A205 alloy and its comparison to Samples 1 and 2 from the excess titanium alloys. The A205 alloy has a larger particle diameter distribution compared to the size distributions measured for Samples 1 and 2. Of Samples 1 and 2, Sample 1 had the smaller grain size distribution with a mean particle size value of 17µm compared to 18µm.

Table 4.2.8 Statistical analysis of the diameter values for the free titanium experiments

	Reference (0.26wt%)	**Sample 1 (0.43wt%)**	**Sample 2 (0.48wt%)**
Number of grains	335	786	675
Mean (µm)	20.90	16.62	18.13
Max value (µm)	41.84	51.16	53.43
Q3+1.5(IQR) (µm)	51.46	37.62	44.90
Quartile 3 (µm)	29.06	21.60	23.34
Quartile 2 (µm)	20.53	15.49	18.09
Quartile 1 (µm)	13.95	10.92	10.63
Q1-1.5(IQR) (µm)	Fixed at 0	Fixed at 0	Fixed at 0
Min value (µm)	2.29	1.02	1.02

Table 4.2.8 shows the statistical analysis of the diameter values for the free titanium experiments. The mean values show Sample 1 to have the smallest grains (16.6µm), with the next largest found in Sample 2 (18.1µm) then the reference sample (20.9µm). This pattern is reflected in both the 3rd and 2nd quartile values. The first quartile values, however, were calculated to be lowest in Sample 2 (18.1µm), then Sample 1 (15.5µm), with the largest quartile value belonging to the standard A205 alloy (20.5µm). The Q1-1.5(IQR) values have been set to zero as the calculated values were negative.

Table 4.2.9 shows the volume fraction of grain to grain boundary material for the free Ti experiments

	Grain (%)	**Grain boundary (%)**
Reference (0.26wt%)	72.70 ± 1.22	27.30 ± 1.22
Sample 1 (0.43wt%)	72.19 ± 2.10	27.81 ± 2.10
Sample 2 (0.48wt%)	74.50 ± 2.13	25.50 ± 2.13

Table 4.2.9 shows the volume fraction of grain to grain boundary material for the standard sample of A205, and the free titanium experiments 1 and 2. The table shows the similarities between the standard A205 alloy which had a volume fraction of grain boundary material of 27.3%, Sample 1 which had a 27.8% volume fraction of grain boundary material, and Sample 2 had the lowest volume fraction of grain boundary material at 25.5%.

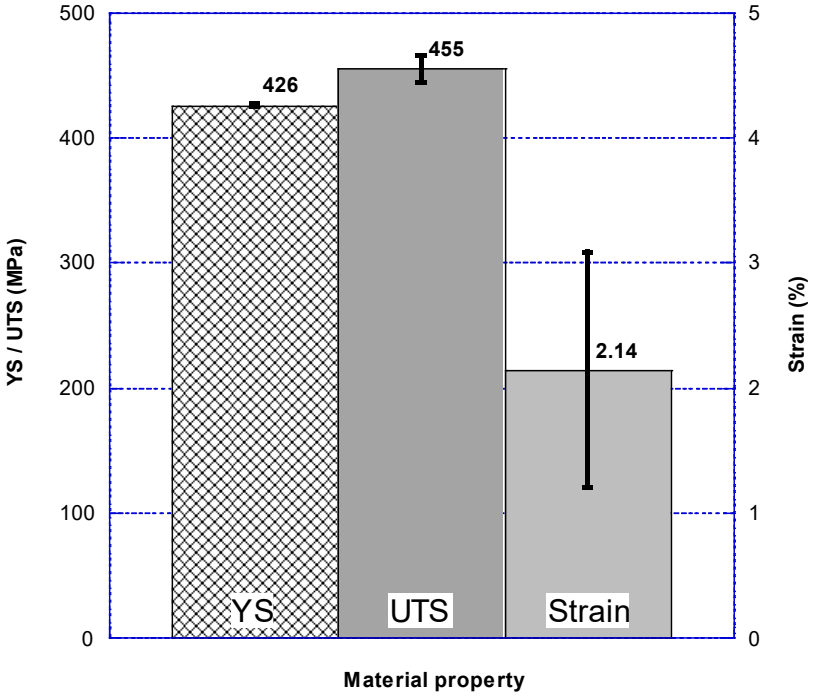

Figure 4-20 Bar chart showing the Yield Strength, Ultimate Tensile Strength and Strain for standard heat treated A205 (0.26wt%)

Figure 4-20 shows a bar chart of the measured tensile results detailing the yield strength, Ultimate Tensile Strength and strain for heat treated A205 alloy. The value for the yield strength was 438MPa, the value for the UTS was 455MPa and the value for the strain was 2.14%.

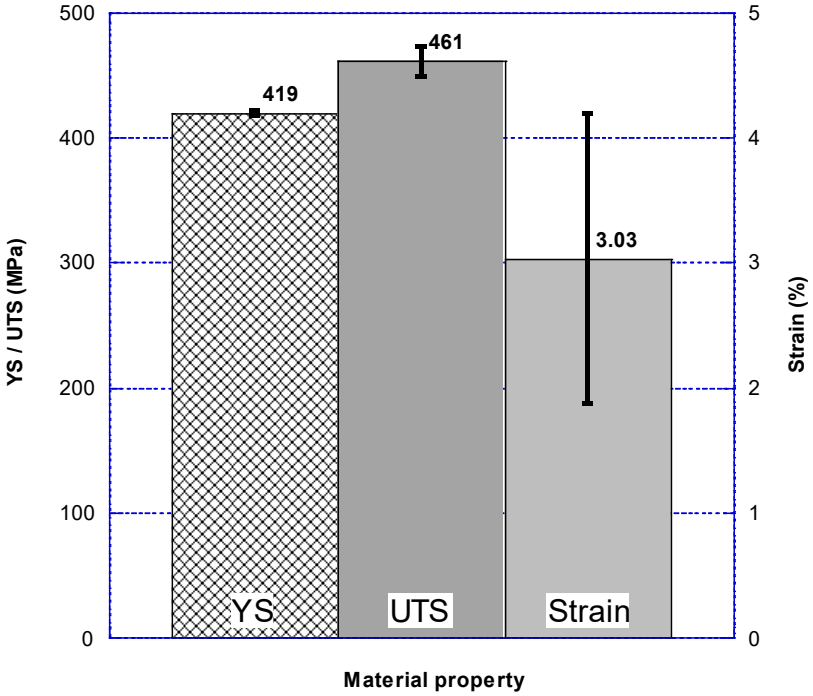

Figure 4-21 Bar chart showing the Yield Strength, Ultimate Tensile Strength and Strain for an alloy of A205 with an increased free Ti concentration (0.43wt%)

Figure 4-21 shows a bar chart detailing the yield strength, Ultimate Tensile Strength and strain for an alloy of A205 containing increased free titanium value of 0.43%. The value for the yield strength was 419MPa, the value for the UTS was 461MPa and the value for the strain was 3.03%.

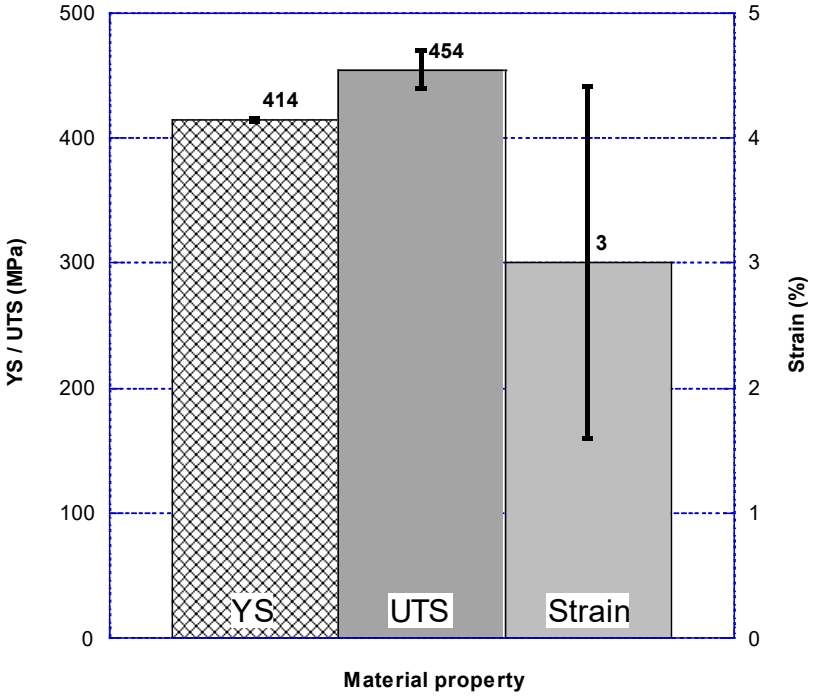

Figure 4-22 Bar chart showing the Yield Strength, Ultimate Tensile Strength and Strain for an alloy of A205 with an increased free Ti concentration (0.48wt%)

Figure 4-22 shows a bar chart detailing the yield strength, Ultimate Tensile Strength and strain for an alloy of A205 containing an increased free titanium value of 0.48%. The value for the yield strength was 414MPa, the value for the UTS was 454MPa and the value for the strain was 3.00%.

Table 4.2.10 Summary of the tensile properties of the excess titanium series of experiments

	YS ± σ (MPa)	UTS ± σ (MPa)	Elongation ± σ (%)
Standard (0.26wt%)	426 ± 1.1	455 ± 11.2	2.14 ± 0.94
Sample 1 (0.43wt%)	419 ± 1.8	461 ± 12.0	3.03 ± 1.15
Sample 2 (0.48wt%)	414 ± 0.8	454 ± 15.2	3.00 ± 1.40

Table 4.2.10 shows a summary of the tensile properties of the excess titanium experiments, which shows that the standard A205 alloy had a measured yield strength

result of 426MPa, while Sample 1 and Sample 2 had 419MPa and 414MPa respectively. Sample 1 had the highest measured value of UTS 461MPa while the standard A205 reference sample and Sample 2 both had similar UTS values of 455 and 454MPa respectively. Sample 1 and 2 both had similar strain results of 3.03 and 3.00%. The reference sample had a lower measured strain result of 2.14%.

4.3 Particle size analysis

The particle size of the Titanium Diboride (TiB_2) in A205 alloy is responsible, both directly and indirectly, for some of the strength characteristics of A205. TiB_2 is a ceramic, plate-like, particle which is precipitated into the molten aluminium by a salt-salt reaction, as such no complete direct size measurements of these particles has ever been previously made.

Previous examples of particle size analysis were based upon SEM image analysis -which might give a poor representation of the size distribution of the TiB_2 particles as a whole. By removing the TiB_2 particles from the matrix by dissolution in hydrochloric acid, as described in the experimental procedure section, it is possible to analyse the TiB_2 size distribution in its entirety.

4.3.1 Purchased TiB_2 particle size

To assess the stability of the TiB_2 particles during analysis a series of test were conducted on purchased TiB_2 to determine whether the particle size distribution was altered during measurement. The purchased TiB_2 used for these tests was provided by Sigma Aldrich and had a given size distribution of <10μm.

4.3.1.1 SEM expected results Vs. various size transformations

The apparatus chosen to determine the TiB_2 particle size distribution was a Malvern Mastersizer. As described in the experimental section the material was circulated around the machine during analysis and underwent an ultrasonic agitation stage pre-analysis to minimise the chance of measuring agglomerated particles. It was unknown how the TiB_2, and hence the measured particle size distribution, would behave under these conditions. For this reason initial results collected from the Malvern Mastersizer apparatus were compared to SEM images of the purchased TiB_2.

4.3.1.1.1 SEM of purchased TiB_2

As shown in Figure 4-23 the TiB_2 particles were up to approximately 10µm along their longest axis. The measured sample mostly contained fragments of TiB_2 particles with dimensions less than 1µm.

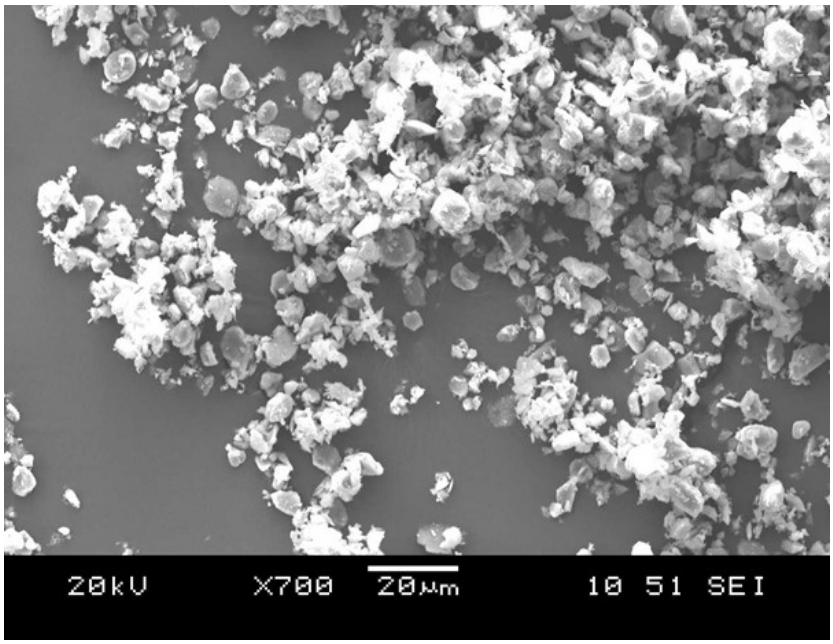

Figure 4-23 SEM image of TiB_2 supplied by Sigma Aldrich with a given size distribution of <10µm

4.3.1.1.2 Various transformations

As previously described in the experimental section; the used Malvern equipment calculated the size distribution from the diffraction patterns created by laser light diffracting around the sample particles. The standard output from this process was based on modelling the particles causing the diffraction to be spherical and hence their diameter calculable to form a 'volume based' particle size distribution. The suitability of this particle size distribution calculation was under review as the model emphasised larger particles. For this reason other size distribution transformations were tested to determine their suitability on reporting smaller particles an example of which is shown in Figure 4-23.

4.3.1.1.2.1 Volume

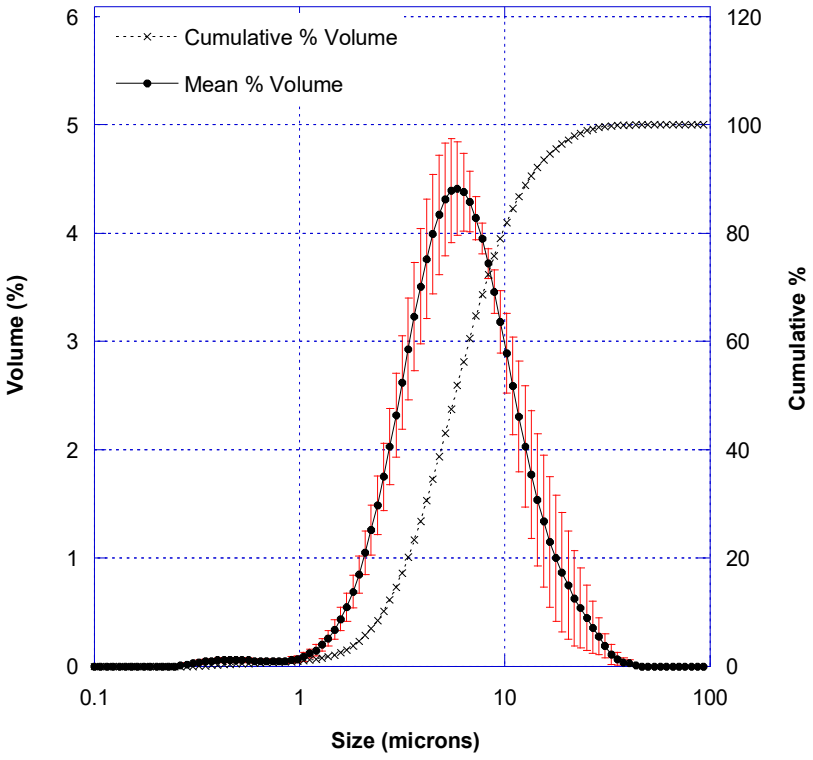

Figure 4-24 Standard output from Malvern particle size analysis based on the particle volume of the purchased TiB_2 particles

Figure 4-24 shows the particle size distribution of the purchased TiB_2 particles when the outputted data was based on their respective diffraction patterns being back-calculated from spheres. The measured distribution is approximately Gaussian. The sub 1µm particles present within the distribution accounted for less than 2% of the cumulative particle size distribution. The modal volume percentage value of the distribution was 6µm. Based on the cumulative distribution, 50% of the samples had a measured upper size range of between 6 and 50 µm.

4.3.1.1.2.2 Surface

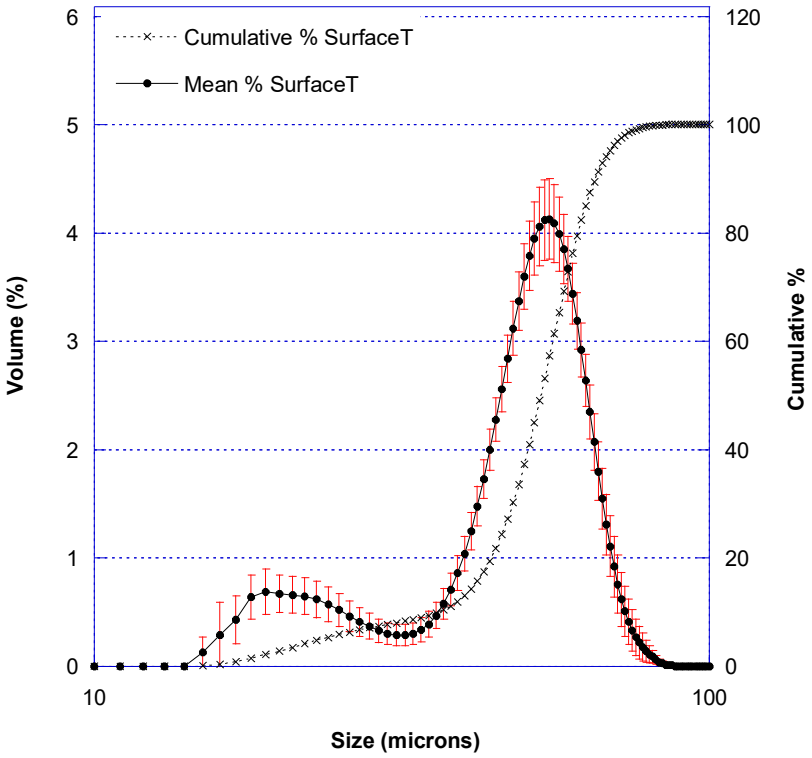

Figure 4-25 Converted volume based particle size distribution to show size distribution calculated from the surface area transformation of purchased TiB_2 particles

Figure 4-25 shows the particle size distribution of purchased TiB_2 particles when the outputted data was internally transformed to weight the distribution in terms of the particles surface area ratio. The distribution comprised of 2 peaks, with the lower particle size distribution peak located at approximately 20µm and containing <5% of the sample volume. The second larger peak was located at 55µm -approximately the value at which the cumulative volume = 50%.

4.3.1.1.2.3 Length

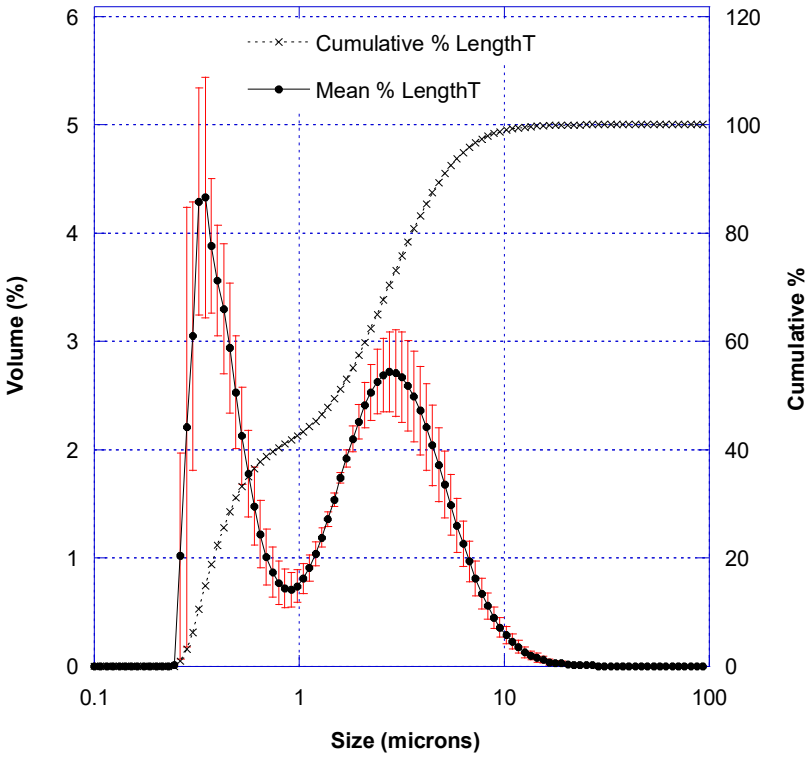

Figure 4-26 Converted volume based particle size distribution to show size distribution calculated from the length transformation of purchased TiB_2 particles

Figure 4-26 shows a length transformation distribution of the purchased TiB_2 particles. This distribution showed 2 peaks. Cumulatively, 50% of the particles occurred in a narrow particle range of between 0.3 and 1.5µm, with the other 50% of the particles located over a broader particle size range of between 1.5 and 20µm.

4.3.1.1.2.4 Number

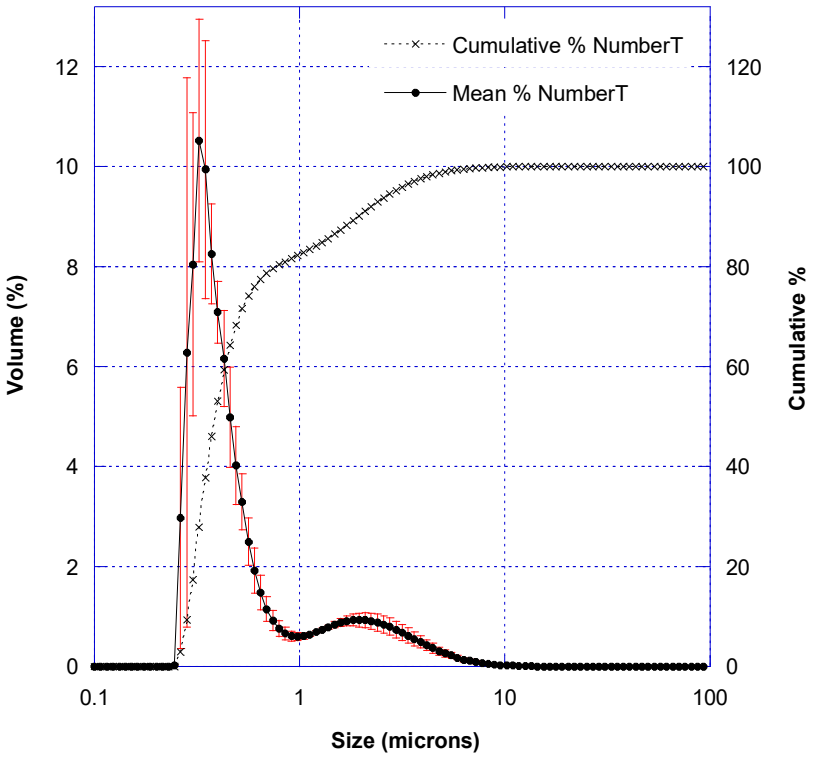

Figure 4-27 Converted volume based particle size distribution to show size distribution calculated from the number transformation of purchased TiB_2 particles

Figure 4-27 shows a number transformation particle size distribution for the purchased TiB_2 particles. The distribution consisted of one major peak and one minor peak. The major peak has a size distribution of less than 1µm, with its highest volume percentage situated at 10.5%. The minor peak, found with a size distribution of greater than 1µm, had a peak volume percentage of 0.9% located at a particle size of 2µm. The cumulative volume percentage showed that 50% of the sample lay between 0.25 and 0.4µm, 80% of the sample lay between 0.125 and 0.8µm, and 90% of the sample lies between 0.25 and 2µm.

4.3.1.1.3 Drift of particle size distribution during analysis

Due to the nature of the particle size analysis machine used, the sample was continuously recirculated around the system during analysis. As each final particle size distribution comprised the average of 10 individual particle size distribution data sets, where each data set was formed using tens of thousands of measurements, it was necessary to investigate how the material behaved during analysis.

4.3.1.1.3.1 Drift characteristics of TiB_2 without ultrasonic agitation

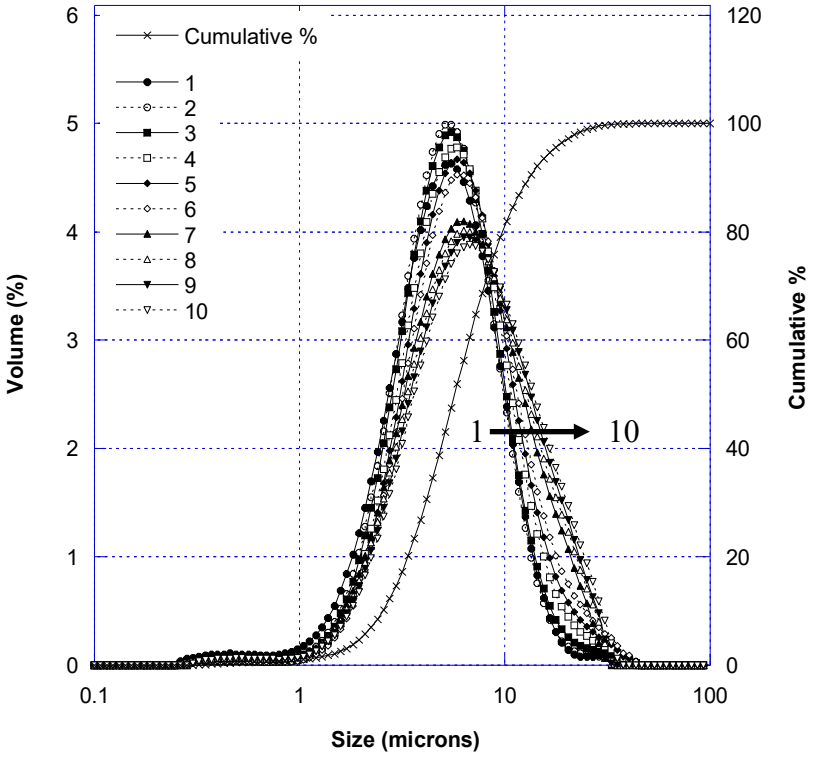

Figure 4-28 Drift characteristics of 10 consecutive particle size distributions which average together to give the final reported particle size distribution for purchased TiB_2 without ultrasonic agitation pre-treatment

Figure 4-28 shows 10 individual particle size distributions which average together to give the final reported particle size distribution for the measured sample -in this instance

purchased TiB_2 without the ultrasonic pre-treatment stage. The graph shows how the particle size distribution evolves with time whilst being analysed. As can be seen, the first 6 measurements followed a close distribution to one another, with a peak volume percentage of 4.5 to 5%, located between 5 and 6µm. There was then a slight step change between the 6th and 7th data set where the volume percentage for scans 7 to 10 dropped to between 3.9 and 4.1% for particle sizes of 6 to 7µm. The evolution of the particle size distribution was most apparent on the right hand edge of the data peak where, upon close examination, the reported particle size increased between each data set. A similar relationship was also found at the rising edge of the peak.

4.3.1.1.3.2 Drift characteristics of TiB_2 after ultrasonic agitation

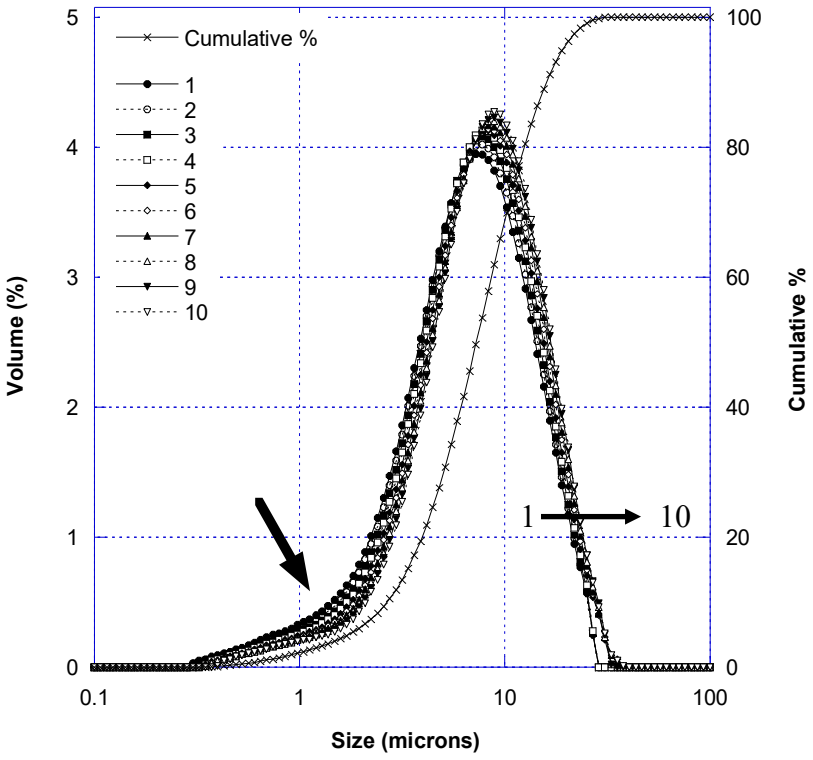

Figure 4-29 Drift characteristics of 10 consecutive particle size distributions which average together to give the final reported particle size distribution. Pre-analysis the sample was subjected to 10mintues of ultrasonic agitation at displacement level 10

Figure 4-29 shows 10 individual data sets which averaged together to give the final reported particle size distribution. Before this measurement the material was subject to 10 minutes of ultrasonic agitation at a probe displacement of 10 (where the probe displacement was simply a feature of the machine, ranging from 0 to 20, where 0 was without the ultrasonic agitation feature active and 20 was the most powerful ultrasonic agitation setting available). The recorded particle size distributions showed some variation between each increase in data set, again with a slight shift towards larger particle size distributions with each measurement. The peak volume percentage, of scan 1, was at approximately 3.9% at 7μm, compared to 4.3% at 9μm for scan 10. The leading edge of this particle size distribution showed a shallow step in volume % for smaller particle sizes, until about 2μm when a step change increase in volume percentage was observed (as indicated by the arrow in Figure 4-29). This shallow section of the particle size distribution was not present in non-ultrasonically agitated samples and represented a greater number of smaller particles present within the sample.

4.3.1.1.4 Particle size distribution descriptions

4.3.1.1.4.1 D(0.1) for non-ultrasonically agitated purchased TiB_2

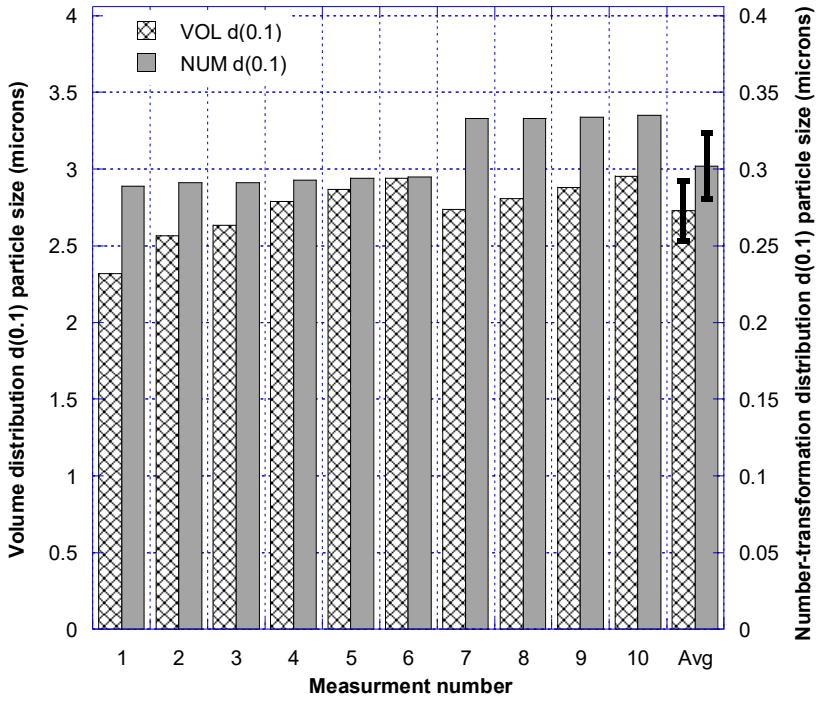

Figure 4-30 Bar graph to show the evolution of d(0.1) with increasing measurement number for both volume and number particle size distributions

Figure 4-30 shows the d(0.1) value, i.e. the value at which the sample's cumulative volume distribution has reached 10%, for non-ultrasonically agitated TiB_2 particles (see Figure 4-28), for both volume and number particle size distributions. The volume distribution showed an observable variation between each measurement number where for the first 6 scans there was an increase in the measured d(0.1) particle sizes from 2.3 to 2.9µm. There was then a reduction in the measured particle size from scans 6 (2.9µm) to 7 (2.75µm) followed by an increase to 2.9µm. Regarding the number particle size distribution; the initial 6 scans have little variation between their reported d(0.1) values of 0.29µm. There is then a step change between scan 6 and 7 to 0.33µm -which was

approximately maintained through to measurement number 10. The average of the volume distributions of ten d(0.1) scans was 2.7µm. The average of the number distributions ten d(0.1) scans was 0.31µm.

4.3.1.1.4.2 D(0.5)

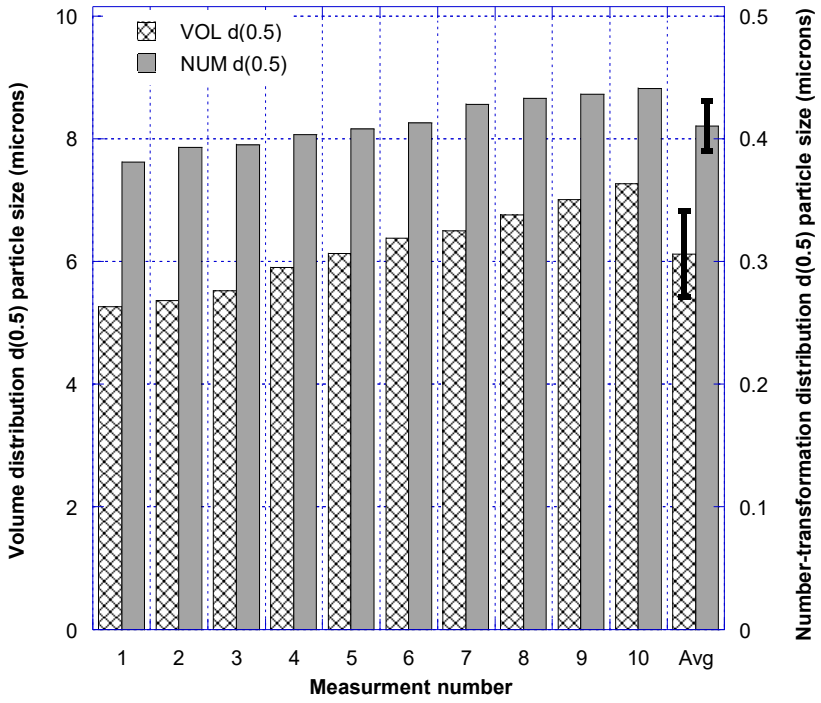

Figure 4-31 Bar graph to show the evolution of d(0.5), i.e. the mean value, with increasing measurement number for both volume and number particle size distributions

Figure 4-31 shows the d(0.5) value, i.e. the median particle size, for non-ultrasonically agitated material, and its variation with repeated measurement for both volume and number distributions. The volume distribution d(0.5) particle size increased with each measurement number from approximately 5.2µm at measurement 1 to 7.2 at measurement 10. The number distribution d(0.5) particle size also increased with measurement number from 3.8µm at measurement 1, to 4.4µm at measurement 10.

4.3.1.1.4.3 D(0.9)

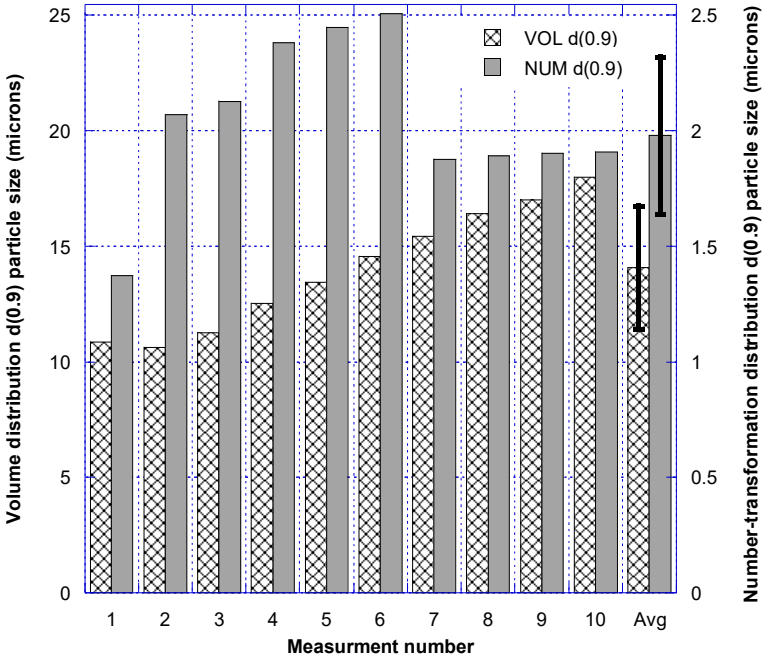

Figure 4-32 Bar graph to show the evolution of d(0.9), with increasing measurement number for both volume and number particle size distributions

Figure 4-32 shows the d(0.9) number distribution, i.e. the particle size below which 90% of the particle size distribution lies, and its variation with measurement number for both volume and number particle size distributions. For the volume distribution the first measurement recorded a d(0.9) of approximately 10.1µm, the second measurement records a similar value of 10.05µm. The 3rd to 10th measurements increase from a d(0.9) particle size of 10.1µm, to 18µm at scan number 10. The number transformed particle size distribution d(0.9) value did not follow such a smooth profile. The first scan recorded a d(0.9) value of 1.37µm which then increased to 2.51µm with measurement 6. The number transformation profile then decreased and roughly maintained a d(0.9) value of 1.9µm for scan number 7 to 10.

4.3.1.1.4.4 D[4,3]

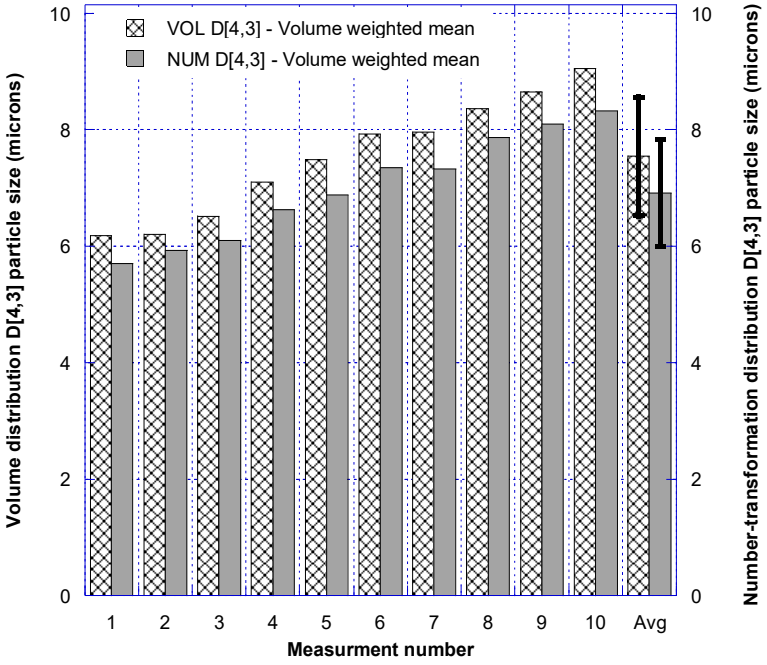

Figure 4-33 Bar graph to show the evolution of D[4,3], with increasing measurement number for both volume and number particle size distributions

Figure 4-33 shows the volume weighted mean (D[4,3]) of each measurement used to calculate the final averaged particle size distribution, and its variation with measurement number for both volume and number transformed particle size distributions. For the volume particle size distribution the first measurement number recorded a D[4,3] value of 6.2µm, which then increased with each measurement number to a value of 9.1µm at scan number 10. For the number transformed particle size distribution the first scan recorded gave a D[4,3] value of 5.7µm, which then increased to 8.3µm by data set 10.

4.3.1.1.4.5 D[3,2]

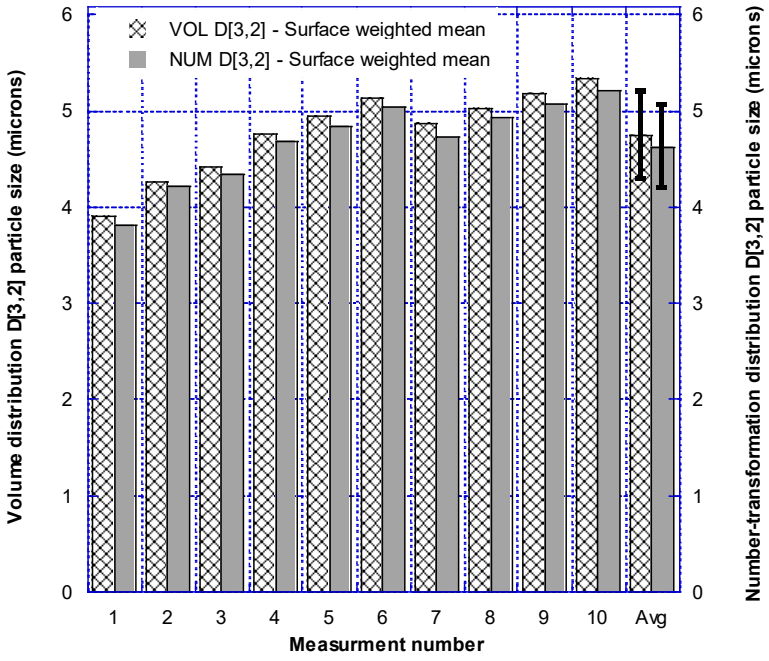

Figure 4-34 Bar graph to show the evolution of D[3,2], with increasing measurement number for both volume and number particle size distributions

Figure 4-34 shows the surface area weighted mean (D[3,2]) particle size distribution, and how it varied with measurement number for both volume and number transformed particle size distributions. The volume particle size distribution D[3,2] value, for scan 1, was 3.9µm which then increased up to 5.1µm at measurement number 6. This was then followed by a slight decrease in the measured D[3,2] value between measurement number 6 and 7, from 5.1µm to 4.9µm. This value then increased to 5.4µm at scan number 10. With respect to the number-based particle size distribution, the D[3,2] value for measurement number 1 was 3.8µm, which increased to 5.0µm for measurement number 6. Similarly to the volume based particle size distribution there was then a decrease in

the measured D[3,2] particle size distribution down to 4.7µm, which then increased to 5.21µm by scan number 10.

4.3.1.1.4.6 Average comparison

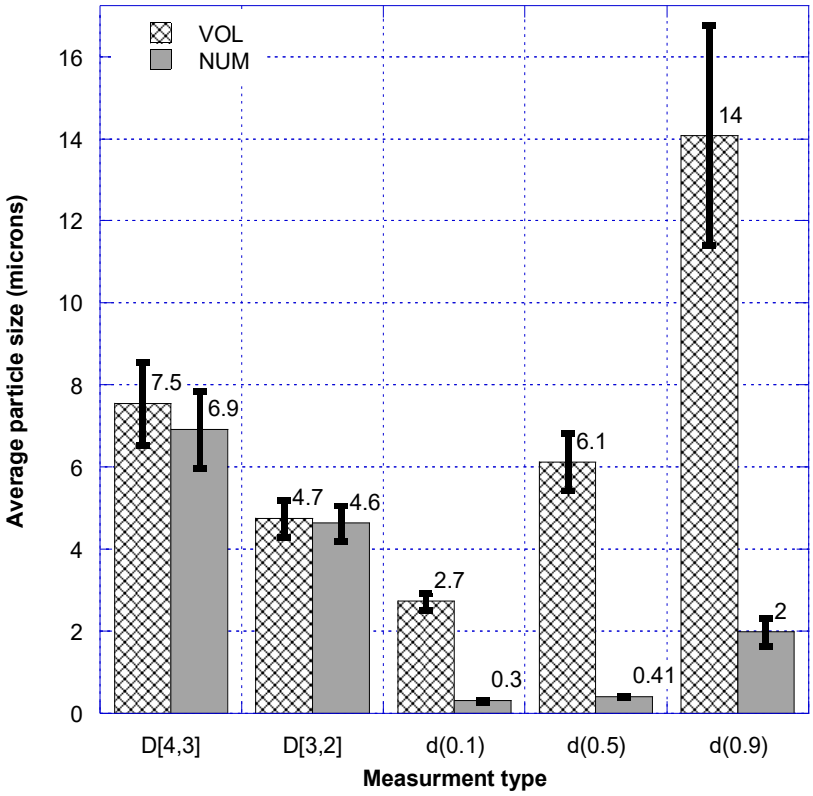

Figure 4-35 Bar graph comparing the average value for each of the 5 different calculated mean types for both the volume and number calculated particle size distribution

Figure 4-35 shows a bar chart comparing the average value for each of the 5 mean particle size calculations, for both the volume particle size distribution and also the number particle size distribution. The values show which of the different particle size methods would be most suitable for representing the dimensions of the purchased TiB_2 particles. Regarding the volume distribution; the D[4,3] mean gave a value of 7.5µm, which when compared to micrographs of the particles size (see Figure 4-5) was considered too high

to be representative of the measured, experimentally collected, TiB_2 particles. The volume distribution D[2,3] value of 4.7μm was also to be considered too large to be representative of the measured sample sizes. Only the volume distribution d(0.1) value, which had the lowest particle size measurement of 2.7μm, did the volume distribution calculated mean become low enough to be considered representative of the observed particles. The volume distributions d(0.5) value averaged at 6.1μm, which lay between the D[4,3] and the D[3,2] values. The average d(0.9) value for the volume distribution was 14μm, and it was this value which indicated that a few larger particles within the sample were present and therefore able to obscure the particle size contribution from the more numerous smaller particles. In contrast to these measurements, the number distribution calculated means were lower than their volume distribution counterparts. The number distribution D[4,3] value was measured to be 6.9μm, which was similar to the volume distribution 7.5μm. The number distribution D[3,2] value was also similar to the volume distribution d[3,2] value at 4.6μm and 4.7μm, respectively. The number distributions d(0.1), d(0.5) and d(0.9) results at 0.3, 0.41 and 2μm gave the most representative values when compared to the SEM sample (see Figure 4-23).

4.3.1.1.4.7 Span

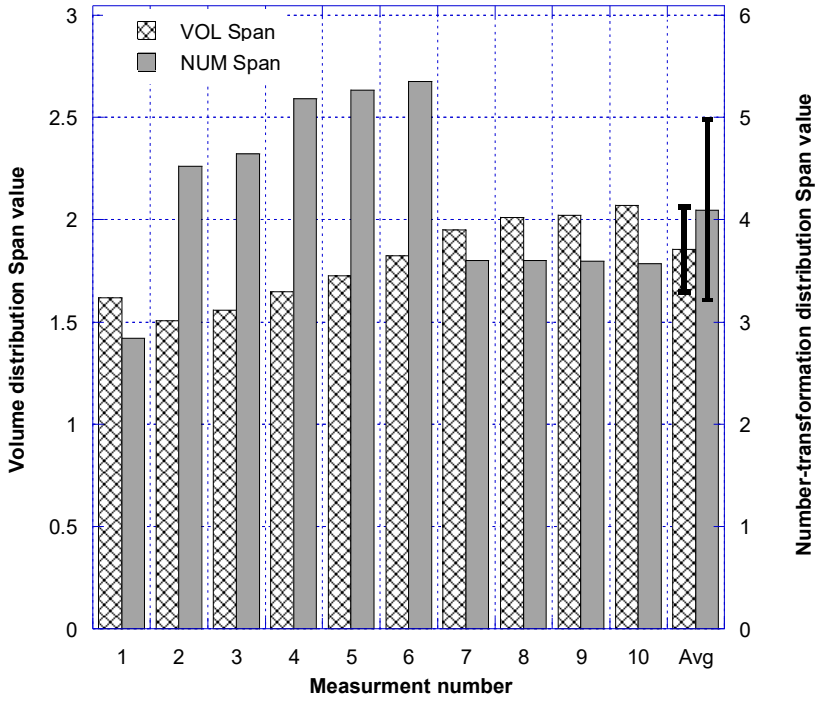

Figure 4-36 Bar graph to show the evolution of span value, with increasing measurement number for both volume and number particle size distributions

Figure 4-36 shows how the span value, defined as; (d(0.9) – d(0.1)) / d(0.5), varied in accordance with scan number for the volume and number particle size distributions. As can be seen the span value for scan 1 of the volume particle size distribution was 1.62, which then decreased to 1.5 in measurement number 2 before continuing to rise to 2.07 for measurement number 10. For the number particle size distribution, measurement number 1 had a span value of 2.84, which was the lowest scan value for the number distribution series, and yet was higher than any of the volume distribution particle size scans. The number distribution span value then increased up to 5.35 by scan 6. From measurement number 7 the span value decreased to 3.6 where it plateaued.

4.3.1.1.5 Effect of various ultrasonic agitation times

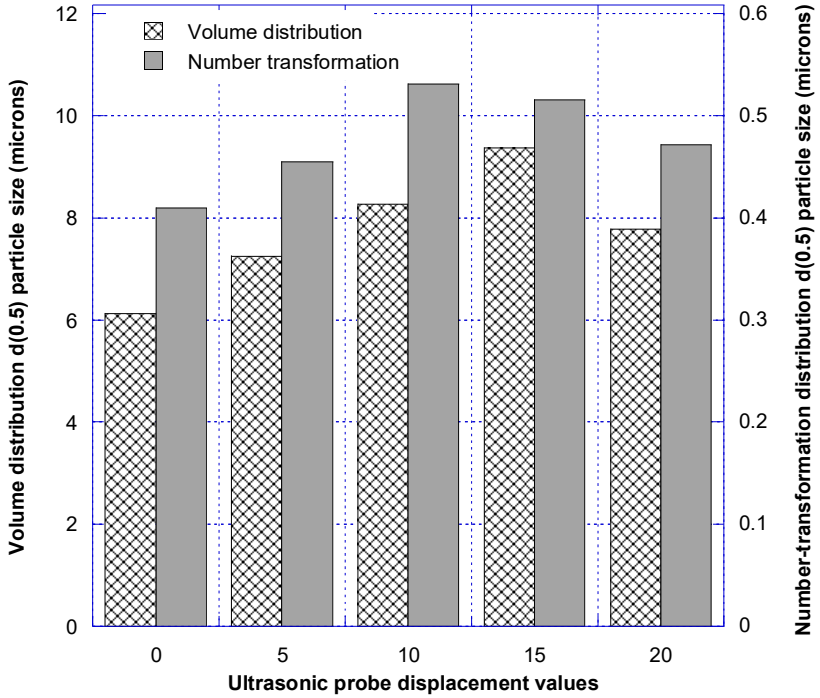

Figure 4-37 d(0.5) comparison for volume and number transformation distributions for varying ultrasonic probe displacement levels (1min holding time)

Figure 4-37 compares the d(0.5) mean particle size for both volume and number particle size distributions, following different probe displacement values. (Probe displacement values give a non-quantitative measure of the ultrasonic power level used during sample treatment before measurement, with a value of 0 for not used). For the volume particle size distribution not using the ultrasonic agitation device pre-treatment, a d(0.5) value of 6.12µm was obtained. The d(0.5) value increased when using the ultrasonic probe. At a displacement level of 5 the d(0.5) value increased to 7.26µm, and roses to 9.37µm at a probe displacement value of 15. Increasing the probe displacement value from 15 to 20 decreased the d(0.5) value to 7.77µm. For the number transformation particle size distribution not using the ultrasonic probe gave a d(0.5) value of 0.41µm. When the ultrasonic probe was used at a displacement level of 5 the d(0.5) particle size was

increased to 0.46µm. The maximum d(0.5) value, 0.53µm, was recorded at a probe displacement level of 10. The d(0.5) mean particle size then decreased for probe displacement values of 15 and 20, giving 0.52 and 0.47µm, respectively.

4.3.1.1.6 Effect of various ultrasonic levels

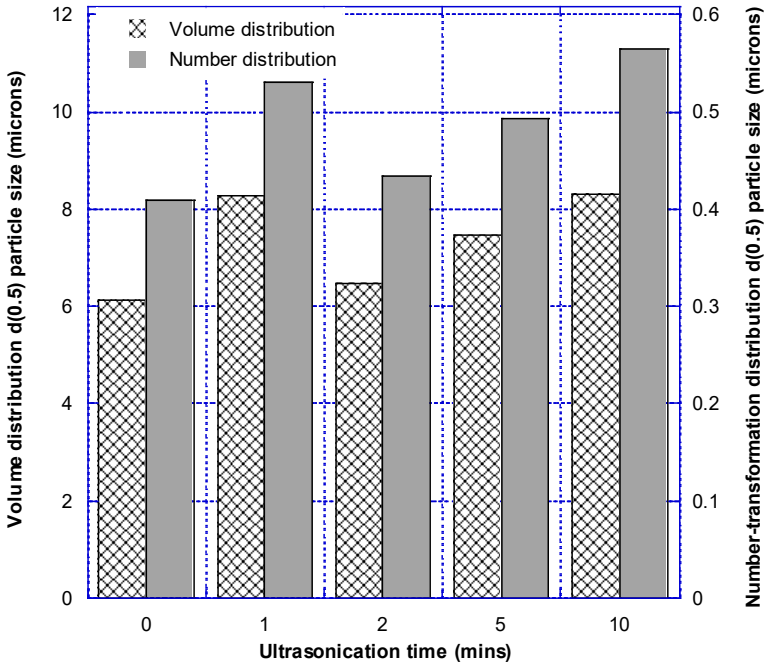

Figure 4-38 d(0.5) mean particle size variation with sample ultrasonic agitation time (pre-analysis) for both the volume and number transformation size distributions (at a fixed ultrasonic probe displacement level of 10)

Figure 4-38 shows how, at a fixed level of ultrasonic displacement of 10, the d(0.5) mean particle size varied with time of operation of the ultrasonic agitation probe. For the volume particle size distribution, a 1minute period of ultrasonic agitation raised the d(0.5) value from 6.12 to 8.27µm. Doubling the ultrasonic agitation to 2minutes reduced the d(0.5) value to 6.48µm. Increasing the time further to 5minutes then increased the mean value to 7.46µm. A 10 minute ultrasonic agitation period raised the d(0.5) value to 8.29µm. For the number transformed particle size distribution there was also an increase

in d(0.5) size between ultrasonically agitating the sample for 1minute before analysis (0.41µm) and not agitating the sample, (0.53µm). The d(0.5) value then decreases to 0.44µm following 2 minutes agitation, then increased to 0.49µm and 0.56µm for 5 minutes and 10 minutes ultrasonic agitation, respectively.

4.3.2 Particle size analysis of TiBAl grain refiners

The analysis of TiBAl aluminium grain refiners is of importance to this research as the process of incorporating the TiB_2 into the refiner, i.e. by salt-salt reactions, is identical to the process by which TiB_2 is added to A205. For this reason, a series of non-adjoining sections of 3:1 and 5:1 TiBAl grain refiners (rod type) followed the same dissolution procedure in HCl as the A205 alloy, as described in the experimental section of this thesis, and subsequently underwent particle size analysis. Although TiBAl grain refiners are known to contain 10-30µm sized $TiAl_3$ particles, it should be noted that there is evidence that hydrochloric acid will dissolve these particles[110–112]. However, if any large $TiAl_3$ particles were to make it though to size analysis, the transformation from volume to number distribution will significantly reduce their contribution to the final measured particle size distribution profile. Hence the analysis of TiBAl grain refiners, which do not contain copper in their elemental composition, will allow for the comparison between materials which do and do not contain Cu in their compositions.

4.3.2.1 TiBAl (3:1)

4.3.2.1.1 Particle Size Analysis

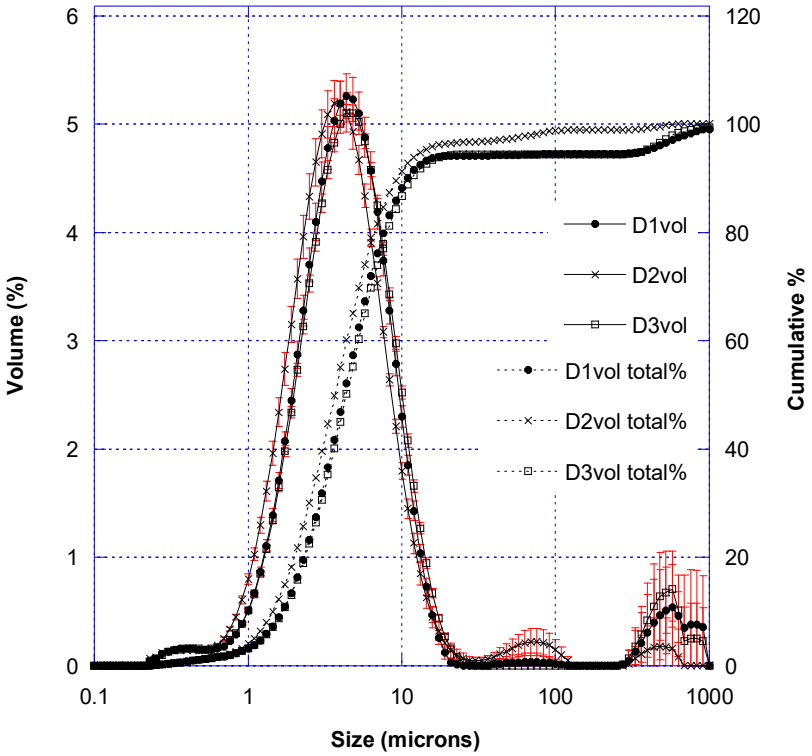

Figure 4-39 Volume based particle size distribution for TiBAl 3-1 following dissolution in HCl

Figure 4-39 shows the volume based particle size distribution for TiBAl 3-1 following dissolution in HCl. The distribution showed that 90% of the sample was <10µm, 50% of the sample was approximately <4µm and 10% of the sample was <2µm. The cumulative percentage showed that the highest 10% of the distribution was linked to 2 separate peaks located at 80µm and 500µm respectively -as these peaks represented particles with a diameter larger than the observed grain size it was assumed that these particle size measurements were agglomerates.

Table 4.3.1 d(0.1), d(0.5) and d(0.9) values for the volume based particle size distribution for TiBAl 3:1

Sample	d (0.1)	d (0.5)	d (0.9)
D1 (Vol)	1.83	4.61	11.98
D2 (Vol)	1.59	3.99	10.22
D3 (Vol)	1.84	4.77	12.81
Avg (Vol)	1.74	4.44	11.66

Table 4.3.1 shows the d(0.1), d(0.5) and d(0.9) values for the number transformed particle size distribution of TiBAl 3:1 grain refiner material. The results show the average d(0.1), d(0.5) and d(0.9) values to be 1.74, 4.44 and 11.66µm respectively.

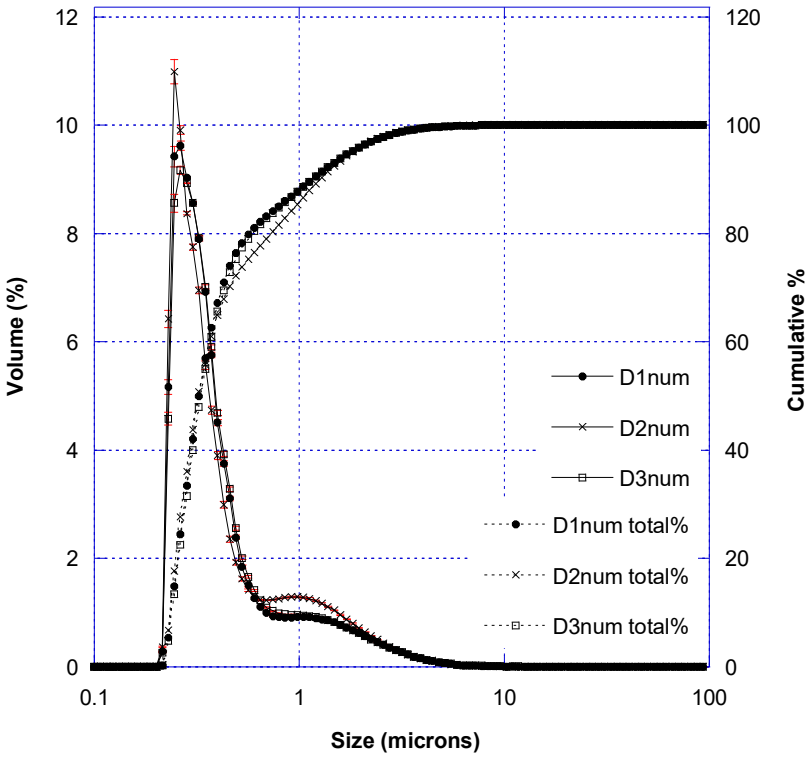

Figure 4-40 Number based particle size distribution for TiBAl 3-1 following dissolution in HCl

Figure 4-40 shows the number transformed particle size distribution from TiBAl 3-1. The distribution showed that 90% of the sample had particles which were < than about 1.5µm, 50% of the measured particles were <0.3µm and 10% were between 0.2 and 0.25µm. The

distribution showed the beginning of a second peak on the tail end of the main distribution, this peak (from about 0.7 to 10µm) accounted for about 20% of the distribution.

Table 4.3.2 d(0.1), d(0.5) and d(0.9) values for the number transformed particle size distribution for TiBAl 3:1

Sample	d (0.1)	d (0.5)	d (0.9)
D1 (NumT)	0.25	0.35	1.24
D2 (NumT)	0.25	0.34	1.35
D3 (NumT)	0.26	0.35	1.24
Avg (NumT)	0.25	0.35	1.29

Table 4.3.2 shows the d(0.1), d(0.5) and d(0.9) values for the number transformed particle size distribution of TiBAl 3:1 grain refiner material. The results show the average d(0.1), d(0.5) and d(0.9) values to be 0.25, 0.35 and 1.29µm respectively.

4.3.2.1.2 Tensile test

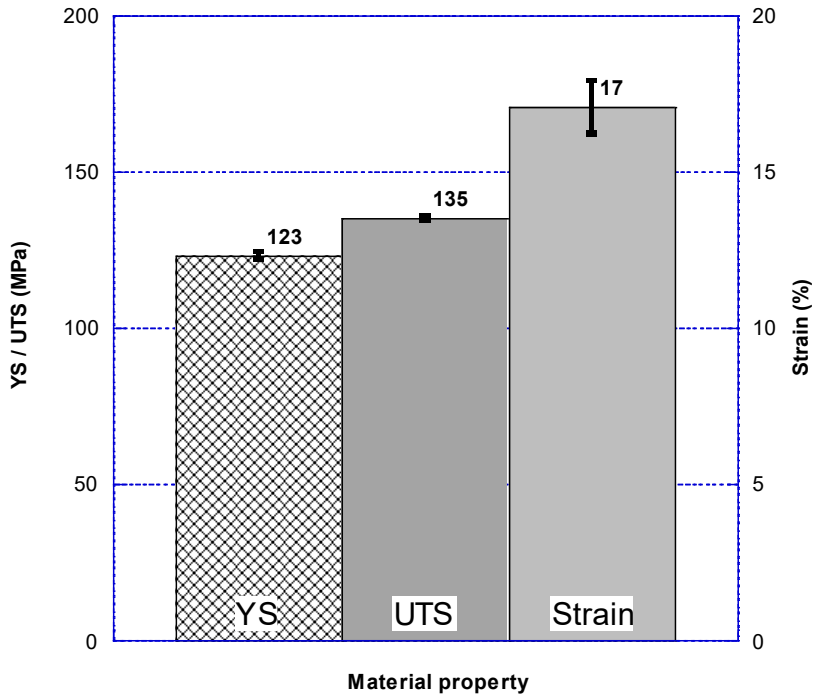

Figure 4-41 Yield Strength (YS), Ultimate Tensile Strength (UTS), and Strain for TiBAl 3-1

Figure 4-41 shows the yield strength, UTS and strain for TiBAl 3-1. The tensile results showed the yield strength to be 123MPa, the UTS to be 135MPa and the strain to be 17%.

4.3.2.2 TiBAl (5:1)

4.3.2.2.1 Particle Size Analysis

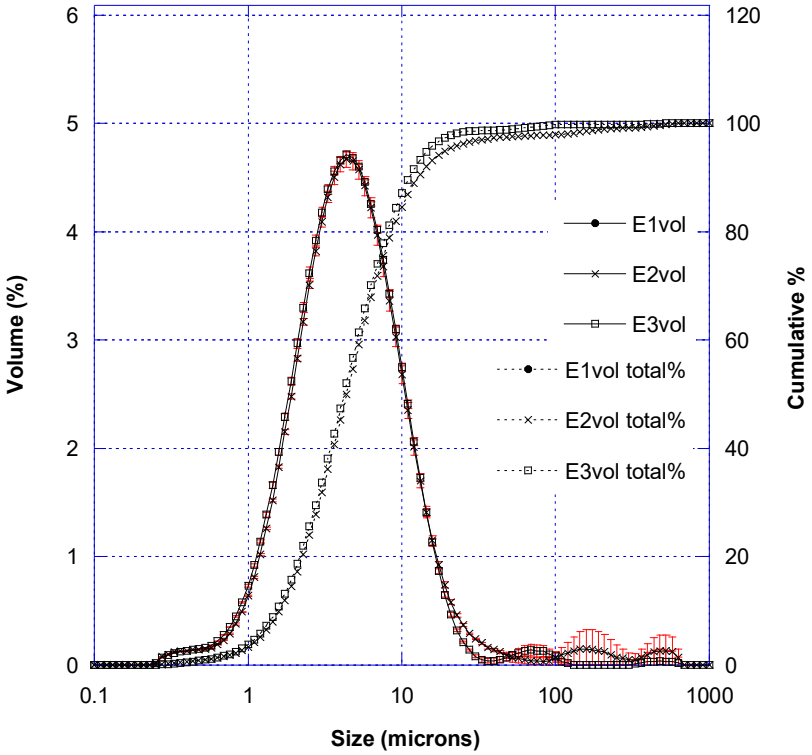

Figure 4-42 Volume based particle size distribution for TiBAl 5-1 following dissolution in HCl

Figure 4-42 shows the volume based particle size distribution for material from TiBAl 5-1 alloy following dissolution in HCl. The distribution showed 90% of the distribution to be <13µm, 50% of the sample to be <5µm and 10% of the sample to be <2µm. Analysis of the sample showed some agglomeration events at particle sizes >60µm, however this accounted for about 2% of the cumulative volume percentage of the sample.

Table 4.3.3 d(0.1), d(0.5) and d(0.9) values for the volume based particle size distribution for TiBAl 5:1

Sample	d (0.1)	d (0.5)	d (0.9)
E1 (Vol)	1.77	4.78	13.84
E2 (Vol)	1.75	4.79	13.95
E3 (Vol)	1.67	4.60	12.28
Avg (Vol)	1.73	4.72	13.31

Table 4.3.3 d(0.1), d(0.5) and d(0.9) values for the number transformed particle size distribution of TiBAl 5:1 grain refiner material. The results show the average d(0.1), d(0.5) and d(0.9) values to be 1.73, 4.72 and 13.31µm respectively.

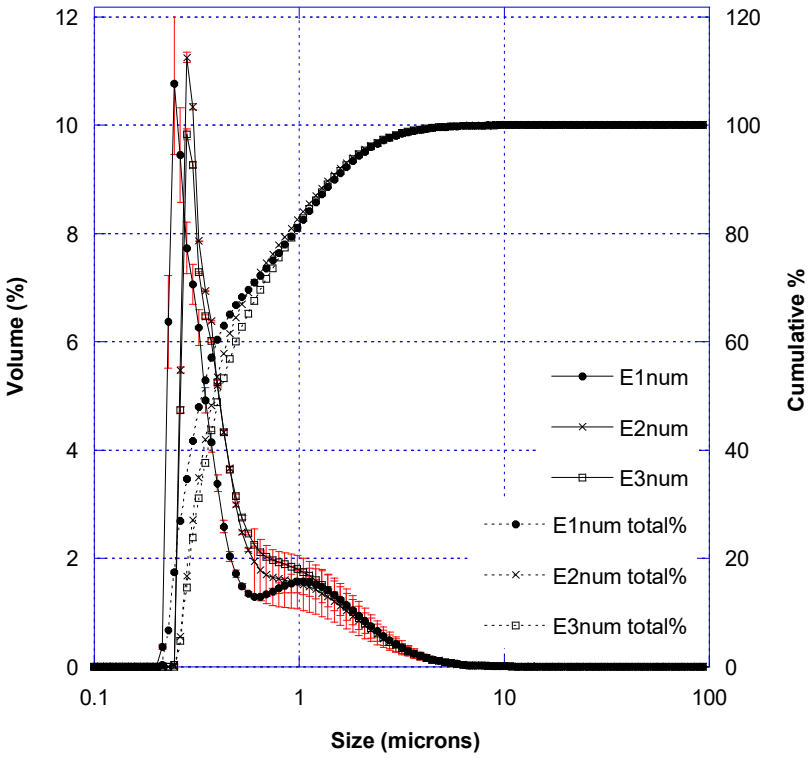

Figure 4-43 Number based particle size distribution for TiBAl 5-1 following dissolution in HCl

Figure 4-43 shows the number transformed particle size distribution for TiBAl 5-1 following dissolution in HCl. The distribution shows 90% of the sample was <1.5µm in diameter and 50% of the sample <0.4µm. There was some discrepancy between the 3

separate samples measured for this particle size distribution, highlighted by the mismatch between the volume distribution plots and the cumulative distribution plots. The discrepancy was most pronounced between 0.2 and 1µm.

Table 4.3.4 d(0.1), d(0.5) and d(0.9) values for the number transformed particle size distribution for TiBAl 5:1

Sample	d (0.1)	d (0.5)	d (0.9)
E1 (NumT)	0.25	0.35	1.53
E2 (NumT)	0.29	0.41	1.51
E3 (NumT)	0.29	0.43	1.55
Avg (NumT)	0.27	0.40	1.53

Table 4.3.4 shows the d(0.1), d(0.5) and d(0.9) values for the number transformed particle size distribution of TiBAl 5:1 grain refiner material. The results show the average d(0.1), d(0.5) and d(0.9) values to be 0.27, 0.40 and 1.53µm respectively.

4.3.2.2.2 Tensile test

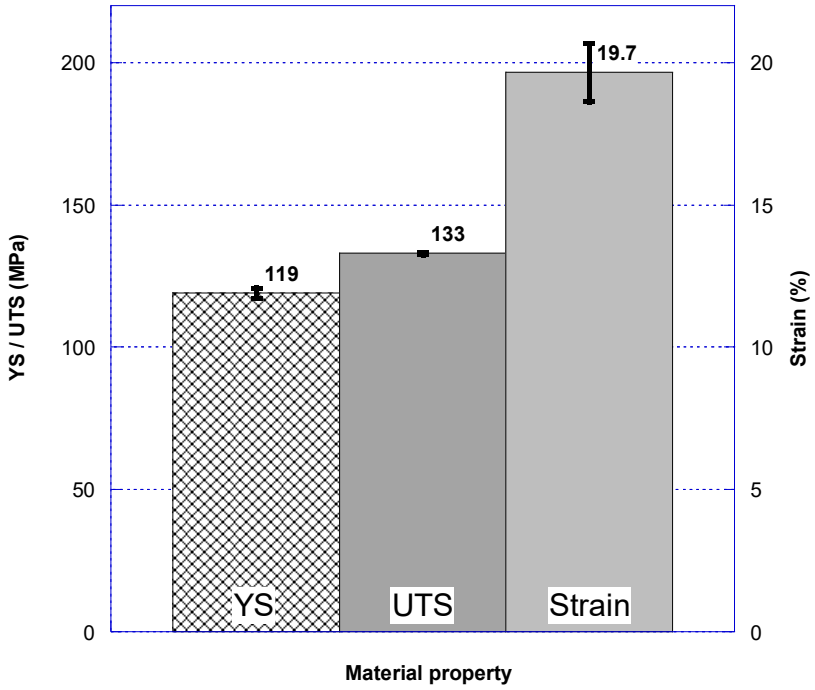

Figure 4-44 Yield Strength (YS), Ultimate Tensile Strength (UTS), and Strain for TiBAl 5-1

Figure 4-44 shows the yield strength, UTS and strain for TiBAl 5-1. The tensile results showed the yield strength to be 119MPa, the UTS to be 133MPa and the strain to be 19.7%.

4.3.2.3 TiBAl 3:1 and TiBAl 5:1 comparison

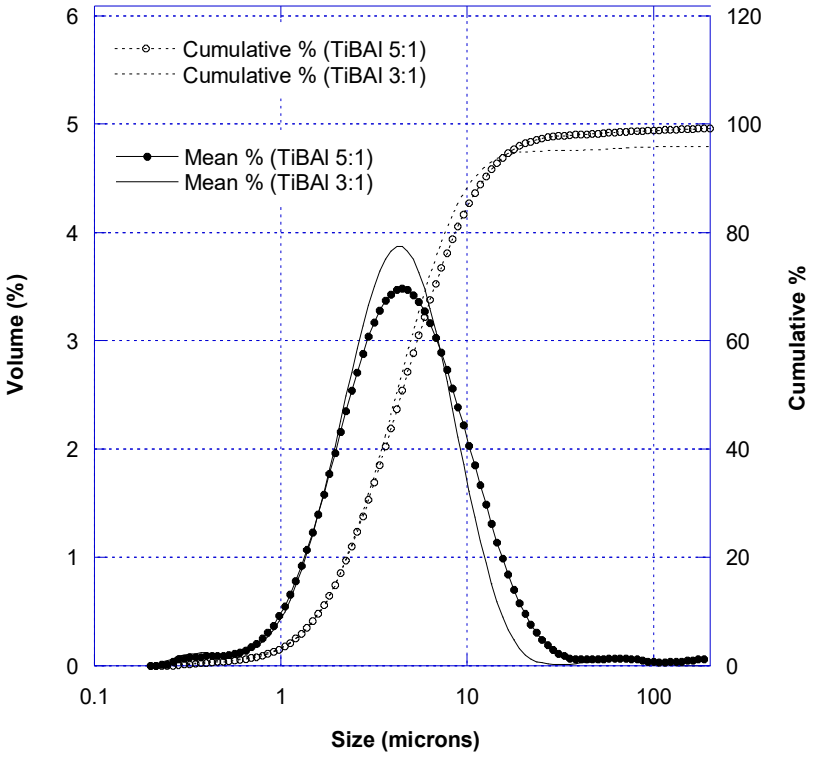

Figure 4-45 Volume based particle size distribution for TiBAl 5-1 and TiBAl 3-1 following dissolution in HCl. The right hand y-axis shows the cumulative percentage of the measured distributions.

Figure 4-45 shows the volume based particle size distribution for the 5:1 and 3:1 TiBAl grain refining materials following dissolution in HCl. The peak of each distribution was located at approximately 4µm. The 5:1 grain refiner had a slightly broader distribution, which can be seen on the right hand side of its peak and was also identifiable on the appropriate cumulative distribution plot when comparing particle sizes of >4µm.

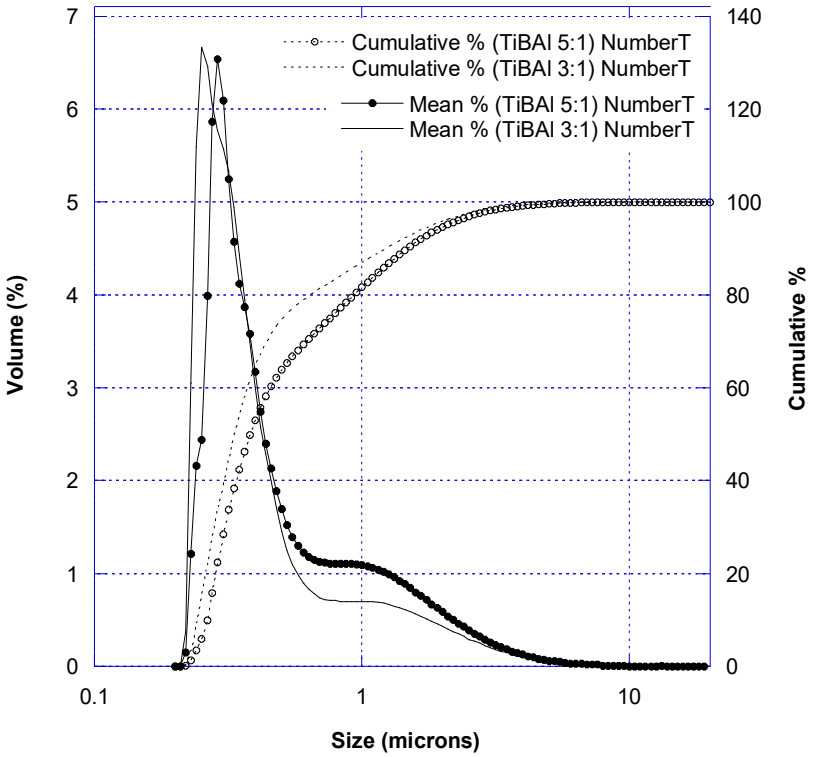

Figure 4-46 Number based particle size distribution for TiBAl 5-1 and TiBAl 3-1 following dissolution in HCl. The right hand y-axis shows the cumulative percentage of the measured distributions.

Figure 4-46 shows the number based particle size distribution of 5:1 and 3:1 TiBAl grain refining rod. The peaks of the size distribution lie at 0.25 and 0.3µm for 3:1 and 5:1 respectively. When comparing the cumulative distribution plots for the grain refiners, the 3:1 grain refiner did have a smaller particle size distribution when compared to the 5:1 grain refiner.

Table 4.3.5 3 particle size traits of the TiBAl 3:1 and 5:1 grain refiners

Sample	d (0.1) µm	d (0.5) µm	d (0.9) µm
TiBAl 3:1 (D123) Vol	1.74	4.44	11.66
TiBAl 5:1 (E123) Vol	1.73	4.72	13.31
TiBAl 3:1 (D123) NumT	0.25	0.35	1.29
TiBAl 5:1 E123) NumT	0.27	0.40	1.53

Table 4.3.5 shows the d(0.1), d(0.5) and d(0.9) particle size values for the TiBAl 3:1 and 5:1 grain refiners respectively. Regarding the volume based particle size distributions; the d(0.1) values were similar, the d(0.5) values for the 5:1 grain refiner are 0.3μm higher than the 3:1 grain refiner, the d(0.9) value for the 5:1 grain refiner were approximately 1.6μm higher than the 3:1 grain refiner. Regarding the number based particle size distributions; both the d(0.1) and d(0.5) values for the two grain refiners were similar, the d(0.9) value for the TiBAl 5:1 grain refiner was 0.2μm larger than its 3:1 counterpart.

4.3.3 Particle size analysis of A205

4.3.3.1 As cast

The grain boundary material was extracted from the A205 as-cast alloy as described in the experimental section. Since the experimentally removed grain boundary material was contained as a suspension within a liquid, a small sample was removed for powder X-ray diffraction, -leaving the remainder of the sample liquid for particle size analysis. 3 samples were analysed using powder X-ray diffraction from each of the 3 individual A205 dissolution experiments.

4.3.3.1.1 XRD

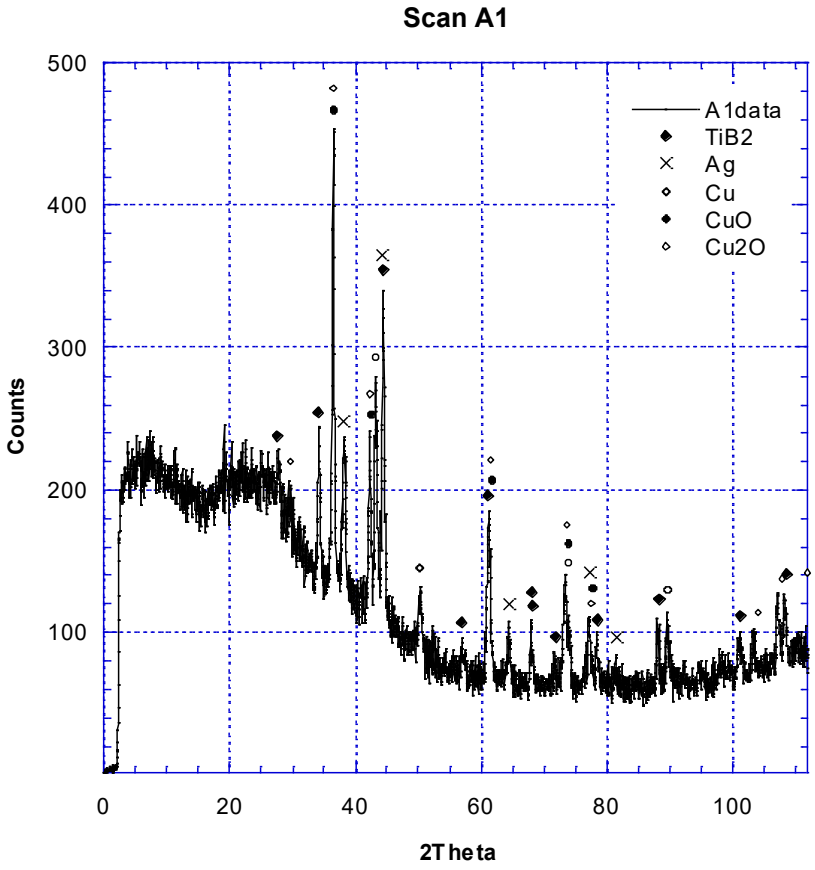

Figure 4-47 P-XRD diffraction spectrum, between 0° and 112°, for an as cast sample of A205 after dissolution in HCl

Figure 4-47 shows the PXRD spectrum between 0° and 112° degrees for the first 3 as-cast samples of A205 following dissolution in HCl. The spectrum shows the counts collected over the total range of angles observed. Despite being a 2-hour scan, only a low count rate was recorded due to the small amount of sample being analysed. The high count rate measured over the lower angles was due the beam width being larger than the sample width. In effort to reduce this effect a sheet of lead was positioned above the rotating sample to reduce stray X-rays from reaching the detector. Due to the design of the sample holder the sample rotated slightly off axis during analysis which can attributed

to a slight shift in peak location across the spectrum. The results showed shows strong matching peaks for TiB_2, Ag, Cu and Cu_2O/CuO, indicating that these compounds were present within the collected sample.

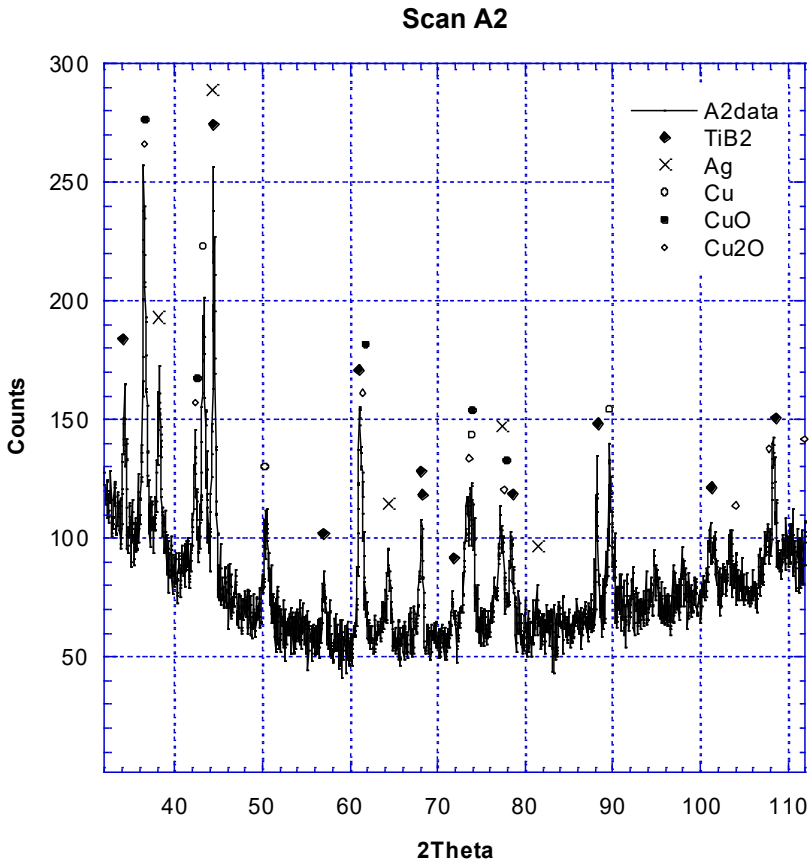

Figure 4-48 P-XRD diffraction spectrum, between 32° and 112°, for as cast A205 after dissolution in HCl

Figure 4-48 shows a PXRD spectrum from 32° to 112° for the second of 3 as-cast samples of A205 following dissolution in HCl. The spectrum shows a narrower range of angles compared to the previous figure. This subsection shows strong matching peaks for TiB_2, Ag, Cu and Cu_2O/CuO.

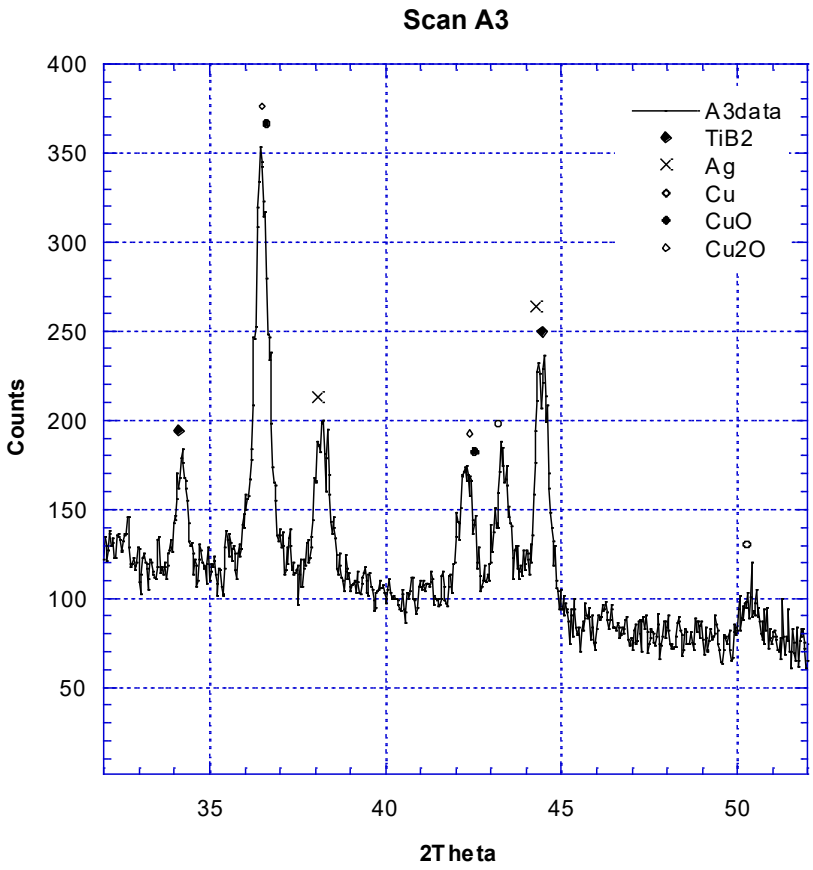

Figure 4-49 P-XRD diffraction spectrum, between 32° and 52°, for as cast A205 after dissolution in HCl

Figure 4-49 shows a PXRD spectrum from between 32° to 52° degrees for the third of the 3 as-cast samples of A205 following dissolution in HCl. The spectrum shows a small section of the total range of angles over which data was collected, and also shows strong matching peaks for TiB_2, Ag, Cu and Cu_2O/CuO.

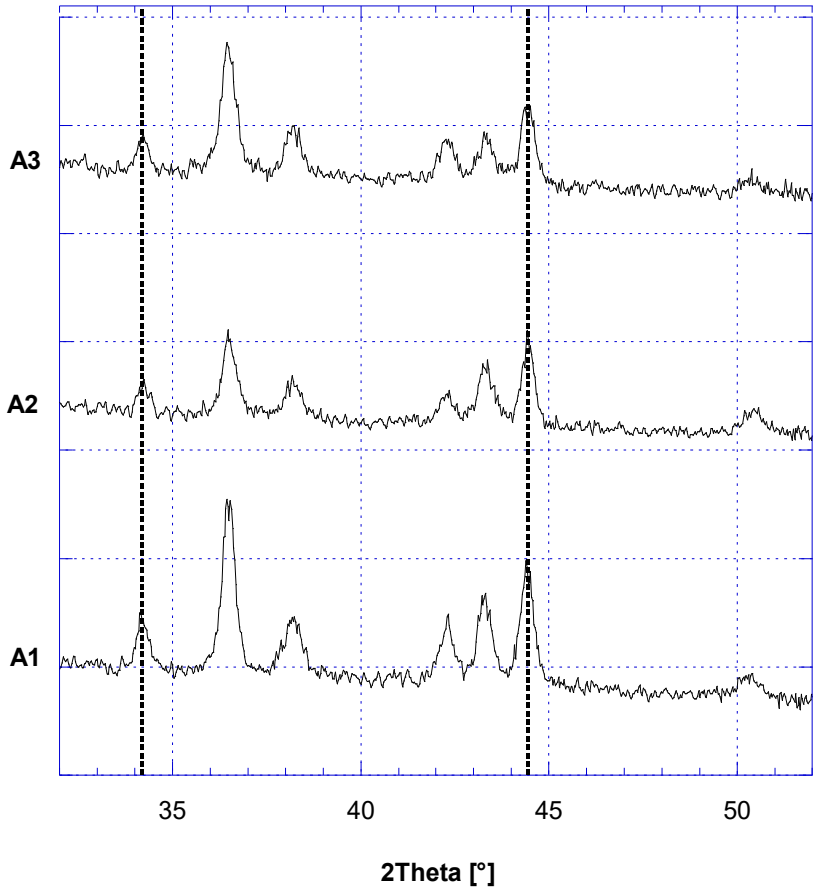

Figure 4-50 P-XRD diffraction spectrum, between 32° and 52°, for all 3 as cast A205 samples after dissolution in HCl. 2θ lines at 34.41° and 44.45° shown for TiB_2 peak locations.

Figure 4-50 shows a PXRD spectrum from between 32° and 52° degrees for all 3 as-cast A205 samples following dissolution in HCl. This figure highlights that the 3 samples of dissolved material were compositionally the same. Each of the 3 samples showed 7 peaks between the angles of 32° and 52° degrees. The first (34.14°) and sixth (44.45°) peak present within the scan were representative of the presence of TiB_2 within the samples within this range. The third and sixth peaks are representative of the presence of Ag. The remaining peaks within this range were indicative of the various phases of copper found within the sample.

4.3.3.1.2 Particle Size Analysis

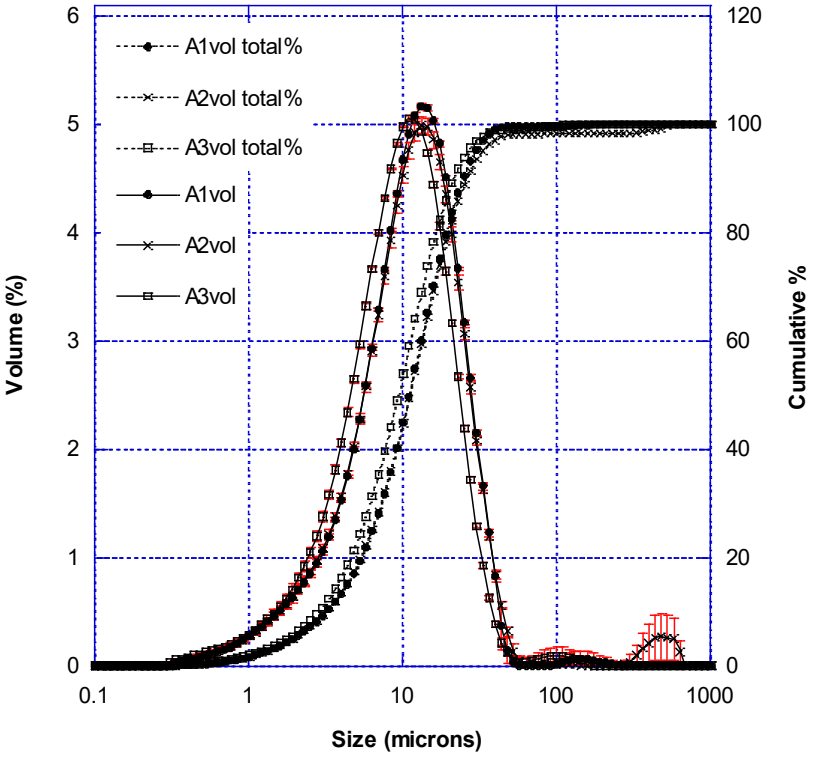

Figure 4-51 Volume particle size distribution collected for the as-cast material

Figure 4-51 shows the volume calculated particle size distribution of the as-cast material following dissolution in HCl. The cumulative percentage plot showed that 10% of the distribution was less than 3µm, and 50% of the distribution was less than approximately 10µm. Inspection of the volume analysis peak revealed a shallow increase in measured particle size indicating the presence of a large number of smaller particles. The tail end of the volume particle size distribution showed the presence of some larger particles, however this was only found within one of the three samples analysed and was probably due to an agglomeration event, (as the size of the measured particles was greater than the size of a grain of A205 at approximately 20µm).

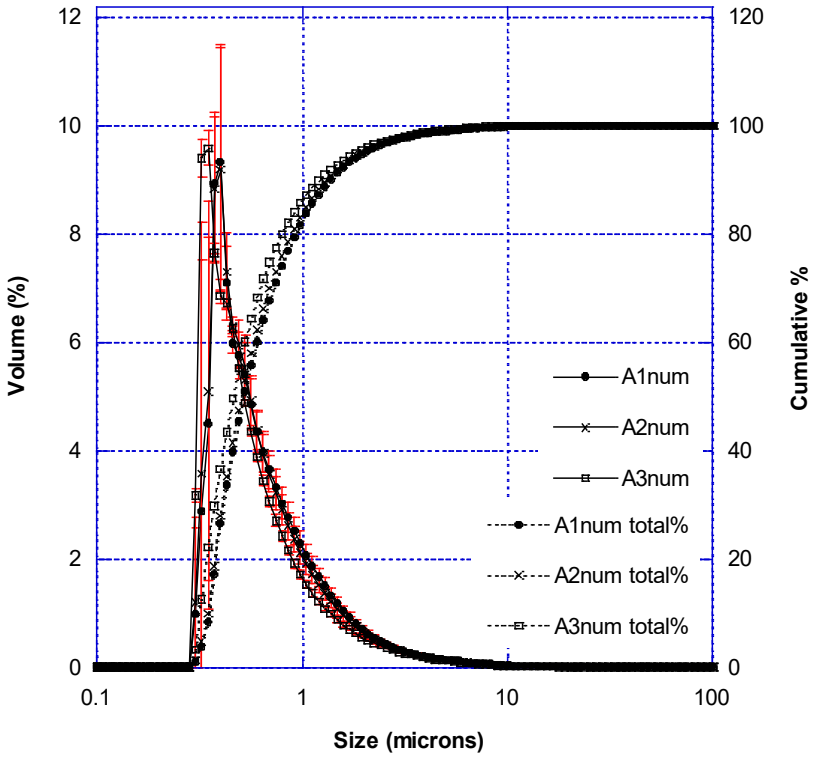

Figure 4-52 Number particle size distribution collected for the as-cast material

Figure 4-52 shows the number transformed particle size distribution for 3 samples of as-cast A205. The cumulative distribution reveals that 10% of the sample was sub 0.40µm, 50% of the sample was approximately 0.5µm and about 95% of the sample was <2µm. The particle size distribution reveals that most of the particles were small in size with the lowest measured particle being 0.3µm in diameter. Flowing the initial spike of small particles, the measured volume percentage dropped with increasing size.

4.3.3.1.3 Strength prediction

The Yield strength prediction for as-cast A205 will be dominated by the Hall-Petch strengthening mechanism for the grain material and the CTE mechanism for the grain boundary material. The Orowan strengthening mechanisms will not be acting within the crystal, or at least not to any significant degree, as there are not yet any precipitates

formed. However, taking into consideration the measured grain size distribution as shown in Table 4.2.4, the calculated volume fraction of both the grain and grain boundary material (Table 4.2.5), and the TiB_2 in the grain boundary material (Figure 4-8), the strength has been calculated using:

- The Hall-Petch strengthening mechanism (Equation 28):

$$\Delta\sigma_{Hall-Petch} = \sigma_{dislocation} + K\, d_m^{(-1/2)}$$

Where; $\sigma_{dislocation}$ is the friction stress of an un-deformed single crystal orientated for multiple slip (41.6MPa), K is the Hall-Petch coefficient (125MPa.$m^{1/2}$) and d_m is the measured grain particle size[113,114, 115]. The Hall-Petch strength contribution for this sample was calculated from the sum of 1/n of each grain size (d_m) measured.

- The Coefficient of Thermal Expansion strengthening mechanism (Equation 31):

$$\Delta\sigma_{CTE} = \sqrt{3}\,\beta\, G_m\, b \left(\frac{12\, V_p\, \Delta\alpha\, \Delta T}{(1 - V_p)\, b\, d_p}\right)^{1/2}$$

Where; β is a strengthening coefficient (1.25), G_m is the shear modulus of the matrix material (23GPa), b is the Burgers vector of the matrix (28.6nm), V_p is the volume fraction of particles within the matrix (measured), Δα is the difference between the coefficients of thermal expansion of the matrix material (2.29e-5) and the particles (7.40e-8), ΔT is the difference between the processing temperature

(538°C) and the testing temperature (23°C), and d_p is the particle size (measured) [2, 88, 116].

- The Load bearing strengthening mechanism (Equation 30):

$$\Delta\sigma_{Load} = 0.5\, V_p\, \sigma_{ym}$$

Where; V_p is the volume fraction of particles within the matrix (measured) and σ_{ym} is the matrix yield strength (35MPa [88]).

Hence, the total theoretical yield strength (Equations 32 and 33) calculated using both the volume and number based TiB_2 particle size distributions gave predictive results of:

- ❖ 110 MPa using the 'number' particle size distribution for TiB_2 particles
- ❖ 53 MPa using the 'volume' particle size distribution for TiB_2 particles

4.3.3.1.4 Tensile test

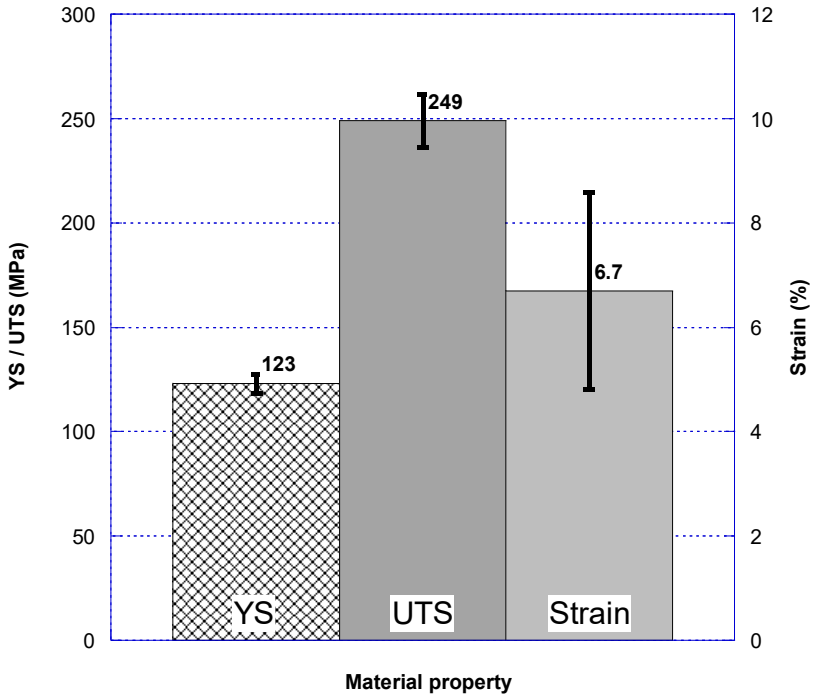

Figure 4-53 Yield Strength (YS), Ultimate Tensile Strength (UTS), and Strain for as-cast A205

Figure 4-53 shows the yield strength, Ultimate Tensile Strength and strain for as-cast A205 alloy. The tensile results showed the yield strength to be 123MPa, the UTS to be 249MPa and the strain to be 6.7%.

4.3.3.2 The Solution Heat Treated Alloy

The grain boundary material was extracted from the solutionised A205 alloy as described in the experimental procedure section of this thesis. This material was expected to contain TiB_2 particles previously contained within the grain boundaries. The experimentally removed grain boundary material was contained as a suspension within a liquid, from which a small sample was removed for powder X-ray diffraction analysis. Again 3 samples were analysed from each of 3 individual A205 dissolution experiments using the powder x-ray diffraction analysis technique.

4.3.3.2.1 XRD

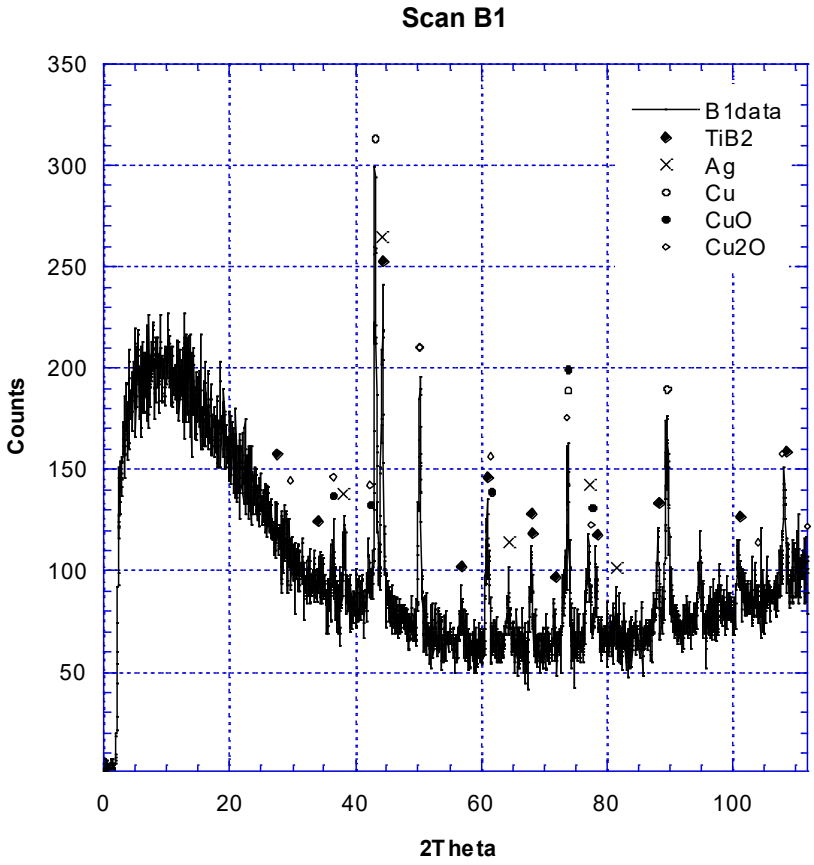

Figure 4-54 P-XRD spectrum, from 0° to 112°, of solution heat treated A205 following dissolution in HCl

Figure 4-54 shows the XRD spectrum of solution heat-treated A205 alloy following dissolution in HCl (sample 1 of 3). The relatively low count rate was partially due to the small quantity of material analysed. The high count rate measured over the low scattering angles 0-30° of the scan were due to the width of the impinging X-ray beam being wider than the sample volume. In effort to reduce the high count rate a lead sheet was placed over the sample to minimise the effect of the stray X-rays. Due to the slight asymmetrical rotation of the sample a slight shift in peak location was noted in the higher angle data.

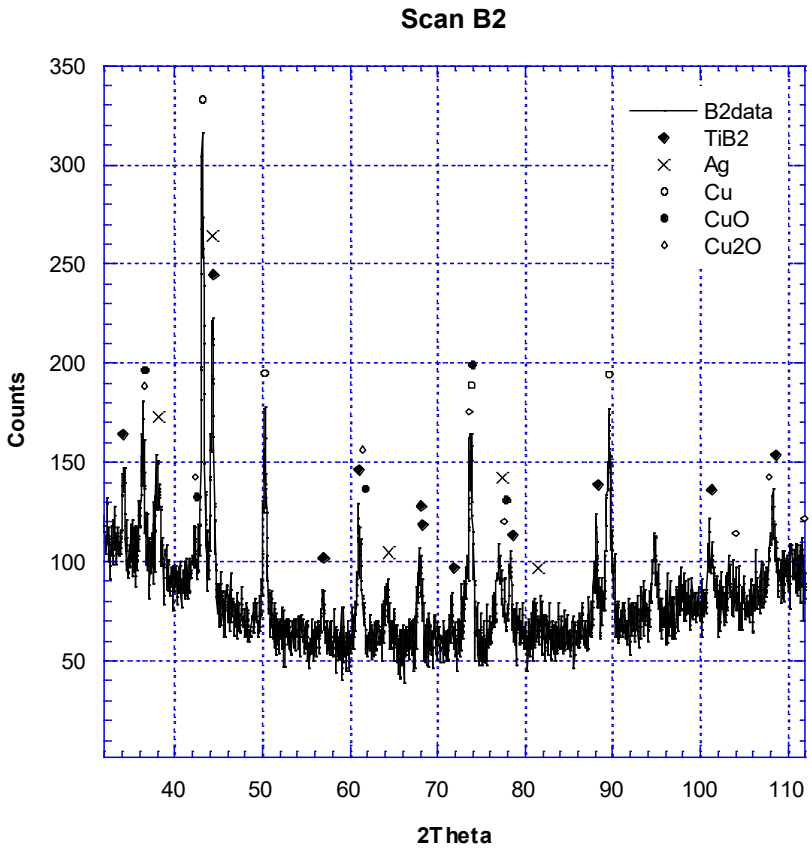

Figure 4-55 Reduced angle (32°-112°) P-XRD spectrum for solution heat treated A205 following dissolution in HCl

Figure 4-55 shows the P-XRD spectrum of solution heat-treated A205 alloy following dissolution in HCl for sample 2 of 3. The spectrum has been narrowed to show angles between 32-112°. The graph shows that all but one peak, located at 95°, was matched to an appropriate XRD pattern.

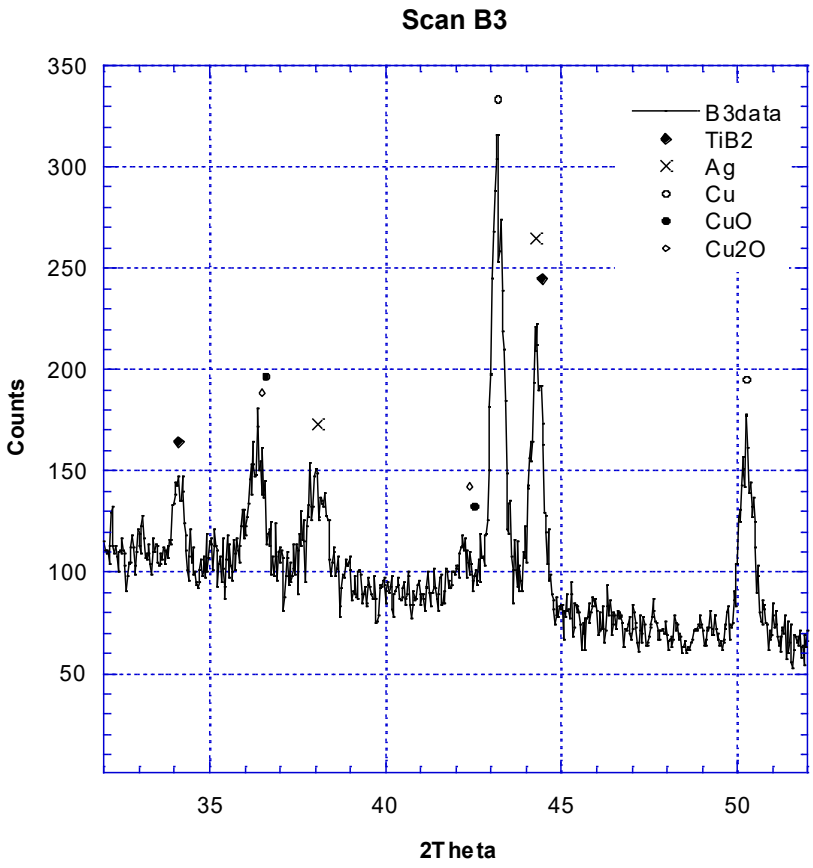

Figure 4-56 P-XRD diffraction spectrum, between 32° and 52°, for solution heat treated A205 after dissolution in HCl

Figure 4-38 shows the P-XRD spectrum for solution heat-treated A205 following dissolution in HCl for sample 3 of 3. The spectrum was reduced to between 32° to 52° to show the lower angle peaks present within the spectrum. The spectrum showed strong matching peaks for TiB_2 and Ag.

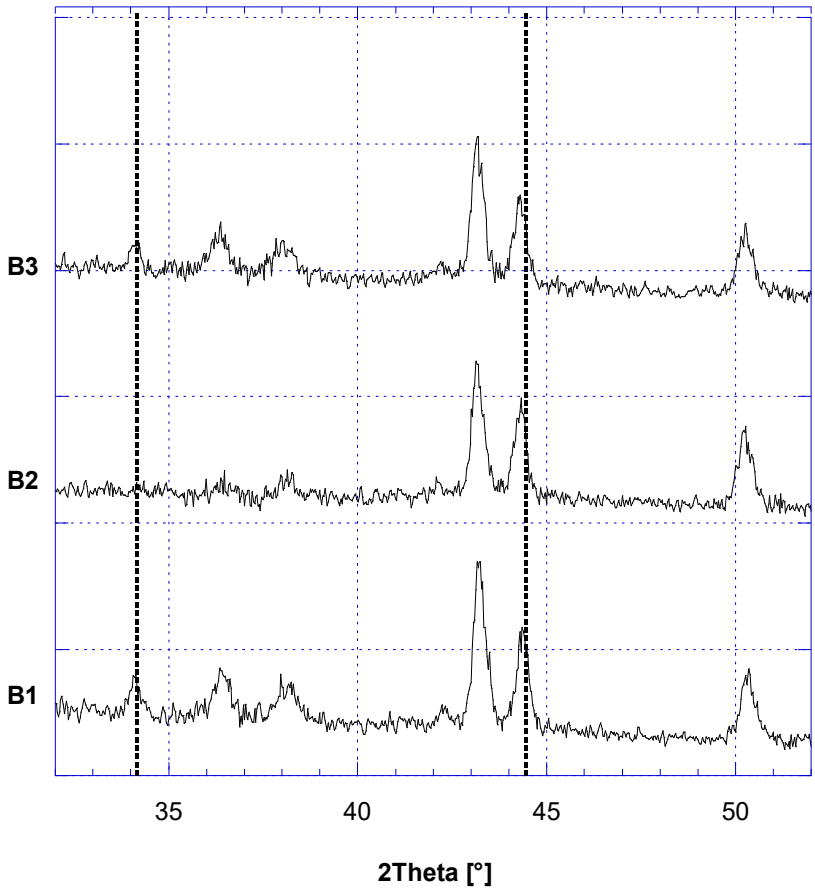

Figure 4-57 P-XRD diffraction spectrum, between 32° and 52°, for all 3 solution heat treated A205 samples after dissolution in HCl. 2θ lines at 34.41° and 44.45° shown for TiB_2 peak locations.

Figure 4-57 shows the P-XRD spectrum between 32 and 52° for all 3 heat treated A205 samples following dissolution in HCl. The two lines drawn at 34.14° and 44.45° indicate the TiB_2 peak locations within this range. The figure reveals slight differences between each of the 3 samples. Sample B1 had 7 discernible peaks within this 2θ range, located at approximately 34, 36.5, 38, 42.5, 43.5, 44.5 and 50.5°. In comparison sample B2 did not show peaks 1, 2, 3 or 4 with such resolution. Sample B3 showed evidence of all 7 peaks within this 2θ range.

4.3.3.2.2 Particle Size Analysis

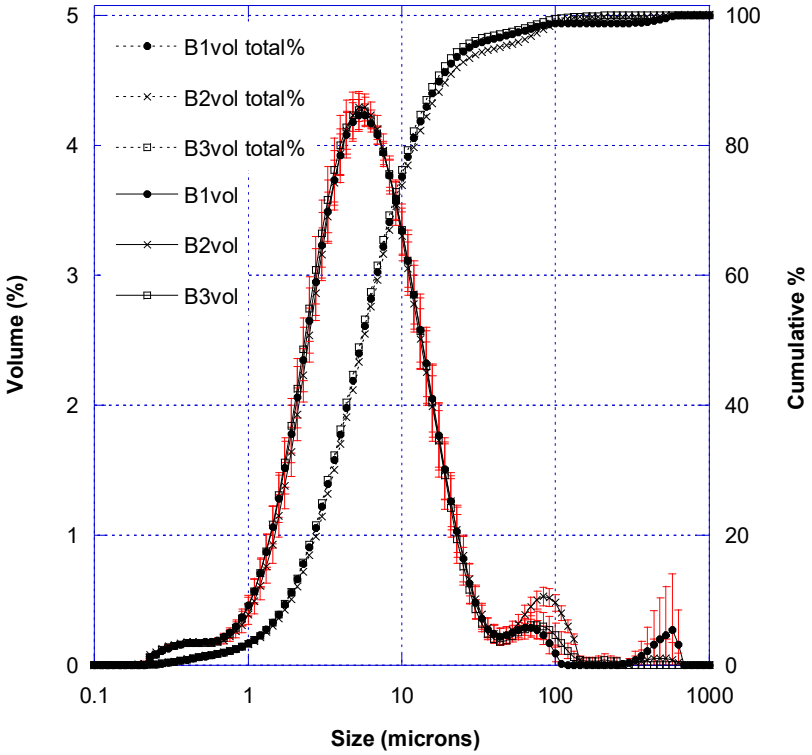

Figure 4-58 Volume particle size distribution for solution heat treated A205

Figure 4-58 shows the volume particle size distribution for solution heat-treated A205 alloy following dissolution in HCl. The distribution comprised 3 individual size analysis profiles from 3 separate samples. Each of the 3 sample profiles lay on top of one another for approximately 90% of the sample, however for the much larger particles there was a slight discrepancy within the profiles most likely resulting from agglomeration. The size distribution profile also revealed that 10% of the sample was sub 2µm in size and that the lowest particle size detected was between 0.2 and 0.3µm. 50% of the measured sample was sub 5.5µm.

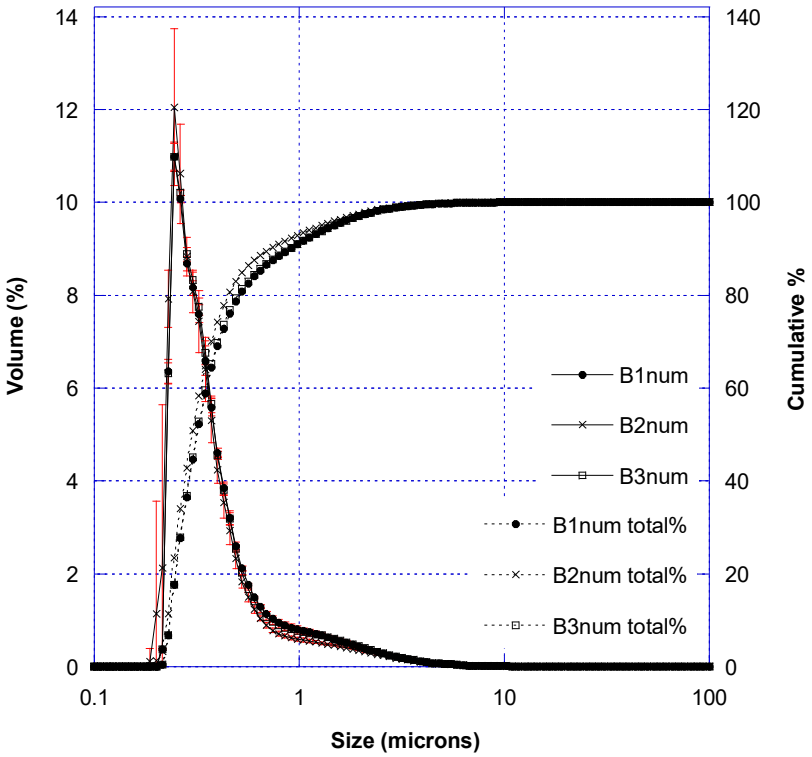

Figure 4-59 Number based particle size distribution for solution heat treated A205

Figure 4-59 shows the number transformed particle size distribution for solution heat-treated A205 alloy. The distribution revealed that 50% of the sample was <0.3µm and 90% of the sample was <0.9µm. The particle size distribution revealed that most of the measured sample contained a large number of small particles.

4.3.3.2.3 Tensile test

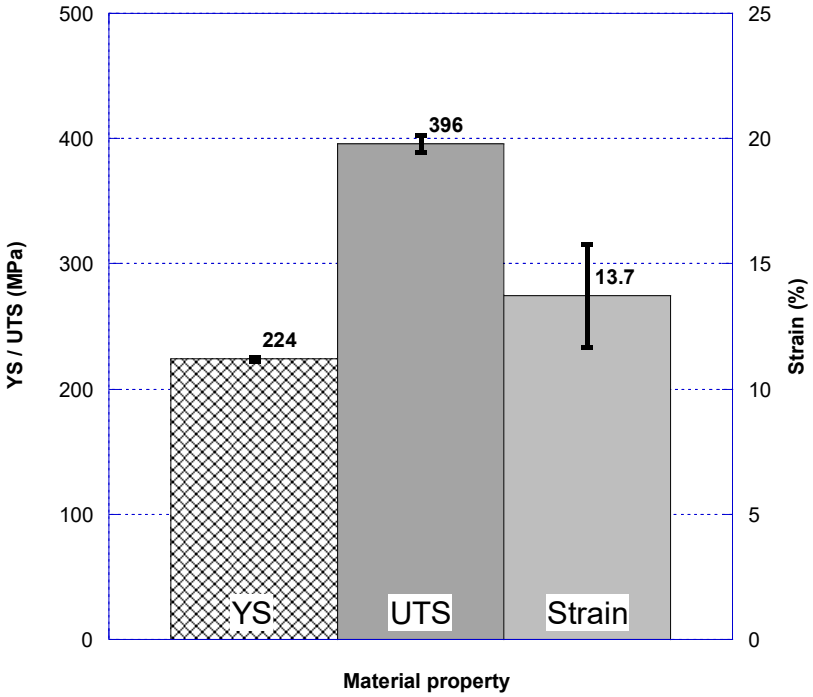

Figure 4-60 Yield Strength (YS), Ultimate Tensile Strength (UTS), and Strain for solution heat treated A205

Figure 4-60 shows the Yield Strength (YS), Ultimate Tensile Strength (UTS), and Strain for solution heat-treated A205 alloy. The tensile results showed the yield strength to be 224MPa, the UTS to be 396MPa and the strain to be 13.7%.

4.3.3.3 Solution Heat-Treated and Precipitation Hardened A205

4.3.3.3.1 XRD

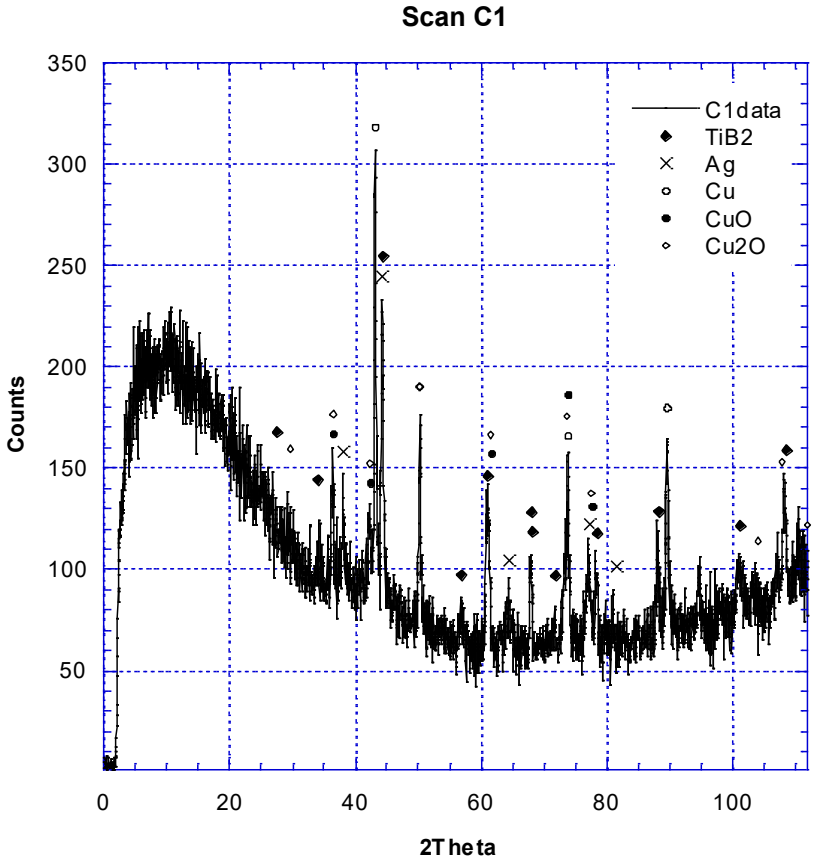

Figure 4-61 P-XRD diffraction spectrum, between 0° and 112° degrees, for a solution heat treated and precipitation hardened sample of A205 after dissolution in HCl

Figure 4-61 shows a P-XRD spectrum for solution heat-treated and precipitation-hardened samples of A205 alloy following dissolution in HCl. The spectrum shows the counts collected over the total range of angles observed, i.e. from 0-112°.

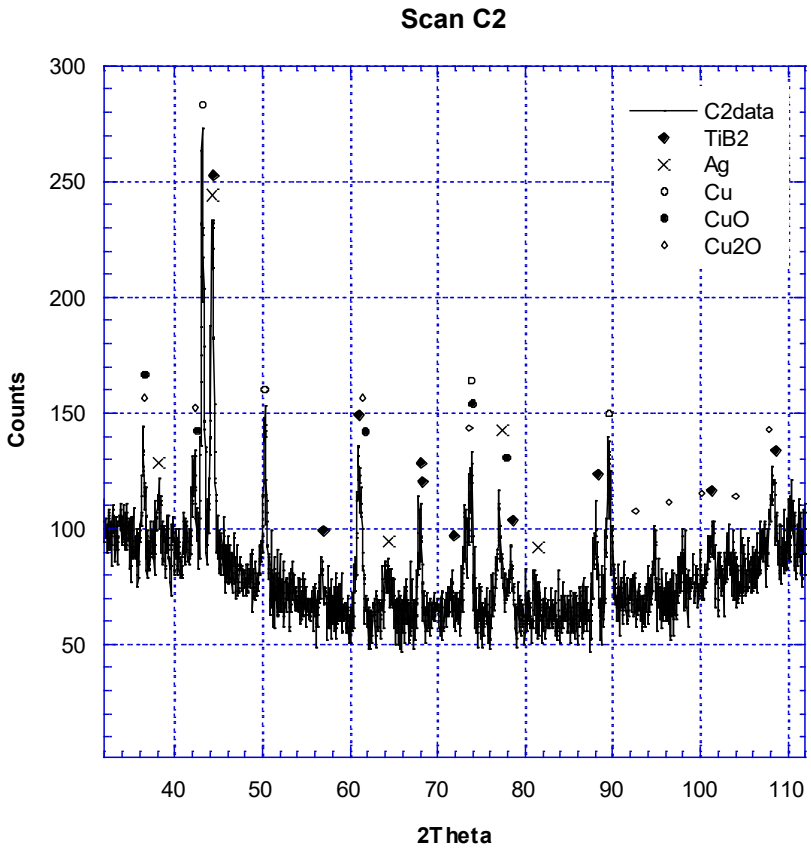

Figure 4-62 P-XRD diffraction spectrum, between 32° and 112°, for solution heat treated and precipitation hardened A205 after dissolution in HCl

Figure 4-62 shows the P-XRD spectrum for solution heat-treated and precipitation-hardened A205 following dissolution in HCl. The lower angles of the scan have been removed for this figure to highlight the total range of peaks matched for this sample.

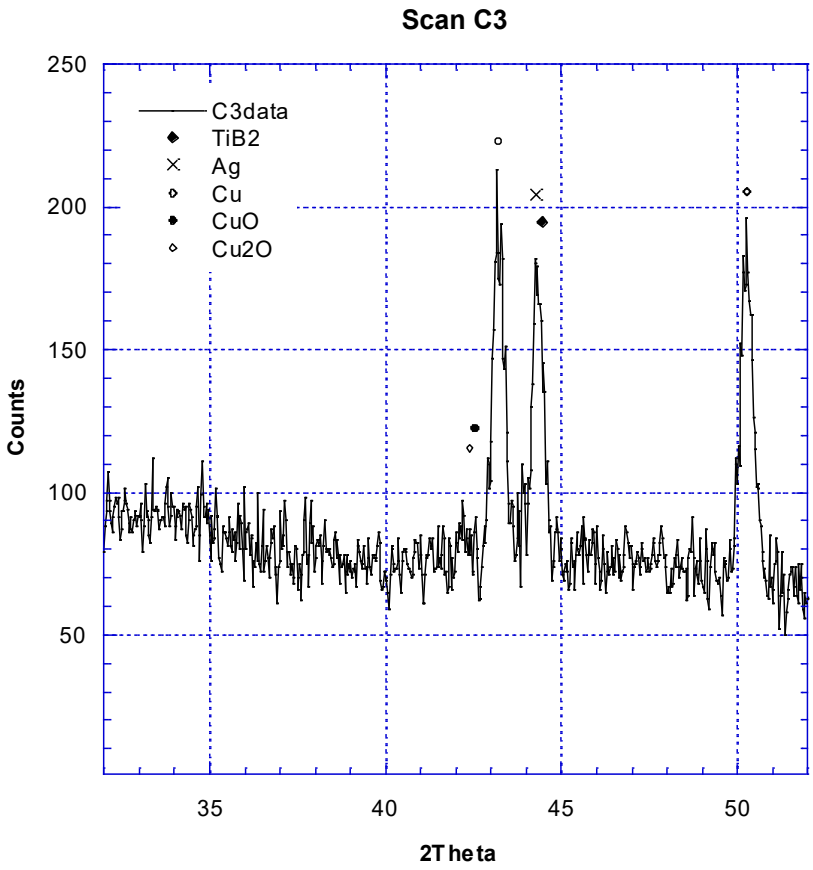

Figure 4-63 P-XRD diffraction spectrum, between 32° and 52°, for solution heat treated and precipitation hardened A205 after dissolution in HCl

Figure 4-63shows the PXRD diffraction spectrum between 32 and 52° for solution heat-treated and precipitation-hardened A205 alloy following dissolution in HCl. The spectrum showed peaks for TiB_2, Cu and Ag.

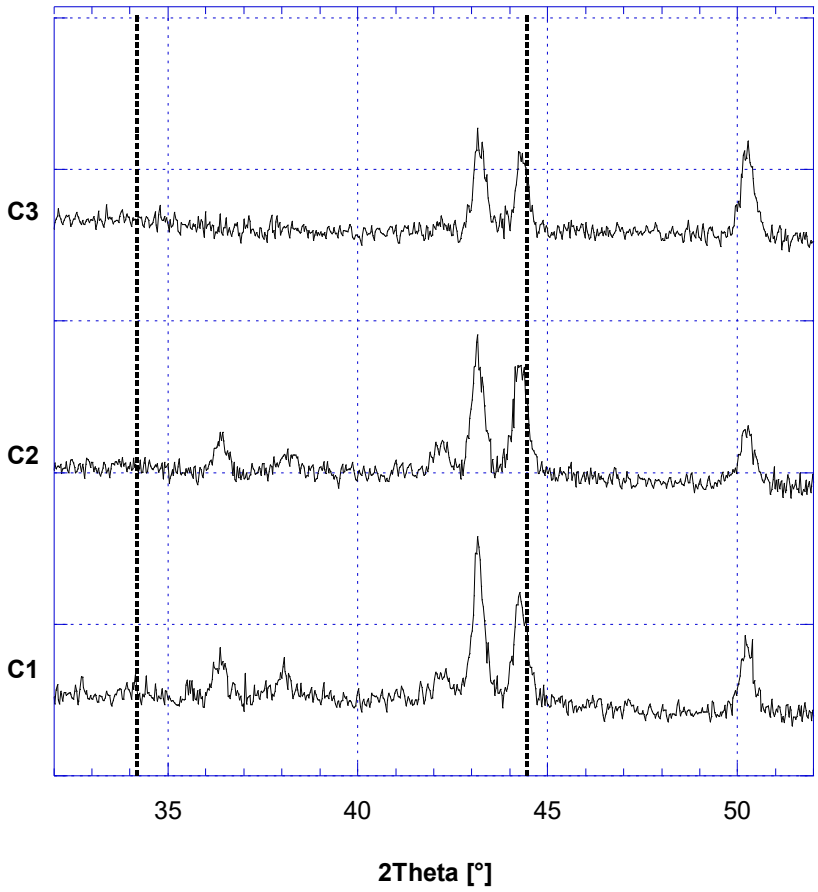

Figure 4-64 P-XRD diffraction spectrum, between 32° and 52°, for all 3 solution heat treated and precipitation hardened samples of A205 after dissolution in HCl. 2θ lines at 34.41° and 44.45° shown for TiB_2 peak locations.

Figure 4-64 shows the P-XRD diffraction spectrums, between 32 and 52°, for all 3 solution heat-treated and precipitation hardened samples of A205 alloy following dissolution in HCl. The two lines drawn at 34.14° and 44.45° indicate the TiB_2 peak locations within this range. The figure shows how each of the 3 individual samples had approximately the same peak profiles between 40 and 52°.

4.3.3.3.2 Particle Size Analysis

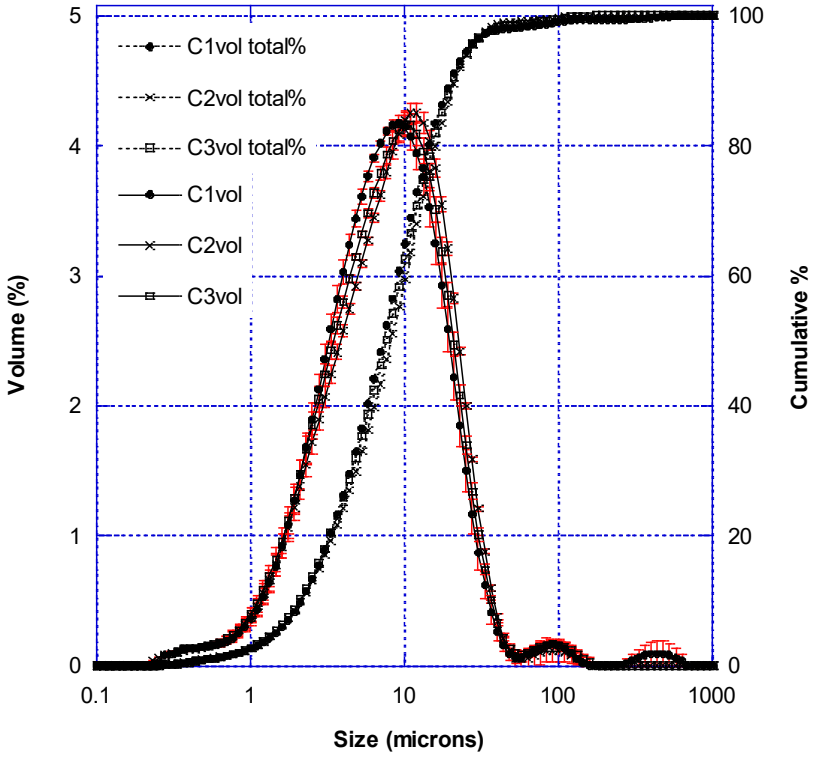

Figure 4-65 Volume calculated particle size distribution for the 3 solution heat treated and precipitation hardened samples following dissolution in HCl

Figure 4-65 shows the volume based particle size distribution for the solution heat-treated and precipitation-hardened A205 alloy following dissolution in HCl. The distribution shows that 10% of the sample material was <2µm, 50% of the sample was <7µm and 90% of the sample was <20µm. The rising edge of the distribution showed the presence of small sub-micron sized particles. The 2 small peaks present at approximately 100 and 500µm were likely due to agglomeration events.

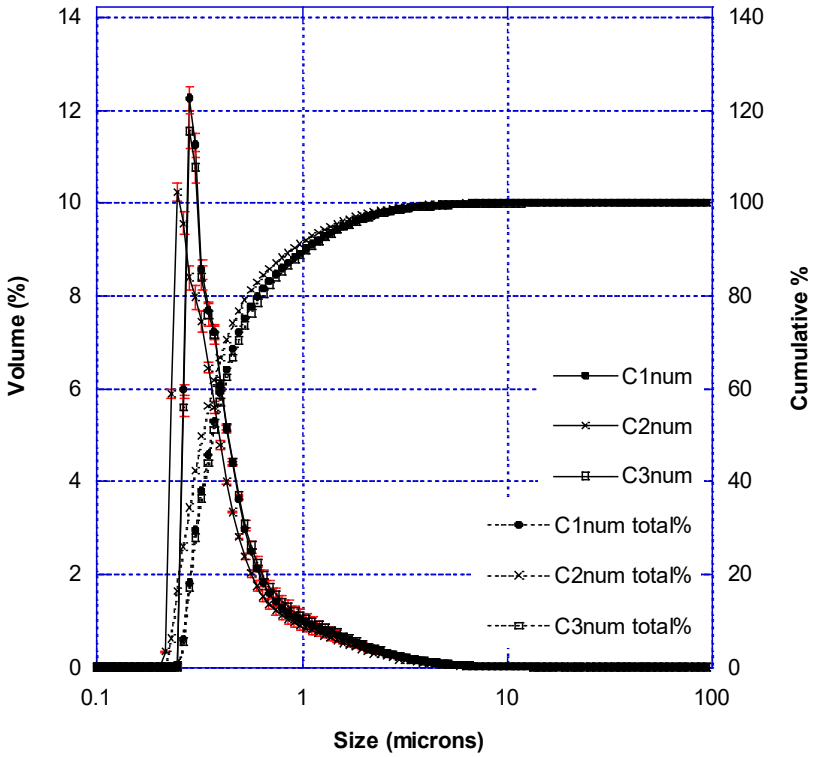

Figure 4-66 Number based particle size distribution for solution heat treated and precipitation hardened A205 alloy following dissolution in HCl

Figure 4-66 shows the number based particle size distribution for solution heat-treated and precipitation-hardened A205 alloy following dissolution in HCl. The distribution showed that 50% of the particles were below 0.35µm and 90% of the particles were below 1µm.

4.3.3.3.3 Strength prediction

The Yield strength prediction for solution heat-treated and precipitation hardened A205 included; the Orowan strengthening mechanism, the Hall-Petch strengthening mechanism, the CTE mechanism and the Load strengthening mechanisms where;

The active strength mechanisms within the grain include:

- The Hall-Petch strengthening mechanism (Equation 28);

$$\Delta\sigma_{Hall-Petch} = \sigma_{dislocations} + K\, d_m^{(-1/2)}$$

Where; $\sigma_{dislocation}$ is the friction stress of an un-deformed single crystal orientated for multiple slip (41.6MPa), K is the Hall-Petch coefficient (125MPa.m$^{1/2}$) and d_m is the measured grain particle size[113,114, 115]. The Hall-Petch strength contribution for this sample was calculated from the sum of 1/n of each grain size (d_m) measured.

- The Orowan strengthening mechanism for Ω and θ precipitates (Equation 29);

$$\Delta\tau_{\Omega/\theta} = 0.12\, MG\, \frac{b}{2\sqrt{rh}} .\left\{\phi^2 + 0.70\left(\frac{r}{h}\right)^2 + 0.12\left(\frac{r}{h}\right)^2 \phi^{(3/2)}\right\} \ln\left[\frac{0.158\, r}{r_0}\right]$$

Where; G is the magnitude of the shear modulus (23GPa), M is the Taylor factor, b is the Burgers vector, r is the radius of the precipitate (30-80nm), r_0 is the precipitate lower cut of radius, h is the thickness of the precipitate, and ϕ is the volume fraction)[89,90,117–125].

The active strength mechanisms within the grain boundary include:

- The Coefficient of Thermal Expansion (CTE) strengthening mechanism (Equation 31);

$$\Delta\sigma_{CTE} = \sqrt{3}\, \beta\, G_m\, b \left(\frac{12\, V_p\, \Delta\alpha\, \Delta T}{(1 - V_p)\, b\, d_p}\right)^{1/2}$$

Where; β is a strengthening coefficient (1.25), G_m is the shear modulus of the matrix material (23GPa), b is the Burgers vector of the matrix (28.6nm), V_p is the volume fraction of particles within the matrix (measured), Δα is the difference between the coefficients of thermal expansion of the matrix material (2.29e-5) and the particles (7.40e-8), ΔT is the difference between the processing temperature (538°C) and the testing temperature (23°C), and d_p is the particle size (measured) [2, 88, 116].

- The Load Bearing strengthening mechanism (Equation 30);

$$\Delta\sigma_{Load} = 0.5\, V_p\, \sigma_{ym}$$

Where; V_p is the volume fraction of particles within the matrix (measured) and σ_{ym} is the matrix yield strength (35MPa [88]).

Taking into consideration the measured grain size distribution, (Table 4.2.4), the calculated volume fraction of both the grain and grain boundary material (Table 4.2.5), the volume fraction of TiB_2 in the grain boundary material, and the size of the TiB_2 particles (Figure 4-8), the total predictive yield strength was calculated using Equations 32 and 33 to be:

- 398 MPa using the 'number' particle size distribution for TiB_2 particles
- 331 MPa using the 'volume' particle size distribution for TiB_2 particles

4.3.3.3.4 Tensile test

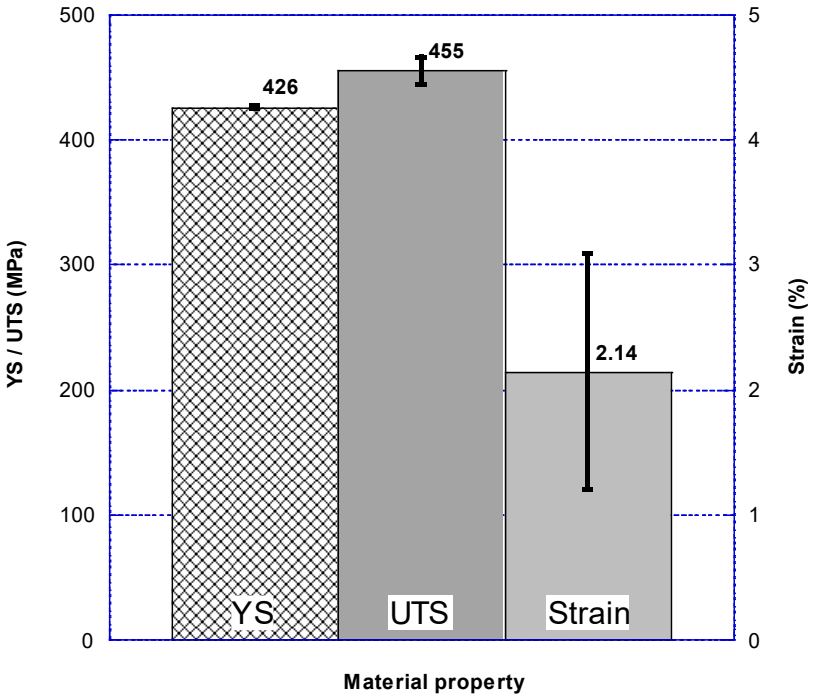

Figure 4-67 Yield Strength (YS), Ultimate Tensile Strength (UTS), and Strain for solution heat treated and precipitation hardened A205

Figure 4-67 shows the yield strength, UTS and strain for solution heat-treated and precipitation hardened A205 alloy. The tensile results showed the yield strength to be 426MPa, the UTS to be 455MPa and the strain to be 2.14%.

4.3.3.4 *Comparison of As-Cast, Solution Heat-Treated, and Solution Heat-Treated and Precipitation Hardened TiB_2 Particle Size Distributions*

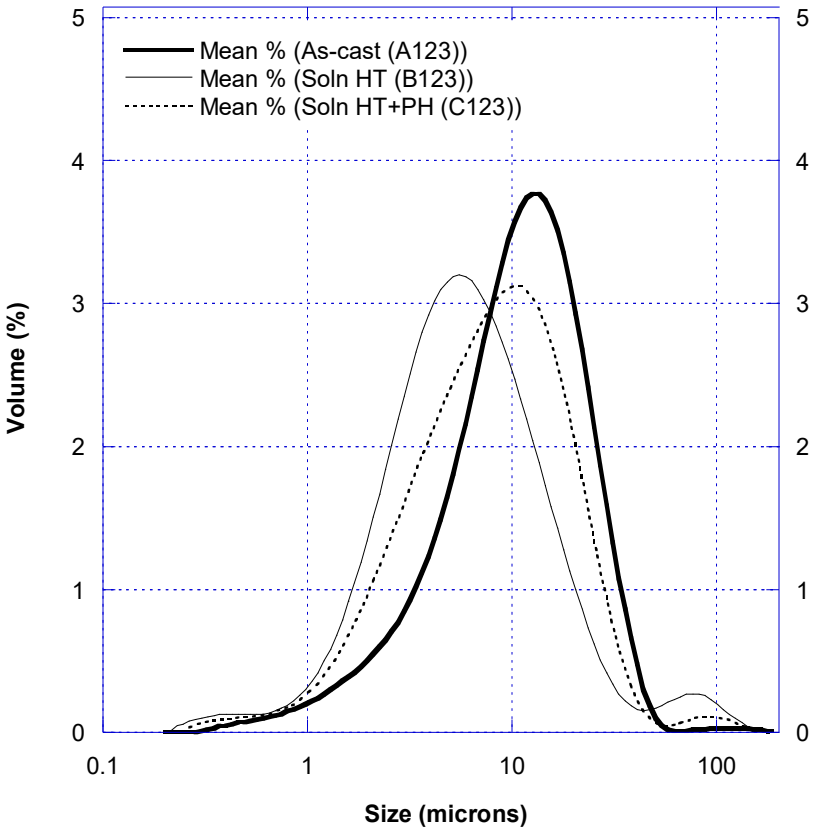

Figure 4-68 Comparison between the volume particle size distributions collected for As-cast, Solution Heat Treated, and Solution Heat Treated + Precipitation Hardened materials

Figure 4-68 shows the volume based particle size distributions collected for as-cast A205, solution heat-treated A205, and solution heat-treated and precipitation hardened A205. The distribution shows the collected precipitate from the as-cast material had the largest particle size distribution with a peak located at approximately 15µm. The solution heat-treated material had the smallest particle size distribution with a peak measured at approximately 5.5µm. The solution heat-treated and precipitation hardened material had a particle size distribution located between the as-cast and solution heat-treated particle size distributions with a peak located at 10µm.

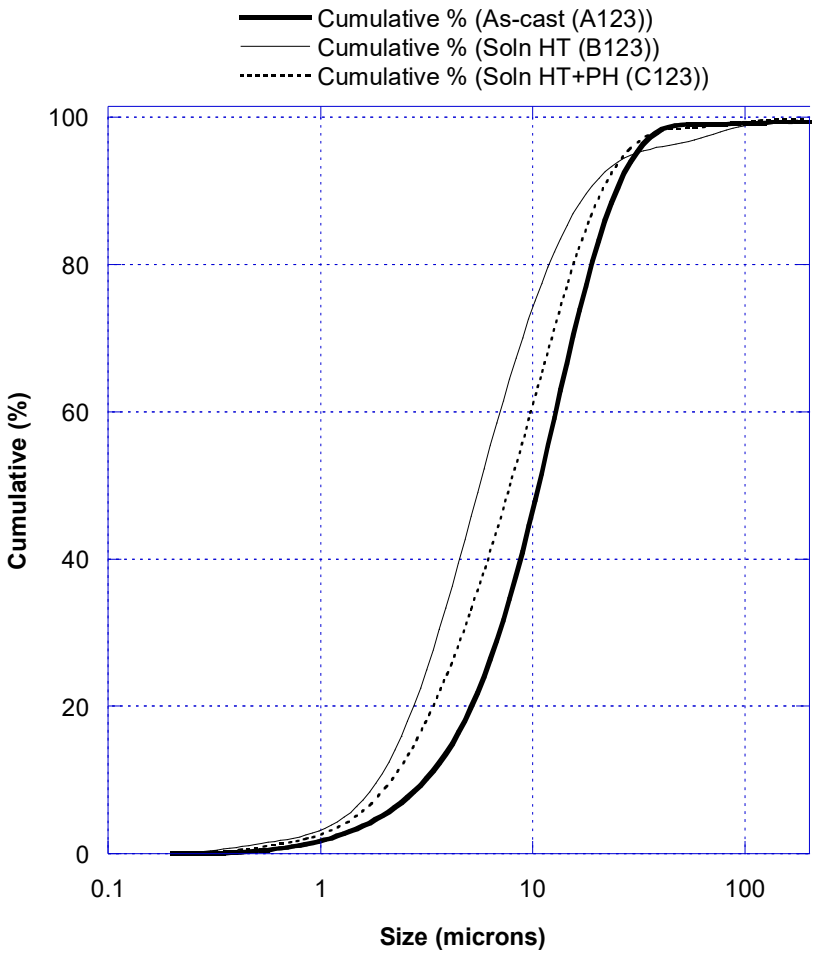

Figure 4-69 Volume based cumulative particle size distribution for As-cast A205, Solution Heat Treated A205, and Solution Heat Treated + Precipitation Hardened A205

Figure 4-69 shows the volume based cumulative particle size distribution for as-cast A205, solution heat-treated A205, and solution heat-treated and precipitation hardened A205. The cumulative distribution shows that the as-cast material had the largest particle size distribution. The solution heat treated material had the smallest measured particle size distribution. The solution and precipitation hardened material had a particle size distribution in between the as-cast and solution heat treated particle size distributions. The d(0.5) values for these distributions were; 11.42, 6.03 and 22.55µm for the as-cast,

solution heat treated and solution heat treated and precipitation hardened material respectfully.

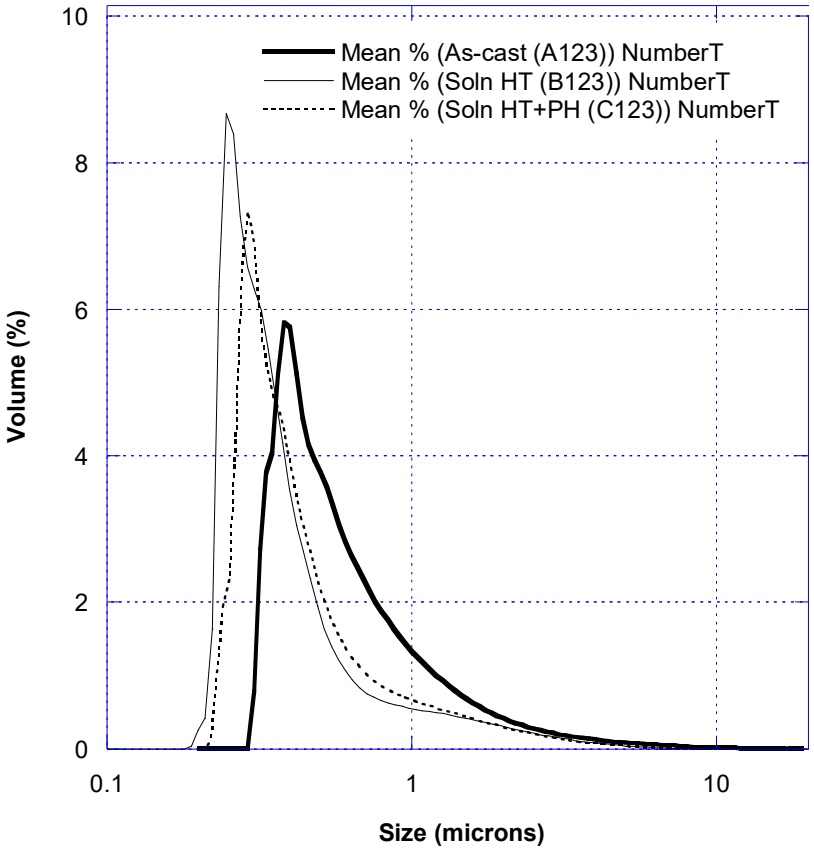

Figure 4-70 Comparison between the number based particle size distributions collected for As-cast, Solution Heat Treated, and Solution Heat Treated and Precipitation Hardened A205 alloy

Figure 4-70 shows a comparison between the number based particle size distribution for as-cast, solution heat treated, and solution heat treated and precipitation hardened A205 alloy. Again the largest particle size distribution was the as-cast material. The smallest particle size distribution was the solution heat treated material. The solution heat treated and precipitation hardened material has a particle size distribution in between the as-cast material and the solution heat treated material. The approximate peak locations were 1.5,

2 and 3µm for the as-cast, solution heat treated, and the solution heat treated and precipitation hardened materials respectively.

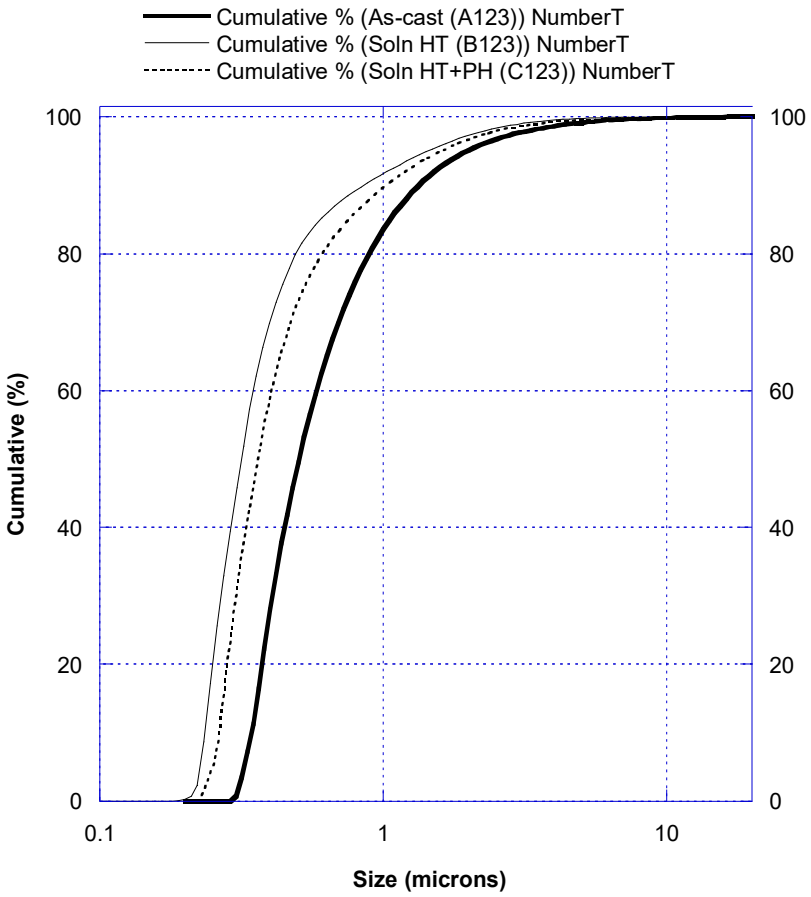

Figure 4-71 Number based cumulative particle size distribution for As-cast A205, Solution Heat Treated A205, and Solution Heat Treated + Precipitation Hardened A205

Figure 4-71 shows the number based cumulative particle size distribution for the as-cast, solution heat treated and solution heat treated and precipitation hardened materials. The distribution revealed the solution heat treated material to have the smallest particle size distribution, followed by the solution heat treated and precipitation hardened material. The as-cast material had the largest particle size distribution. The d(0.5) values for these

distributions were: 0.52, 0.33 and 0.37μm for the as-cast, solution heat treated and solution heat treated and precipitation hardened material respectfully.

Table 4.3.6 3 particle size traits for the as-cast A205, solution heat treated A205, and solution heat treated and precipitation hardened A205

Sample	d (0.1)	d (0.5)	d (0.9)
As-cast (A123) Vol	3.34	11.42	26.54
Soln HT (B123) Vol	2.00	6.03	19.55
Soln HT + PH (C123) Vol	2.30	8.34	22.55
As-cast (A123) Num	0.36	0.52	1.38
Soln HT (B123) Num	0.25	0.33	0.90
Soln HT + PH (C123) Num	0.27	0.37	1.06

Table 4.3.6 shows the d(0.1), d(0.5) and d(0.9) values for the as-cast, solution heat treated, and solution heat treated and precipitation hardened A205 alloy. Both the number and volume particle size distributions had the same trend, i.e. the solution heat treated material had the smallest particle size distribution and the as-cast material the largest.

4.3.4 Comparison of TiBAl and A205 TiB_2 Particle Size Distributions

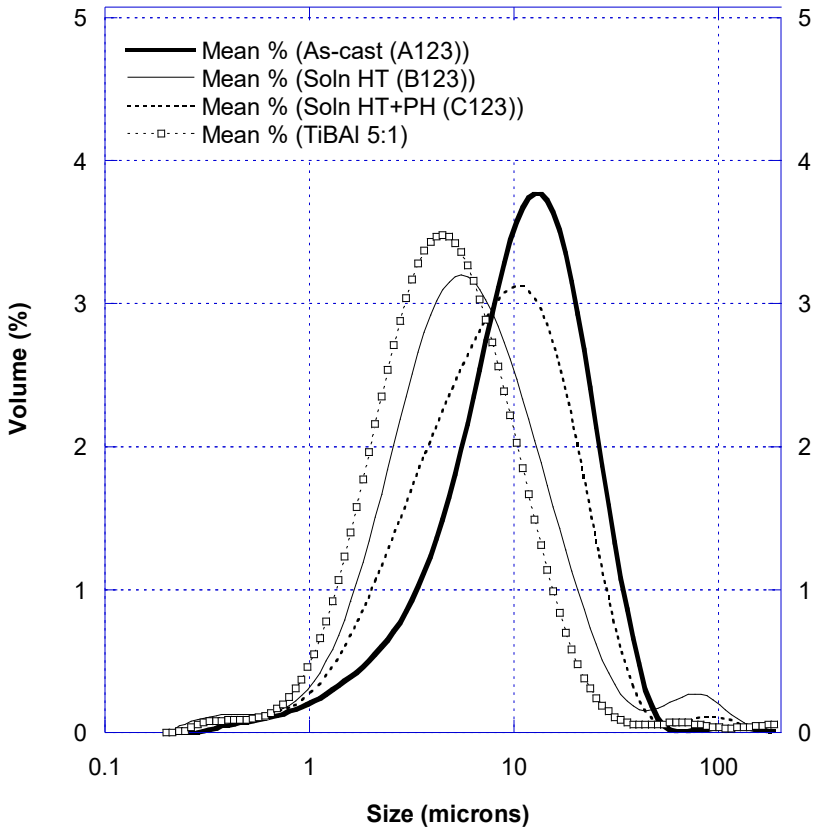

Figure 4-72 Volume based particle size distribution comparing TiBAl (5:1) to; as-cast A205, solution heat treated A205, and solution heat treated and precipitation hardened A205

Figure 4-72 shows the volume based particle size distribution comparing TiBAl 5:1 to; the as-cast, solution heat treated, and solution heat treated and precipitation hardened A205 alloy. The distribution shows that the TiBAl alloy had the smallest TiB_2 particle size distribution with a peak located at 4.5µm. The next largest particle size distribution was solution heat treated A205 with a peak location at 5.5µm. The following particle size distribution was then solution heat treated and precipitation hardened A205 with a peak location at 10µm. The largest particle size distribution was as-cast material with a peak located at approximately 15µm. Comparatively the TiBAl peak had a much steeper leading edge than when compared to the leading edge of the As-cast material -which by

comparison started shallower. The TiB_2 particle size distribution which was most similar to the 5:1 TiBAl's distribution was the solution heat treated A205 alloy.

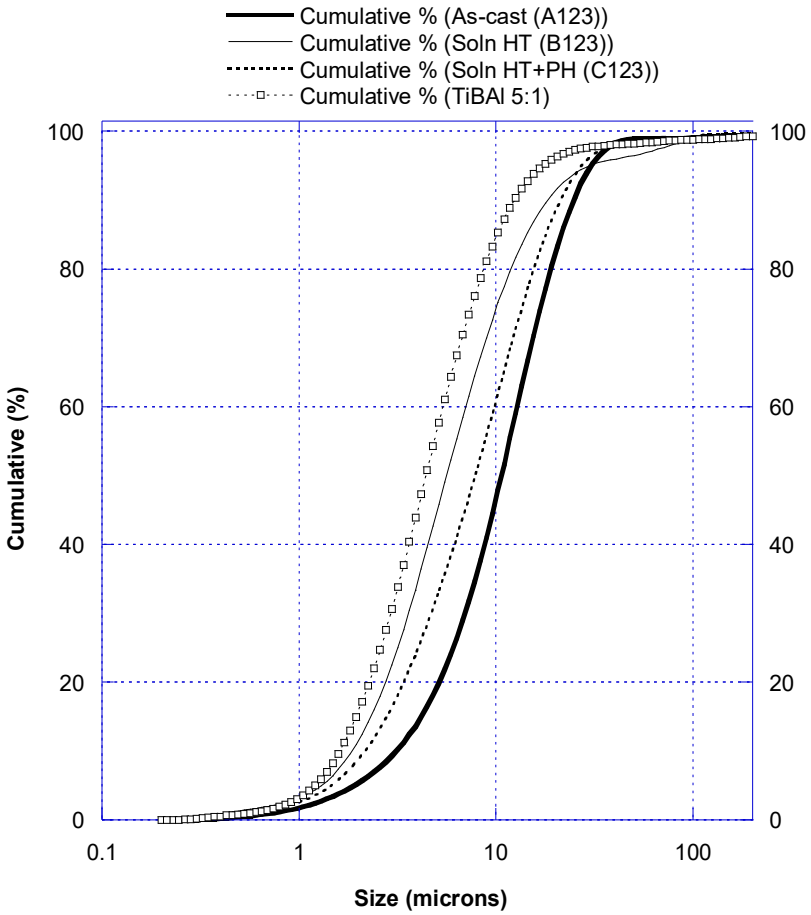

Figure 4-73 Cumulative percentage of each of the volume based particle size distributions comparing TiBAl (5:1) to; as-cast A205, solution heat treated A205, and solution heat treated and precipitation hardened A205.

Figure 4-73 shows the cumulative percentage of each of the volume based TiB_2 particle size distributions comparing TiBAl 5:1 to; the as-cast, solution heat treated, and solution heat treated and precipitation hardened A205 alloys. The distribution confirms that the smallest TiB2 particle size distribution was from the TiBAl 5:1 alloy, increasing to solution heat treated A205 alloy, followed by solution heat treated and precipitation hardened material, with as-cast A205 having the largest TiB_2 particle size distribution.

The d(0.5) values for each of these distributions were; 4.72, 6.03, 8.34 and 11.42µm respectively.

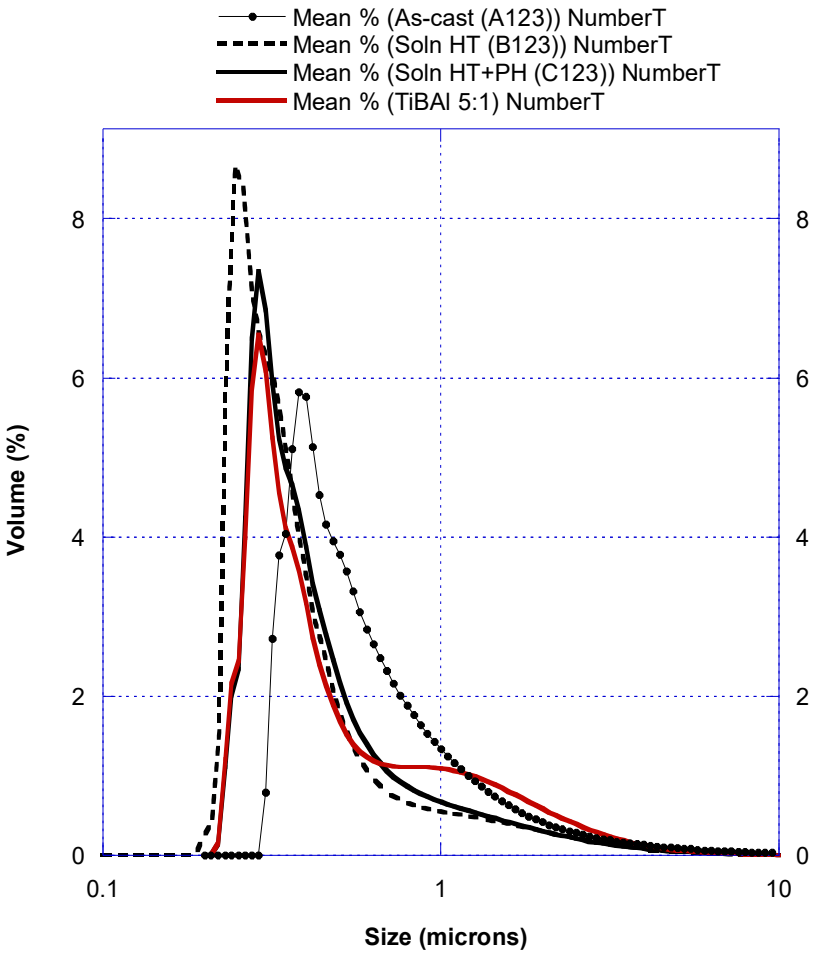

Figure 4-74 Number based particle size distribution comparing TiBAl (5:1) to; as-cast A205, solution heat treated A205, and solution heat treated and precipitation hardened A205.

Figure 4-74 shows the number based TiB_2 particle size distribution of TiBAl 5:1 and its comparison to; as-cast A205, solution heat treated A205, and solution heat treated and precipitation hardened A205. The smallest particle size distribution was measured from the solution heat treated A205, the largest particle size distribution was as-cast A205. The TiBAl grain refiner followed a similar particle size distribution to the solution heat treated

and precipitation hardened material until approximately 0.6µm at which point the TiBAl material had an increase in ≈1µm sized particles -ultimately leading to the sample having a greater number of particles above 1.5µm than when compared the as-cast A205 alloy.

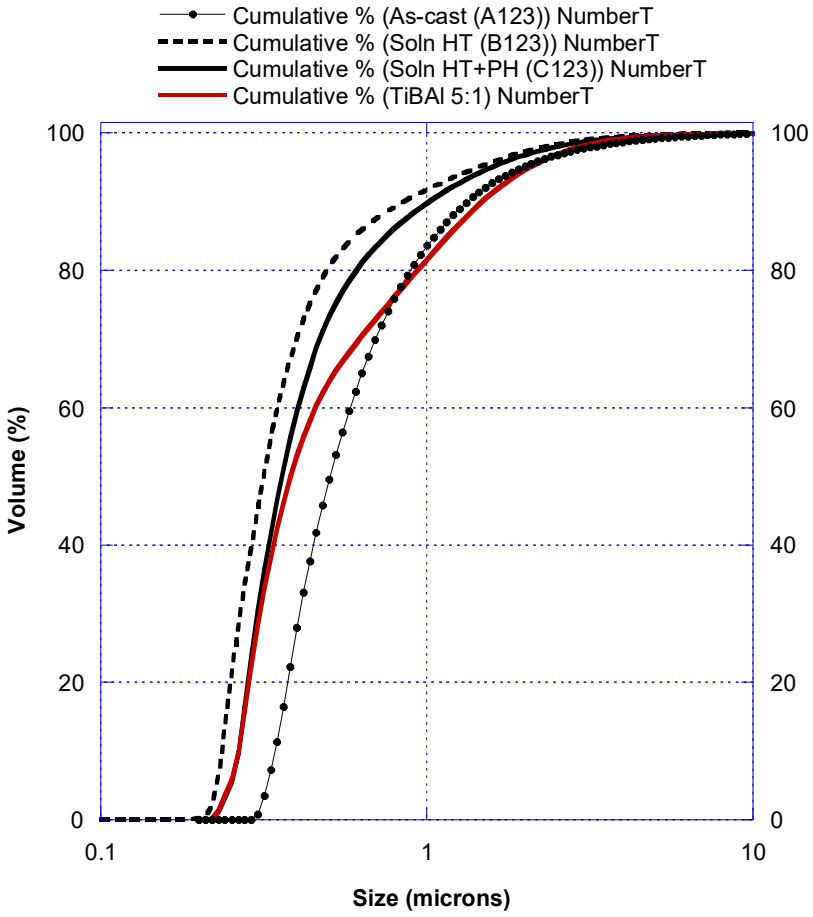

Figure 4-75 Cumulative percentage of each of the number based particle size distributions comparing TiBAl (5:1) to; as-cast A205, solution heat treated A205, and solution heat treated and precipitation hardened A205.

Figure 4-75 shows the cumulative percentage of each of the number based TiB_2 particle size distributions comparing TiBAl 5:1 to; the as-cast, solution heat treated, and solution heat treated and precipitation hardened A205 alloys. The distribution shows that the smallest TiB_2 particle size distribution was from the solution heat treated A205 alloy followed by the solution heat treated and precipitation hardened A205 alloy. The TiBAl

5:1 material approximately followed the same cumulative distribution profile as the solution heat treated and precipitation hardened A205 alloys from 0 to 40% at which point the TiBAl material then altered its distribution profile and surpassed the as-cast A205 alloys cumulative distribution profile by 75%.

Table 4.3.7 3 Particle size traits for the TiBAl 5:1 material, the as-cast A205 alloy, the solution heat treated A205 alloy, and the solution heat treated and precipitation hardened A205 alloy

Sample	d (0.1)	d (0.5)	d (0.9)
E123 (TiBAl 5:1) Vol	1.73	4.72	13.31
As-cast (A123) Vol	3.34	11.42	26.54
Soln HT (B123) Vol	2.00	6.03	19.55
Soln HT + PH (C123) Vol	2.30	8.34	22.55
E123 (TiBAl 5:1) NumT	0.27	0.40	1.53
As-cast (A123) NumT	0.36	0.52	1.38
Soln HT (B123) NumT	0.25	0.33	0.90
Soln HT + PH (C123) NumT	0.27	0.37	1.06

Table 4.3.7 shows the d(0.1), d(0.5) and d(0.9) volume and number transformed TiB_2 particle size values for; TiBAl 5:1, as-cast A205 alloy, solution heat treated A205 alloy, and solution heat treated and precipitation hardened A205 alloy. The table shows that for the volume based TiB_2 particle size distribution the smallest particle size distribution was consistently the TiBAl material throughout the d(0.1), d(0.5) and d(0.9) values. The order, in increasing TiB_2 particle size, was then; the solution heat treated material, the solution heat-treated and precipitation hardened material followed by the as-cast material. For the number based TiB_2 particle size distributions the d(0.1) value, with increasing TiB_2 size, followed; the solution heat treated material, jointly the TiBAl 5:1 and solution heat treated and precipitation hardened A205 alloy, followed by the as-cast material. For the d(0.5) value, in increasing size, followed; the solution heat-treated material, the solution heat treated and precipitation hardened A205 alloy, the TiBAl 5:1 material, then

the as-cast material. For the d(0.9) value, in increasing particle size, the order followed; the solution heat treated material, the solution heat treated and precipitation hardened material, the as-cast material, followed by the TiBAl 5:1 material. The solution heat treated material consistently held the smallest particle distribution across the d(0.1), d(0.5) and d(0.9) values.

The Al-5Ti-1B and A205 alloys should have almost identical TiB_2 particle size distributions based on their similar production methods. As particle size analysis of the experimentally collected materials were found to vary with heat treatment, it can de deduced that a second material -linked with heat treatment (i.e. copper), was coating the inert TiB_2 particles hence altering their perceived particle size distribution. In effort to remove the copper contaminates from the collected TiB_2 particle size distributions, an electrochemical approach was explored.

4.4 Electrochemistry Introduction

The high strength of A205 is partially due to a reinforcing phase of titanium diboride (TiB_2) contained within the material. This reinforcing phase is introduced to the melt using a combination of salts added during production which form TiB_2 as a precipitate in the reaction [126]:

$3K_2TiF_6 + 22Al + 6KBF_4 \rightarrow 3Al_3Ti + 3AlB_2 + 9KAlF_4 + K_3AlF_6 + Heat$

And $3Al_3Ti + 3AlB_2 \rightarrow 12Al + 3TiB_2$

To accurately determine the strength contribution from the TiB_2 phase the particles were removed from the supporting aluminium alloy by dissolving the supporting aluminium matrix using 2 ML^{-1} hydrochloric acid (HCl) in the reaction;

$2Al + 6HCl \rightarrow 2AlCl_3 + 3H_2$

Following dissolution of the alloy in HCl, Powder X-Ray Diffraction (P-XRD) analysis revealed the remaining material to be a mixture of TiB_2, Cu -and its oxides, and Ag, (see Figure 4-63). Following this analysis an electrochemical approach was taken to remove the Cu from the material in question.

4.4.1 Viability of removing Cu via oxidation

Copper can be oxidised at or above several potential voltages, depending on the oxidation state required (shown below with reference to both a Standard Hydrogen Electrode (SHE) and a silver / silver chloride reference electrode (Ag/AgCl)):

$Cu \rightarrow Cu^{2+} + 2e^-$ at >0.337 V vs. SHE OR >0.140 V vs. Ag/AgCl

$Cu \rightarrow Cu^{+} + e^-$ at >0.520 V vs. SHE OR >0.323 V vs. Ag/AgCl

$Cu^{+} \rightarrow Cu^{2+} + e^-$ at >0.159 V vs. SHE OR >-0.038 V vs. Ag/AgCl

The oxidisation voltages for copper are less than other potential electrochemical reactions which occur in the sample:

$Ag(s) \rightarrow Ag^{+} + e-$ at >0.7996 V vs. SHE OR >0.603 V vs. g/AgCl

$2H_2O \rightarrow H_2O_2(aq) + 2H^{+} + 2e^-$ at >1.78 V vs. SHE OR >1.583 V vs. Ag/AgCl

$H_2(g) + 2OH^- \rightarrow 2H_2O + 2e^-$ at >-0.828 V vs. SHE OR >-1.025 V vs. Ag/AgCl

Hence it was possible to limit the voltage range used to oxidise Cu exclusively. By using a background electrolyte of KCl [0.1M] the copper ions bonded with the disassociated

Cl^- ions present around the electrode, forming $CuCl_2$ or CuCl, and consequently become removed from the TiB_2 particles.

4.4.2 TiB_2 compatibility

To ensure that the TiB_2 particles would not be electrochemically altered during processing, purchased TiB_2 underwent cyclic voltammetry (CV) over 3 different potential ranges to confirm TiB_2's electrochemical stability during experimentation.

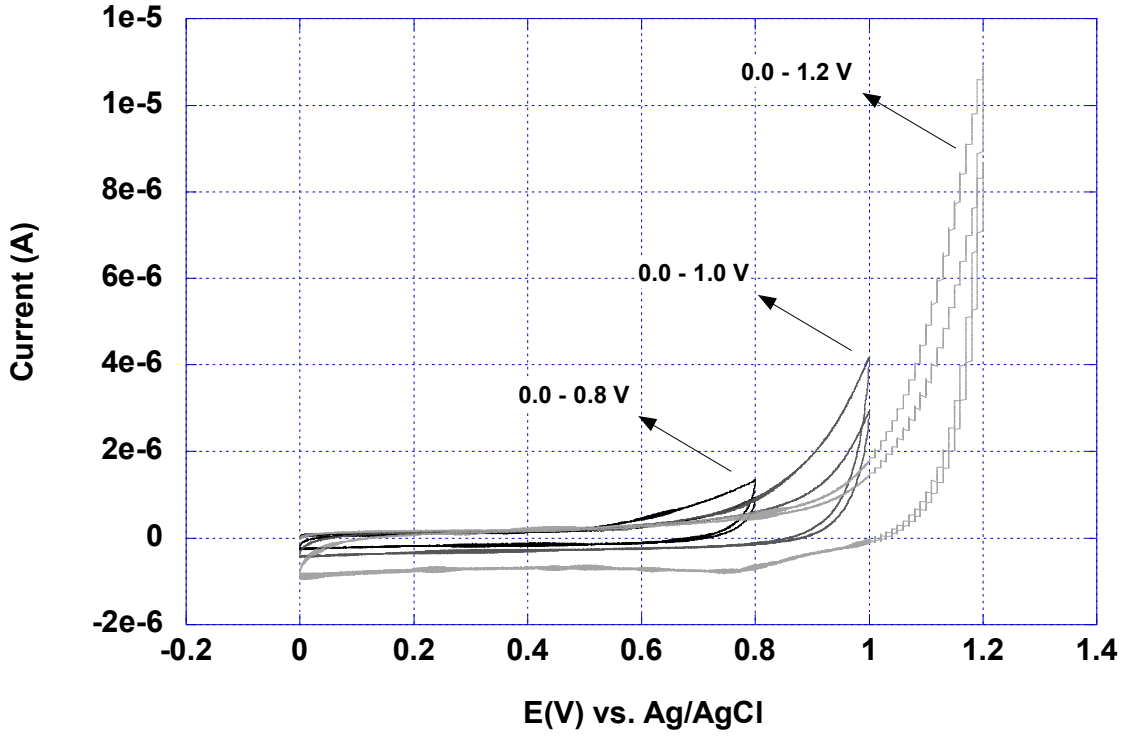

Figure 4-76 CV for 10µL of purchased TiB_2 using a GC electrode in 2mV steps at 50mV/s. Equilibration time of 15 seconds with 2 scans per cycle.

Figure 4-76 shows 3 Cyclic Voltammetry (CV) scan ranges, each with 2 repeats, over the voltage range expected to oxidise copper, (i.e., 0.140 V vs. Ag/AgCl). As can be seen, between 0 and +0.6V no peak occurred in the current profile which would have otherwise

indicated that electrochemical oxidation/reduction events were taking place. Hence TiB_2 was stable within this voltage range.

4.4.3 Material behaviour

4.4.3.1 Effect of sample volume on material oxidisation

To ensure the sample material, TiB_2 originating from solution heat-treated and precipitation hardened A205 following dissolution in HCl, was suitable for electrochemical processing a series of experiments were then undertaken to indicate the feasibility of the procedure. For the initial tests an Indium Tin Oxide (ITO) working electrode was used to compare the effect of various sample volumes on the scan profile.

Figure 4-77 shows how the data collected from scan 1 and scan 50 of a 50 CV scan cycle varied. The distribution contained large amounts of noise, and therefore the signal had to be processed before analysis -as described in the experimental procedure section of this thesis. The Cu signal was located at 0.14V and decreased from approximately 6.5µA to 1µA with increased scan number. If the process was reversible and the copper was not being removed from the particles a negative current (which would have been independent of scan rate) would have been seen at (0.14 - 0.059 =) 0.08 V. Similar scan profiles were obtained for 10 and 20µL sample volumes.

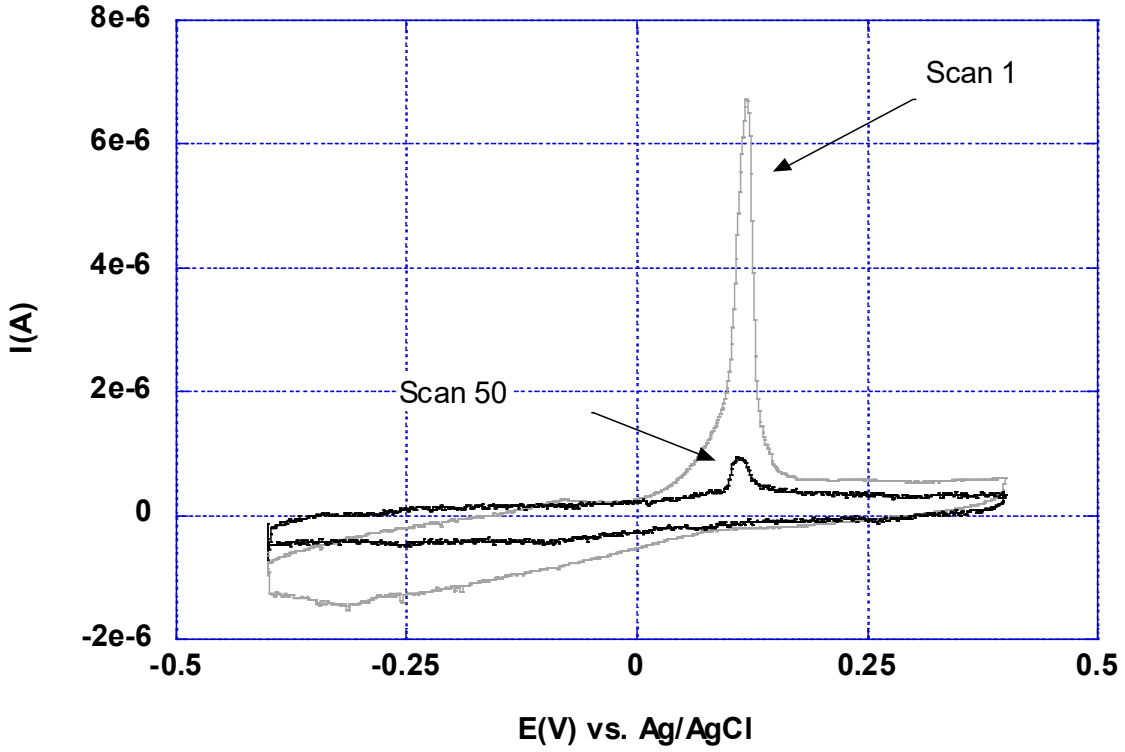

Figure 4-77 Cyclic Voltammetry from 5µL of sample C dried onto an ITO electrode, scanning from -0.4 --> 0.4V with respect to a Ag/AgCl reference electrode at 25mV/s using a 0.1M KCl carrier electrolyte. Y-axis = current. X-axis = potential. Showing scans 1 and 50 of a 50 scan cycle.

Figure 4-78 shows how the measured charge varied with scan number for 5, 10 and 20µL of sample dried onto an ITO electrode, respectively. The charge, (i.e., the area under each peak), in each case initially increased as equilibrium conditions at the electrode surface were met. For 20µL the charge decreased from 25µC, for 10µL the charge decreased from 15µC, and for 5µL the charge decreased from 8µC. For each sample volume the charge decreased to 1µC within 50 scans. The following decrease in charge transferred from each scan number showed that, for each sample volume, Cu was being removed from the surface of the electrode.

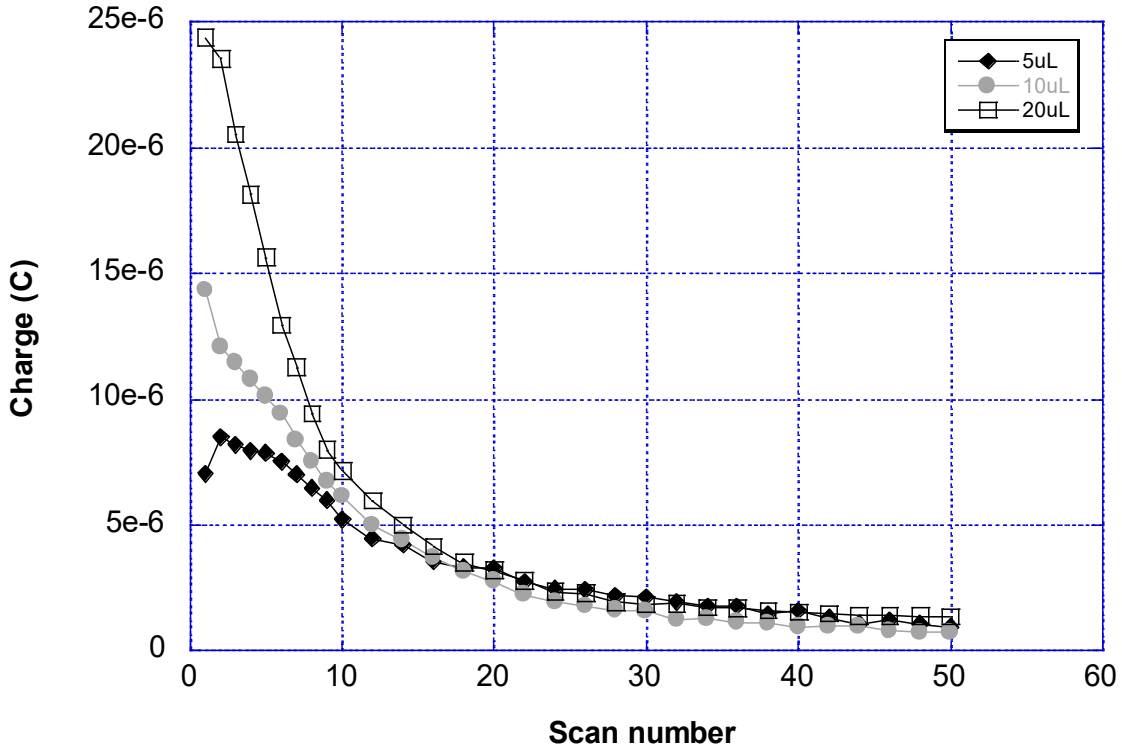

Figure 4-78 Comparison of how the peak copper signal decreases with scan number for the three different sample volumes (5µL, 10µL and 20µL). Y-axis = current, X-axis = scan number

4.4.3.1.1 Optical examination

Figure 4-79 and Figure 4-80 show visually the sample was unchanged after the electrochemical processing -which indicated that the decrease in signal strength was due to copper oxidation as opposed to the sample becoming detached from the electrode surface.

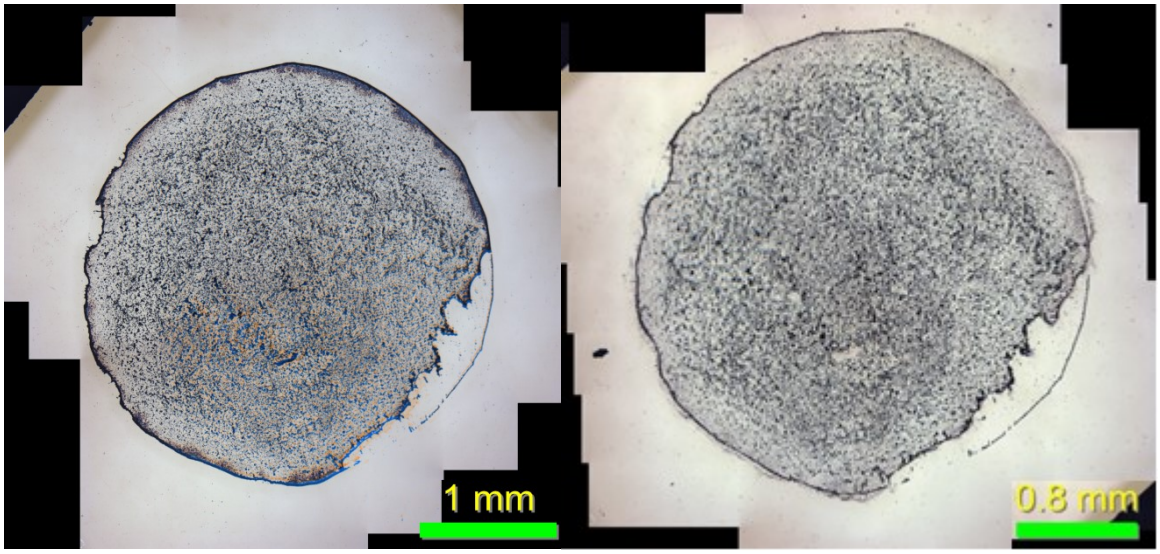

Figure 4-79 Optical examination of 5µL ITO sample pre(left) and post(right) electrochemistry

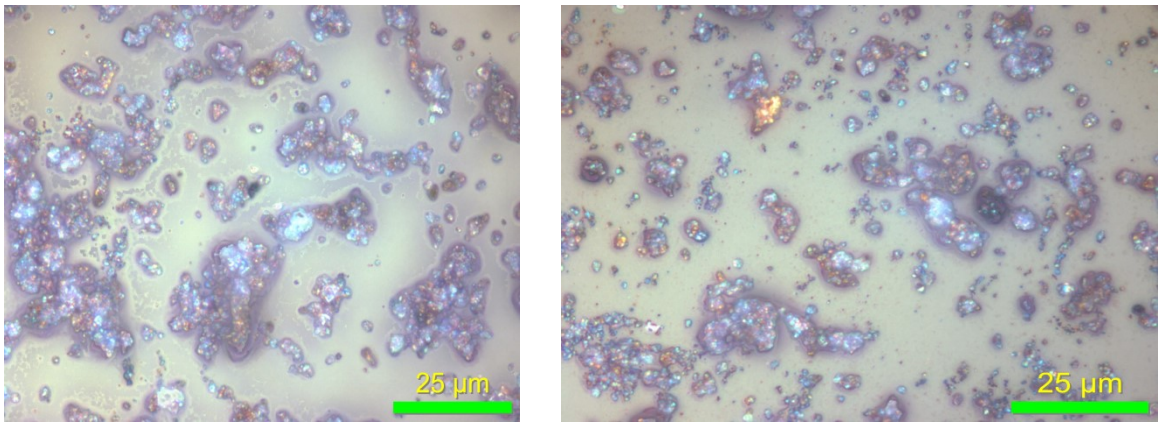

Figure 4-80 Magnified optical examination of 5µL ITO sample pre(left) and post(right) electrochemistry

4.4.3.1.2 SEM examination

Figure 4-81 shows an SEM image of a pre-electrochemistry (a) and post-electrochemistry (b) particle located on the surface of the 10µL ITO sample. Each image shows the location of the EDX spot.

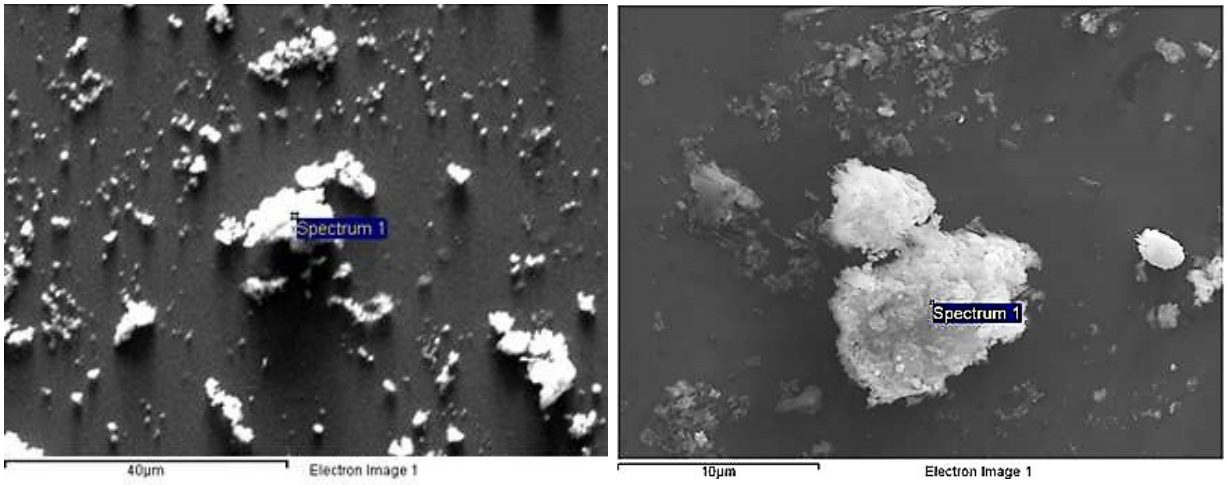

(a) (b)

Figure 4-81 SEM examination of 10µL ITO electrode sample pre-electrochemistry (a) and post-electrochemistry (b)

Figure 4-82 shows the EDX analysis results for the respective particles. Both EDX spectra reported; In, Ti and O, due to the ITO (indium tin oxide) electrode type used, as well as Si and Na from the composition. Mg, Al and Ag were also detected due to the elemental composition of the alloy dissolved.

Element	Weight%	Atomic%
B	0.49 +/- 0.36	1.62
C	2.45 +/- 0.17	7.33
O	17.41 +/- 0.45	39.09
Mg	0.42 +/- 0.06	0.62
Al	0.80 +/- 0.05	1.06
Si	5.11 +/- 0.09	6.54
Ti	38.57 +/- 0.32	28.93
Cu	14.93 +/- 0.23	8.44
Ag	8.87 +/- 0.18	2.96
In	9.04 +/- 0.18	2.83
Sn	1.91 +/- 0.17	0.58
Totals	100.00	100.00

Element	Weight%	Atomic%
C	2.80 +/- 2.16	7.14
O	24.42 +/- 0.81	46.79
Mg	0.98 +/- 0.07	1.23
Al	0.53 +/- 0.06	0.61
Si	14.52 +/- 0.37	15.85
Cl	0.52 +/- 0.06	0.45
K	3.00 +/- 0.16	2.35
Ti	26.28 +/- 0.65	16.82
Cu	7.38 +/- 0.26	3.56
Ag	0.57 +/- 0.13	0.16
In	13.10 +/- 0.41	3.50
Sn	5.91 +/- 0.30	1.53
Totals	100.00	100.00

Figure 4-82 EDX analysis results for the 10µL ITO electrode sample pre-electrochemistry (left) and post-electrochemistry (right)

The EDX spectrum shown in Figure 4-82 also indicated high Ti and Cu levels. (Both analysis reports contained inaccurate values for B content due to its low intensity and low energy K_α peaks). Visual examination of the SEM image revealed the particle to still be coated in another substance –most likely Cu or Ti from its large detected weight percentage.

4.4.3.2 Comparison of ITO sample volumes

A comparison between the ITO electrode Cu oxidation peak indicated whether the experiment was scalable with volume, or, whether the process was limited by other factors. As can be seen in Figure 4-83, the total charge transferred during the second cyclic voltammetry scan, i.e., the area under the CV curve, increased with the volume of sample analysed. The second scan cycles were chosen for comparative area analysis as the first cycle scan in each of the 5µL, 10µL and 20µL sample volumes were unsuitable for comparison, either due to noise or due to possible surface equilibration effects (as previously mentioned). The 20µL scan increased in current from 6µC at a potential of 0.102V (vs. Ag/AgCl) to 21µA at a potential of 0.126V, before sharply decreasing back to 6µC by 0.138V. The 10µL scan increased in current from 6µC at a potential of 0.126V (vs. Ag/AgCl) to 18µA at a potential of 0.138V, before sharply decreasing back to 6µC by 0.144V. The 5µL scan increased in current from 6µC at a potential of 0.118V (vs. Ag/AgCl) to 12µA at a potential of 0.125V, before sharply decreasing back to 6µC by 0.13V.

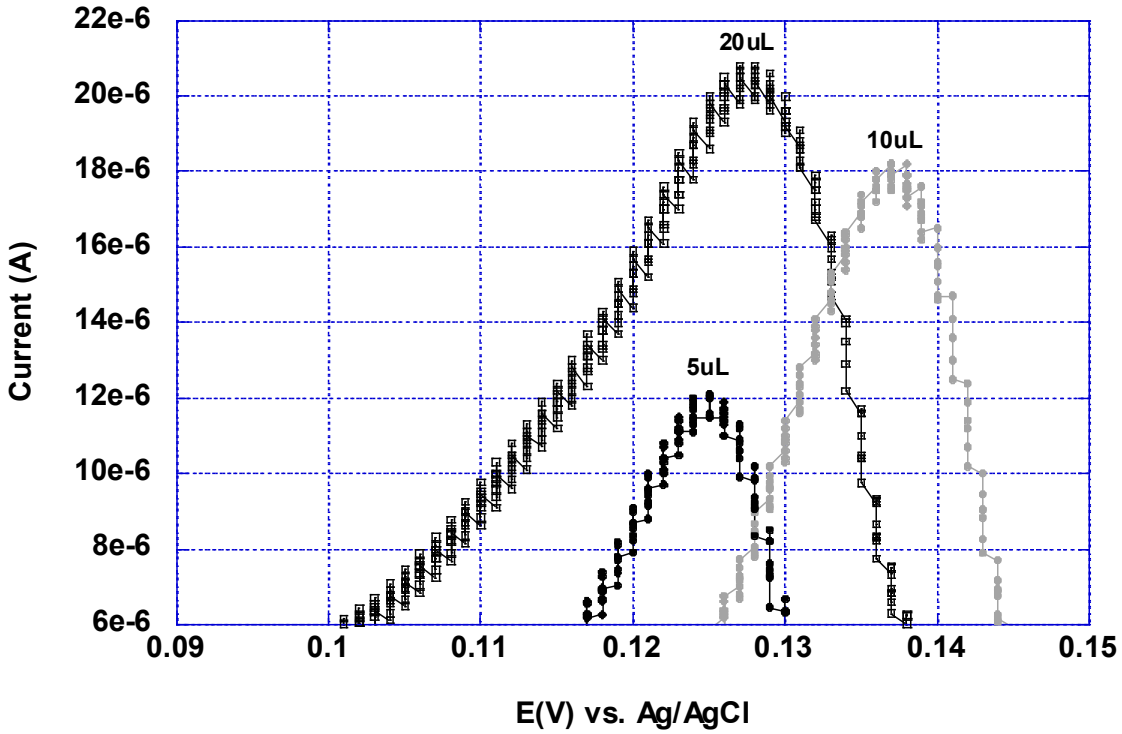

Figure 4-83 Comparison of the oxidation signal from the copper peak for the three different sample volumes (5µL, 10µL and 20µL) using the ITO electrode. Y-axis = current, X-axis = scan number.

Figure 4-83 shows how the maximum current signal from the oxidisation of Cu, for the 3 different volumes of sample on the ITO electrode surface, decreased with scan number. It was shown that, despite the difference in sample volumes, the signals decayed in a similar manner, which suggested that sample volumes of up to 20µL stayed attached to the electrode surface for the duration of the experiment.

Figure 4-84 shows how the total charge transferred during each experiment varied with sample volume. Calculating the area under each curve gives the value of the number of electrons transferred for each volume. In the instance of $Cu \rightarrow Cu^{2+} + 2e^-$, the number of Cu atoms oxidised was half this number. Extrapolating the results allowed for an estimation of the amount of sample dissolved in the initial volume of acid.

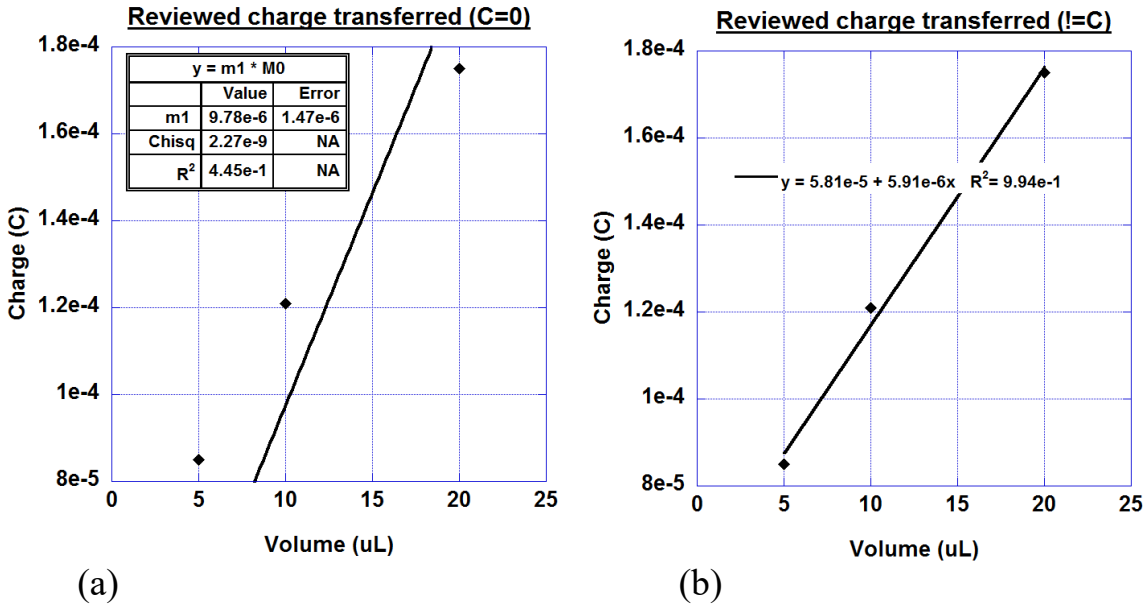

Figure 4-84 Total charge transferred for the 5, 10 and 20uL samples using an ITO electrode with a 25mV/s scan rate in 0.1M KCl. (a)'s data set's trend line goes through the origin whereas (b)'s data set has a non-zero Y intercept.

As a comparison between extrapolation results, the trend line for the collected results was forced through the origin in Figure 4-84 (a) and had a non-zero Y intercept in (b). The results for the non-zero (Figure 4-84 (a)) Y intercept had a R^2 value closer to 1 than when compared to the intercept equal to origin data set (Figure 4-84 (b)).

4.4.3.3 Electrode comparison on material oxidisation

The energy required for an electron transfer process to occur is compound specific. Therefore, the process can be adjusted by the nature of the electrode surface and also the structure of the interfacial region over which the electron transfer occurs. For this reason, different electrode types were tested for the most efficient oxidation of the sample material. The electrode types tested were; Edge-Plane Pyrolytic Graphite (EPPG), Indium Tin Oxide (ITO), Basal Plane Pyrolytic Graphite (BPPG) and Glassy Carbon

(GC). To ensure that comparable signals were detected the volume of sample tested (5µL) and scan parameters used (-0.4 --> 0.4V with respect to a Ag/AgCl reference electrode at 25mV/s) were kept constant throughout the comparison tests. The charge decay profile for each of these electrode types is shown in Figure 4-85. The figure shows the EPPG electrode transferred the most charge with each scan, followed by the ITO electrode. The BPPG and GC electrodes transferred comparable amounts of charge.

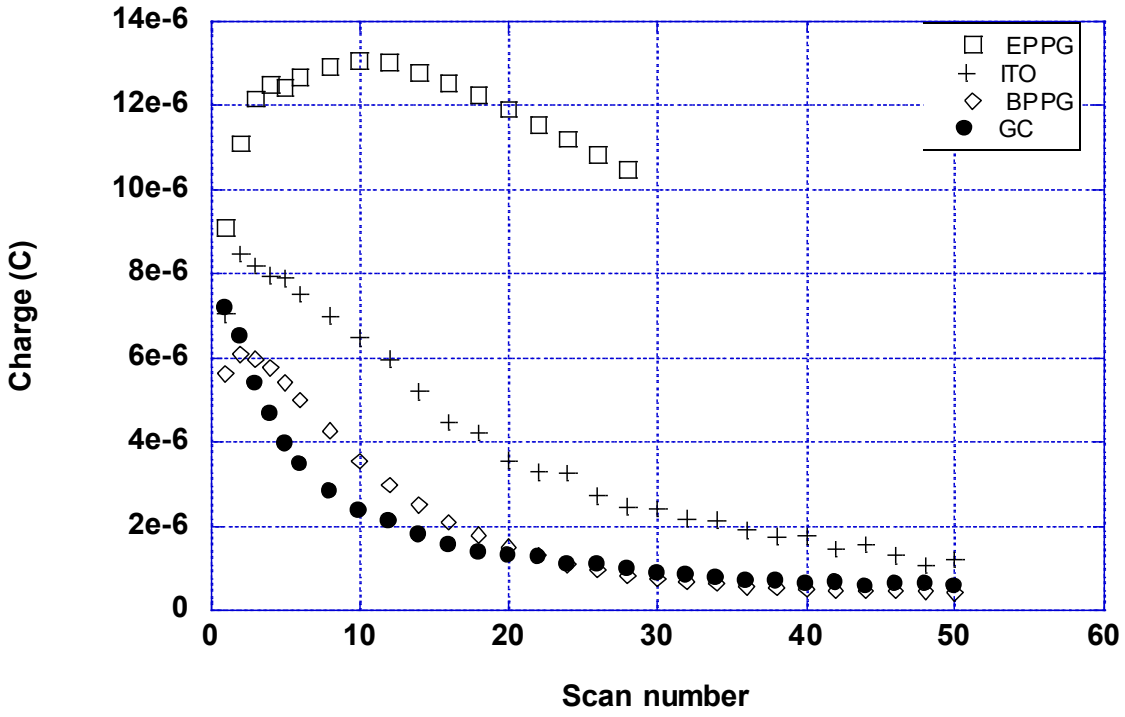

Figure 4-85 Charge vs. Scan number for EPPG, ITO, BPPG and GC electrodes revealing how the peak current detected decreased with scan number.

4.4.4 Review of electrode types used

Of the 4 electrode types tested, all scans show how the charge transferred during each scan decreased with scan number, illustrating a clear reduction in the Cu content of the sample. The EPPG electrode measured the highest peak current value at 13µC (reached at scan 10) and therefore was the most efficient electrode type to use for this experiment.

The second most efficient electrode type was ITO which reached a peak current of 8.5µA by scan 2. The next most efficient electrode type was GC which reached a peak current of 7µC at scan 1. BPPG had the lowest detected peak current at 6µC by scan 2. Despite this the electrode material taken forward for subsequent experimentation was chosen to be the Glassy Carbon (GC) electrodes. This was due to cost and their relative availability. The other electrode types were not chosen due to cost restrictions in sourcing the number of electrodes required for a time efficient series of experiments.

4.4.5 Re-evaluation of sample material

As indicated by the optical and SEM images a more quantitative measurement of Cu and Ti content in the samples was needed for a true comparative analysis. An X-Ray Fluorescence (XRF) technique was chosen which required pH neutral liquid samples. For this reason, the samples' pH values were raised from 0.5 to 7.

4.4.6 Neutralisation using serial dilution with deionised water (sample X)

As can be seen in Figure 4-86 the neutralisation of the sample material, i.e. TiB_2 originating from solution heat-treated and precipitation hardened A205 following dissolution in HCl, using a serial dilution approach caused a significant change in the profile of the results. There was still a peak present at the location where Cu was predicted to be, (i.e., 0.14V), however larger peaks were present on either side of this, effectively overpowering the signal. Experimentation continued with this material for three reasons. Firstly, it allowed the material to be neutralised, secondly, the material physically remained attached to the electrode throughout the analysis and, thirdly despite the complexity of the materials profile i.e. an additional decay peak was present in the profile of the results, however, the measured current did eventually decrease to near zero values.

To accurately determine the quantity of Cu removed from the neutralised material a series of 3 sample volumes were analysed; 5, 10 and 20µL, 5 and 10µL were repeated 3 times, the 20µL samples was repeated twice. The first repeat of the 5µL experiment is shown in Figure 4-86.

4.4.6.1 Sample X Glassy Carbon electrode 5µL (repeat 1 of 3)

Figure 4-86 (a) shows the analysis for 5µL of a sample undergoing electrochemical processing (repeat 1 of 3). Since the original Cu signal was on the shoulder of a larger peak, a second peak had to be used to analyse the signals decay with time. The peak chosen was the first positive current peak (highlighted) and shown in Figure 4-86 (b). Figure 4-86 (b) also shows that a peak drifting effect was present during the experiment. The peak shown in the figure drifted to lower potential with increasing cycle number. Scan 2 had a current of 75µA at a potential of 0.06V, which then 'shifted' to the lower potential of 0.03V by scan 6 with a current of 48µA. By scan 10 the peak had shifted to 0.02V with a measured current of 18µA. One possible cause of this effect is may have been the presence of Cl- ions which altered the local potential surrounding the electrode.

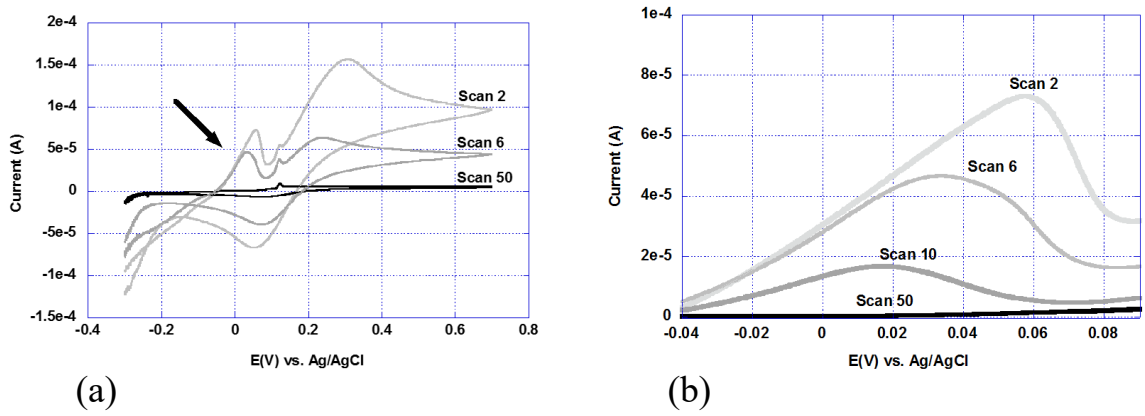

Figure 4-86 (a) Cyclic Voltammetry of 5µL sample (post-neutralised with deionised water) dried onto a GC electrode scanning from -0.3V --> 0.7V with respect to a Ag/AgCl reference

electrode at 100mV/s. Y-axis = current, X-axis = potential. Showing scans 2, 6 and 50 of a 50 scan CV cycle. (b) Magnified section of plot.

Figure 4-87 shows the charge transferred from the scan series as shown in Figure 4-86. The distribution revealed how the charge decayed, and also how well the trend line fitted the data series, (given by the R^2 value). Scans 1 and 2 were omitted due to the maximum peak current not having been reached at these scan numbers. Scan 3 had a peak charge of 55µA. Scan 16 had a peak charge of 3µA. Scans >16 have been omitted due to the change in transferred charge having reached approximately zero.

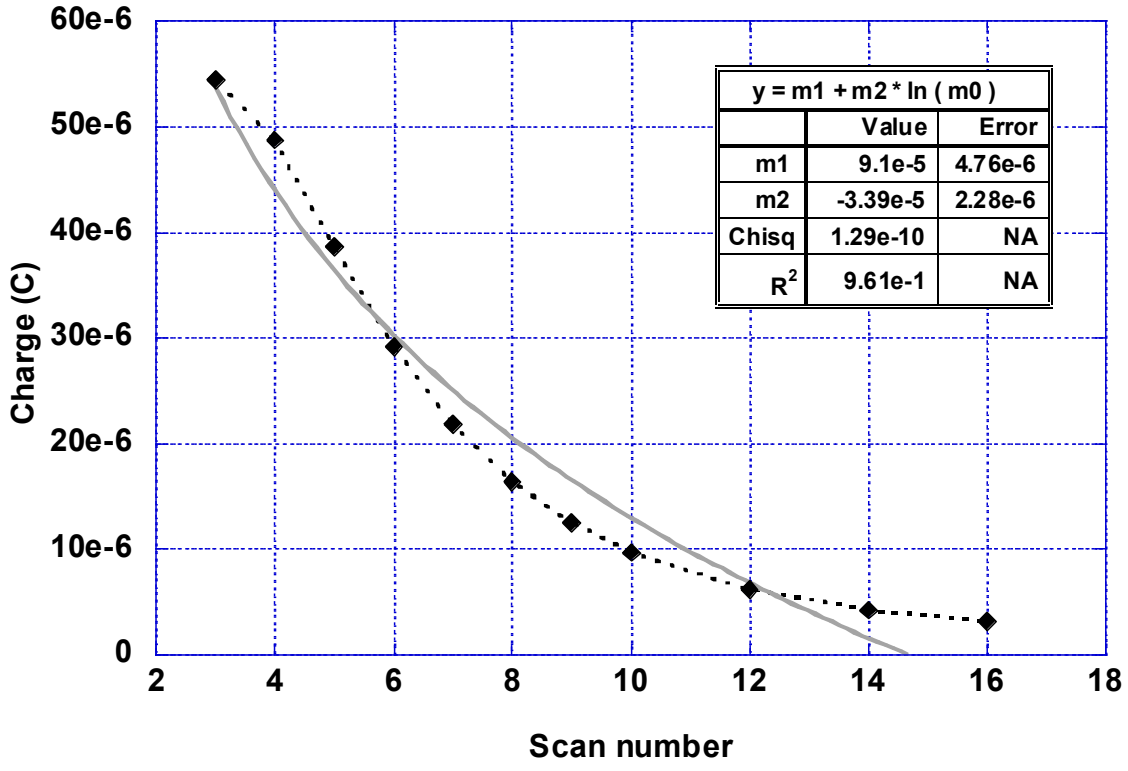

Figure 4-87 Charge vs. scan number for GC electrode excluding 2 scans present before the peak current was achieved (omitting scans > 16): logarithmic line showing best fit

4.4.6.2 Summary of sample X's transferred charge values when using GC electrode

An overview of the serially diluted electrochemical processes is shown in Table 4.4.1. Each section shows the (theoretical) percentage of Cu removed from each repeat of each sample volume. The sections show the difference between using the full scan range and the reviewed scan range. The tables also take into consideration whether the peak being analysed was a Cu -> $Cu^{2+} + 2e^-$ or a Cu -> $Cu^+ + e^-$ reaction by the ratio of electrons required for each process. As shown, only a small percentage of the predicted available Cu was removed from the system in each instance.

Table 4.4.1 Percentage of Cu removed from pH7 sample materials calculated using 2 copper oxidisation formulas and 2 ranges of measured data (full or reviewed)

e^- to Cu ratio = 1:1			
Sample volume (µL)	**5**	**10**	**20**
Full Scan Repeat **1 %**	1.92	3.22	5.63
Full Scan Repeat **2 %**	5.53	6.30	8.21
Full Scan Repeat **3 %**	2.04	4.54	N/A
Average %	**3.16**	**4.69**	**6.92**

e^- to Cu ratio = 1:1			
Sample volume (µL)	**5**	**10**	**20**
Reviewed Repeat **1 %**	1.50	2.39	2.75
Reviewed Repeat **2 %**	2.54	3.75	5.38
Reviewed Repeat **3 %**	1.35	3.33	N/A
Average %	**1.80**	**3.16**	**4.07**

e^- to Cu ratio = 2:1			
Sample volume (µL)	**5**	**10**	**20**
Full Scan Repeat **1 %**	0.96	1.61	2.82
Full Scan Repeat **2 %**	2.76	3.15	4.11
Full Scan Repeat **3 %**	1.02	2.27	N/A
Average %	**1.58**	**2.76**	**1.02**

Continued overleaf

Continued

e^- to Cu ratio = 2:1			
Sample volume (µL)	**5**	**10**	**20**
Reviewed Repeat **1 %**	0.75	1.20	2.82
Reviewed Repeat **2 %**	1.27	1.87	4.11
Reviewed Repeat **3 %**	0.67	1.67	N/A
Average %	**0.90**	**1.58**	**3.47**

4.4.6.3 Average of sample X's transferred charge values when using GC electrode

The calculation of how much charge was transferred during the electrochemical processing gave a numerical indication of how much copper was removed from the system (see above). From these values it was possible to calculate a theoretical estimate of the amount of Cu which would have been removed from the full dissolved sample. This estimation was based on the selection of data analysed (full scan or reviewed) and

the trend line used (intercept dependent), therefore it was necessary to consider all 4 data scenarios; the full charge transferred during the electrochemical processing with and without the trend line going through y=0, and the reviewed charge transferred during the electrochemical processing with and without the trend line going through y=0; as shown in Figure 4-88.

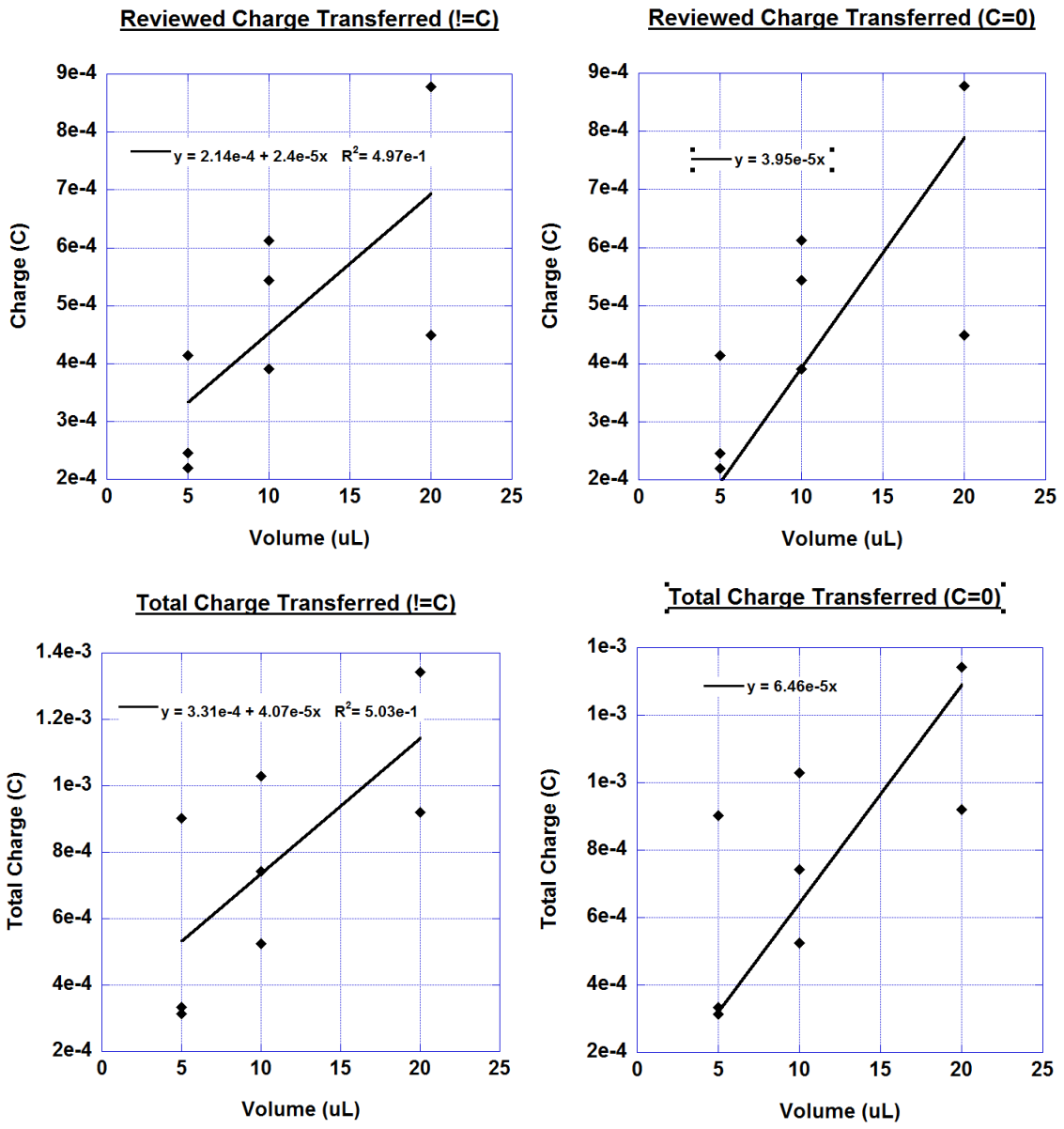

Figure 4-88 Full and reviewed charge transferred from 5, 10 and 20µL of pH7 sample material with zero and non-zero Y intercepts

Table 4.4.2 shows the percentage of Cu which would have theoretically been removed from the full volume of sample material, predicted by the straight line formulae shown in Figure 4-88.

Table 4.4.2 Predicted theoretical percentage of Cu removed from the full dissolved samples

Graph type	**Full scan range**	**Revised scan range**
Y=0	5.7 %	3.5 %
Y≠0	3.6 %	2.1 %

As can be seen in Table 4.4.2 the amount of Cu removed from this process was minimal with the highest estimate being 5.7%. In order to increase the experimental estimates further experiments were conducted.

4.4.6.4 Re-acidification of sample X using H_2SO_4

As the pH7 samples contained a series of additional peaks within the CV scan cycle, the carrier electrolyte was changed from 0.1M KCl to 0.1M H_2SO_4, which had the effect of suppressing the higher potential peaks present in the previous scans. Using this electrolyte, the Cu^{2+} ions formed at the electrode surface bonded with the dissociated SO_4^{2-} ions to produce $CuSO_4$ which could then be lost to the system.

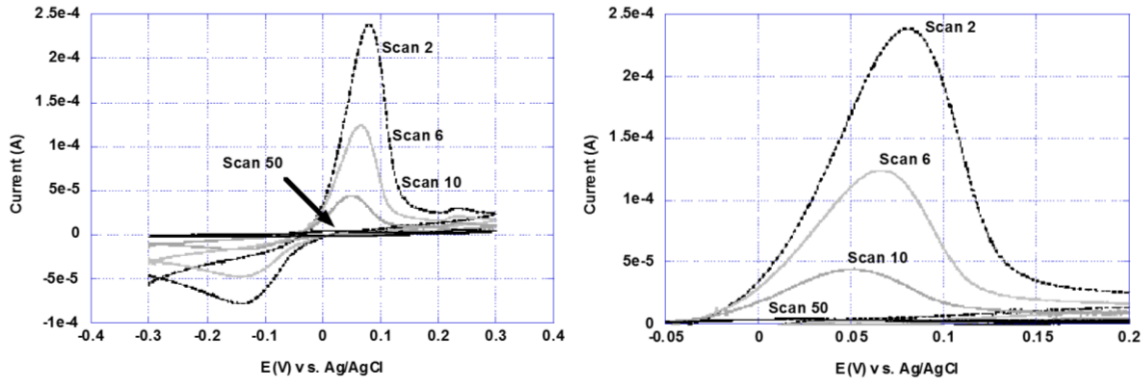

(a) (b)

Figure 4-89 (a) Cyclic Voltammetry of 5µL sample (post-neutralised with deionised water) dried onto a GC electrode scanning from -0.3V --> 0.3V with respect to a Ag/AgCl reference electrode at 100mV/s in a 0.1M H_2SO_4, carrier electrolyte. Y-axis = current, X-axis = potential. Showing scans 2, 6 and 50 of a 50 scan CV cycle. (b) Magnified section of plot.

Figure 4-89 (a) shows the CV scan profile of 5µL of sample dried onto a GC electrode while using 0.1M H_2SO_4 as a carrier electrolyte. The scan showed there was a peak present in the positive quadrant of the graph, however there was also a slight negative current signal which occurred on the return signal (at approximately -0.15V). The negative current signal was indicative of the sample being re-deposited back onto the electrode surface. As the negative current peak magnitude was lower than the positive peaks current magnitude, the net movement of sample was into the solution as opposed to re-plating the electrode.

Figure 4-89 (b) shows a larger view of Figure 4-89 (a). The peaks showed how the sample was being oxidised/removed from the system. Peak drift was also a feature of this graph. Scan 2 peak location was at 0.08V (vs. Ag/AgCl) and had an associated current of 240µA.

Scan 6 peak was located at .065V with an associated current of 120µA. Scan 10 peak was located at 0.05V with an associated current of 40µA.

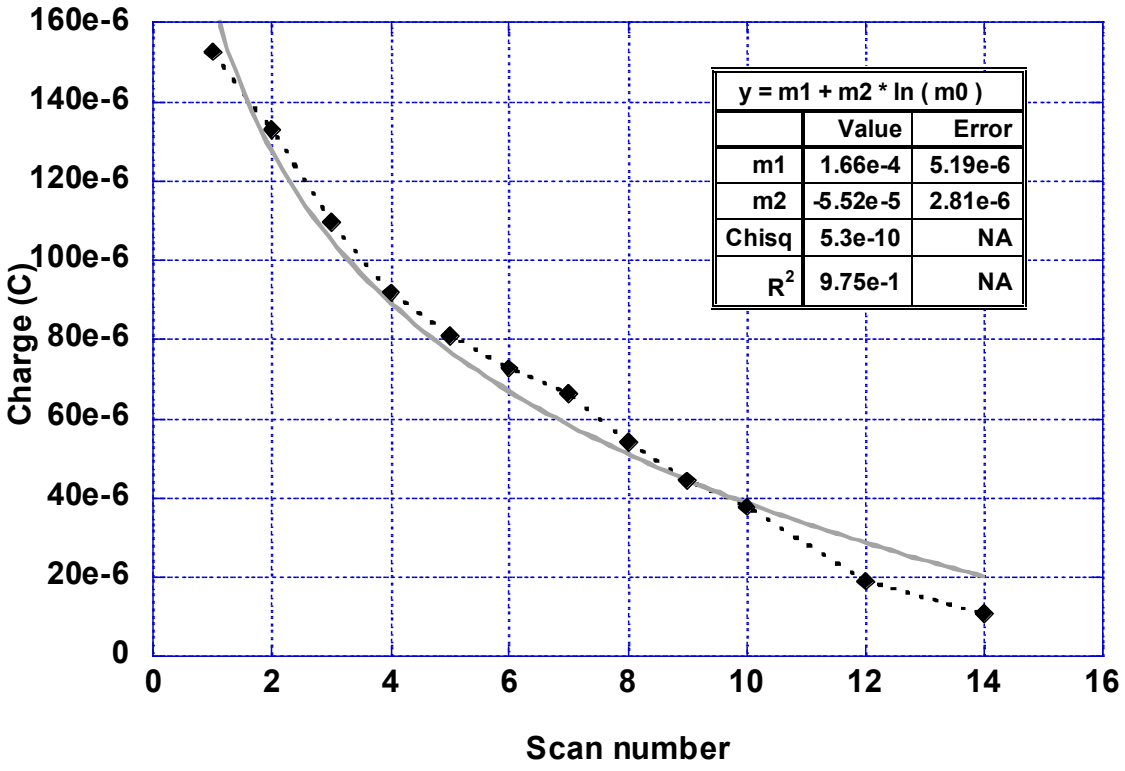

Figure 4-90 Charge vs. scan number for GC electrode excluding 2 scans present before the peak current was achieved (omitting scans > 14): logarithmic line showing best fit

Figure 4-90 shows how charge transferred during the reaction varied with scan number. Scan 1 charge decreased from approximately 150µA to 10µA by scan 14, therefore scan numbers above 15 were excluded from this figure. The trend line fitted to this graph had an R^2 value of 0.98 indicating a good fit.

An overview of the serially diluted electrochemical processes has been shown in Table 4.4.3. The table shows the (theoretical) percentage amount of Cu removed from 5, 10 and 15µL volumes of sample X while using 0.1M H_2SO_4 as a carrier electrolyte. The table shows the difference between using the full scan range and the reviewed scan range.

Table 4.4.3 Percentage of Cu removed from sample, serial dilution with H_2SO_4 carrier electrolyte, based on full scan and revised scan in a 2:1 electron to copper ratio during redox reaction

Sample volume (µL)	**5 (2:1)**	**10**	**15**
Total scan	2.83	8.45	1.63
Revised	2.67	8.10	1.41

The calculation of how much charge was transferred during the electrochemical processing gave a numerical indication of how much copper was removed from the system during the electrochemical processing. From these values it was possible to calculate a theoretical estimate of the amount of Cu which would have been removed from the full dissolved sample. This estimation was based on the selection of data analysed and the trend line used, therefore it was necessary to consider all 4 data scenarios; the full charge transferred during the electrochemical processing with and without the trend line going through y=0, and the reviewed charge transferred during the electrochemical processing with and without the trend line going through y=0, as shown in Figure 4-91.

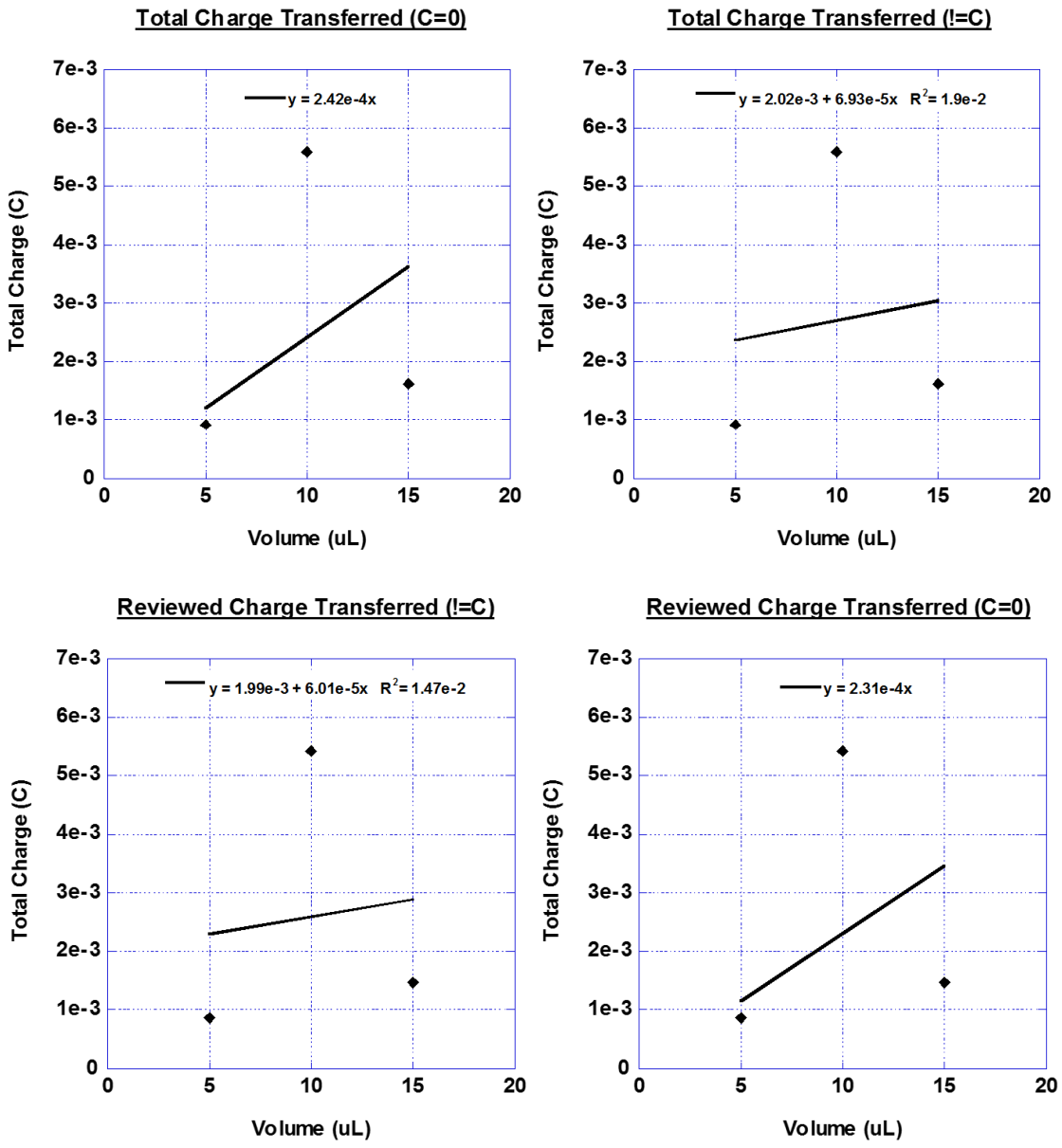

Figure 4-91 Full and reviewed charge transferred from 5, 10 and 15µL of 0.1M H_2SO_4 sample material with zero and non-zero Y intercepts.

Following a review of the initial plotted data it was deemed necessary to repeat each set of graphs with the amendment of excluding the 15µL data point from the total charge calculations, as shown in Figure 4-92. It should be noted that the 2 graphs which allowed

a non-zero Y intercept are negative values at -3.74e-3 C and -3.69e-3 C for the total and reviewed charge respectively.

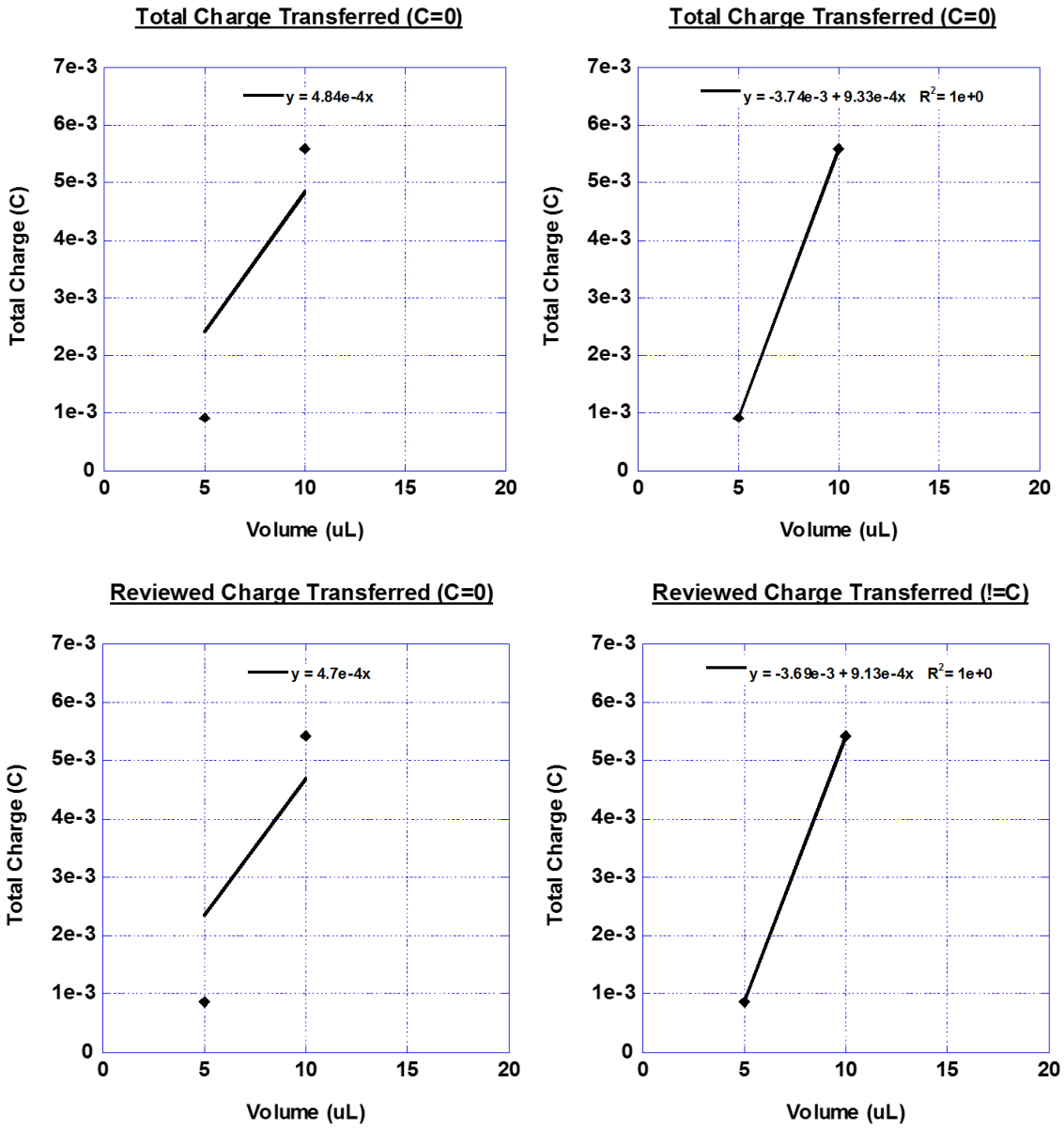

Figure 4-92 Full and reviewed charge transferred from 5 and 10µL of 0.1M H_2SO_4 sample material with zero and non-zero Y intercepts.

Table 4.4.4 shows the percentage of Cu which would have theoretically been removed from the full volume of sample material, predicted by the straight line formulae shown in Figure 4-91 and Figure 4-92.

Table 4.4.4 Predicted theoretical percentage of Cu removed from the full dissolved sample

Graph type	**Y=0 (%)**	**Y≠0 (%)**
Total (5ul, 10ul, 20ul)	17.73	5.07
Total (5ul, 10ul)	35.42	68.24
Reviewed (5ul, 10ul, 20ul)	16.90	4.40
Reviewed (5ul, 10ul)	34.37	66.78

4.4.6.5 Chronoamperometry

In a large batch attempt to remove the Cu from the sample material a Chronoamperometry technique was employed in which a working electrode was placed within the sample and held at a constant +0.8V for three 1hr periods, the results of which can be found in Figure 4-93.

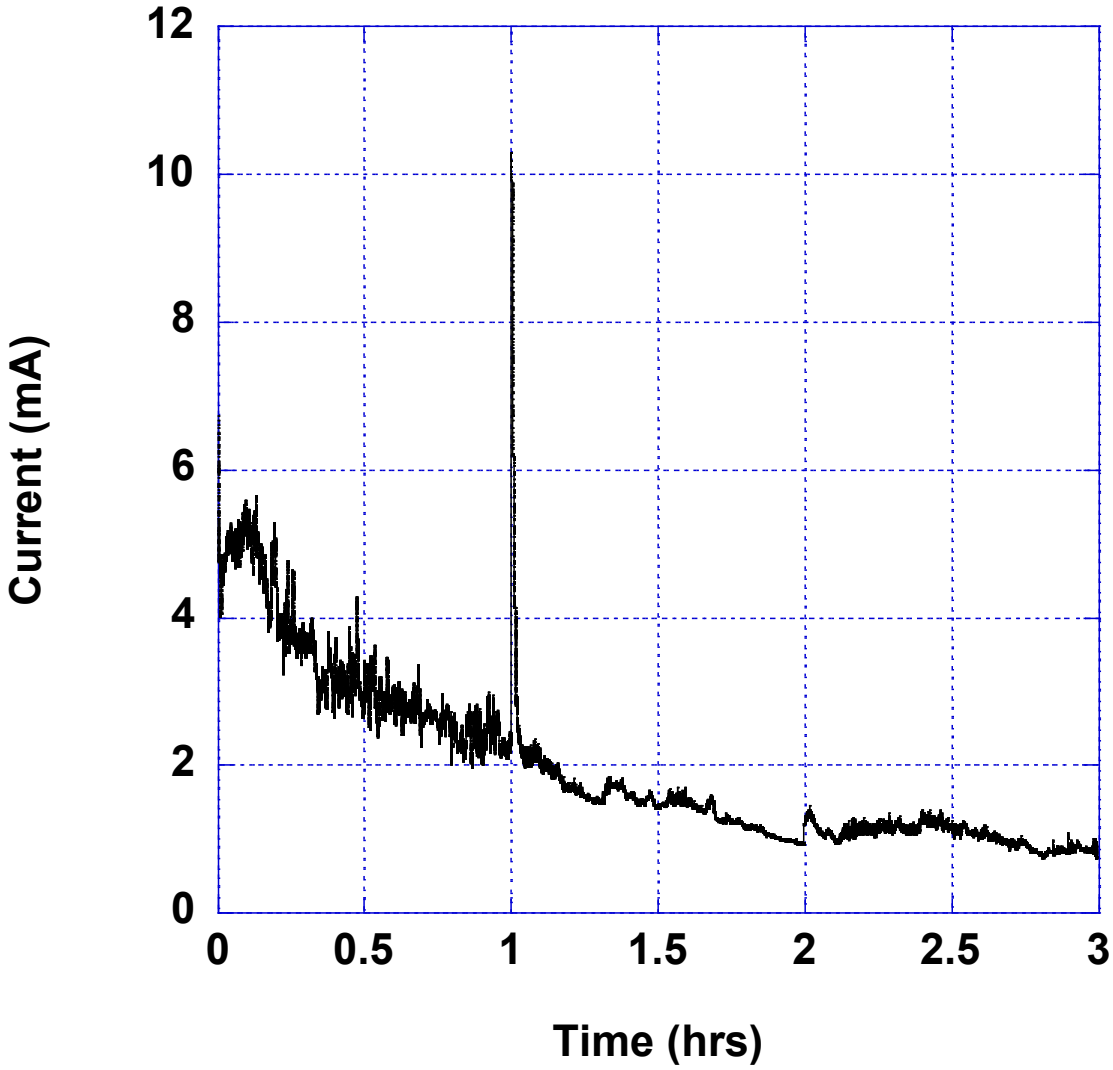

Figure 4-93 3hr +0.8V chronoamperometry scan

Figure 4-93 shows three consecutive 1hr, +0.8V chronoamperometry scans for the processing of a large batch of sample material. The spike in measured current at time locations of 1hr and 2hrs were due to noise caused by resetting the experiment for the following hour of processing. The line had a negative gradient as the charge was transferred due to the oxidation of copper, which decreased with increasing time due to the Cu becoming lost to the system. To ensure all samples came into contact with the

electrode the solution was stirred with a magnetic 'flea' stir bar throughout the experiment. The XRF results of this experiment are shown in Table 4.4.5.

Table 4.4.5 XRF 'wet' analysis of 3hr +0.8V chronoamperometry processed material

Sample volume (approx)			18ml
Sum (sample detected)			24.2%
Element	**Z**	**Wt%**	**Error (%)**
Cu	29	11.24	0.07
Ti	22	11.16	0.19
Ag	47	1.31	1.16
Cl	17	0.18	2.88
K	19	0.12	2.08
P	15	0.10	3.76
Ca	20	0.06	3.58
Al	13	0.05	7.20
Fe	26	52ppm	13.50
Ni	28	53ppm	18.00

Table 4.4.5 shows the elemental analysis of the resultant material following 3hrs at +0.8V chronoamperometry. The low detection rate of 24.2% was due to the resultant material being analysed as a suspension in a liquid. The two main constituents of the sample were Cu and Ti in a near 50:50 ratio, however copper dissolved into the supernatant would also have contributed to this value. To further analyse the composition of this 3hr +0.8V

chronoamperometry processed material by taking into account elements with lower atomic weights than Na (a limitation of the XRF X-ray set), P-XRD was used.

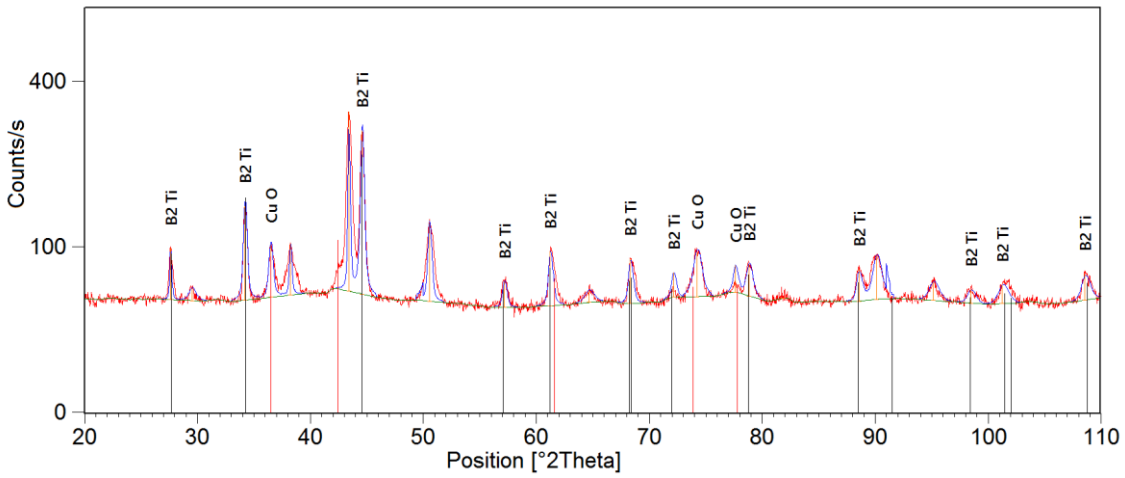

Figure 4-94 P-XRD spectrum of the post processed chronoamperometry material, overlaid with the matching TiB_2 and CuO XRD pattern locations

Figure 4-94 shows the P-XRD spectrum of the post chronoamperometry sample overlaid with the TiB_2 XRD pattern. The spectrum shows that TiB_2 was still a constituent part of the sample material, although contamination from CuO was present. Cu_2O was not expected to be in the processed material, as Cu_2O undergoes a redox reaction at >-0.557V vs. Ag/AgCl (see below).

$Cu_2O\ (s) + H_2O + 2e^- \rightarrow 2\ Cu(s) + 2\ OH^-$

at >-0.360 V vs. SHE OR >-0.557 V vs. Ag/AgCl

The semi-quantitative volume percentage of this sample was calculated to be: 56% TiB_2, 39% Cu/CuO and 4% Ag.

4.4.6.6 Electrochemistry Particle Size Analysis

In effort to determine whether the electrochemistry process had removed any copper from the TiB_2 particles the particle size distribution of pre and post electrochemically processed materials were compared.

4.4.6.6.1 Pre-electrochemistry

4.4.6.6.1.1 Volume based particle size distribution

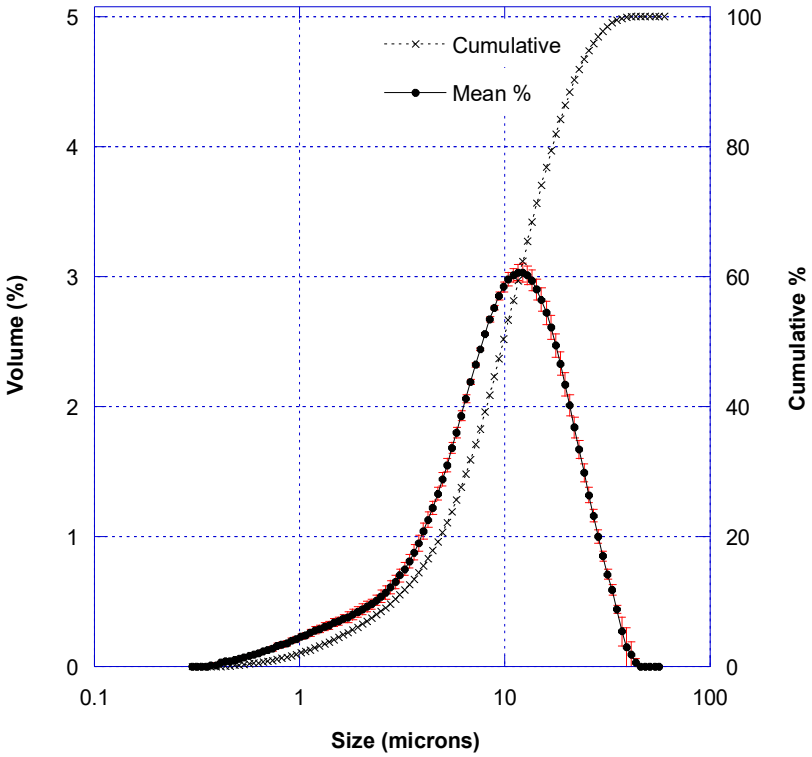

Figure 4-95 Volume based particle size distribution for the pre-electrochemically processed material, and the cumulative volume distribution plot

Figure 4-95 shows the volume based particle size distribution for the pre-electrochemically processed material. The figure also includes a cumulative distribution

plot. The particle size distribution had a peak at 15µm and shallow rising edge to the distribution.

4.4.6.6.1.2 Number based particle size distribution

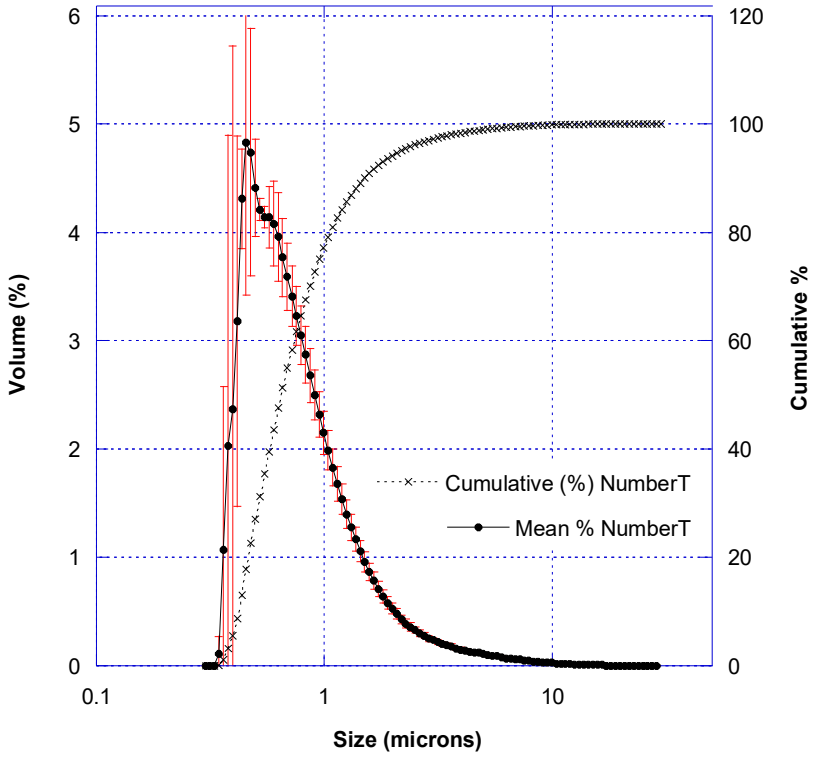

Figure 4-96 Number based particle size distribution for the pre-electrochemically processed material, and the cumulative volume distribution plot

Figure 4-96 shows the number based particle size distribution for pre-electrochemistry material. The particle size distribution's peak lies at 0.5µm. The cumulative volume distribution present on this plot indicated that 80% of the sample material was below 1µm.

4.4.6.6.2 Post electrochemistry

4.4.6.6.2.1 Volume based particle size distribution

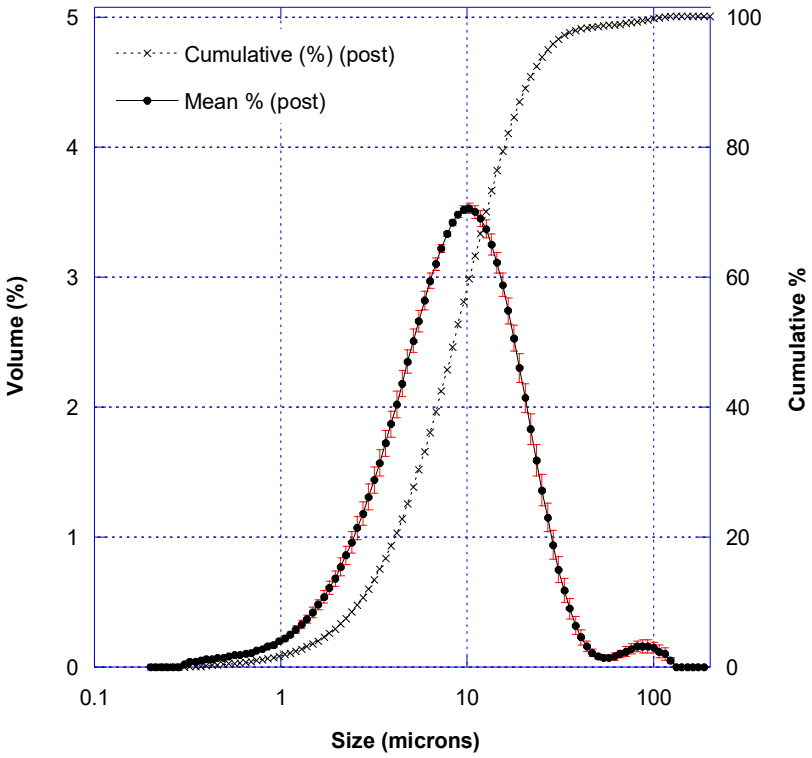

Figure 4-97 Volume based particle size distribution for the post-electrochemistry material, including a cumulative volume distribution plot

Figure 4-97 shows the volume based particle size distribution for post-electrochemically processed material. The distribution contained a peak located at 10µm. A second smaller peak was located at approximately 100µm however this was most likely the result of agglomeration effects within the processed material.

4.4.6.6.2.2 Number particle size distribution

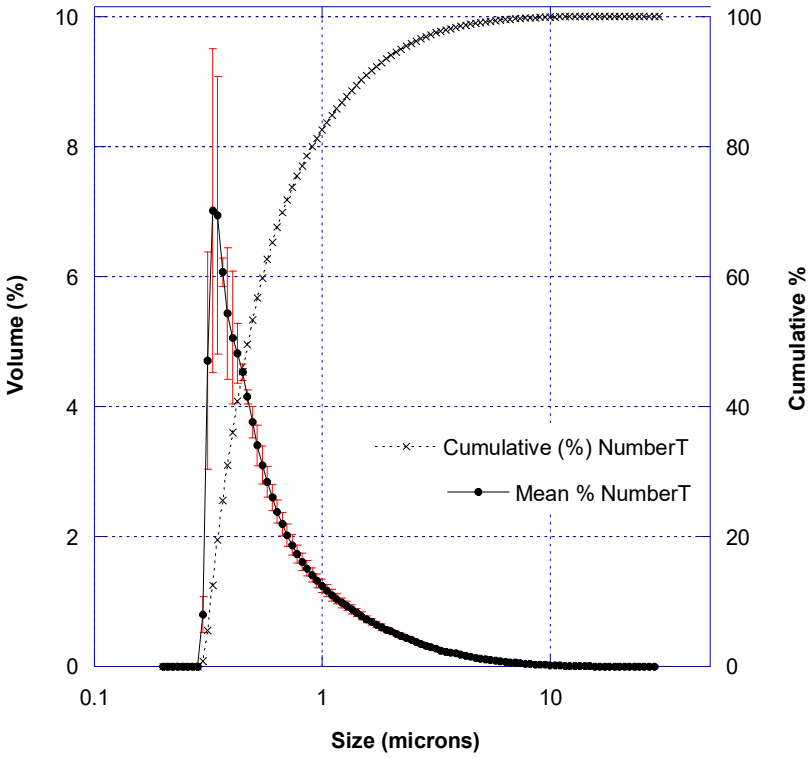

Figure 4-98 Number based particle size distribution for the post-electrochemistry material, including a cumulative volume distribution plot.

Figure 4-98 shows the number based particle size distribution for the post electrochemically processed material. The distribution showed a peak located at 0.35µm.

4.4.6.6.3 Pre and Post Electrochemically Processed Material Particle Size Comparisons

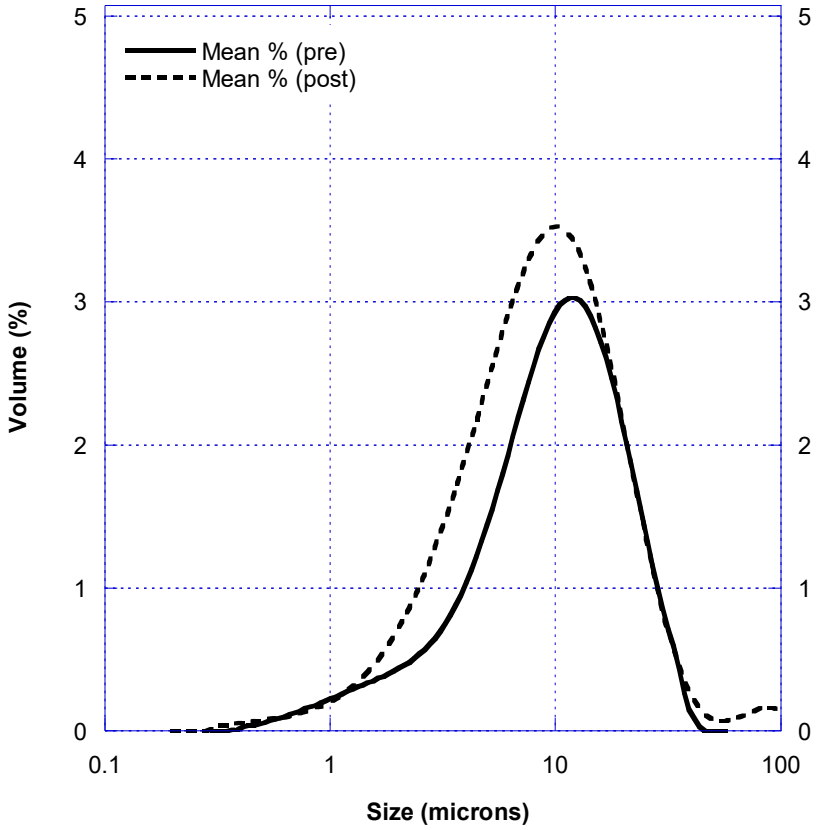

Figure 4-99 Comparison between the volume based distribution for the pre and post electrochemically processed material

Figure 4-99 shows the comparison between the pre and post electrochemical processing volume based TiB_2 particle size distributions. The pre electrochemistry peak was located at 12µm whereas the post processing peak was located at 10µm.

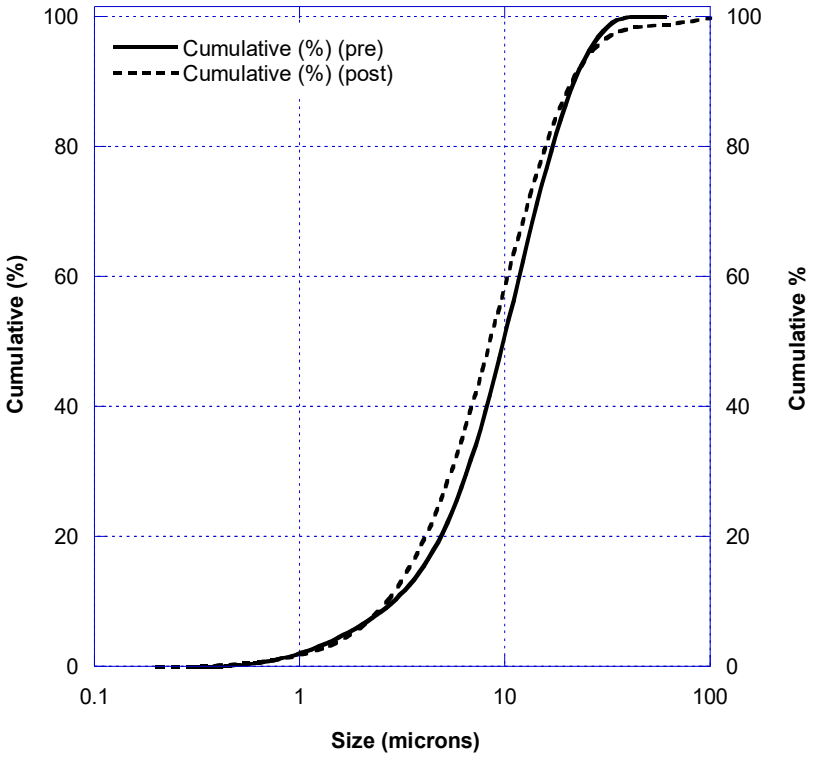

Figure 4-100 Comparison between the volume based cumulative distribution for the pre and post electrochemically processed material

Figure 4-100 shows the comparison between the volume based cumulative distribution for the pre and post electrochemically processed material. The distribution shows that the post electrochemically processed material had a smaller particle size than the pre-electrochemically processed material. The d(0.5) values for the pre and post electrochemically processed materials were; 10.4 and 9.1µm respectively.

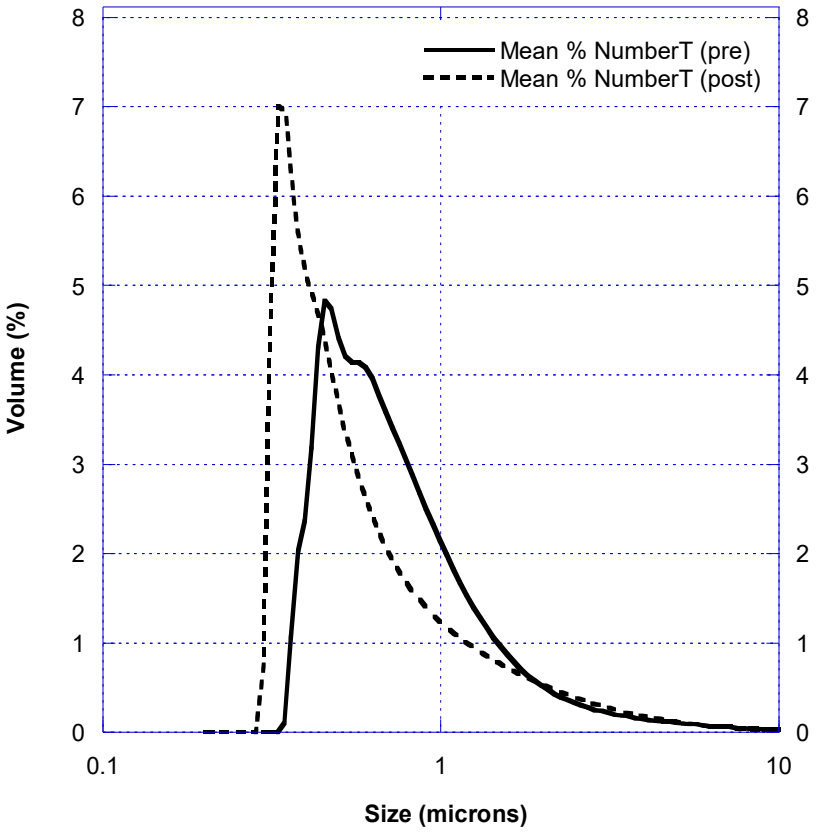

Figure 4-101 Comparison between the number based distribution for the pre and post electrochemically processed material

Figure 4-101 shows the number transformed particle size distribution comparison between pre and post electrochemical processed materials. The pre electrochemically processed material had a peak located at 4.5µm, the post electrochemically processed material has a peak located at 3.5µm.

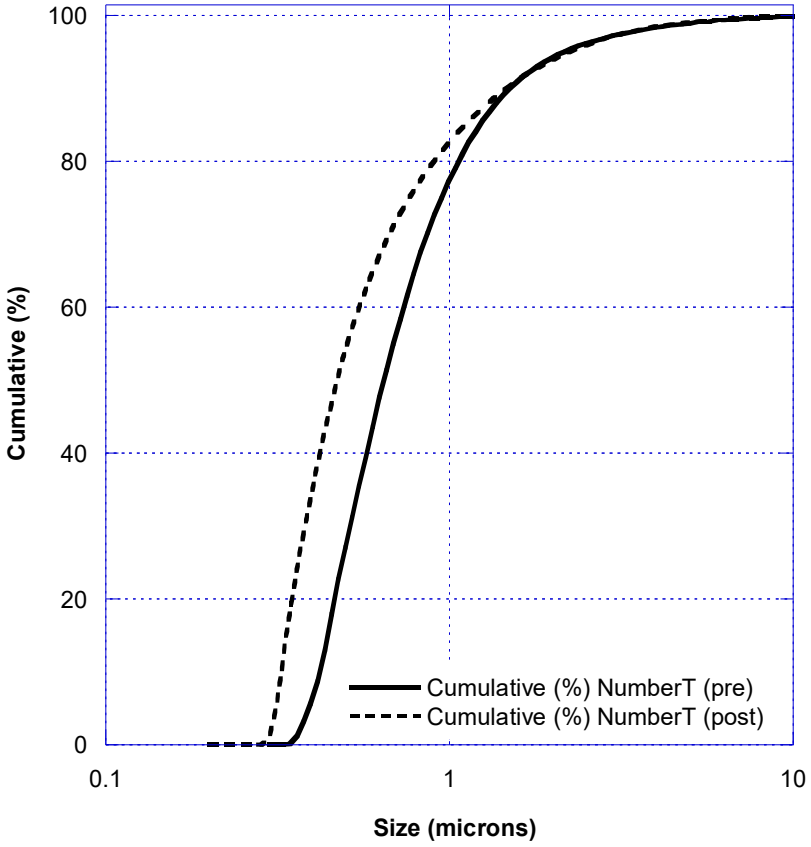

Figure 4-102 Comparison between the number based cumulative distribution for the pre and post electrochemically processed material

Figure 4-102 shows the comparison between the number based cumulative distribution for the pre and post electrochemically processed materials. The distribution for the pre electrochemically processed material had a d(0.5) of 0.68µm, whereas the post electrochemically processed material had a d(0.5) of 0.49µm.

Table 4.4.6 d(0.1), d(05) and d(0.9) values for both the volume and number based particle size distributions, for both of the pre and post electrochemically processed materials

Sample	d (0.1)	d (0.5)	d (0.9)
preVOL	3.00	10.38	22.96
postVOL	2.84	9.08	22.78
preNUM	0.44	0.68	1.57
postNUM	0.34	0.49	1.53

Table 4.4.6 shows the d(0.1), d(0.5) and d(0.9) for both number and volume based particle size distributions for pre and post electrochemically processed material. The results show that for both volume and number based particle size distributions, the post processed material had a smaller particle size distribution than the pre-electrochemical processed material.

4.4.6.6.4 Electrochemistry Particle Size Comparisons to other distributions

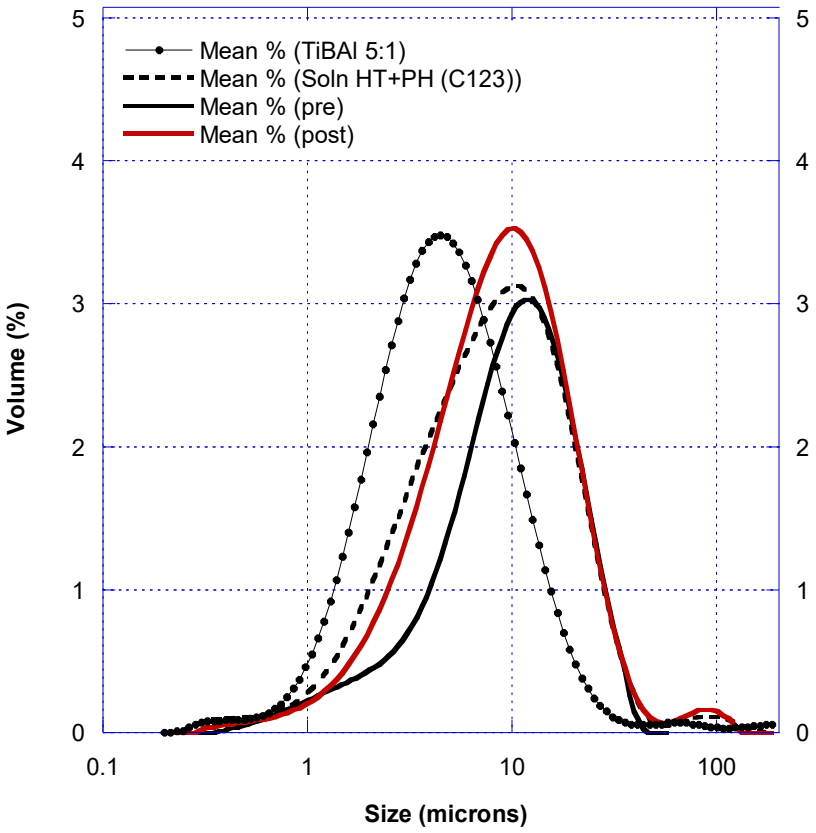

Figure 4-103 Volume based particle size distributions for: pre and post electrochemically processed material, for comparison with TiBAl 5:1, and solution heat treated and precipitation hardened A205

Figure 4-103 shows the volume based particle size distribution for pre and post electrochemically processed materials (TiB_2 originating from solution heat-treated and precipitation hardened A205 following dissolution in HCl) and their comparison to; solution heat treated and precipitation hardened A205 alloy, and TiBAl 5:1 material. The distribution showed that the TiBAl material had the smallest particle size distribution with a peak located at 4.5μm. From smallest to largest the remaining particle size distributions followed the following order; solution heat treated and precipitation hardened, then post electrochemically processed material. The largest particle size distribution measured was that of the pre-electrochemically processed material.

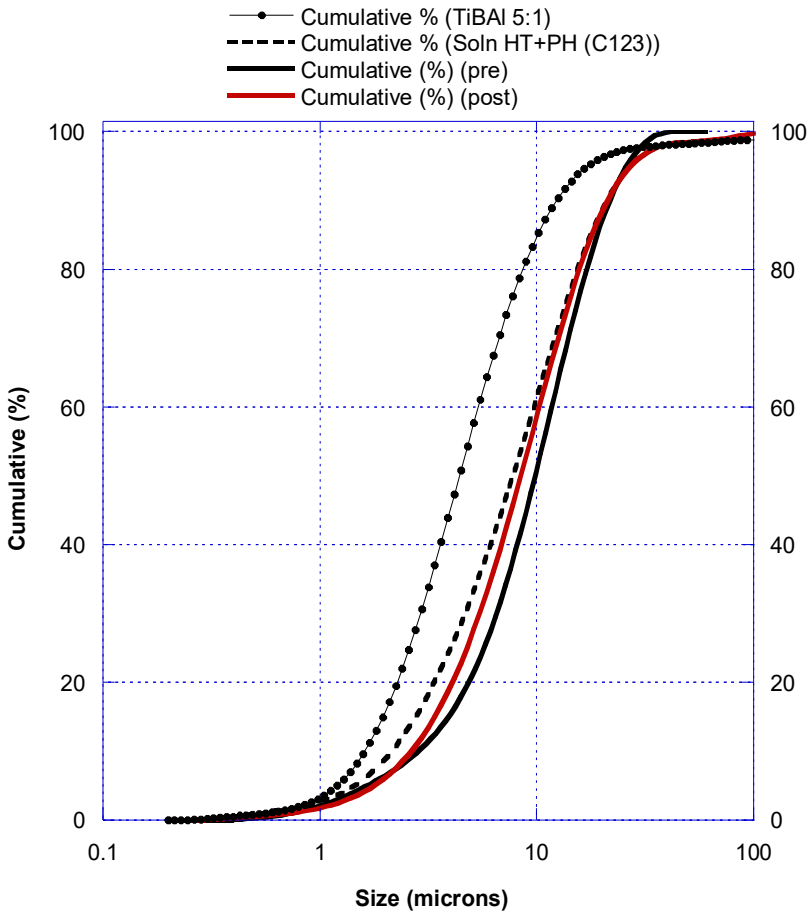

Figure 4-104 Volume based cumulative distribution for: pre and post electrochemically processed material, for comparison with TiBAl 5:1, and solution heat-treated and precipitation hardened A205

Figure 4-104 shows the volume based cumulative distribution for pre and post electrochemically processed materials (TiB_2 originating from solution heat-treated and precipitation hardened A205 following dissolution in HCl) and their comparison to; solution heat treated and precipitation hardened A205 alloy, and TiBAl 5:1 material. The distribution showed that the TiBAl material had the smallest particle size distribution. The post electrochemically processed material had a smaller particle size distribution than the solution heat treated and precipitation hardened A205 alloy. The pre electrochemically processed material had the largest particle size distribution.

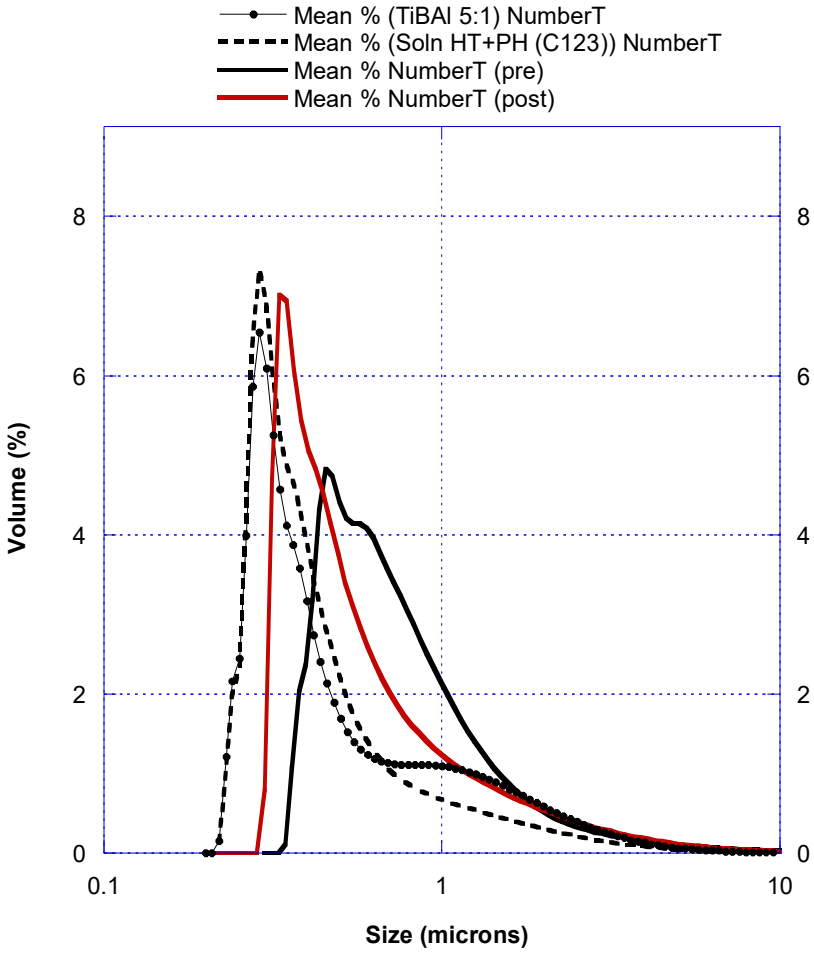

Figure 4-105 Number based particle size distributions for: pre and post electrochemically processed material, for comparison with TiBAl 5:1, and solution heat treated and precipitation hardened A205

Figure 4-105 shows the number based particle size distribution comparing the pre and post electrochemically processed material (TiB_2 originating from solution heat-treated and precipitation hardened A205 following dissolution in HCl) to the TiBAl 5:1 grain refiner material and the solution heat treated and precipitation hardened A205 alloy. The cumulative particle size distribution plot showed that the pre-electrochemically processed material had the largest particle size distribution when compared to the other number based particle size distributions, with a peak value of 0.45µm. The smallest cumulative

particle size distributions, based on corresponding peak values, are jointly the TiBAl and the solution heat treated and precipitation hardened materials, with a peak location of 0.29µm. The middle particle size distribution was the post electrochemically processed material, with a peak location of 0.35µm.

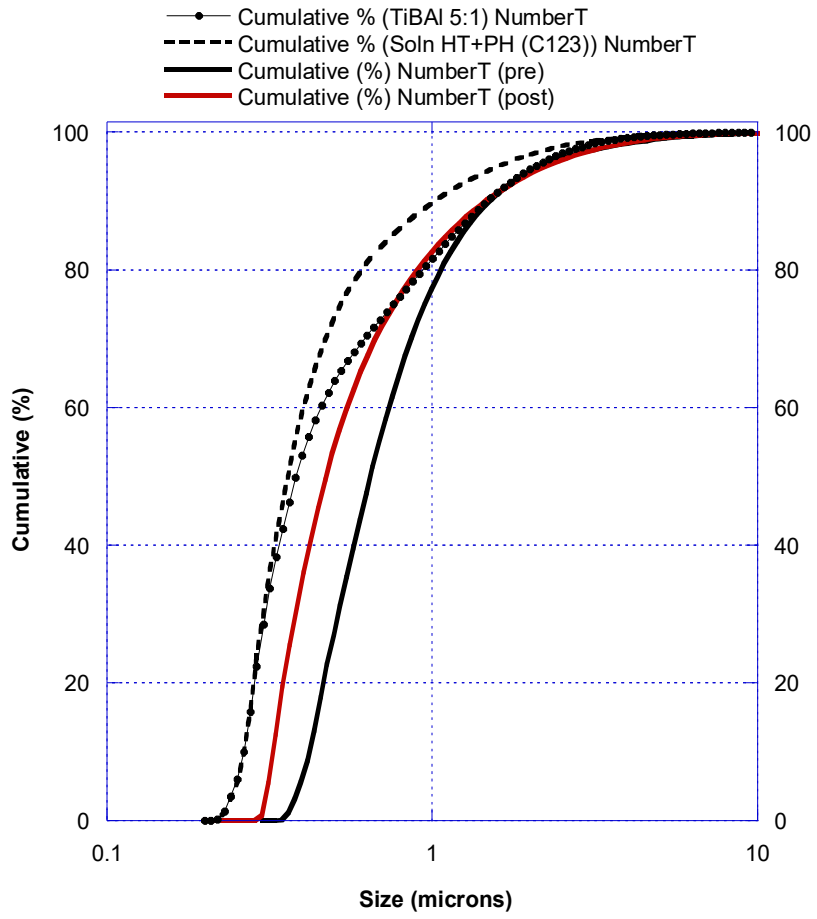

Figure 4-106 Number based cumulative distribution for: pre and post electrochemically processed material, for comparison with TiBAl 5:1, and solution heat-treated and precipitation hardened A205

Figure 4-106 shows the cumulative number based particle size distribution profile for the TiBAl grain refiner material, the solution heat-treated and precipitation hardened material, and the pre and post electrochemically processed materials (TiB_2 originating from solution heat-treated and precipitation hardened A205 following dissolution in

HCl). The distribution showed that until a cumulative percentage of approximately 40% the TiBAl grain refining material and the solution heat-treated and precipitation hardened material followed a similar distribution profile, after which point the TiBAl grain refiner material followed a larger particle size distribution profile than the solution heat-treated and precipitation hardened material. The post-electrochemically processed material had a comparatively middle sized particle size distribution. The pre-electrochemically processed material had the largest measured particle size distribution.

Table 4.4.7 d(0.1), d(05) and d(0.9) values, for both the volume and number based particle size distributions, for the pre and post electrochemically processed material, the TiBAl 5:1 material and the solution heat-treated and precipitation hardened material

Sample	d (0.1)	d (0.5)	d (0.9)
Pre-eChem (VOL)	3	10.38	22.96
Post-eChem (VOL)	2.84	9.08	22.78
TiBAl 5:1 (VOL)	1.73	4.72	13.31
Soln HT + PH (VOL)	2.3	8.34	22.55
Pre-eChem (NUM)	0.44	0.68	1.57
Post-eChem (NUM)	0.34	0.49	1.53
TiBAl 5:1 (NUM)	0.27	0.4	1.53
Soln HT + PH (NUM)	0.27	0.37	1.06

Table 4.4.7 shows the d(0.1), d(0.5) and d(0.9) values for both the volume based and number based particle size distributions. For the volume based particle size distributions, the smallest measured particle size distribution belonged to the TiBAl 5:1 grain refiner material. The next largest particle size distribution was the solution heat-treated and precipitation hardened material, followed by the post-electrochemically processed material. The largest particle size distribution belonged to the pre-electrochemically processed material. When considering the number based particle size distributions the TiBAl and solution heat-treated and precipitation hardened material had the joint lowest

d(0.1) values. Regarding the d(0.5) values, the solution heat-treated and precipitation hardened material had the lowest value at 0.37µm, the next highest d(0.5) value belonged to the TiBAl grain refiner material. The next largest d(0.5) value belonged to the post-electrochemically processed material with a value of 0.49µm. The largest d(0.5) value was taken from the pre-electrochemically processed material.

4.4.6.7 Potential future work (electro-bombardment)

Due to time considerations some of the interesting areas of this work have remained un-investigated. One such topic would be the use of an electro-bombardment technique to remove Cu phases from the surface of a TiB_2 particle. This technique would not only be used for determining the amount of Cu within a system, but also in quantifying the amount on each particle. The compatibility of this material with the electro-bombardment process is shown in Figure 4-107.

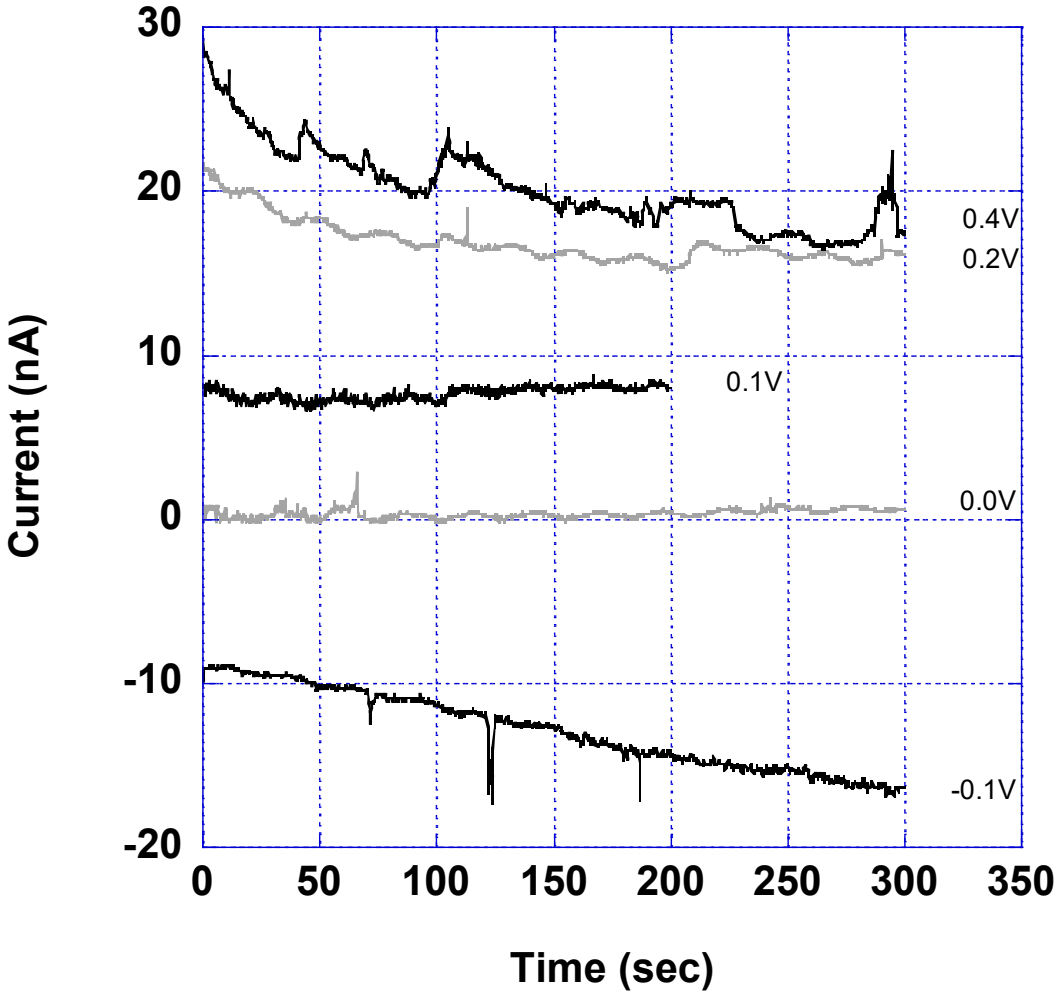

Figure 4-107 Electro-bombardment

Figure 4-107 shows 5 lines, indicating the 5 potentials at which an electrode was held at during the experiment; -0.1V, 0V +0.1V, +0.2V and +0.4V. Potential lines below 0.2V showed little evidence of redox reactions taking places, however the +0.4V potential line showed peaks in the detected current whenever a larger copper particle struck the electrode. By measuring the transferred charge across the duration of the impact event, it would be possible to demine the amount of Cu transferred and also give some identification as to the size of the particle, or, when compared alongside particle size

analysis results, the thickness of the Cu coating, a property which may influence further work in alloy strength calculations.

4.5 Results from TP1 grain refiner tests

Al-5Ti-1B grain refiner contains TiB_2 particles. When these particles were removed from the supporting material by dissolution they underwent particle size analysis. Particle size analysis found the particles to occupy a range of sizes. The purposes of this section of research was to learn to what effect the different TiB_2 particle sizes have on the resulting solidified grain structure. In effort to answer this question a series of settling experiments were conducted. From the settled material narrow size bands were sectioned and later used for quantitative grain size analysis using TP1 tests and subsequently compared using the Kolmogorov-Smirnov statistics test.

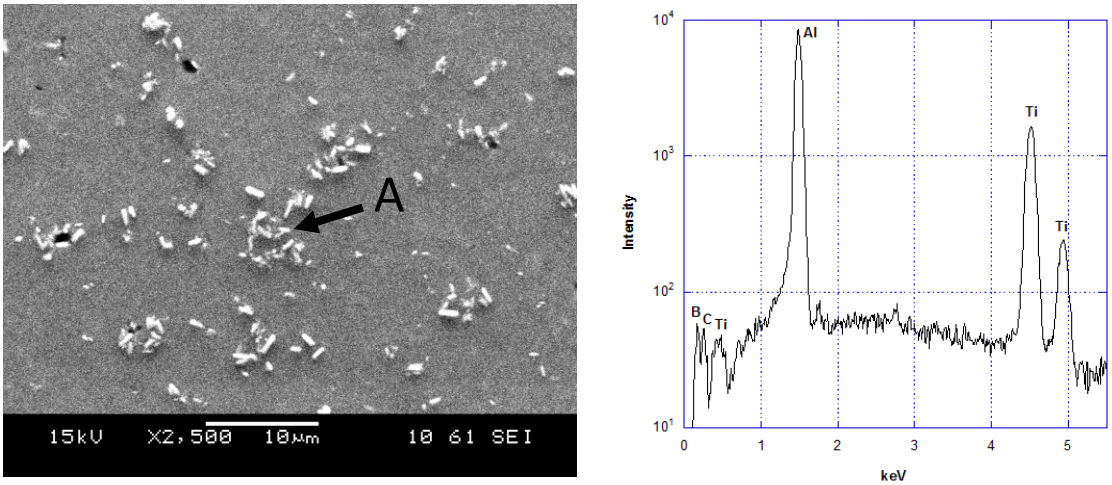

Figure 4-108 SEM image of Al–5Ti–1B showing refining particle size and distribution and its associated EDX spectrum

Figure 4-108 shows an SEM image of Al-5Ti-1B grain refiner, the location marker A indicates the area selected for EDX analysis -the spectrum of which is also given. The

light coloured particles are shown to have a high aspect ratio with an approximate length of 1µm and width of 0.5µm.

Table 4.5.1 Elemental composition from EDX results for location A

Element	Weight%	Atomic%
B	7.48	33.59
C	1.45	5.85
Al	23.22	41.78
Ti	15.52	18.78
Total	50.67	100.00

Table 4.5.1 shows the collected EDX elemental composition from location A. The results of which reported an atomic ratio of Titanium and Boron to be approximately 1:1.8 which confirmed that the particles were titanium diboride (TiB_2) and that there was a slight excess of Titanium within the sample.

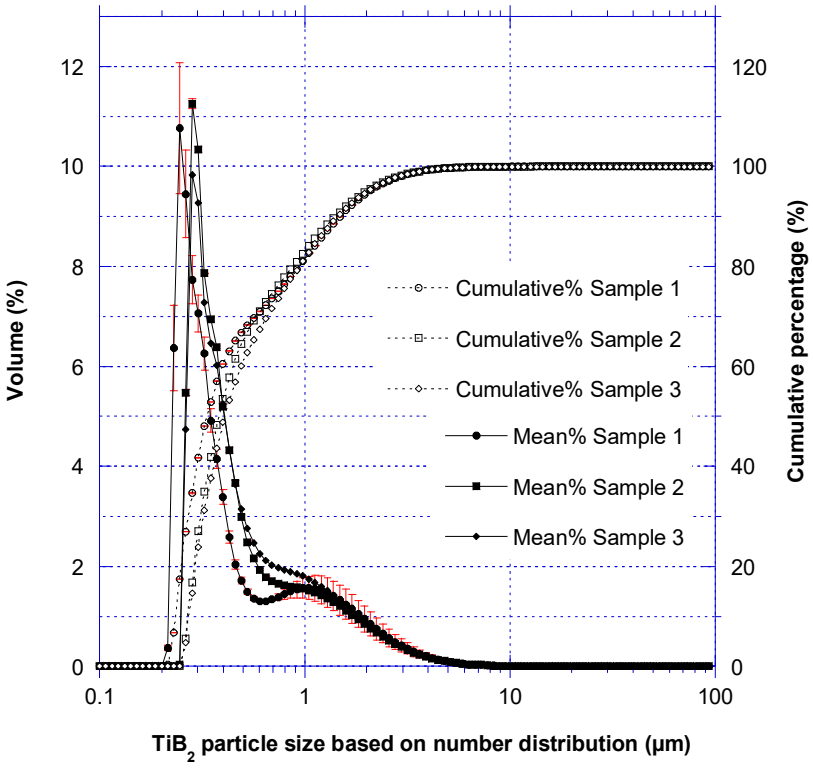

Figure 4-109 Number transformed particle size distribution of TiB_2 particles removed from Al-5Ti-1B

Figure 4-109 shows the number transformed particle size distribution and cumulative volume distribution of TiB_2 particles which were removed from Al-5Ti-1B grain refiner by dissolution in HCl. The figure showed the number transformed particle size analysis of 3 non-adjoining section of grain refining rod, the peaks of which all lie within 0.2 and 0.3µm.

Table 4.5.2 3 sample summary of TiBAl 5:1 particle size distributions

Sample Number	d(0.1) µm	d(0.5) µm	d(0.9) µm
Sample 1	0.25	0.35	1.53
Sample 2	0.29	0.41	1.51
Sample 3	0.29	0.43	1.55
Average	0.28	0.40	1.53

Table 4.5.2 shows the 3 sample summary of the d(0.1), d(0.5) and d(0.9) values for the number transformed particle size distribution of the Al-5Ti-1B material. The values show that 80% of the TiB_2 particles within the sample occupied a range of between 0.3 and 1.5µm.

Table 4.5.3 ICP elemental summary (in weight%) of the settled sample materials. The grey rows highlight the 4 chosen TP1 settling samples and their compositions, labelled TP1.A/B/C/D respectively

Settling Time		Al	Si	Fe	Cu	Mn	Mg	Ti	B	TiB_2	Free Ti
	TiBAl (TP1.A)	Rem	0.10	0.12	<0.01	<0.01	<0.01	5.00	1.00	3.21	2.79
30min	Top	Rem	0.11	0.11	<0.01	<0.01	<0.01	5.37	0.95	3.05	3.27
	Bottom (TP1.B)	Rem	0.10	0.12	<0.01	<0.01	<0.01	4.55	0.81	2.60	2.76
90min	Top (TP1.C)	Rem	0.14	0.12	<0.01	<0.01	<0.01	7.44	1.29	4.15	4.58
	Bottom	Rem	0.12	0.11	<0.01	<0.01	<0.01	6.31	1.09	3.50	3.90
24hr	Top (TP1.D)	Rem	0.15	0.13	<0.01	<0.01	0.02	7.06	1.88	6.04	2.90
	Bottom	Rem	0.15	0.11	<0.01	<0.01	0.02	8.53	2.20	7.07	3.66
72hr	Top	Rem	0.12	0.11	<0.01	<0.01	0.02	6.84	1.81	5.82	2.83
	Bottom	Rem	0.13	0.11	<0.01	<0.01	0.02	7.73	2.01	6.46	3.28

Table 4.5.3 shows the elemental composition, determined by ICP, of the samples of material which were held at the specified times in effort to promote a settling effect. The 4 rows highlighted in grey indicate the elemental composition of the materials which were taken forwards for grain size tests.

Table 4.5.4 Ti and B concentration in ppm for each TP1 sample

	TiBAl (sample A)		**30min BOT (sample B)**		**90min TOP (sample C)**		**24hr Top (sample D)**	
	1	2	1	2	1	2	1	2
Ti (ppm)	99.8	100.1	112.7	112.9	115.2	115.1	99.9	99.9
B (ppm)	20.0	20.0	20.1	20.1	20.0	20.0	20.0	19.9
TiB_2 (ppm)	64.2	64.3	64.5	64.6	64.2	64.2	64.2	64.1
Free Ti (ppm)	55.6	55.8	68.3	68.4	71.0	70.9	55.7	55.7

Table 4.5.4 details the total titanium, total boron, TiB_2 and free Ti weight percentages for each of the 8 TP1 castings required for analysis.

Table 4.5.5 Melt temperatures and times at which the TP1 test pieces were taken

Sample	**Temp** (°C) of melt at time = 0 sec	**Temp** (°C) of TP1 ladle at time of removal	**Time** (min:sec) at TP1 sample removal
A1	726	712	2:30
A2	718	716	1:56
B1	722	718	2:30
B2	718	715	2:18
C1	713	712	2:20
C2	723	718	2:15
D1	716	720	2:05
D2	717	719	2:02

Table 4.5.5 shows a record of the melt temperature, TP1 ladle temperature, and time following grain refining addition that each of the samples were removed from the crucible.

Table 4.5.6 Total number of grains analysed for each TP1 sample

Sample	Casting Trial	
	# grains (1+2)	# grains total
A1+A2	1948+596	2544
B1+B2	1137+546	1683
C1+C2	1343+462	1805
D1+D2	424+613	1037

Table 4.5.6 Total number of grains analysed from each sample of material from both tests, followed by the total number of grains analysed for that sample type (i.e. A total = A1 + A2).

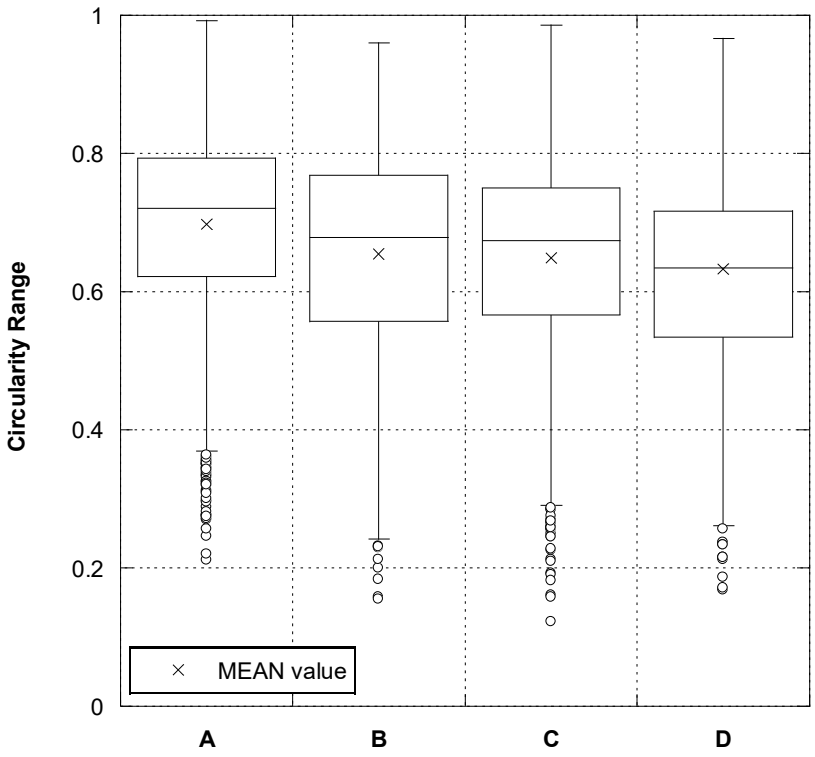

Figure 4-110 Comparing the circularity value ranges for TP1 samples: A, B, C and D

Figure 4-110 shows a comparison between the circularity values calculated for each of the TP1 samples. Due to the fact that each of the mean values had a circularity value of

greater than 0.6, the measured grains were assumed to be circular for grain size analysis purposes i.e. for the determination of grain diameter.

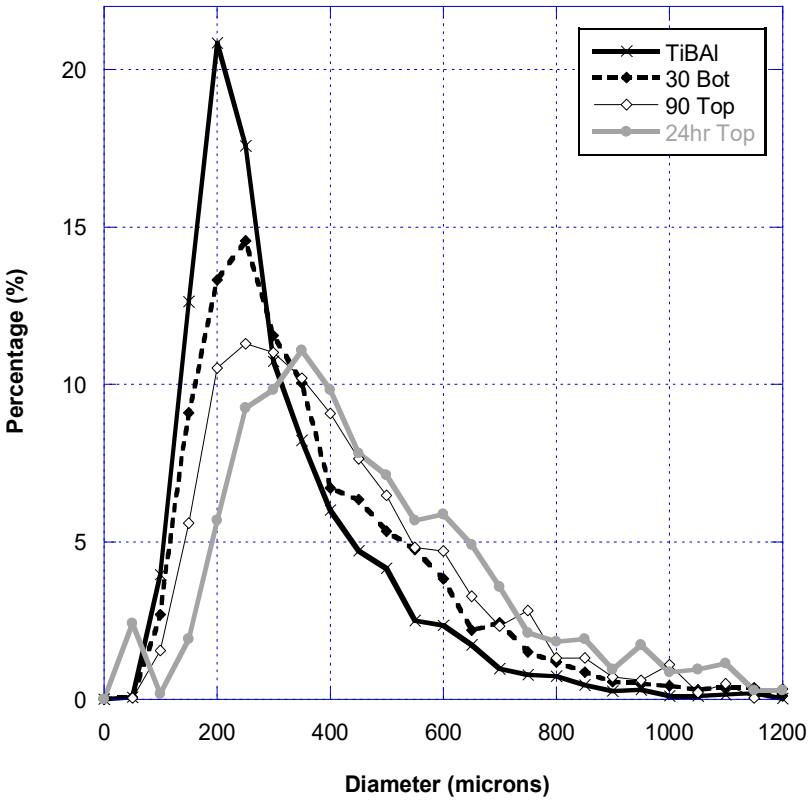

Figure 4-111 Diameter vs. percentage occurrence for TP1 sample: A, B, C and D.

Figure 4-111 shows the diameter vs. percentage occurrence for TP1 samples A (TiBAl), B (30 Bot), C (90 Top) and D (24hr Top). The distribution was non-Gaussian. The TiBAl grain refining material had the narrowest grain size distribution. Material which had been allowed to settle for 24hrs had the largest grain size distribution.

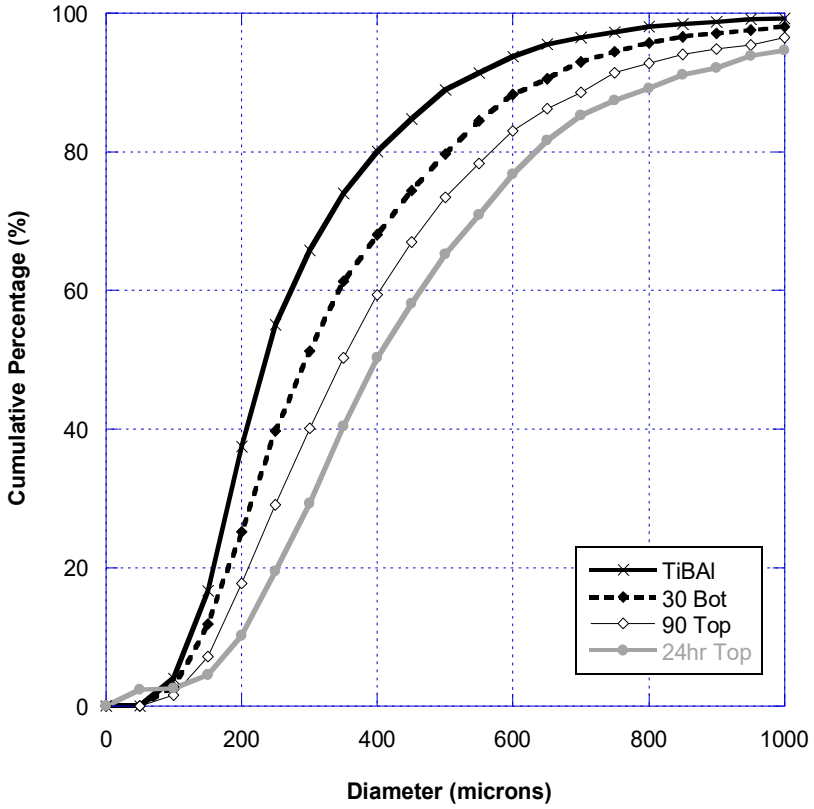

Figure 4-112 Cumulative distribution comparison between TP1 samples: A, B, C and D

Figure 4-112 shows the cumulative distribution of TP1 samples A, B, C and D. The distribution shows that the TiBAl 5:1 grain refiner material had the smallest grain size distribution. Sample B (30min bot) had the next largest grain size distribution followed by sample C (90 min top). Sample D (24hr top) had the largest grain size distribution.

Table 4.5.7 Summary of cumulative distribution figure

	Grain size bin (µm)	
Sample	Peak %	Cumulative 50%
A	200 - 249	250 - 299
B	250 - 299	300 - 349
C	250 - 299	350 - 399
D	350 - 399	400 - 449

Table 4.5.7 compares the location of the peak grain size to the 50% cumulative percentage value for each sample type. The results showed that the location of the peak percentage increased from a location of between 200-249µm for sample A, to between 250-299µm for samples B and C, to 350-399µm for sample D. During the peaks shift to larger grain sizes, the 50% cumulative percentage value also increased from a value of between; 250-299µm for sample A, 300-349µm for sample B, 350-399µm for sample C, and 400-499µm for sample D.

Table 4.5.8 K-S test results show that each grain size distribution was significantly different from the others

A to B

p-value	3.49E-11
size 1	2544
size 2	1593
Sig diff?	yes

A to C

p-value	1.99E-04
size 1	2544
size 2	1805
Sig diff?	yes

A to D

p-value	1.52E-03
size 1	2544
size 2	1037
Sig diff?	yes

B to C

p-value	8.92E-10
size 1	1593
size 2	1805
Sig diff?	yes

B to D

p-value	8.98E-09
size 1	1593
size 2	1037
Sig diff?	yes

C to D

p-value	4.35E-07
size 1	1805
size 2	1037
Sig diff?	yes

Table 4.5.8 shows the comparison between each sample with all other samples and whether there was a statistical difference between them. The results showed that each sample analysed was statistically different from all other samples analysed.

5 DISCUSSION

5.1 The TiB_2 particle size distribution

Optical microscopy and SEM are common methods of quantifying particle size analysis. Areas of interest from a material are sectioned, polished and subsequently analysed under an optical or electron microscope. Once under the microscope these small subsections are analysed from which assumptions are made regarding the sample as a whole. For the analysis of crystal structures these methods are often acceptable however for the analysis of small sub-gran-sized non-symmetrical structures contained within the grain boundary material, limitations exist. The author appreciates that useful information can be made from the micrographs of a material, however in the pursuit of a more encompassing strength prediction where a fuller description of a materials constituents can be used to develop additional strength models, alternative methods should be explored and where possible combined. For this reason, the TiB_2 was removed from the A205 alloy via HCl, as described in the Experimental section, and subjected to an external particle size analysis technique.

5.1.1 Experimentally determined TiB_2 particle size results

As mentioned in the results section, SEM analysis indicated the TiB_2 particles to be plate-like in structure and only a few microns along their longest axis. The technique used by the Malvern apparatus for analysing particle size used a scattering theory which assumed the particles in question were spherical and as such reported its results based upon the particles perceived volume. This method had limitations when considering small particles, as only a few larger particles would skew the reported results to larger sizes

based proportionately on their significantly larger volume contribution to the sample as a whole. The analysis software developed by Malvern International provided a solution to this problem by being able to transform the raw volume results into either; surface area, length or number based particle size distributions (as shown in Figure 5-1), which removed the distributions bias from the particles volume allowing for a more representative size distribution when considering smaller particles.

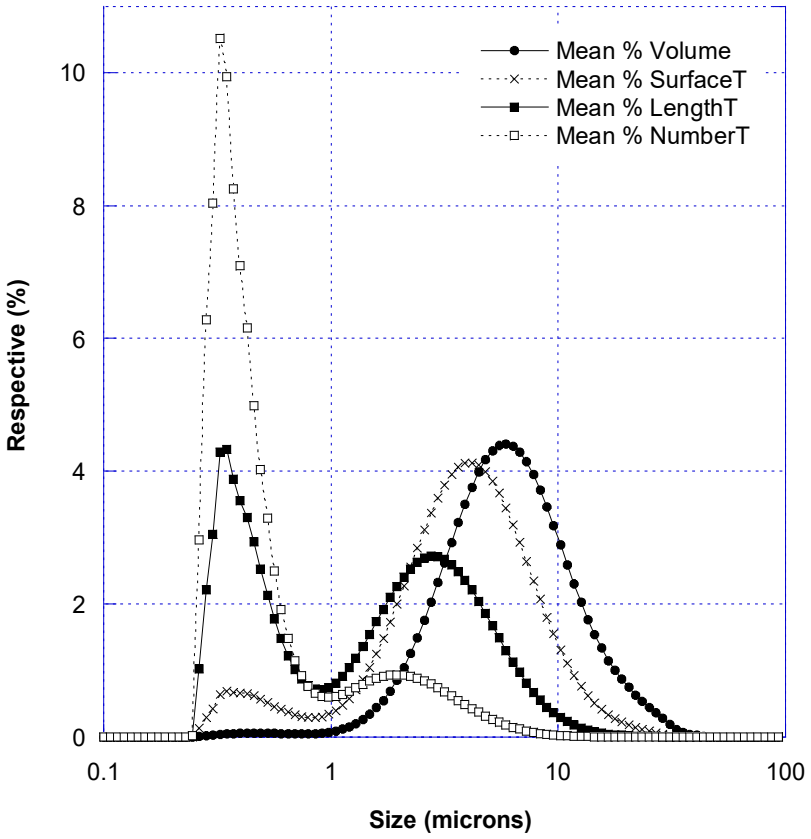

Figure 5-1 Comparison between volume, surface, length and number particle transformations for purchased TiB_2 particles

Figure 5-1 shows a comparison between the volume, surface, length and number transformations for purchased TiB_2 particles. The comparison between the particle size distributions revealed a shift in the particle size peaks to smaller values, when comparing

and transforming from the volume particle size distribution. The particle size distribution which was most related to the TiB_2 particles in the SEM images was the number transformed particle size distribution as the distribution type was most sensitive to sub-micron particle sizes. It was from this comparison that TiB_2 particle sizes within this research were quoted as having come from either a volume or number particle size distribution.

5.1.2 Effect of machine on particle size

The Malvern apparatus analysed data by processing the diffraction of laser light around the sample particles. The diffraction patterns, given the term 'snaps', were collected by the machine in 1ms time intervals. To ensure that an accurate representation of the material was reported 30,000 'snaps' were recorded and analysed to give a 'measurement'. A series of 30,000 snaps were also taken at the beginning of each measurement to give a background value which was then internally subtracted from the measurement value at the end of each run. This process was repeated allowing for a number of measurements to be collected which were then averaged to give a final result. For this research each result was averaged from 10 measurements, with each measurement consisting of 30 seconds background, and 30 seconds of data acquisition time; each comprising of 30,000 recorded snaps. To determine how the TiB_2 sample material would behave in such an environment, the sample materials agglomeration tendencies and resilience to ultrasonic agitation were investigated.

5.1.2.1 Circulating material and agglomeration tendencies

During operation the Malvern Mastersizer machine continuously circulated a sample through a measurement cell while capturing particle size information. As it was unknown

how the material would behave in such an environment, a range of test were conducted to ensure that the most appropriate experimental procedure was employed.

To determine whether the process of circulating TiB_2 material continuously for a period of approximately 6 minutes in deionised water effected the particle size distribution, the first measurement, 10^{th} measurement and the average of measurements 1 to 10 were compared (see Table 5.1.1).

Table 5.1.1 d(0.1), d(0.5) and d(0.9) values for a volume based particle size distribution of non-ultrasonically agitated TiB_2

Measurement	d (0.1) µm	d (0.5) µm	d (0.9) µm
No. 1	2.32	5.27	10.85
No. 10	2.96	7.27	17.99
Mean (1-10)	2.73	6.12	14.08

Table 5.1.1 shows how the non-ultrasonically agitated volume based particle size distribution for the purchased TiB_2 particles varied with measurement number. The first and tenth measurements show how the size distribution varied between the first and last measurements. The size change of the d(0.1), d(0.5) and d(0.9) values, between the first and tenth measurement cycle was approximately; 0.6, 2 and 7.1µm respectively. The increase in the value from measurement 1 to 10 indicated that the particles being analysed were increasing in size -a possible explanation for this could be due to agglomeration of the particles with time.

Table 5.1.2 d(0.1), d(0.5) and d(0.9) values for a volume based particle size distribution of ultrasonically agitated TiB_2 (10mins ultrasonic agitation at level 10)

Measurement	d (0.1) µm	d (0.5) µm	d (0.9) µm
No. 1	2.37	7.01	15.88
No. 10	3.33	8.53	18.23
Mean (1-10)	2.86	7.81	17.15

Table 5.1.2 shows how the ultrasonically agitated volume based particle size distribution for the purchased TiB_2 particles varied with measurement number. In comparison to Table 5.1.1 the d(0.1), d(0.5) and d(0.9) values were higher, as indicated by their increase in Mean (1-10) values, approximately; 0.1, 1.7 and 3.1µm respectively. However, the increase in value from measurement number 1 to 10 was comparatively less being; 0.9, 1.5 and 2.4µm. Due to the materials increased stability following ultrasonic agitation further investigation into ultrasonic levels and timings was carried out.

5.1.2.2 Ultrasonic agitation level

Investigation into the sample behaviour following ultrasonic agitation was examined. An integral section of the Malvern Mastersizer equipment was the Hydro 2000MU sample handling unit, responsible for circulating the fluid around the device and also responsible for any ultrasonic pre-treatment stages. The sample handling unit's ultrasonic function is basic with a value of 0 for off and 20 for full.

Table 5.1.3 d(0.5) values for both volume and number particle size distributions comparing different ultrasonic probe displacement levels for a fixed time of 1min

Displacement	Volume (µm)	Number (µm)
0	6.12	0.41
5	7.26	0.46
10	8.27	0.53
15	9.37	0.52
20	7.77	0.47

Table 5.1.3 shows the d(0.5) values for both volume and number particle size distribution comparing different ultrasonic probe displacement levels for a fixed time of 1min. The distribution reveals how under the application of ultrasonic agitation both the volume-based and number-based particle size distributions increased. One possible reason for this effect could be due to the presence of larger agglomerates, above the monitored size range, which under the action of ultrasonic agitation disintegrated towards their constituent particle sizes, hence increasing the measured d(0.5) value. For experimentation purposes the probe displacement value was set at a level of 10.0 as it was deemed necessary to include ultrasonic agitation into sample pre-treatment stages to minimise possible effects of agglomeration break-up during analysis. Displacement values above 10 were disregarded as inappropriate due to the formation of cavitation bubbles within the sample beaker.

Table 5.1.4 d(0.5) values for both volume and number particle size distributions comparing ultrasonic agitation times for a fixed probe displacement level of 10.0

Time (min)	Volume (µm)	Number (µm)
0	6.12	0.41
1	8.27	0.53
2	6.48	0.44
5	7.46	0.49
10	8.77	0.56

Table 5.1.4 shows the d(0.5) values for both volume and number particle size distributions comparing ultrasonic agitation times for a fixed probe displacement level of 10.0. Similar to the effects seen in Table 5.1.3 an increase in ultrasonic agitation time led to an increase in measured d(0.5) values for both volume and number-based particle size distributions. The ultrasonic agitation time chosen for the actual experiment was set at 10 minutes to ensure that if any large agglomerates were present within the sample then such a period of ultrasonic agitation would help ensure their disintegration prior to analysis.

5.1.3 Particle size comparisons

5.1.3.1 A205

As detailed within the Results section investigation into the experimentally collected material from A205 was examined. The results between the as-cast, solution heat-treated, and solution heat-treated and precipitation-hardened materials were different. The as-cast material had the largest particle size distribution, and solution heat-treated the least. A possible explanation for this result could be due to the TiB_2 particles present within the grain boundaries adhering together by an increased copper content in the grain boundaries. As the copper diffuses into the grain structure during solution heat-treatment, the TiB_2 particles are coated in less Cu than before and therefore appeared to occupy a smaller particle size distribution. Following precipitation hardening the remaining copper within the grain boundaries re-nucleates from the saturated solution and again acts as a binding or covering material between the TiB_2 particles, although to a lesser extent than the as-cast material, hence raising the measured particle size to between the as-cast and solution heat-treated distributions.

5.1.3.2 Al-5Ti-1B and Al-3Ti-1B grain refiners

Al-5Ti-1B and Al-3Ti-1B grain refiners are both produced using the same process, i.e., the TiB_2 particles are formed in the melt by a salt-salt reaction as detailed in the literature[127]. For this reason, the TiB_2 particle sizes were expected to have approximately the same particle size distributions as each other, and experimental measurements of the TiB_2 particle size distributions extracted from the two respective grain refiners confirmed this. As A205 alloy and the grain refiners are probably produced by the same method, the Al-5Ti-1B's TiB_2 distribution has been taken as the standard to which the A205 alloys TiB_2 particle size distribution has been referenced against. The A205 alloy contained copper, which was predominantly located in the grain boundary material. Comparison of the Al-5Ti-1B grain refiner's TiB_2 particle size distribution to the A205's as-cast, solution heat-treated, and solution heat-treated and precipitation hardened TiB_2 particle size distributions revealed the raw volume based d(0.5) value for the Al-5Ti-1B particle size distribution to be smaller than all of the A205 alloys d(0.5) TiB_2 size values by varying amounts. As the TiB_2 material from the Al-5Ti-1B alloy was smaller than the TiB_2 collected from the A205 alloy by varying amounts, it can be assumed that the A205 alloy TiB_2 distributions contained an amount of copper, which effected the particle size distribution by varying amounts according to the samples stage in the heat treatment procedure. In effort to obtain a pure TiB_2 samples from the A205 alloy an electrochemical method of copper decontamination was explored.

5.2 Electrochemical purification of TiB_2

5.2.1 TiB_2 and solution breakdown

Prior to each alloy undergoing particle size analysis, the experimentally collected material from the A205 dissolution experiments was subjected to XRD analysis and found to contain traces of copper. In an effort to remove the copper from the material, to gain a more accurate size distribution for the A205 alloy, an electrochemical approach was investigated. To deduce whether TiB_2 was electrochemically stable over the estimated voltage ranges required to oxidise copper from the surface of the sample material, purchased TiB_2 was used in 3 cyclic voltammetry trials. In each trial a 10µL sample of TiB_2 suspension was dried onto the surface of a Glassy Carbon electrode and the voltage cycled over the required range. The trials; 0.0 to +0.8, 0.0 to +1.0, and 0.0 to +1.2V did not show any evidence of TiB_2 oxidising away from the electrode surface, however, at the higher potential values >0.8V (above the estimated working potentials) evidence of solution break down was present.

5.2.1.1 Carrier electrolyte solution

The carrier electrolyte solution used for this series of experiments was Potassium Chloride (KCl). KCl was chosen as a suitable electrolyte as the copper ions formed at the working electrode would then recombine to form $CuCl_2$ and hence would be dissolved into the solution upon their formation.

To determine whether the experimentally collected material was suitable for oxidation, and to theoretically determine the amount of copper which could be removed using this method, an experiment was carried out, in which 3 different volumes of material were

dried onto the surface of the electrodes for investigation. The electrode type used for this particular investigation was Indium Tin Oxide (ITO). The signal measured had a single peak detected at the appropriate potential for copper (with respect to the Ag/AgCl reference electrode used), did not have a re-deposition peak, and was found to scale appropriately with the volume of sample being analysed. Micrographic observations comparing the pre and post-electrochemically processed material confirmed that the material had remained attached during the analysis and therefore the measured decrease in signal was from the oxidisation of copper (rather than, say, material loss).

5.2.1.2 Electrode types and sample pH

Alterations from the initial experimental trials were made for two main reasons; cost factors relating to the continued use of ITO electrodes, and the pH value of the material to be processed -as both the Malvern Mastersizer and the Bruker XRF machine required pH7 samples for safe analysis.

- Regarding the continued use of ITO; a trial comparing the effectiveness of 4 different electrode types was undertaken, the results of which showed that electrode performance, from best to worst, was as follows; EPPG, ITO, GC then BPPG. Despite GC having the second lowest efficiency when oxidising copper from the sample, this electrode type was chosen for the subsequent experiments due to its cost and availability.
- Regarding the acidity of the sample material; the supernatant of the material collected material in the experiment was raised though serial dilution with deionised water to pH7.

5.2.1.3 The Pourbaix diagram

Following neutralisation of the sample material the observed CV scan altered from showing 1 single peak to a multi peak profile. The reason for the single to twin peak distribution can be explained by reference to the Potential vs. pH Pourbaix diagram, shown in Figure 5-2. The initial material analysed had an acidic pH of approximately 0.5 and was processed over a voltage range of -0.4 to 0.4V with respect to a Ag/AgCl reference electrode, approximately –0.2 to 0.6V vs. a Standard Hydrogen Electrode (SHE) marked on Figure 5-2 as A. This location on the Pourbaix diagram indicates how the only species copper could oxidise to, at a pH value of 0.5 and between -0.2 to 0.6V vs. SHE, was Cu^{2+}. Comparatively, the neutralised material (neutralised by serial dilution), shown on the Pourbaix diagram as B, indicates how the copper, when raised through a potential of -0.1 to 0.9V vs. SHE, oxidised through Cu_2O and CuO -hence the double peak on the CV scan. Following re-acidification of the sample down to a pH of 1 (label C), the sample material was electrochemically processed between -0.1 and 0.5V vs. SHE. The resulting single peak, as indicated in the Pourbaix diagram (Figure 5-3) as C, was associated with the $Cu \rightarrow Cu^{2+} + 2e^-$ oxidation process.

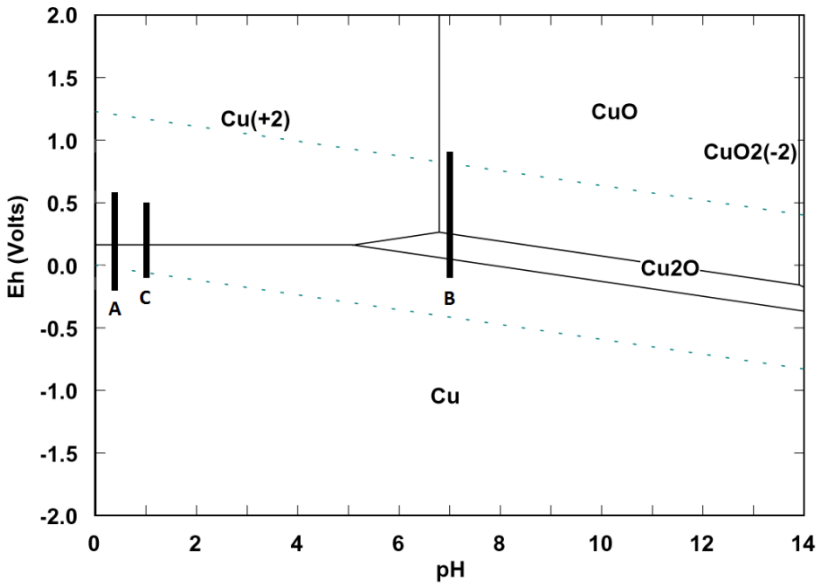

Figure 5-2 Potential (with respect to SHE) vs. pH Pourbaix diagram for Copper. Lines A, B, and C indicate the pH and potential range of the undertaken CV scans[128]

Following analysis of the Pourbaix diagram it was deemed that electrochemistry series B on Figure 5-2 (pH 7 -0.1 to 0.9V vs. SHE) was unsuitable for the removal of copper from the material collected from the A205 alloy by dissolution in HCl. The diagram revealed the oxidation products of the copper, while oxidised at pH7, to be Cu_2O and CuO. As Cu_2O and CuO were not soluble within the carrier electrolyte solution, and also as they are both electrical insulators and could theoretically depositing an insulating layer around a TiB_2 particle, isolating it from further oxidation, this range of processing was deemed unsuitable for further investigations. However, when the oxidisation of Cu in an acidic medium was undertaken, represented by labels A and C in the Pourbaix diagram, the oxidised product was Cu^{2+}. Cu^{2+} is a suitable oxidisation product for the Cu contained within the experimentally collected TiB_2, as it was electrostatically repelled by the cathodic working electrode and was also soluble within the electrolyte.

Table 5.2.1 shows the predicted percentage values of the amounts of copper within the ~1L 'parent' samples of dissolved material -from which the respective microliter samples were taken from, which would have been removed by oxidation had the electrochemical experiments been scaled up to process the entire amount of dissolved material. The value was calculated through the extrapolation of results and their comparison to the volume and weight of the respective initial dissolution experiments. The results show how the oxidation process, followed by the re-acidified material (label C) would offer the more effective method of copper removal.

Table 5.2.1 Predicted values of copper which would have been removed via oxidation had the experimental set up theoretically processed 1 litre of sample

Experiment		**Calculated % of Cu oxidised (extrapolated from Y = 0)**
A	Total charge	2.32
	Reviewed charge	2.01
C	Total charge (5µl, 10µl, 20µl)	17.73
	Total charge (5µl, 10µl)	35.42
	Reviewed charge (5µl, 10µl, 20µl)	16.90
	Reviewed charge (5µl, 10µl)	34.73

Regarding the difference between the levels of copper oxidised when comparing the two electrochemistry trials (A and C) it should be noted that experimental trial A was scanned at 25mV/s, whereas trial C was scanned at 100mV/s -a parameter known for its oxidisation peak broadening effects. Additional reasons offered in explanation of the different oxidised copper values include:

- The two trials were carried out using different electrodes; trial A used ITO whereas trial C used a GC electrode type.

- Additionally, the carrier electrolyte solution for trial C was 0.1M H_2SO_4, giving the total solution a pH of 1. For trial A, the carrier electrolyte solution was 0.1M KCl, the low pH value was present within the original material following A205's dissolution in 2M HCl -a process leaving the solutions final pH value to be approximately 0.5. It was therefore possible that any remaining HCl present in the original material was extracted with the sample to be tested resulting in its crystallisation as the sample dried onto the GC electrode. Upon the samples exposure to the carrier electrolyte solution the HCl then re-dissolved lowering the pH locally around the electrode enough to satisfy the conditions of Cu^{2+} production, but at different rates to trial C hence resulting in the differing copper oxidisation values for the same sample volumes.

The conclusion drawn from the first stages of the electrochemical trials suggested that the copper containing material collected from the dissolution of A205 could be electrochemically purified whilst preserving the TiB_2 particles contained for further analysis. This lead onto the processing of the experimentally collected material using a chronoamperometry technique.

5.2.2 Removed copper

As detailed in the electrochemistry results section, a chronoamperometry technique was used in an effort to scale up the electrochemical process. The process required an electrode to be held at a set voltage within a suspension of the sample. The supernatant of the material was altered to 0.1M H_2SO_4 to act as a carrier electrolyte. The results showed a decrease in the measured current over the 3hr treatment, indicating a reduction in the amount of copper within the sample. Over the 3hr period the measured charge

decreased by 85% from approximately 5.3 to 0.75mA, indicating oxidation of copper and hence removal into solution. In an effort to quantify the success of the technique a sample of the processed material was analysed using an XRF liquid analysis technique, however, the results indicated that both titanium and copper were still present within the processed material, although this may have been, in part, due to the copper containing supernatant of the sample being detected during analysis. For this reason, a sample of the processed precipitate was removed and dried for PXRD analysis, which revealed the sample to be comprised of TiB_2 and Cu_2O. It is unclear how the Cu_2O material developed within the sample material as the carrier electrolyte solution was pH 1, but, with the assumption that up to approximately 70% of the copper (Table 4.4.4) was oxidised from the sample into Cu^{2+}, this material was subject to particle size analysis.

5.2.3 Particle size analysis

Comparison of the particle size analysis results between the pre and post-electrochemically processed material revealed a reduction in the measured particle size which indicated that the electrochemical processing had been at least partially successful. Comparison of pre and post electrochemically processed materials showed a reduction in both the volume based and number based particle size TiB_2 particle size distributions, with reductions in d(0.5) values of 10.38 to 9.08µm for the volume distribution and, 0.68 to 0.49µm for the number transformed particle size distribution.

5.3 A205's Predicted Yield Stress

The strength of an alloy can be thought of as a combination of strengthening effects. Each strengthening effect is itself a combination of different factors -some of which are irrelevant during the different stages of the alloys processing, while other properties have

historically been made from comparatively coarse measurements, for example the use of a single average rather than a more representative selection of measured values. In this research effort was made towards refining A205's predicted yield strength, with specific attention being focused on the strength contributions attributed to the presence of the TiB_2 particle size distribution, at 4.26wt% within the standard alloy, and located primarily within the grain boundaries.

5.3.1 Predicting A205's as-cast yield strength

The yield strength of as-cast A205 can be thought of as being a combination of contributions from both the grain and grain boundaries. Without the resulting contributions caused by heat treatment the grain materials' strength can be thought of as predominantly originating from the Hall-Petch mechanism (since few TiB_2 particles are expected in the matrix). The grain boundary's strength originates from; the Coefficient of Thermal Expansion (CTE), and the Load bearing strengthening mechanism present between the TiB_2 crystals and the surrounding grain boundary material.

For the as-cast material the Hall-Petch strength contribution was calculated from the individual size of each of the 335 grains analysed. Similarly, the CTE and load strengthening mechanisms were calculated from the measured TiB_2 particle size distribution. The resulting grain and grain boundary's strengths were then combined weighted by their measured area fractions.

Comparison between the experimentally measured yield strength of 123 MPa and the predicted yield strength values calculated using either; the volume-based (53 MPa) or number transformed (110 MPa) TiB_2 particle size distributions collected from as-cast A205 has been summarised in Table 5.3.1. Analysis revealed the predicted Yield

Strength from the TiB_2 particle size distribution generated using the number transformation function of the Malvern machine to be closer to the experimentally determined value (at 89% of the measured yield strength) than the volume calculated particle size distribution (at 43% of the measured yield strength). Furthermore, in respect to the number transformed particle size distribution, specifically for the as-cast material, the strength provided by the grain boundary material was calculated to have contributed 72% to the yield strength as a whole.

Table 5.3.1 Total predicted Yield Strength and the respective contributions from both the grain and grain boundary materials based on measured TiB_2 particle size data collected from as-cast A205

TiB_2 particle size distribution type	Total predicted Yield Strength (MPa) and comparative percentage to measured value of 123 MPa	**Grain** (Volume fraction = 72.7%)		**Grain Boundary** (Volume fraction = 27.3%)	
		Strength (MPa)	Contribution to total predicted YS (%)	Strength (MPa)	Contribution to total predicted YS (%)
As-cast Volume	53 (43%)	30	57	22	43
As-cast Number	110 (89%)	30	28	79	72

5.3.2 Predicting A205's fully heat-treated Yield strength

The main strengthening mechanisms in solution heat-treated and precipitation-hardened A205 are; Hall-Petch, Orowan, Coefficient of Thermal Expansion (CTE) and the Load bearing strengthening mechanisms. The Hall-Petch and Orowan strengthening mechanisms are linked to the grain material, the CTE and Load strengthening mechanisms are linked to the grain boundary material. The strengthening mechanisms present within the grain are due to grain size and the Ω and θ precipitates present due to

the heat treatment process. The strengthening mechanisms present within the grain boundary material are primarily due to the size of the TiB_2 particles and their CTE mismatch with the grain boundary material (α-Al). In each instant the grain boundaries Load contribution was calculated to be <1% of the total yield strength and hence has been neglected.

A summary of each mechanism contributing to the predicted yield strength, for each of the measured number-transformed particle size distributions, can be found in Figure 5-3. In each instance the results showed that the Orowan strengthening mechanisms, provided the first and third greatest strengthening contributions to the alloy when considering the Ω and θ precipitates, respectively. The second largest contributing strengthening mechanism was the CTE mechanism, contributing approximately one quarter of the overall predicted yield strength of the alloy. This highlights the importance of considering the grain boundary material as a separate material which gives the grain boundary material its strength, hence the necessity to accurately measure and control the TiB_2 particle size distribution. The strengthening mechanism with the 4^{th} most significant strengthening contribution to the alloy was found to be the Hall-Petch strengthening mechanisms, which contributed just under 10% of the material yield strength.

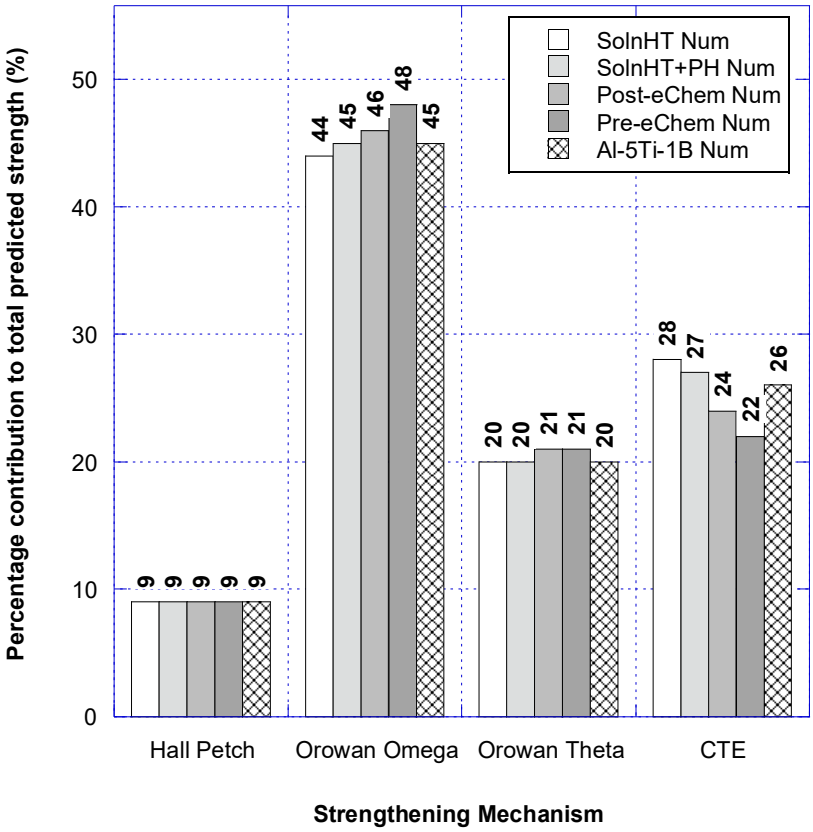

Figure 5-3 Strengthening mechanisms percentage contribution to total predicted yield strength for each measured TiB_2 number transformed particle size distribution -based on the strengthening mechanisms required for fully heat treated A205.

A further summary of the effects of the various measured TiB_2 particle size distributions is shown in Table 5.3.2. This revealed that the predicted yield strength calculated using the number-transformed particle size distribution gave a value closer to that of the experimentally measured yield strength, than when compared to a predicted yield strength calculated using the volume-based particle size distribution -shown in the second column of the of the table by comparison of the percentage contributions from the volume or number particle size distributions. Furthermore, the variation between each number based TiB_2 particle size distribution, although slight, led to a variation of 27 MPa. For instance, the predicted yield strength increased when comparing the post-

electrochemically (335 MPa) to pre-electrochemically (325 MPa) values of TiB_2 particle size distribution -suggesting that the copper removal from the electrochemistry trials were at least in part successful.

Table 5.3.2 Total predicted Yield Strength and the respective contributions from both the grain and grain boundary materials based on; volume and number transformed TiB_2 particle size distributions collected from; both A205 heat treatment stages, Al-5Ti-1B grain refiner material, and pre/post electrochemically processed materials

TiB_2 particle size distribution type	Total predicted Yield Strength (MPa) and comparative percentage to measured value of 426 MPa	**Grain** (Volume fraction = 72.7%)		**Grain Boundary** (Volume fraction = 27.3%)	
		Strength (MPa)	Contribution to total predicted YS (%)	Strength (MPa)	Contribution to total predicted YS (%)
SolnHT: Volume distribution	283 (66%)	254	90	29	10
SolnHT: Number distribution	352 (83%)	254	72	98	28
SolnHT+PH: Volume dist	280 (66%)	254	91	26	9
SolnHT+PH: Number dist	346 (81%)	254	73	92	27
Al-5Ti-1B: Volume dist	285 (67%)	254	89	31	11
Al-5Ti-1B: Number dist	342 (80%)	254	74	87	26
Pre-eChem: Volume dist	277 (65%)	254	92	23	8
Pre-eChem: Number dist	325 (76%)	254	78	71	22
Post-eChem: Volume dist	278 (65%)	254	91	24	9
Post-eChem: Number dist	335 (79%)	254	76	80	24

5.4 Microstructure

Globularity is a key feature of A205 alloy, it increases strength by lowering sharp angled features present in dendritic materials, and lowers porosity by promoting uninhibited feeding routes into the inter-grain areas of a solidifying casting. To refine A205's globular structure an investigation into the separate effects of TiB_2 and free titanium content was carried out.

5.4.1 Globularity and TiB_2

In comparison to A205 alloy's standard composition of 4.26wt% TiB_2 (as measured by XRF), the TiB_2 content was reduced to 2.49 wt% and 1.16 wt% for measurement of globularity. To dilute TiB_2 content alloying additions were made to ensure that the remainder of the melt remained within specification limits. For the 4.26% (unmodified A205 sample), 2.49%, and 1.16% alloys; 335, 379 and 465 grains were imaged respectively. For each grain the perimeter was compared to its area in order to determine its circularity. The mean circularity values calculated for the 4.26 wt%, 2.49 wt% and 1.16 wt% were 0.72, 0.73 and 0.74 respectively. As the mean grain circularity values calculated for each alloy type was higher than the circularity value of a regular geometric hexagram -a bench mark profile (with a circularity value of approximately 0.44) chosen for its visual similarity to that of a cell representing half way between dendritic and thamnitic, the assumption was made that each grain could be approximated to a perfect circle therefore allowing the respective diameter of each grain to be calculated. The standard TiB_2 content (4.26% TiB_2) had a grain size of 21µm, while the 2.49% TiB_2 and 1.16 wt% had grain sizes of 26µm and 22µm. Analysis of the calculated diameters revealed that a decrease in TiB_2 content from 4.26 wt% to 1.16 wt% did not have a significant effect on the grain size of the alloy.

It is well documented that TiB_2 is a grain refiner[129], and logic dictates that a threshold value must exist whereby the addition of more TiB_2 will not refine the formation of subsequent grains due to neighbouring crystals already occupying the remaining available space -hence limiting further growth and supressing dendrite formation. The rate at which a casting solidifies also plays a part in grain refinement and the formation of a globular microstructure; as a slow solidifying front, below a critical velocity will push particles ahead of its solid-liquid interface rather than engulfing them. A large concentration of particles in front of the solidifying crystal will also act to suppress dendrite formation[130]. If the particles are in a high concentration, or clustered together, the front can have a greater velocity and still push the particles ahead of the advancing interface[130].

In consideration of this the globularity of the solidified grains remains an important feature of the microstructure and therefore its principal should be incorporated into Yield Strength calculations. Therefore, the author suggests that the circularity value should be incorporated into the Hall-Petch strengthening mechanism, as it is the effects of the TiB_2 particles on grain size and shape which affect the resulting strength of the material. The circularity should be incorporated so that the current Hall-Petch equation predicts the maximum available contribution to yield strength at a circularity of value of 1.0 and reduces with lower circularity values to a threshold value set at the strength of a dendritic microstructure.

Following calculations of the grain to grain boundary area fraction, it was found that the grain boundary area fraction measurements decreased with reduced TiB_2 weight percentages from; 27% for standard A205, to 16.7% for 2.49wt%. This area fraction decrease was attributed to the physical reduction of available grain boundary material. A

similar reduction in the grain boundary area fraction for 1.16 wt% TiB_2 was expected, however a value of 22% was measured. A comparable finding was previously documented at 0.9wt% TiB_2 by Butler (2000)[1], in which the cause of such a reduction in elongation properties was confirmed as porosity (using a dye penetration test).

5.4.2 Globularity and Free Titanium

The standard composition of A205 had a free titanium value of 0.26wt%, which was increased to 0.43 and 0.48wt% for subsequent experiments.

The grain analysis results revealed the initial alloy to have similar circularity values to both the 0.43 and 0.78wt% free titanium samples. The reference standard had a value of 0.72. The mean circularity value for the 0.43wt% and 0.48wt% free titanium samples were 0.75, and 0.74 respectively. The measured circularity values were again deemed high enough for all measured grains to be treated as perfect circles allowing grain size calculations. The two higher free titanium alloys had comparable mean grain size when compared to the standard (21µm) alloy, with mean grain size values of; 17µm and 18µm for the 0.43% and 0.48% free titanium alloy respectfully. The grain boundary area fractions were measured to be: 0.26wt%, 0.43wt% and 0.48wt% samples at: 27%, 28% and 26%.

Comparison of the tensile properties of solution heat-treated and precipitation hardened A205-as detailed in the effect of composition on globularity -free titanium, experimental section, revealed the yield stress to decrease with increased (free) titanium from 426 MPa, to 419 MPa and 414 MPa. UTS values for the initial alloy (0.26 wt%), 0.43 wt% and 0.48 wt% (free) titanium samples varied little and were measured to be 455 MPa, 461 MPa and 454 MPa respectively. Regarding elongation values both of the increased free

titanium alloys had % elongation values of 3.0% whereas the initial alloy had a value of 2.1%.

5.5 TiB_2 particle size and its influence on grain refinement

To establish the effect of TiB_2 particle size on the grain size of aluminium a series of TP1 tests were carried out in which the TiB_2 particles were qualitatively characterised into 3 size groups and the resulting grain sizes compared.

5.5.1 Particle size analysis

The TiB_2 particles required for this analysis was extracted from a sample of Al-5Ti-1B grain refiner. The reasons for using Al-5Ti-1B grain refiner as a source of TiB_2 particles include that it was possible to remove the particles without contamination from copper, and also that 80% of the measured particle size distribution fell between 0.27μm and 1.53μm in size as shown in Figure 5-4 and Table 5.5.1.

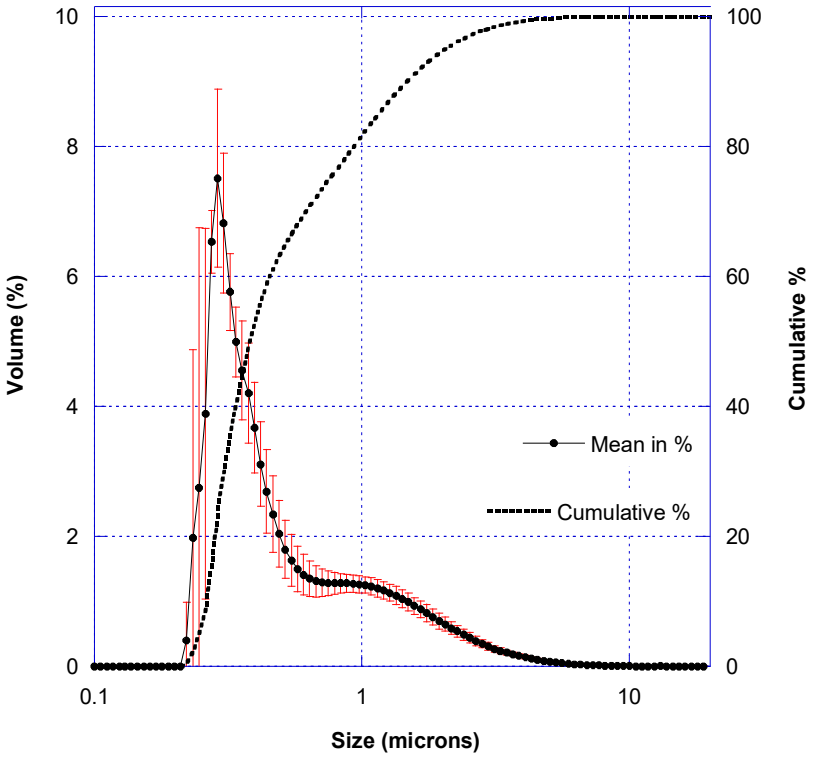

Figure 5-4 Number transformed particle size distribution of Al-5Ti-1B grain refiner

Table 5.5.1 d(0.1), d(0.5) and d(0.9) values for the number transformed particle size distribution of Al-5Ti-1B grain refiner

Sample	d (0.1) µm	d (0.5) µm	d (0.9) µm
E123 Avg (NumT)	0.27	0.40	1.53

5.5.2 Settling theory

The settling velocity of a particle is primarily based on the following properties; the difference in density between the particle and liquid, the dimensions/shape of the particle, the viscosity of the medium that the particle is falling thorough, and the acceleration due to gravity. By holding samples of molten aluminium in a resistance furnace for differing amounts of time it was possible to create material containing variable TiB_2 particle sizes.

5.5.3 XRF analysis

As an initial experiment a sample which had undergone an arbitrary 10 minute period of settling was vertically sectioned. Visual examination, revealed that a line of material was present approximately 5 to 10mm below the top surface of the casting, above which the material had an increased lustre when compared to the material below the line (see Figure 5-5).

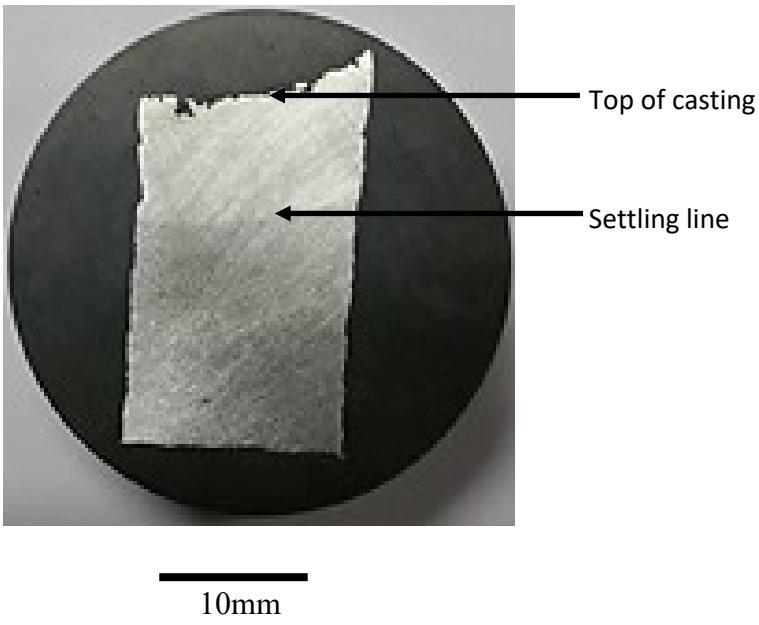

Figure 5-5 Mounted section from the top of a settled casting showing the settling line

XRF analysis showed that the top of the casting, i.e. above the settled line comprised of 97% Al and 0.18wt% Ti. Below this line the Top, Middle and Bottom sample locations contained 5.0, 4.9 and 5.8 wt% Ti respectively, as shown in Figure 5-6.

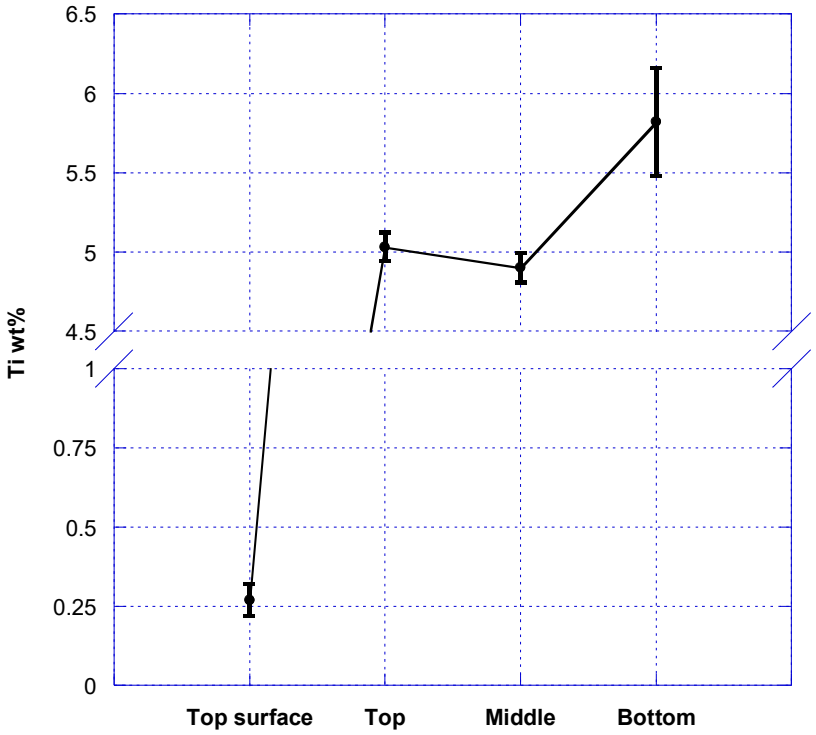

Figure 5-6 Titanium weight % levels of the top surface, top, middle and bottom of the 10min settled Al-5Ti-1B grain refiner

Figure 5-6 shows the Ti content within the sample, held for 10 minutes, measured using XRF. The results showed that the Ti, as TiB_2 settled within the casting over a period of 10 minutes. The post-settled casting can be thought of as being comprised of two layers; the upper layer (which has a lustrous surface and small titanium content), and the lower layer which was duller in appearance and contained titanium content measured to be greater than 4.5%. Within the lower layer the Ti underwent a further settling process in which the material at the bottom of the lower layer had a higher Ti content than when compared to the material at the top of the upper layer as a result of density difference and hence the settling effect.

5.5.4 ICP analysis

To further distinguish the settling of the TiB_2 particles samples after settling were analysed by ICP (Rotech Laboratories Ltd). From the reported titanium and boron values, the TiB_2 composition was calculated.

5.5.4.1 ICP: TiB_2

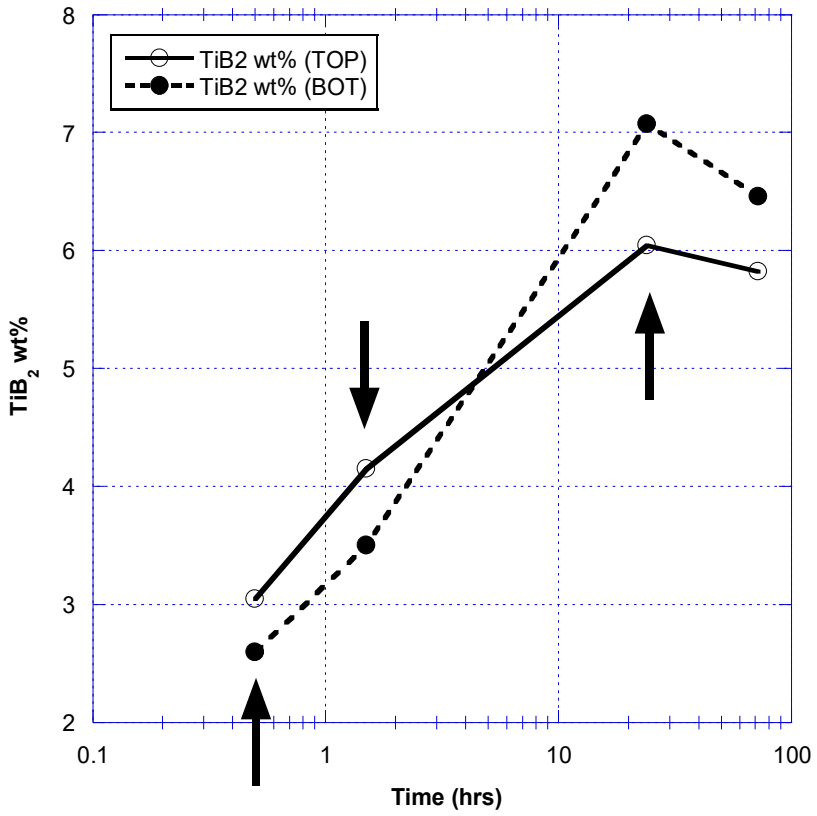

Figure 5-7 ICP determined TiB_2 weight% values for the settled material taken from the top and bottom of each sample

Figure 5-7 shows the TiB_2 content in each of the settled samples as quantified using ICP. The two lines on the graph represent whether the sample was taken from a slice located in the top half of the casting or the bottom. The 3 arrows present indicate the 3 samples which were chosen for further grain size measurement. The measured TiB_2 content of

the settled sampled increase with time. Regarding the relative TiB_2 content at the 'top' and 'bottom' for the different settling times; the TiB_2 content of the 30 minute and 90 minute samples were higher at the top of the sample than the bottom of the sample, and the TiB_2 content of the 24 hr and 72 hr samples was higher at the bottom of the sample than at the top of the sample. This effect could be explained by the settling time required for the particles to travel the 0.10m length of the settling crucibles having between 90 minutes and 24 hrs -as an approximation the intersection of the crossing lines indicates a time of between 4 and 5 hrs, and hence the accumulation of TiB_2 particles at the bottom of the casting after this period of time.

5.5.4.2 ICP: Free Ti

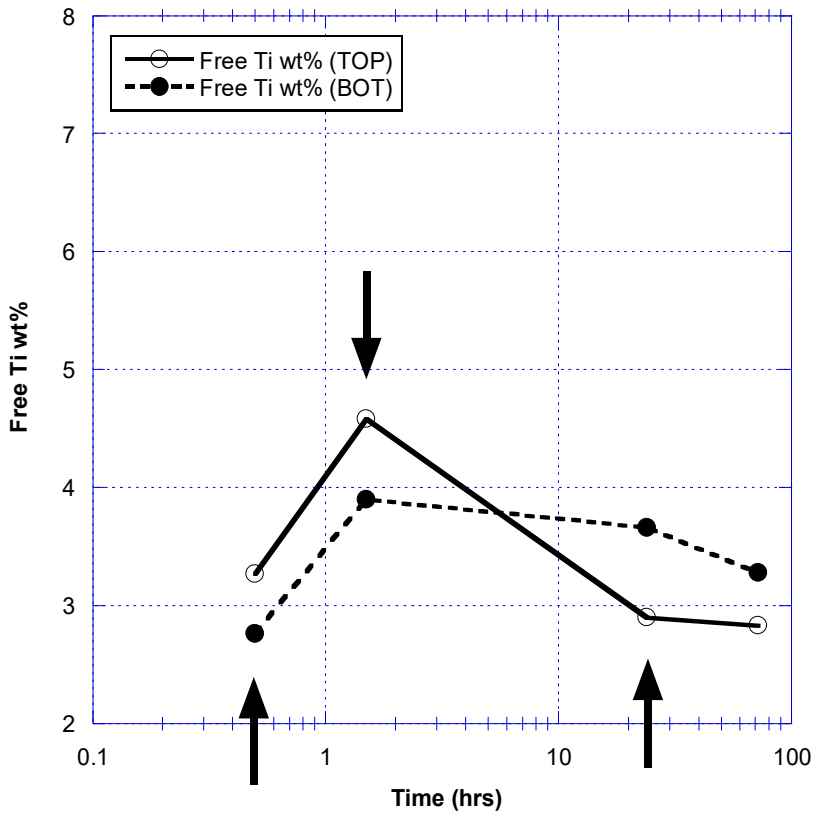

Figure 5-8 ICP determined free Ti weight% values for the settled material taken from the top and bottom of each sample

Figure 5-8 shows the free Titanium content in each of the settled samples quantified using ICP. The two lines present on the graph represent whether the sample was taken from a slice located in the top half of the casting or the bottom. The 3 arrows present indicate the 3 samples which were chosen for further grain size measurement. Similarly, when compared to Figure 5-7, the free Ti content (i.e., the titanium which contained within the TiB_2 but was present as Ti in solution) was higher in the top of the sample for the first two settling times, and higher in the bottom of the sample for the last two settling times.

5.5.5 TP1 grain size analysis

In effort to ascertain whether the size of the TiB_2 particles had any effect on the grain size, several TP1 tests were carried out. The material chosen for analysis was the 30 minute, 90 minute and 24 hr settled materials. These settled materials, based on their composition determined by ICP, were added to commercial purity Al in order to being the melt into the TP1 defined specification of 100ppm Ti, 20ppm B. As there was not enough material available to quantitatively run simultaneous particle size analysis on the settled material (despite Malvern Instruments' best efforts), a qualitative method of determining the TiB_2 particle size was used.

Standard Al-5Ti-1B grain refiner was used as the reference samples (Sample A).

30 min bottom (sample B) - this sample should have had the largest TiB_2 particle size compared to the other 2 samples as it was the only sample to be taken from the bottom of the settled material and from a time period of when only the largest TiB_2 particles have settled.

90min top (sample C) - this sample should have contained a TiB_2 particle size distribution between those found in samples B and D - as it was taken from the top of a settled casting and within a time frame during which only the largest particles will have settled in the alloy.

24hr top (sample D) - this sample should contain the finest TiB_2 particles at it was taken from the top of the 24hr settled material -after a time period which would have ensured that all of the largest TiB_2 particle should have settled out from this location.

5.5.5.1 Circularity values and grain size estimations

Table 5.5.2 Quartile spread of each of the TP1 sample's solidified grain circularity values

	A (ref)	**B**	**C**	**D**
# grains	2544	1593	1805	1037
Mean	0.698	0.654	0.649	0.614
Max value	0.993	0.960	0.986	0.967
Upper whisker	1.050	1.087	1.026	0.982
Quartile 3	0.793	0.769	0.750	0.712
Quartile 2	0.720	0.678	0.674	0.632
Quartile 1	0.622	0.558	0.566	0.533
Lower whisker	0.366	0.240	0.290	0.263
Min value	0.212	0.156	0.123	0.169

Table 5.5.2 shows the quartile spread of each of the circularity values, which help describe the spread of a distribution. The second quartile is the median value of the data, the 1st and 3rd quartiles are values which are half-way between the 2nd quartile and the smallest or largest measured value, respectively. The table also shows the mean value of the collected circularity values for each sample. Compared to the Al-5Ti-1B grain refiner

reference sample (0.72), samples; B (0.68), C (0.67) and D (0.63) all had comparatively smaller mean circularity values. In each instance 75% of the measured circularity values had a value greater than 0.5. For this reason, the method of determining the grain diameter of each sample by taking each grain to be a true circle and hence calculating its diameter based upon its area was deemed acceptable.

5.5.5.2 Diameter vs. percentage occurrence for TP1 samples; A, B, C and D

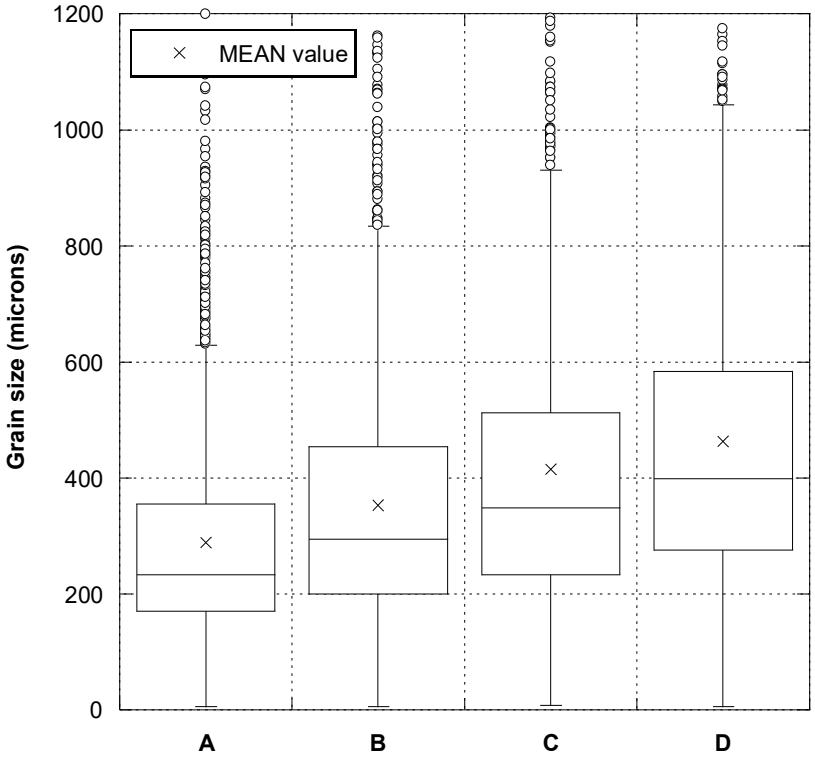

Figure 5-9 Comparison between the measured grain sizes for TP1 samples: A, B, C and D

Figure 5-9 shows a comparison between the measured grain sizes for TP1 samples; A, B, C and D. The figure shows how the measured grain size distribution increased to larger grain size values between sample A, B, C and D, respectfully. By comparing the 1st, 2nd

and 3rd Quartile values, a non-Gaussian distribution type was apparent by the separation between the 2nd and 3rd quartiles being greater than the 1st and 2nd quartiles.

Table 5.5.3 Quartile spread of each of the TP1 sample's gran size distributions

	A	B	C	D
Number of grains analysed	2544	1593	1805	1037
Mean (µm)	288.6	353.1	415.3	463.3
Max value (µm)	1424.0	1530.2	3484.1	2122.1
Upper whisker (µm)	630.6	836.8	932.6	1045.1
Quartile 3 (µm)	354.7	454.4	513.2	583.7
Quartile 2 (µm)	233.5	294.0	348.6	398.5
Quartile 1 (µm)	170.8	199.5	233.6	276.2
Lower whisker (µm)	< 0	< 0	< 0	< 0
Min value (µm)	6.1	6.1	8.8	6.0

Table 5.5.3 shows the quartile spread of each of the TP1 grain size distributions as shown in Figure 5-9. Comparing the mean and quartile values between the samples highlights the varying grain size distributions. In each case the mean value and the 1st, 2nd and 3rd quartile values increased between samples A, B, C and D.

5.5.5.3 Kolmogorov-Smirnov test

The basis of the Kolmogorov-Smirnov test is to compare the cumulative distribution between two samples. The test is non-parametric and as such does not assume that the distribution follows any particular distribution type and is sensitive to a distribution's shape as well as its median and spread. The null hypothesis of the test is to assume that both distributions are from the same population of data. The p-value gives the probability

of the two distributions originating from the same population of data, i.e., the smaller the p-value the more likely the data sets are statistically different. The value often considered as the value threshold for determining whether two distributions are different is 0.05. As each of the reported sample comparison p-values was less than 0.05 it can be concluded that each of the samples were statistically different from one another, see Table 5.5.4. However, due to the samples originating from different sized data sets the comparison between these values would be inaccurate. A more suitable method of comparison would be analysis between the difference in D-stat and D-crit values between each of the statistical trials. Such a comparison yielded: A to D to be the most statistically dissimilar distribution, followed by; A to C, B to D, A to B, B to C, then C to D.

Table 5.5.4 Kolmogorov-Smirnov statistical values for each partied variation of samples A, B, C and D

A to B

D-stat	0.153
p-value	3.49E-11
D-crit	0.043
size 1	2544
size 2	1593
Sig diff?	yes

A to C

D-stat	0.260
p-value	1.99E-04
D-crit	0.042
size 1	2544
size 2	1805
Sig diff?	yes

A to D

D-stat	0.365
p-value	1.52E-03
D-crit	0.050
size 1	2544
size 2	1037
Sig diff?	yes

B to C

D-stat	0.112
p-value	8.92E-10
D-crit	0.046
size 1	1593
size 2	1805
Sig diff?	yes

B to D

D-stat	0.220
p-value	8.98E-09
D-crit	0.054
size 1	1593
size 2	1037
Sig diff?	yes

C to D

D-stat	0.107
p-value	4.35E-07
D-crit	0.053
size 1	1805
size 2	1037
Sig diff?	yes

Theoretically similar work was investigated by Quested et al, [131] who carried out research into the importance of the (TiB_2) particle size distribution for grain refinement purposes using hypothetical log-normal distributions in a thermal model. Quested's calculations predict the most effective TiB_2 grain size, which gives the finest crystal structure, to be 0.7μm in diameter, a value already comparable to the commercially available Al-5Ti-1B grain refiners TiB_2 distribution of 1.0μm. On either side of this value the resulting grain diameter increase. From a decrease in TiB_2 diameter the increase in the resulting grain diameter will be larger than if the TiB_2 particle size distribution had been increased as shown in Figure 5-10.

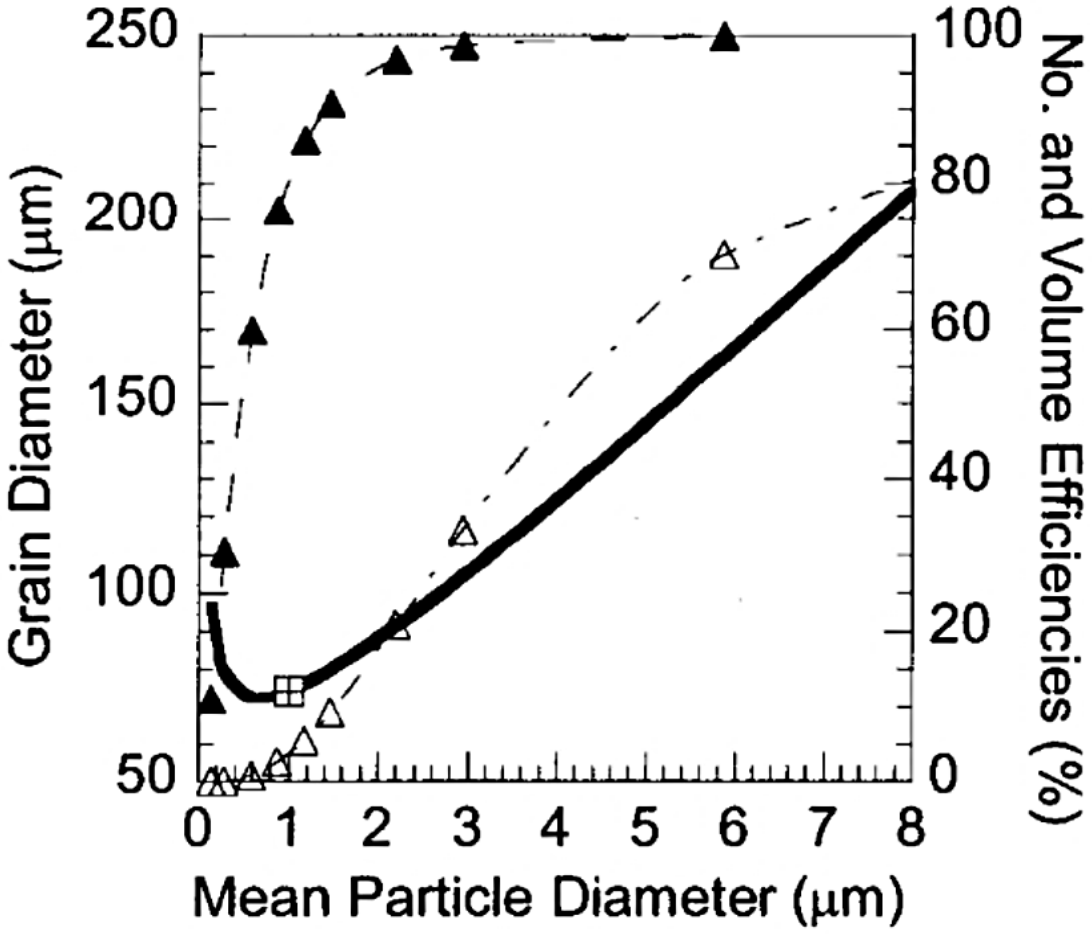

Calculated grain diameter (bold line), volume efficiency (▲), number efficiency (Δ) against mean particle diameter. (⊞) denotes the values for commercial Al-5Ti-1B.

Figure 5-10 Quested et al's[132] graph on TiB_2 particle size vs. resulting grain diameter

This research experimentally determined the Al-5Ti-1B to have a TiB_2 particle size distribution of 0.27, 0.40 and 1.53µm for the d(0.1), d(0.5) and d(0.9) values respectively. By allowing the material to settle for differing amounts of time different bands of TiB_2 particle sizes were created and used for grain refinement testing.

The measured grain sizes of samples A, B, C and D were all proven to be statistically different from one another. Sample A, the un-settled Al-5Ti-1B reference sample, gave the smallest grain size at 289µm. Sample B, which qualitatively contained the largest

TiB_2 particles, had the next largest measured mean grain size of 353µm. Sample C, which contained smaller TiB_2 particles than sample B had a larger measured mean grain size of 415µm. Sample D, with qualitatively the smallest TiB_2 particle size distribution had the largest measured mean grain size of 463µm. Such results were predicted by Quested, Greer and Cooper[133] and therefore can be used in support of this model.

6 CONCLUSION

6.1 The TiB_2 particle size distribution

6.1.1 Best practice for the particle size analysis of TiB_2

Extracted TiB_2 underwent particle size analysis on a Malvern Mastersizer particle size analysis machine. Such machines report the volume based particle size distribution as standard, a method which skews the distribution towards fewer larger particles therefore obscuring particle size contributions from potentially more numerous smaller particles. Hence best practice for measuring extracted TiB_2 was found to be a 10minute medium-strength[2] ultrasonic pre-treatment procedure, incorporated to breakup any agglomerates within the experimentally collected material, followed by ten 30 second measurement periods from which an average particle size distribution was calculated and subsequently transformed by the supplied software into a number based particle size distribution.

6.1.2 Al-3Ti-1B

The TiB_2 particle size distribution contained within Al-3Ti-1B grain refiner was measured after dissolution in hydrochloric acid. Following conversion from a volume based particle size distribution to a number based particle size distribution the d(0.1), d(0.5) and d(0.9) values were measured to be 0.25µm, 0.35µm and 1.29µm respectively.

6.1.3 Al-5Ti-1B

The TiB_2 particle size distribution contained within Al-5Ti-1B grain refiner was measured following dissolution in hydrochloric acid. Following a conversion from a

[2] The Malvern Mastersizer's ultrasonic probe follows a company defined scale

volume based particle size distribution to a number based particle size distribution the d(0.1), d(0.5) and d(0.9) values were measured to be 0.27µm, 0.40µm and 1.53µm respectively.

6.1.4 A205

A205 contains approximately 4.26 wt% TiB_2 particles, predominantly located within the grain boundary material of the alloy. The TiB_2 particles were incorporated into the alloy using the same manufacturing process as was used for the TiBAl grain refiners. The particles from, (i). as-cast, (ii). solution heat-treated, and (iii). solution heat-treated and precipitation hardened materials were removed from the alloy by dissolution in hydrochloric acid for the purpose of particle size analysis.

6.1.4.1 As-cast A205

Following dissolution in hydrochloric acid the TiB2 particles collected from the as-cast A205 underwent particle size analysis. The resulting volume based particle size distribution was converted into a number based particle size distribution, the d(0.1), d(0.5) and d(0.9) values were measured to be 0.36µm, 0.52µm and 1.38µm respectively.

6.1.4.2 Solution heat-treated A205

Following dissolution in hydrochloric acid the TiB_2 particles collected from the solution heat-treated A205 underwent particle size analysis. The resulting volume based particle size distribution was converted into a number based particle size distribution, the d(0.1), d(0.5) and d(0.9) values were measured to be 0.25µm, 0.33µm and 0.90µm respectively.

6.1.4.3 *Solution heat-treated and precipitation hardened A205*

Following dissolution in hydrochloric acid the TiB_2 particles collected from the solution heat-treated and precipitation hardened A205 underwent particle size analysis. The resulting volume based particle size distribution was converted into a number based particle size distribution, the d(0.1), d(0.5) and d(0.9) values were measured to be 0.27µm, 0.37µm and 1.06µm respectively.

6.1.4.4 *TiB_2 particle size vs. heat treatment*

The variation measured between the 3 particle size distributions was attributed to the alloys heat treatment state and the subsequent availability of copper within the grain boundaries to stick to the TiB_2 particles, hence increasing their apparent particle size. Following a comparison of the A205 TiB_2 particle size distributions to the Al-5Ti-1B TiB_2 particle size distribution, (a copper-free source of TiB_2 particles), it was found that all of the A205 TiB_2 particle size distributions were larger than the Al-5Ti-1B's TiB_2 particle size distribution. The largest A205 TiB_2 particle size distribution was measured from the as-cast material. Solution heat-treated and precipitation hardened A205's TiB_2 particle size distribution was smaller than the as-cast's distribution. Solution heat-treated A205's TiB_2 particle size distribution was the smallest of A205's TiB_2 size distributions.

6.2 The electrochemical purification of TiB_2

In effort to remove the copper contamination from the TiB_2 particles extracted from solution heat-treated and precipitation hardened A205 an electrochemical approach was trialled. TiB_2 was found to be electrochemically inert between -0.197 and 1.003V vs SHE, hence underwent an electrochemical process intended to oxidise and remove copper from the material of interest. Comparing the pre and post electrochemically processed

TiB_2 materials both the volume and number based particle size distributions reduced in d(0.1), d(0.5) and d(0.9) values, from; (pre) = 3.0, 10.4, 23.0µm, to (post) = 2.8, 9.1 and 22.8µm respectively for the volume based particle size distributions, and (pre) = 0.4, 0.7, 1.6µm, to (post) = 0.3, 0.5 and 1.5µm respectively for the number based particle size distributions. As the post-electrochemically processed particle size distribution was smaller than the pre-electrochemically processed particle size distribution the principal of the technique can be confirmed as viable, however the experimental parameters used would require further refinements to be deemed a truly successful process.

6.3 A205's predicted yield strength

6.3.1 A205's most significant strengthening mechanisms

The yield strength of A205 can be thought of as originating from both the grain and grain boundary material, based on their respective volume fractions. The most significant strengthening mechanism within the grain material was the Orowan mechanism, which when applied to the Ω precipitates, contributed 45% of the total predicted strength of the fully heat treated alloy. The most significant strengthening mechanism when considering the grain boundary material was the Coefficient of Thermal Expansion mechanism, which contributed 27% of the total predicted yield strength of the material.

6.3.2 The Yield Strengths sensitivity to the TiB2 particle size distribution

The macrostructure of A205 was approximately split into 73% grain material and 27% grain boundary material. The coefficient of thermal expansions strength contribution is due to the TiB_2 particles contained within the grain boundary material and is calculated, in part, with knowledge of the TiB_2 particle size distribution. Comparison of A205's

solution heat treated and precipitation hardened predicted yield strength value when substituting, in turn, the various collected number-based TiB_2 particle size distributions from; as-cast A205, solution heat treated A205, solution heat treated and precipitation hardened A205, Al-3Ti-1B grain refiner and Al-5Ti-1B grain refiner, revealed a variation in the predicted yield strength value of 27 MPa (8% of the total predicted yield strength value). As the d(0.5) variation in TiB_2 particle size between the materials was only 0.19µm it can be concluded that the TiB_2 particle size distribution had a significant effect on the predicted yield strength of the alloy, and was responsible for grain boundary predicted yield strength contribution variations of between 98 and 87MPa.

6.4 A205 microstructure

6.4.1 TiB_2 wt%

The A205 alloy contained approximately 4.26 wt% TiB_2 and had a globular microstructure. Comparison of the standard alloy to alloys containing 2.49 wt% TiB_2 and 1.16 wt% TiB_2 revealed the measured circularity values to remain unchanged at 0.72, 0.73, and 0.74 respectively. It can therefore be concluded that a reduction of TiB_2 wt% from 4.26 to 1.16 did not affect the globularity of the alloy.

Comparison of the calculated grain sizes for the standard alloy to the A205 alloys containing 2.49 wt% TiB_2 and 1.16 wt% TiB_2 alloys remained consistent at; 21µm, 26µm and 22µm respectively. It can therefore be concluded that a reduction of TiB_2 wt% from 4.26 wt% to 1.16 wt% did not affect the grain size of the alloy.

6.4.2 Free Titanium wt%

A205 contains approximately 0.26 wt% free titanium and has a globular microstructure. Comparison of the standard alloy to alloys containing 0.43 wt% free Ti and 0.48 wt% free Ti revealed the measured circularity values to remain unchanged at 0.72, 0.75, and 0.74 respectively. It can therefore be concluded that raising the free titanium levels from 0.26 wt% to 0.48 wt% did not affect the globularity of the alloy.

Comparison of the calculated grain sizes for the standard alloy to the A205 alloys containing 0.43wt% free Ti and 0.48 wt% free Ti alloys was calculated to be; 21µm, 17µm and 18µm respectively. It can therefore be concluded that raising the free titanium levels from 0.26 wt% to 0.48 wt% did not significantly reduce the grain size of the alloy.

6.5 TP1 Grain refinement tests

6.5.1 Settling

Al-5Ti-1B grain refiner was allowed to settle in a 0.10m crucible heated by a resistance furnace. After a settling period of 10 minutes, the sample was allowed to cool in air. During this time the titanium level 5mm below the top surface of the casting had dropped to 0.27±0.005 wt%. Approximately 25mm below the top surface the titanium level was 5.03±0.09 wt%, in the middle of the casting the Ti level was 4.90±0.09 wt %, and approximately 10mm above the bottom of the surface the Ti level was 5.82±0.34 wt%.

Al-5Ti-1B grain refiner was allowed to settle for, 30 minutes, 90 minutes and 24 hours in a 0.10m crucible heated by a resistance furnace before being allowed to cool in air. Samples of each casting were sectioned approximately 25mm from the top surface, and 10mm from the bottom of the casting for ICP analysis. After 30 minutes of settling the

TiB_2 wt% in the top and bottom of the casting was measured to be 3.05 and 2.76 wt% respectfully. After 90 minutes of settling the TiB_2 wt% in the top and bottom of the casting was measured to be 4.15 and 3.90 wt% respectfully. After 24 hours of settling the TiB_2 wt% in the top and bottom of the casting was measured to be 6.04 and 7.07 wt% respectfully.

6.5.2 Grain size

Samples taken from the bottom of the 30 minute settled Al-5Ti-1B casting, and top of the 30 minute and 90 minute settled Al-5Ti-1B castings were selected for TP1 grain refinement tests. Comparison of the resulting TP1 samples revealed each casting to have a significantly different grain size profile than the other settled samples -as determined by the Kolmogorov-Smirnov test. Standard unsettled Al-5Ti-1B grain refiner, taken as a reference sample, had the finest grain size profile with a mean value of 289µm. Sample B which used material taken from the bottom of a 30 minute settled casting had the next largest mean grain size of 353µm. Sample C which used material taken from the top of a 90 minute settled casting had the next largest mean grain size of 415µm. Sample D which used material taken from the top of a 24 hour settled casting had the next largest mean grain size of 463µm. It was therefore concluded that unsettled Al-5Ti-1B grain refiner had the most effective TiB_2 particle size required for grain refinement. 30 minute settled Al-5Ti-1B grain refiner, with qualitatively larger TiB_2 particles, was a less efficient grain refiner than unsettled Al-5Ti-1B. 90 minute settled Al-5Ti-1B grain refiner, with qualitatively smaller TiB_2 particles, was a less efficient grain refiner than 30 minute settled Al-5Ti-1B. 24 hour settled Al-5Ti-1B grain refiner, with qualitatively even smaller TiB_2 particles, was found to be a less efficient grain refiner than 90 minute settled Al-5Ti-1B -a result found to be in support of Quested's model of grain refinement [131].

7 FUTURE WORK

Further refine the electrochemical processing procedure to remove all copper from the experimentally collected TiB_2 to ensure that an accurate particle size distribution is measured, then link to nucleation efficiency and particle pushing.

Further refine predictive yield strength equation to take into consideration all post heat treatment precipitates, then develop additional strengthening mechanisms specific to the grain boundary material (and its treatment as a separate strength contributor to the alloy as a whole), and the effect of final solidified grain shape.

Develop a model which details the relationship and possible compromise between; TiB_2 particle size and strength contribution through grain refinement, and, TiB_2 particle size and strength contribution though grain boundary strengthening.

8 REFERENCES

1. Butler, S. A. The development of a reliable high strength aluminium casting alloy. (University of Birmingham, 2000).

2. Munro, R. G. Material properties of titanium diboride. *J. Res. Natl. Inst. Stand. Technol.* **105,** 709 (2000).

3. Tarr, M. (Bolton U. Metals Basics. *Online postgraduate programme* Available at: http://www.mtarr.co.uk/courses/topics/0131_mb/index.html. (Accessed: 5th June 2017)

4. D.R. Uhlmann, T.P. Seward III, and B. C. No Title. *Trans. AIME* **236,** 527 (1966).

5. J.A. Spittle, G.W. Delamore, and R. W. S. The Solidification of Metals. *Iron Steel Inst.* **110,** 318 (1968).

6. R. Morando, H. Biloni, G.S. Cole, and G. F. B. No Title. *Met. Trans* **1,** 1407 (1970).

7. R.D. Doherty and D. Melford. No Title. *J. Iron Steel Inst* **204,** 1131 (1964).

8. S.C. Flood and J.D. Hunt. No Title. *J. Cryst. Growth* **82,** 552 (1987).

9. H. Fredriksson and A. Olsson. No Title. *Mater. Sci. Technol* **2,** 508 (1986).

10. J. Lipton, W. Kurz, and W. H. No Title. *Concast Technol. News* **22,** 4 (1983).

11. B. Chalmers. in *Principles of Solidification* (John Wiley and Sons, 1964).

12. I. Laren and H. Fredriksson. No Title. *Scand. J. Met.* **1,** 59–69 (1972).

13. L.A. Tarshis, J.L. Walker, and J. W. R. No Title. *Met. Trans* **2,** 2589 (1971).

14. R.D. Doherty, P.D. Cooper, M.H. Bradbury, and F. J. H. No Title. *Met. Trans* **8A,** 397 (1977).

15. J.D. Hunt. No Title. *Mater. Sci. Eng* **65,** 75 (1965).

16. G.S. Cole and G.F. Bolling. No Title. *Trans. AIME* **242,** 153 (1968).

17. J. Campbell. Solidification Technology in the Foundry and Casthouse. *Met. Soc.* 61 (1980).

18. J. Campbell. No Title. *Int. Met. Rev* **26,** 71 (1981).

19. Ph. Thévoz, Zon Jie, and M. R. Proceedings of the Third International Conference on Solidification Processing (Sheffield, U.K.). *Inst. Met.* (1988).

20. I. Maxwell and A. Hellawell. No Title. *Acta Met.* **23,** 229 (1975).

21. J. Leszezynski and N.J. Petch. No Title. *Met. Sci.* **8,** 5 (1974).

22. G.S. Cole and G.F. Bolling. No Title. *Trans. AIME* **239,** 1824 (1967).

23. G.S. Cole and G.F. Bolling. No Title. *Trans. AIME* **236,** 1366 (1966).

24. G.S. Cole and G.F. Bolling. No Title. *Trans. AIME* **233,** 1568 (1968).

25. J.M. Papazian and T.Z. Kattamis. No Title. *Met. Trans* **11A,** 483 (1980).

26. Willian D. Callister, J. *Materials science and engineering an introduction*. (John and Sons. Inc., 2003).

27. Willian D. Callister, J. *Materials science and engineering an introduction*. (John Wiley and Sons Inc, 2003).

28. Campbell, J. in 1200 (Butterworth-Heinemann; 1 edition, 2011).

29. Campbell, J. *Castings (Google eBook)*. (Butterworth-Heinemann, 2003).

30. J.L. Walker. No Title. in *Transactions of the Sixth Vacuum Metallurgy Conference* 33 (New York University Press, 1963).

31. S. O'Hara and W.A. Tiller. No Title. *Trans. AIME* **239,** 497 (1967).

32. J.A. Spittle, G.W. Delamore, and R. W. S. The Solidification of Metals. *Iron Steel Inst.* 318 (1968).

33. B. Chalmers. No Title. *J. Aust. Inst. Met* **8,** 225 (1962).

34. K.A. Jackson, J.D. Hunt, D. Uhlmann, and T. P. S. No Title. *Trans. AIME* **236,** 149 (1966).

35. M.H. Burden. No Title. (Oxford, 1973).

36. Chan, J., Hannah-Moore, N. & Rananavare, S. Controlled Deposition of Tin Oxide and Silver Nanoparticles Using Microcontact Printing. *Crystals* **5,** 116–142 (2015).

37. D.M. Stefanescu. *ASM Handbook Volume 15 Casting*. (ASM International, 1992).

38. Porter, D. A., Easterling, K. E. & Sherif, M. Y. *Phase transformations in metals and alloys.* (CRC Press, 2009).

39. A. Cibula. No Title. *J. Inst. Met.* **76,** 321–360 (1949).

40. A. Cibula. No Title. *J. Inst. Met.* **80,** 1–16 (1951).

41. F. Crossley and L. Mondolfo. No Title. *JOM* **191,** 1143–1151 (1951).

42. I. Maxwell and A. Hellawell. No Title. *Acta Met.* **23,** 901–909 (1975).

43. G. Jones and J. Pearson. No Title. *Met. Trans. B,* **7B,** 223–234 (1976).

44. G. Sigworth. No Title. *Met. Trans* **15A,** 277–282 (1984).

45. M. Guzowski, G. Sigworth, and D. S. No Title. *Met. Trans* **18A,** 603–619 (1987).

46. M. Johnsson, L. Bäckerud, and G. S. No Title. *Met. Trans* **24A,** 481–491 (1993).

47. P. Mohanty and J. Gruzleski. No Title. *Acta Met. Mater.* **43,** 2001–2012 (1995).

48. P. Schumacher, A. Greer, J. Worth, P. Evans, M. & Kearns, P. Fisher, and A. G. No Title. *Mater. Sci. Technol.* **14(5),** 394–404 (1998).

49. J. Spittle and S. Sadli. No Title. *Mater. Sci. Technol.* **11,** 533–537 (1995).

50. M. Kearns and P. Couper. No Title. *Mater. Sci. Technol* **13,** 650–654 (1997).

51. M. Johnsson. No Title. *Z. Met.* **85,** 781–785 (1994).

52. G. Chai, L. Bäckerud, and L. A. No Title. *Mater. Sci. Technol* **11,** 1099–1103 (1995).

53. A.L. Greer, A.M. Bunn, A. Tronche, P. V. E. & and D.J. Bristow. No Title. *Acta Mater* **48,** 2823–2835 (2000).

54. W. Kurz and D. Fisher. in (eds. Tech, T. & Publications) (1988).

55. Easton, M. & Stjohn, D. Grain Refinement of Aluminum Alloys : Part I . The Nucleant and Solute Paradigms — A Review of the Literature. **30,** 1613–1623 (1999).

56. P. Mohanty, F. Samuel, and J. G. No Title. *Met. Mater. Trans B* **26B,** 103–109 (1995).

57. Easton, M. & Stjohn, D. Grain Refinement of Aluminum Alloys : Part II . Confirmation of , and a Mechanism for , the Solute Paradigm. **30,** 1625–1633 (1999).

58. W. Winegard and B. Chalmers. No Title. *Trans. Am. Soc. Met.* **46,** 1214–1224 (1954).

59. Easton, M. & Stjohn, D. Theoretical advances leading to improvement in commercial grain refinement practices in al alloys. **31,** 1–7 (2007).

60. M.A. Easton and D.H. StJohn. No Title. *Acta Mater* **49(10),** 1867–1878 (2001).

61. Uhlmann, D. R., Chalmers, B. & Jackson, K. a. Interaction Between Particles and a Solid-Liquid Interface. *J. Appl. Phys.* **35,** 2986 (1964).

62. D.M. Stefanescu, B.K. Dhindaw, S.A. Kacar, and A. M. Behaviour of ceramic particles at the solid liquid metal interface in metal matrix composites. *Met. Trans*

63. Stefanescu DM, Dhindaw BK, Kacar SA, M. A. Behavior of ceramic particles at the solid/liquid metal interface in metal matrix composites. *Met. Trans* **19A,** 2847–2855 (1988).

64. Kim, J. K. & Rohatgi, P. K. An analytical solution of the critical interface velocity for the encapturing of insoluble particles by a moving solid/liquid interface. *Metall. Mater. Trans. A* **29,** 351–358 (1998).

65. S.N, O. and A. W. N. Thermodynamic aspects of particle engulfment by solidifying melts. *J. Appl. Phys* **47,** 3956 (1976).

66. D.R. Uhlmann, B. Chalmers, and K. A. J. Interaction Between Particles and a Solid-Liquid Interface. *J. Appl. Phys* **35,** 2896 (1964).

67. Chernov, A. A., Temkin, D. E. & Mel'Nikova, A. M. Theory of the capture of solid inclusions during the growth of crystals from the melt. *Sov. Phys. Crystallogr* **21,** 369–373 (1976).

68. Sprul, R. *Modern Physics*. *Modern Physics* (John Wiley and Sons, 1956).

69. De Boer, J., Bird, R. B., Hirschfelder, J. O., Curtiss, C. F. & Bird, R. B. Molecular Theory of Gases and Liquids. *Hirschfelder, Curtiss Bird), lohn Wiley Sons, Inc., New York* (1954).

70. Cisse, G. F. B. and J. A theory for the interaction of particles with a solidifying front. *J. Cryst. Growth* **10,** 56 (1971).

71. Schvezov, C. E. & Weinberg, F. Interaction of iron particles with a solid-liquid interface in lead and lead alloys. *Metall. Trans. B* **16,** 367–375 (1985).

72. P. K. ROHATGI, R. ASTHANA, and S. DAS. No Title. *Int. Met. Rev.* **31,** 115–139 (1986).

73. P. K. ROHATGI, R. ASTHANA, and F. Y. Solidification of metal matrix composites. *Miner. Met. Mater. Soc.* 51–75 (1990).

74. B. C. PAl, S. G. K. PILLAI, R. M. PILLAI, and K. G. S. *Solidification of metal matrix composites*. (The Minerals, Metals and Materials Society).

75. R. TRUMPER and v. SCOTT. Developments in the science and technology of composite materials. in *Proc. 1st European Conf. on Composite Materials, ECCM-1,* 139–144 (1985).

76. J. W. McCOY and F. E. WAWNER: Advances in cast reinforced metal composites. *ASM Int.* 237–242 (1988).

77. P. K. ROHATGI. Interfaces in metal matrix composites. *Metall. Soc. AIME* 185–202 (1986).

78. N. I. ABDUL-LATTEF, A. RAZZAQ, I. .KHEDAR, and s. K. G. No Title. *J. Mater. Sci.* **22,** 466–472 (1987).

79. B. N. KESHAVARAM, P. K. ROHATGI, R. ASTHANA, A. & K. G. SATHYANARAYANA. Solidification of metal matrix composites'. *Miner. Met. Mater. Soc.* 151–167 (1990).

80. Zweben, C. *Composite Materials and Mechanical Design, Mechanical Engineer's Handbook*. (John Wiley & Sons, 1998).

81. Hertzberg, R. W. *Deformation and fracture mechanics of engineering materials*. (USA: John Wiley and Sons Inc, 1996).

82. Zhang, Z. & Chen, D. L. Contribution of Orowan strengthening effect in particulate-reinforced metal matrix nanocomposites. *Mater. Sci. Eng. A* **483–484,** 148–152 (2008).

83. Moataz, A. Microstructure property development in friction stir welds of aluminium based alloys. (University of Birmingham, 2008).

84. Embury, J. D., A. Kelly., R. B. N. in *Strengthening methods in crystals* (Amsterdam: Elsevier publishing company Ltd, 1971).

85. Shanmugasundaram, T., Heilmaier, M., Murty, B. S. & Sarma, V. S. On the Hall – Petch relationship in a nanostructured Al – Cu alloy. *Mater. Sci. Eng.* **A 527,** 7821–7825 (2010).

86. Hansen, N. Hall–Petch relation and boundary strengthening. *Scr. Mater.* **51,** 801–806 (2004).

87. Huskins, E. L., Cao, B. & Ramesh, K. T. Strengthening mechanisms in an Al–Mg alloy. *Mater. Sci. Eng. A* **527,** 1292–1298 (2010).

88. Habibnejad-Korayem, M., Mahmudi, R. & Poole, W. J. Enhanced properties of Mg-based nano-composites reinforced with Al2O3 nano-particles. *Mater. Sci. Eng. A* **519,** 198–203 (2009).

89. Zhang, Z. & Chen, D. Consideration of Orowan strengthening effect in particulate-reinforced metal matrix nanocomposites: A model for predicting their yield strength. *Scr. Mater.* **54,** 1321–1326 (2006).

90. Hou, Y., Gu, Y., Liu, Z., Li, Y. & Chen, X. Modeling of whole process of ageing

precipitation and strengthening in Al-Cu-Mg-Ag alloys with high Cu-to-Mg mass ratio. *Trans. Nonferrous Met. Soc. China* **20,** 863–869 (2010).

91. Zhang Q, C. D. No Title. *Scr. Mater* **51,** 863–867 (2004).

92. Zhang Q, C. D. No Title. *Int J Fatigue* **27,** 417–427 (2005).

93. Koppad, P. G., Aniruddha Ram, H. R. & Kashyap, K. T. On shear-lag and thermal mismatch model in multiwalled carbon nanotube/copper matrix nanocomposites. *J. Alloys Compd.* **549,** 82–87 (2013).

94. Esawi, A. M. K. & El Borady, M. a. Carbon nanotube-reinforced aluminium strips. *Compos. Sci. Technol.* **68,** 486–492 (2008).

95. Lahiri, D., Bakshi, S. R., Keshri, a. K., Liu, Y. & Agarwal, A. Dual strengthening mechanisms induced by carbon nanotubes in roll bonded aluminum composites. *Mater. Sci. Eng. A* **523,** 263–270 (2009).

96. Bagdade, S. D. & ASM. *ASM Ready Reference: Thermal Properties of Metals (Materials Data Series)*. (ASM International, 2002).

97. Deng, C. F., Ma, Y. X., Zhang, P., Zhang, X. X. & Wang, D. Z. Thermal expansion behaviors of aluminum composite reinforced with carbon nanotubes. *Mater. Lett.* **62,** 2301–2303 (2008).

98. X. l. Zhong L. L. E Wong, M. G. Enhancing strength and ductility of magnesium by integrating it with aluminum nanoparticles. *Acta Mater* **55,** 6338–6344 (2007).

99. C. S. Goh, M. Guptaoh, J. Wei, L. C. L. No Title. *Acta Mater* 5115–5121 (2007).

100. Horiba Scientific. a Guidebook To Particle Size Analysis.

101. Murray, D. M. & Holtum, D. a. Inter-conversion of malvern and sieve size distributions. *Miner. Eng.* **9,** 1263–1268 (1996).

102. Rawle, A., Limited, M. I., Park, E. B. & Road, G. Basic Principles of Particle. *Surf. Coatings Int. Part A Coatings J.* **44,** 1–8 (2003).

103. Instruments, M. Inform White Paper Dynamic Light Scattering. *Malvern Guid.* 1–6 (2011).

104. Levoguer, C. Using laser diffraction to measure particle size and distribution. *Met. Powder Rep.* **68,** 15–18 (2013).

105. Horn, A. B. in *digital Encyclopedia of Applied Physics* (Wiley-VCH Verlag GmbH & Co. KGaA, 2003). doi:10.1002/3527600434.eap690

106. Park, S. O. & East, M. User training- Dynamic Light Scattering Achieving reliable Nano particle sizing. (2012).

107. *Standard Test Methods for Tension Testing Wrought and Cast Aluminum- and Magnesium-Alloy Products (Metric)*. *ASTM International* **Designatio,** (2015).

108. Aouadi, S. M., Chladek, J. A., Namavar, F., Finnegan, N. & Rohde, S. L. Characterization of Ti-based nanocrystalline ternary nitride films. *J. Vac. Sci. Technol. B Microelectron. Nanom. Struct.* **20,** 1967 (2002).

109. Murty, B. S., Kori, S. a. & Chakraborty, M. Grain refinement of aluminium and its alloys by heterogeneous nucleation and alloying. *Int. Mater. Rev.* **47,** 3–29 (2002).

110. Mwamba, I. A., Cornish, L. A. & van der Lingen, E. Effect of platinum group metal addition on microstructure and corrosion behaviour of Ti–47·5 at-%Al. *Corros. Eng. Sci. Technol.* **49,** 180–188 (2014).

111. Mikaberidze, M. Corrosion Resistant Titanium Alloys for Medical Tools and Implants. *J. Powder Metall. Min.* **2,** (2013).

112. Lavrenko, V. O., Firstov, S. O., Panasyuk, A. D., Prima, S. B. & Kochubei, V. O. Corrosion of titanium - Aluminum intermetallides. I. High-temperature oxidation of γ-TiAl, TiAl 3, and α 2-Ti 3Al. *Powder Metall. Met. Ceram.* **42,** 184–188 (2003).

113. Hansen, N. Hall – Petch relation and boundary strengthening. *Scr. Mater.* **51,** 801–806 (2004).

114. Il, C. K. *et al.* Prediction models for the yield strength of particle-reinforced unimodal pure magnesium (Mg) metal matrix nanocomposites (MMNCs). 4191–4204 (2013). doi:10.1007/s10853-013-7232-x

115. Wang, T. *et al.* Materials Science & Engineering A Development of TiB 2 reinforced aluminum foundry alloy based in situ composites – Part II : Enhancing the practical aluminum foundry alloys using the improved Al – 5 wt % TiB 2 master composite upon dilution. **605,** 22–32 (2014).

116. Lu, L., Lai, M. O. & Chen, F. L. Al-4 wt% Cu Composite reinforced with in-situ TiB2 particles. *Acta Mater.* **45,** 4297–4309 (1997).

117. Rosalie, J. M., Bourgeois, L. & Muddle, B. C. Precipitate assemblies formed on

dislocation loops in aluminium-silver-copper alloys. *Philos. Mag.* **89,** 2195–2211 (2009).

118. Bakavos, D., Prangnell, P. B., Bes, B. & Eberl, F. The effect of silver on microstructural evolution in two 2xxx series Al-alloys with a high Cu:Mg ratio during ageing to a T8 temper. *Mater. Sci. Eng. A* **491,** 214–223 (2008).

119. Kang-hua, C. & Lan-ping, H. Effects of Ag addition on mechanical properties and microstructures of Al-8Cu-OSMg alloy. (2006).

120. Mukhopadhyay, a. . On the nature of the second phase particles present in an as-cast Al-Cu-Mg-Ag alloy. *Scr. Mater.* **41,** 667–672 (1999).

121. Sun, L., Irving, D. L., Zikry, M. A. & Brenner, D. W. First-principles investigation of the structure and synergistic chemical bonding of Ag and Mg at the Al|Ω interface in a Al–Cu–Mg–Ag alloy. *Acta Mater.* **57,** 3522–3528 (2009).

122. Bourgeois, J. M. R. & L. Silver segregation to θ′ (Al2Cu)-Al interfaces in Al-Cu-Ag alloys. 1–12 (2012).

123. Ringer, S. P., Yeung, W., Muddle, B. C. & Polmear, I. J. Precipitate stability in Al□Cu□Mg□Ag alloys aged at high temperatures. *Acta Metall. Mater.* **42,** 1715–1725 (1994).

124. Carreño-Morelli, E., Urreta, S. E. & Schaller, R. Mechanical spectroscopy of thermal stress relaxation at metal-ceramic interfaces in aluminum-based composites. *Acta Mater.* **48,** 4725–4733 (2000).

125. Zhu, A. W., Chen, J. & Jr, E. A. S. PRECIPITATION STRENGTHENING OF

STRESS-AGED Al ± XCu ALLOYS. **48,** 0–7 (2000).

126. Christy, T. V, Murugan, N. & Kumar, S. A Comparative Study on the Microstructures and Mechanical Properties of Al 6061 Alloy and the MMC Al 6061 / TiB 2 / 12 P. **9,** 57–65 (2010).

127. McCartney, D. G. Grain refining of aluminium and its alloys using inoculants. *Int. Mater. Rev.* **34,** (1989).

128. Introduction to Inorganic Chemistry/Redox Stability and Redox Reactions - Wikibooks, open books for an open world. Available at: https://en.wikibooks.org/wiki/Introduction_to_Inorganic_Chemistry/Redox_Stability_and_Redox_Reactions. (Accessed: 12th June 2017)

129. Fan, Z. *et al.* Grain refining mechanism in the Al/Al–Ti–B system. *Acta Mater.* **84,** 292–304 (2015).

130. Youssef, Y. M., Dashwood, R. J. & Lee, P. D. Effect of clustering on particle pushing and solidification behaviour in TiB2 reinforced aluminium PMMCs. *Compos. Part A Appl. Sci. Manuf.* **36,** 747–763 (2005).

131. Quested, T. E., Greer, A. L. & Cooper, P. S. The variable potency of TiB2 nucleant particles in the grain refinement of aluminium by Al-Ti-B additions. *Alum. Alloy. 2002 Their Phys. Mech. Prop. Pts 1-3* **396–4,** 53–58 (2002).

132. Greer, B. A. L. *et al.* Grain Refinement of Aluminium Alloys by Inoculation. 81–91 (2003).

133. Quested, T. . & Greer, a. . The effect of the size distribution of inoculant particles

on as-cast grain size in aluminium alloys. *Acta Mater.* **52,** 3859–3868 (2004).